

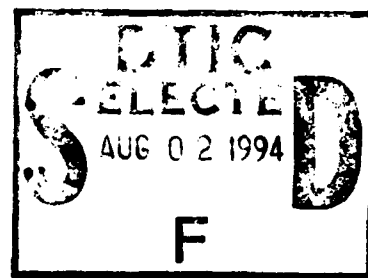
WL-TR-94-5028

**AD-A282 880**



**DIGITAL LOGIC AND RECONFIGURABLE  
INTERCONNECTS USING ALUMINUM GALLIUM  
ARSENIDE ELECTRO-OPTIC FREDKIN GATES**

**JAMES G. GROTE  
E-O Techniques & Applications Branch  
Solid State Electronics Directorate  
Air Force Materiel Command**



**June 1994**

**Interim Report For 10/01/92-05/31/94**

**APPROVED FOR PUBLIC RELEASE; DISTRIBUTION IS UNLIMITED.**

**DTIC QUALITY INSPECTED 1**

**Solid State Electronics Directorate  
Wright Laboratory  
Air Force Materiel Command  
Wright-Patterson Air Force Base, OH 45433-7331**

**94-24292**



**94 8 01 0511**

## NOTICE

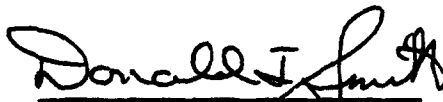
WHEN GOVERNMENT DRAWINGS, SPECIFICATIONS, OR OTHER DATA ARE USED FOR ANY PURPOSE OTHER THAN IN CONNECTION WITH A DEFINITELY GOVERNMENT-RELATED PROCUREMENT, THE UNITED STATES GOVERNMENT INCURS NO RESPONSIBILITY OR ANY OBLIGATION WHATSOEVER. THE FACT THAT THE GOVERNMENT MAY HAVE FORMULATED OR IN ANY WAY SUPPLIED THE SAID DRAWINGS, SPECIFICATIONS, OR OTHER DATA, IS NOT TO BE REGARDED BY IMPLICATION, OR OTHERWISE IN ANY MANNER CONSTRUED, AS LICENSING THE HOLDER, OR ANY OTHER PERSON OR CORPORATION: OR AS CONVEYING ANY RIGHTS OR PERMISSION TO MANUFACTURE, USE, OR SELL ANY PATENTED INVENTION THAT MAY IN ANY WAY BE RELATED THERETO.

This report is releasable to the National Information Service (NTIS). At NTIS, it will be available to the general public, including foreign nations.

THIS TECHNICAL REPORT HAS BEEN REVIEWED AND IS APPROVED FOR PUBLICATION.

  
JAMES G. GROTE, Sr. EE  
E-O Techniques & Appl. Branch  
Electro-Optics Division

  
JOHN O. CRIST, Actg. Chief  
E-O Techniques & Appl. Branch  
Electro-Optics Division

  
DONALD J. SMITH, Actg. Chief  
Electro-Optics Division  
S. S. Electronics Directorate

If your address has changed, if you wish to be removed from our mailing list, or if the addressee is no longer employed by your organization please notify WL/ELOT, WPAFB, OH 45433-7331 to help us maintain a current mailing list.

Copies of this report should not be returned unless return is required by security considerations, contractual obligations, or notice on a specific document.

REPORT DOCUMENTATION PAGE			Form Approved OMB No. 0704-0188	
<small>Public reporting burden for this collection of information is estimated to average 1 hour per response, including the time for reviewing instructions, searching existing data sources, gathering and maintaining the data needed, and completing and reviewing the collection of information. Send comments regarding this burden estimate or any other aspect of this collection of information, including suggestions for reducing this burden, to Washington Headquarters Services, Directorate for Information Operations and Reports, 1215 Jefferson Davis Highway, Suite 1204, Arlington, VA 22202-4302, and to the Office of Management and Budget, Paperwork Reduction Project (0704-0188), Washington, DC 20503.</small>				
1. AGENCY USE ONLY (Leave blank)		2. REPORT DATE June 1994		3. REPORT TYPE AND DATES COVERED Interim, Oct 92 - May 94
4. TITLE AND SUBTITLE  Digital Logic and Reconfigurable Interconnects Using Aluminum Gallium Arsenide Electro-Optic Fredkin Gates			5. FUNDING NUMBERS  PE 62204F PR 2001 TA 05 WU 12	
6. AUTHOR(S)  James G. Grote				
7. PERFORMING ORGANIZATION NAME(S) AND ADDRESS(ES)  E/O Techniques & Applications Branch WL/ELOT Bldg. 22-B, 2700 D St., Suite 2 Wright-Patterson AFB OH 45433-7405			8. PERFORMING ORGANIZATION REPORT NUMBER	
9. SPONSORING / MONITORING AGENCY NAME(S) AND ADDRESS(ES)  Solid State Electronics Directorate Wright Laboratory Air Force Materiel Command Wright-Patterson AFB OH 45433-7331			10. SPONSORING / MONITORING AGENCY REPORT NUMBER  WL-TR-94-5028	
11. SUPPLEMENTARY NOTES  This is an in-house research report				
12a. DISTRIBUTION / AVAILABILITY STATEMENT  Approved for public release, distribution unlimited			12b. DISTRIBUTION CODE	
13. ABSTRACT (Maximum 200 words)  This report describes digital logic operations and reconfigurable optical interconnects realized from aluminum gallium arsenide (AlGaAs) electro-optic Fredkin gates. The Fredkin gates fabricated for this effort were channel waveguide type passive and active AlGaAs zero-gap directional couplers (ZGDC's). The first AND logic gate reported in the open literature using AlGaAs ZGDC's is demonstrated along with a reconfigurable optical interconnect. Models predicting the refractive index of AlGaAs versus Al concentration and wavelength are treated. A model for predicting the electro-optic coefficient of AlGaAs versus Al concentration and wavelength is developed. Models for predicting the interaction length and switching voltage are optimized for AlGaAs. Fabrication techniques for AlGaAs ZGDC's are formulated. The performance of the actual AlGaAs ZGDC's fabricated for this effort fit the models exceptionally well. Correlation of experimental and theoretical results yielded a mole fraction of Al of 30% for the core and 35% for the cladding. A refractive index of 3.420 for 30% Al and 3.388 for 35% Al at $\lambda = 827$ nm were determined. A linear EO coefficient of $r_{41} = -1.49$ pm/V at $\lambda = 827$ nm was inferred for the core layer. A switching voltage of 7.6 VDC was achieved for an AlGaAs ZGDC with a 5000 $\mu$ m interaction channel length.				
14. SUBJECT TERMS  Integrated Optics, Fredkin Gates, Zero-Gap Directional Couplers, AlGaAs Waveguides			15. NUMBER OF PAGES 301	
			16. PRICE CODE	
17. SECURITY CLASSIFICATION OF REPORT  UNCLASSIFIED	18. SECURITY CLASSIFICATION OF THIS PAGE  UNCLASSIFIED	19. SECURITY CLASSIFICATION OF ABSTRACT  UNCLASSIFIED	20. LIMITATION OF ABSTRACT  UNLIMITED	

*To My Parents*

*Robert Joseph and Marianne Grote*



## FOREWORD

This dissertation describes digital logic operations and reconfigurable optical interconnects realized from aluminum gallium arsenide (AlGaAs) electro-optic Fredkin gates. The Fredkin gates fabricated for this effort were channel waveguide type passive and active AlGaAs zero-gap directional couplers (ZGDC's). The first AND logic gate reported in the open literature using AlGaAs ZGDC's is demonstrated. A reconfigurable optical interconnect is demonstrated. The theory behind the Fredkin gate and the ZGDC is presented. Several models predicting the refractive index of AlGaAs versus Al concentration and wavelength are treated. The electro-optic properties of AlGaAs are also presented. A model for predicting the electro-optic coefficient of AlGaAs versus Al concentration and wavelength is developed. Models for predicting the interaction length and behavior of ZGDC's, as well as the switching voltage, are presented and optimized for AlGaAs. Fabrication techniques for AlGaAs ZGDC's are formulated and analyzed. Device characterization techniques are presented. The performance of the actual AlGaAs ZGDC's fabricated for this effort fit the

models exceptionally well. Fabrication tolerances are also addressed for both passive and active devices. Issues for integration of AlGaAs ZGDC's into practical circuits are addressed.

Correlation of the experimental and theoretical results yielded a mole fraction of Al of 30% for the core layer and 35% for the cladding layers. Refractive indices of  $3.420 \pm 0.003$  for 30% Al and  $3.388 \pm 0.003$  for 35% Al at a wavelength  $\lambda = 827$  nm were determined. A linear electro-optic coefficient of  $r_{41} = -1.49 \pm 0.08 \times 10^{-12}$  m/V at  $\lambda = 827$  nm was inferred for the core layer. A switching voltage of  $7.6 \text{ VDC} \pm 0.3 \text{ VDC}$  was achieved for an AlGaAs ZGDC with a  $5000 \mu\text{m}$  interaction channel length. This is the lowest switching voltage reported in the open literature for an active  $\text{Al}_x\text{Ga}_{1-x}\text{As}$  ZGDC with a  $5000 \mu\text{m}$  interaction channel length. Propagation losses measured  $0.5 - 1 \text{ dB/cm}$ . Device losses measured  $3 - 7 \text{ dB}$ .

Accession For	
NTIS CRA&I	<input checked="" type="checkbox"/>
DTIC TAB	<input type="checkbox"/>
Unannounced	<input type="checkbox"/>
Justification _____	
By _____	
Distribution /	
Availability Codes	
Dist	Avail and/or Special
A-1	

## ACKNOWLEDGEMENTS

I would like to express my sincere appreciation to many individuals for their help and support during the course of this effort. First, I wish to thank my advisor, professor Mohammad Karim, for his guidance and encouragement during my studies at the University of Dayton. His integrity and commitment to his students are qualities to be commended. I would also like to thank professors Frank Scarpino, Bernhard Schmidt, John Westerkamp and Muhammad Islam for their participation on my dissertation committee (for both advising and reviewing).

My deep appreciation goes to my colleague, Joseph Brandelik, for his helpful discussions and support. He has contributed greatly to my development as a researcher. I would also like to thank other members of the Wright-Laboratory/Solid State Electronics Directorate (WL/EL), which include: Edward Stutz for molecular beam epitaxy material growth; John Barrette for help with fabrication techniques; Charles Havasy for scanning electron microscope (SEM) inspection; Carol Isbill for metallization; Wayland Williams for test circuit design and fabrication; and Samuel Adams and Art Becraft for design and fabrication of the bases and mounts used for the waveguide characterization system

(WCS).

Several employees from Technology Scientific Services and Wright State University, working for WL/EL, were also involved. They include Paul Cassity for reactive ion etch of the waveguides and help with processing; David Via for generation of the waveguide masks and SEM inspection; Donald Reynolds for taking the photoluminescence measurements; and Samuel LeForge for design and fabrication of the bases and mounts for the WCS.

Several of the photographs were taken by Mark Pugel of the WL Multi Media Center. All of the photographs were half-toned by David Gerdeman of the WL Visual Information Branch.

I wish to express my gratitude to Anis Husain of the Advanced Research Projects Agency (ARPA) for the contribution of crystal structures grown by Honeywell for this project as part of the Opto-Electronics Technology Consortia. Thanks to Mary Hibbs-Brenner of Honeywell who performed the metal-organic chemical vapor deposition material growth and characterization. Anthony Ticknor, of Lockheed, was responsible for the beam propagation method computer program. I have also enjoyed valuable discussions with Julian Bristow and Charles Sullivan of Honeywell.

My greatest thanks and appreciation goes to my dear wife, Camden. There are no words to adequately describe the help, patience, understanding and encouragement she gave me during the course of my graduate study.

## TABLE OF CONTENTS

FOREWORD .....	iii
ACKNOWLEDGMENTS .....	v
LIST OF ILLUSTRATIONS .....	x
LIST OF TABLES .....	xvii

### CHAPTER

I. INTRODUCTION .....	1
Fredkin Gate and Conservative Logic	
Digital Logic and the Fredkin Gate	
Optical Fredkin Gates	
Directional Coupler Switch	
Zero-Gap Directional Coupler Switch	
Wavefront Tilt	
Electrode Separation	
Thesis Organization	
II. OPTICAL PROPERTIES OF ALUMINUM GALLIUM ARSENIDE .....	36
Refractive Index	
Section 2.1	
Section 2.2	
Section 2.3	
Refractive Index of the Waveguide Core	
Refractive Index of the Waveguide Clad	
$\text{Al}_x\text{Ga}_{1-x}\text{As}$ Waveguide Structure	

III. DETERMINATION OF THE INTERACTION LENGTH OF THE ZERO-GAP DIRECTIONAL COUPLER .....	76
Marcatili Rectangular Dielectric Waveguide Model	
TE <sub>pq</sub> Modes	
TM <sub>pq</sub> Modes	
Marcuse Rectangular Dielectric Waveguide Model	
TE <sub>pq</sub> Modes	
TM <sub>pq</sub> Modes	
Burns and Milton Effective Index Method	
TE <sub>pq</sub> Modes	
TM <sub>pq</sub> Modes	
Fleck, Morris and Feit Beam Propagation Method	
IV. ELECTRO-OPTIC PROPERTIES OF ALUMINUM GALLIUM ARSENIDE .....	129
Linear Electro-Optic Effect	
Index Ellipsoid	
Electro-Optic Coefficients	
Induced Refractive Indices and Birefringence	
Electro-Optic Modulation	
V. EXPERIMENTAL PROCEDURES AND DEVICE CHARACTERIZATION .....	161
Material Growth	
Determination of $r_{41}$	
Al <sub>x</sub> Ga <sub>1-x</sub> As Device Fabrication and Characterization	
Straight and Crossthrough Waveguides	
Passive Zero-Gap Directional Couplers	
Active Zero-Gap Directional Couplers	
Optical Digital Logic	
VI. RESULTS .....	223
Interaction Length	
Passive Zero-Gap Directional Coupler	
Active Zero-Gap Directional Coupler	
Switching Voltage	
Digital Logic and Reconfigurable Interconnects	

VII. SUMMARY AND CONCLUSIONS .....	242
Suggestions for Improvement and Further Research	
APPENDICES	
Appendix A - Photoluminescence Measurements .....	251
Appendix B - Processing Techniques .....	258
Passive Devices	
Active Devices	
Appendix C - Equipment List .....	265
Modelling	
Material Growth	
Fabrication	
Characterization	
Miscellaneous	
BIBLIOGRAPHY .....	268

## LIST OF ILLUSTRATIONS

1.0.1	Power Requirements for Optical and Electrical Interconnects versus Data Rate .....	2
1.1.1	Basic Fredkin Gate .....	7
1.1.2	Operation of Fredkin Gate with Control Line Low .....	8
1.1.3	Operation of Fredkin Gate with Control Line High .....	9
1.2.1	AND Operation using Fredkin Gate .....	11
1.2.2	OR Operation using Fredkin Gate .....	12
1.2.3	NAND Operation using Fredkin Gates .....	13
1.2.4	J-K Flip Flop Operation using Fredkin Gates .....	14
1.2.5	Conservative Logic Operation and its Inverse using Fredkin Gates .....	16
1.2.6	NAND Operation Connected to its Inverse using Fredkin Gates .....	18
1.2.7	Garbageless NAND Operation using Conservative and Inverse Conservative Logic Fredkin Gates with "Spy" Fredkin Gate .....	19
1.3.1	Schematic of a Zero-Gap Directional Coupler .....	23
1.4.1	Operation of a Directional Coupler .....	28
1.5.1	Operation of a Zero-Gap Directional Coupler .....	32



2.1.1	Refractive Index of $\text{Al}_x\text{Ga}_{1-x}\text{As}$ versus Wavelength . . . . .	42
2.2.1	Critical Point Energies for $\text{Al}_x\text{Ga}_{1-x}\text{As}$ versus Al Concentration . . . . .	46
2.2.2	Refractive Index of $\text{Al}_x\text{Ga}_{1-x}\text{As}$ versus Photon Energy for $x = 0.200 \pm 0.020$ . . . . .	47
2.2.3	Refractive Index of $\text{Al}_x\text{Ga}_{1-x}\text{As}$ versus Photon Energy for $x = 0.240 \pm 0.020$ . . . . .	48
2.2.4	Refractive Index of $\text{Al}_x\text{Ga}_{1-x}\text{As}$ versus Photon Energy for $x = 0.290 \pm 0.020$ . . . . .	49
2.2.5	Refractive Index of $\text{Al}_x\text{Ga}_{1-x}\text{As}$ versus Photon Energy for $x = 0.380 \pm 0.020$ . . . . .	50
2.3.1	Critical Point Energies for $\text{Al}_x\text{Ga}_{1-x}\text{As}$ versus Al Concentration . . . . .	54
2.3.2	Refractive Index of $\text{Al}_x\text{Ga}_{1-x}\text{As}$ versus Photon Energy for $x = 0.198 \pm 0.020$ . . . . .	61
2.3.3	Refractive Index of $\text{Al}_x\text{Ga}_{1-x}\text{As}$ versus Photon Energy for $x = 0.315 \pm 0.020$ . . . . .	62
2.3.4	Refractive Index of $\text{Al}_x\text{Ga}_{1-x}\text{As}$ versus Photon Energy for $x = 0.419 \pm 0.020$ . . . . .	63
2.4.1	Refractive Index of $\text{Al}_x\text{Ga}_{1-x}\text{As}$ versus Wavelength for $x = 0.300$ . . . . .	64
2.4.2	Refractive Index of $\text{Al}_x\text{Ga}_{1-x}\text{As}$ versus Wavelength for $x = 0.300 \pm 0.020$ . . . . .	66
2.4.3	Refractive Index of $\text{Al}_x\text{Ga}_{1-x}\text{As}$ versus Wavelength For $x = 0.300 \pm 0.020$ . . . . .	68
2.5.1	Single Mode $n_{\text{cutoff}}$ for $\text{Al}_{0.30}\text{Ga}_{0.70}\text{As}$ Core and $n_{\text{clad}}$ for $\text{Al}_{0.35}\text{Ga}_{0.65}\text{As}$ Clad versus Wavelength . . . . .	70

2.5.2	Single Mode $n_{\text{cutoff}}$ for $\text{Al}_{0.295}\text{Ga}_{0.705}\text{As}$ Core and $n_{\text{clad}}$ for $\text{Al}_{0.365}\text{Ga}_{0.645}\text{As}$ Clad versus Wavelength . . . . .	73
3.0.1	Rectangular Waveguide Directional Coupler . . . . .	77
3.1.1	Rectangular Waveguide Directional Coupler Cross Section . . . . .	80
3.1.2	Field Intensity Profiles of the Symmetric and Antisymmetric Modes in a Rectangular Directional Coupler . . . . .	85
3.2.1	Trajectory of a Guided Wave in a Slab Waveguide . . . . .	92
3.3.1	Analytical Model for the Effective Index Method for $\text{TE}_{pq}$ Modes . . . . .	105
3.4.1	Amplitudes of the Propagating Fields in an $\text{Al}_x\text{Ga}_{1-x}\text{As}$ Waveguide with an S-Bend . . . . .	127
4.0.1	Index Surfaces for (a) a Positive Uniaxial Crystal and (b) a Negative Uniaxial Crystal . . . . .	131
4.2.1	Inner Ellipse is the Intersection of the Index Ellipsoid with the Plane Perpendicular to $s$ . . . . .	139
4.4.1	Transverse Electro-Optic Modulator using a Cubic $\bar{4}3m$ Group Crystal . . . . .	152
4.4.2	Representation of a GaAs Crystal . . . . .	153
5.1.1	MBE Growth Process for $\text{Al}_x\text{Ga}_{1-x}\text{As}$ . . . . .	163
5.1.2	MOCVD Growth Process for $\text{Al}_x\text{Ga}_{1-x}\text{As}$ . . . . .	164
5.1.3	Target $\text{Al}_x\text{Ga}_{1-x}\text{As}$ Structure . . . . .	166
5.2.1	Piezoelectric Coefficient for $\text{Al}_x\text{Ga}_{1-x}\text{As}$ versus Al Concentration at $\lambda = 827 \text{ nm}$ . . . . .	181
5.2.2	Piezoelectric Coefficient for $\text{Al}_x\text{Ga}_{1-x}\text{As}$ versus Wavelength for $x = 0.300$ . . . . .	182

5.2.3	Linear Electro-Optic Coefficients for $\text{Al}_x\text{Ga}_{1-x}\text{As}$ versus Al Concentration at $\lambda = 827 \text{ nm}$ . . . . .	187
5.2.4	Linear Electro-Optic Coefficients for $\text{Al}_x\text{Ga}_{1-x}\text{As}$ versus Wavelength for $x = 0.300$ . . . . .	188
5.3.1	SEM Aerial View of an $\text{Al}_x\text{Ga}_{1-x}\text{As}$ Straight Waveguide . . . .	191
5.3.2	Sidewall Morphology of an $\text{Al}_x\text{Ga}_{1-x}\text{As}$ Waveguide using RIE . . . . .	192
5.3.3	Waveguide Characterization System . . . . .	194
5.3.4	CCD Image of Laser Beam Propagating through an $\text{Al}_x\text{Ga}_{1-x}\text{As}$ Straight Waveguide . . . . .	195
5.3.5	Photomicrographic Aerial View of an $\text{Al}_x\text{Ga}_{1-x}\text{As}$ Crossthrough . . . . .	197
5.3.6	CCD Image of Laser Beam Propagating through an $\text{Al}_x\text{Ga}_{1-x}\text{As}$ Crossthrough Waveguide . . . . .	198
5.4.1	Schematic of Mask Layout for a Passive $\text{Al}_x\text{Ga}_{1-x}\text{As}$ Zero-Gap Directional Coupler with a $200 \mu\text{m}$ Interaction Length . . . . .	200
5.4.2	Photomicrographic Aerial View of a Passive $\text{Al}_x\text{Ga}_{1-x}\text{As}$ Zero-Gap Directional Coupler with a $200 \mu\text{m}$ Interaction Length . . . . .	201
5.4.3	SEM Aerial View of the Input Channel of a Passive $\text{Al}_x\text{Ga}_{1-x}\text{As}$ Zero-Gap Directional Coupler . . . . .	202
5.4.4	SEM Aerial View of the Interaction Channel Section of a Passive $\text{Al}_x\text{Ga}_{1-x}\text{As}$ Zero-Gap Directional Coupler . . . . .	203
5.4.5	SEM Aerial View of the Intersection of the Input Channels and the Interaction Channel of a Passive $\text{Al}_x\text{Ga}_{1-x}\text{As}$ Zero-Gap Directional Coupler . . . . .	204

5.4.6	CCD Image of Laser Beam Propagating through a Passive $\text{Al}_x\text{Ga}_{1-x}\text{As}$ Zero-Gap Directional Coupler with a 200 $\mu\text{m}$ Interaction Length .....	206
5.4.7	CCD Image of Laser Beam Propagating through a Passive $\text{Al}_x\text{Ga}_{1-x}\text{As}$ Zero-Gap Directional Coupler with a 400 $\mu\text{m}$ Interaction Length .....	207
5.4.8	Normalized Intensity Plotted against $\sin^2(\Phi_0 L)$ with $L = 196$ $\mu\text{m}$ versus Interaction Channel Length for Passive $\text{Al}_x\text{Ga}_{1-x}\text{As}$ Zero-Gap Directional Coupler .....	208
5.5.1	Schematic of Mask Layout for (a) the Waveguide Pattern and (b) the Electrode Pattern for an Active $\text{Al}_x\text{Ga}_{1-x}\text{As}$ Zero-Gap Directional Coupler with a 5000 $\mu\text{m}$ Interaction Length .....	210
5.5.2	Photomicrographic Aerial View of the Center Region of an Active $\text{Al}_x\text{Ga}_{1-x}\text{As}$ Zero-Gap Directional Coupler .....	213
5.5.3	SEM Aerial View of the Input Channel of an Active $\text{Al}_x\text{Ga}_{1-x}\text{As}$ Zero-Gap Directional Coupler .....	214
5.5.4	SEM Aerial View of the Interaction Channel Section of an Active $\text{Al}_x\text{Ga}_{1-x}\text{As}$ Zero-Gap Directional Coupler .....	215
5.5.5	CCD Image of Laser Beam at the Output of an Active $\text{Al}_x\text{Ga}_{1-x}\text{As}$ Zero-Gap Directional Coupler with Input at Channel 2 (no Voltage Applied) .....	216
5.5.6	CCD Image of Laser Beam at the Output of an Active $\text{Al}_x\text{Ga}_{1-x}\text{As}$ Zero-Gap Directional Coupler with Input at Channel 2 (18 VDC Applied) .....	218
5.5.7	$\sin^2(\Phi_0 L)$ of $\text{TE}_{00}$ Mode Plotted Against $\sin^2(\Phi_0 L)$ and Polarization Rotation versus Applied Voltage for Output Channel 1 .....	219
5.5.8	$\cos^2(\Phi_0 L)$ of $\text{TE}_{00}$ Mode Plotted Against $\cos^2(\Phi_0 L)$ and Polarization Rotation versus Applied Voltage for Output Channel 2 .....	220

5.6.1	AND Gate Realized with a Active $\text{Al}_x\text{Ga}_{1-x}\text{As}$ Zero-Gap Directional Coupler .....	222
6.1.1	Interaction Length versus Waveguide Separation using Marcatili Model .....	225
6.1.2	Amplitudes of the Propagating Fields in a Passive $\text{Al}_{0.298}\text{Ga}_{0.351}\text{As}$ Zero-Gap Directional Coupler with a $189\text{ }\mu\text{m}$ Interaction Length .....	227
6.2.1	Amplitudes of the Propagating Fields in an Active $\text{Al}_{0.298}\text{Ga}_{0.351}\text{As}$ Zero-Gap Directional Coupler with a $123\text{ }\mu\text{m}$ Interaction Length and $5000\text{ }\mu\text{m}$ Interaction Channel (no Voltage Applied) .....	230
6.2.2	Amplitudes of the Propagating Fields in an Active $\text{Al}_{0.298}\text{Ga}_{0.351}\text{As}$ Zero-Gap Directional Coupler with a $124\text{ }\mu\text{m}$ Interaction Length and $5000\text{ }\mu\text{m}$ Interaction Channel (no Voltage Applied) .....	231
6.2.3	Amplitudes of the Propagating Fields in an Active $\text{Al}_{0.298}\text{Ga}_{0.351}\text{As}$ Zero-Gap Directional Coupler with a $123\text{ }\mu\text{m}$ Interaction Length and $5040\text{ }\mu\text{m}$ Interaction Channel (no Voltage Applied) .....	236
6.2.4	Amplitudes of the Propagating Fields in an Active $\text{Al}_{0.298}\text{Ga}_{0.351}\text{As}$ Zero-Gap Directional Coupler with a $123\text{ }\mu\text{m}$ Interaction Length and $5040\text{ }\mu\text{m}$ Interaction Channel (Switching Voltage Applied) .....	237
6.2.5	SEM Aerial View of the Interaction Channel Section of an Active $\text{Al}_x\text{Ga}_{1-x}\text{As}$ Zero-Gap Directional Coupler .....	239
7.1.1	Schematic of a Reconfigurable Integrated Electro-Optic Circuit .....	243
A.1	Photoluminescence Measurement of Sample 121 taken at $3^\circ\text{K}$ .....	252
A.2	Photoluminescence Measurement of Sample 121 taken at $300^\circ\text{K}$ .....	253

<b>A.3</b>	<b>Photoluminescence Measurement of Sample 121 taken at 300°K</b>	<b>254</b>
<b>A.4</b>	<b>Photoluminescence Measurement of Sample 562 taken at 3°K</b>	<b>255</b>
<b>A.5</b>	<b>Photoluminescence Measurement of Sample 1108 taken at 3°K</b>	<b>256</b>
<b>A.6</b>	<b>Photoluminescence Measurement of Sample 179 taken at 3°K</b>	<b>257</b>

## LIST OF TABLES

1.1.1	Representation of Fredkin Gate Logic .....	10
2.1.1	Sellmeir Coefficients for $\text{Al}_x\text{Ga}_{1-x}\text{As}$ .....	40
5.1.1	Growth Parameters for $\text{Al}_x\text{Ga}_{1-x}\text{As}$ Structure using the Varian 360, GEN 1.5 and GEN 2 MBE .....	168
5.1.2	Growth Parameters for $\text{Al}_x\text{Ga}_{1-x}\text{As}$ Structure using the AIX 200 MOCVD .....	169
5.1.3	Al Concentration Determined from Photoluminescence Measurements .....	171
5.1.4	Core and Clad Thickness for $\text{Al}_x\text{Ga}_{1-x}\text{As}$ Samples 121 and 128 .....	175
5.2.1	Linear Electro-Optic Coefficients for $\text{Al}_x\text{Ga}_{1-x}\text{As}$ Samples 121 and 128 at $\lambda = 827 \text{ nm}$ .....	189
6.1.1	Interaction Length versus the Various Waveguide Structures and Channel Widths .....	228
6.2.1	Switching Voltage versus the Various Waveguide Structures and Electro-Optic Coefficients .....	234

## CHAPTER I

### INTRODUCTION

As electronic and optical data processing circuits approach multi-gigahertz operation rates, the need for multi-gigahertz communication between these processing circuits becomes essential. This communication includes chip-to-chip on a common multichip module, multichip module-to-multichip module on a common board and board-to-board through a common backplane. The data rates at which communication through electrical interconnects can be transmitted is limited to the low gigahertz rates, unless one is willing to expend large amounts of power. This results from the fact that electrical wires and striplines possess frequency dependent dissipative losses due to conductive and dielectric properties, and frequency dependent parasitic coupling losses due to radiative and surface wave propagation properties.<sup>1</sup> The higher the frequency, the higher the losses. This is where optics can provide solutions. Optical interconnects can transmit data at optical frequencies with orders of magnitude lower losses than their electrical counterparts. The power requirements of optical and



electrical interconnects versus data rate is illustrated in Fig. 1.0.1. Fig. 1.0.1 was generated using the following: Waveguide lengths for both the electronic and optical interconnects were 50 mm. The total number of interconnects was 600 for both types. For electrical interconnects on an alumina substrate, waveguide widths of  $25\ \mu\text{m}$  and waveguide heights of  $650\ \mu\text{m}$  were assumed. The effective and relative permittivities of the microstrip used were 6.7 and 9.9, respectively.<sup>1</sup> The capacitance used per line was 6 pF and an impedance of  $50\ \Omega$  was assumed.<sup>1</sup> The power versus data rate for the electrical interconnects was determined with the methods given by Edwards.<sup>1</sup> For optical interconnects on a gallium arsenide (GaAs) substrate, waveguide widths of  $3\ \mu\text{m}$  and waveguide heights of  $1\ \mu\text{m}$  were assumed. Waveguide losses of 0.2 dB/cm were used at 1 GHz growing as 0.08 dB/GHz.<sup>58,152</sup> The modulator loss used was  $5 \times 10^{-6}\ \text{W/channel}$  at 1 GHz growing as  $5 \times 10^{-6}\ \text{W/GHz}$ .<sup>152</sup> The detector capacitance used was 0.3 pF and the detector amplifier capacitance used was 1.7 pF.<sup>152</sup> The power used, per detector, was  $1 \times 10^{-3}\ \text{W/channel}$  at 1 GHz growing as  $1 \times 10^{-3}\ \text{W/GHz}$ .<sup>152</sup> The laser power used was 100 mW at 1 GHz lessening at the same rate as the waveguide loss per GHz.<sup>152</sup> Finally, 20% electrical efficiency and 50% optical coupling efficiency was assumed for the laser. The power versus data rate was then determined by adding up the power usage of the separate components.<sup>152</sup>

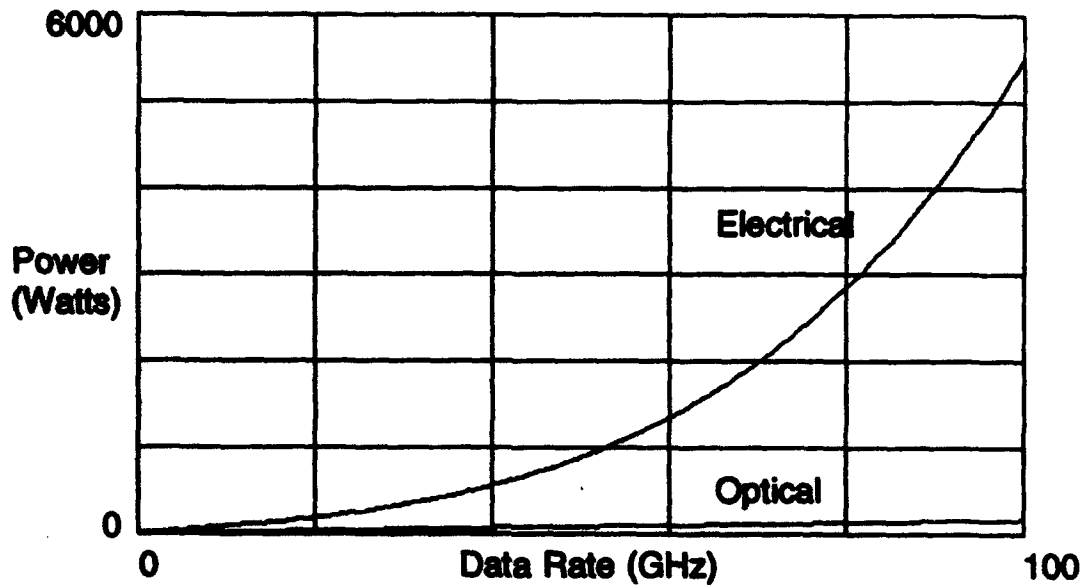


**Figure 1.0.1**  
**Power Requirements for Optical and Electrical**  
**Interconnects versus Data Rate**

In addition to the lower power consumption and higher bandwidth, optical interconnects offer isolation from electro-magnetic interference (EMI).<sup>2</sup> Optical interconnects are starting to be utilized in chassis-to-chassis and board-to-board communication using glass optical fibers.<sup>153</sup> On the smaller scale of multichip modules and within-chip, integrated optics is just beginning to emerge.<sup>2,3,16,39-44,53,67,97,102,106-107,151-155</sup> Integrated optics offers the additional advantages of smaller interconnect widths and in-plane crossover capability with very low crosstalk. This eliminates the need for air bridges. Thus, less wafer and board real estate will be required for optical interconnections, which provides room for additional circuits and devices. Fabrication processes for integrated optics must be compatible with those used for the manufacture of electronic interconnects and devices. This is important from the standpoints of practicality and acceptability. Aluminum gallium arsenide (AlGaAs), as well as other III-V semiconductors, is an attractive material because one can fabricate not only electronic integrated circuits in it, but also laser sources, detectors, opto-electronic integrated circuits and optical waveguides. AlGaAs also possesses electro-optical effects which can be utilized to fabricate optical switches.

Optical switches can be incorporated with optical waveguides and other optical switches to realize digital logic operations or, very importantly, reconfigurable interconnects. Current research to develop processing

techniques for AlGaAs optical waveguides and devices has shown that the processing techniques for these optical circuits are compatible with the techniques used for the fabrication of electronic circuitry in GaAs.<sup>3,138-145</sup> Therefore, by using AlGaAs and GaAs, one can house the entire electronic/opto-electronic circuit on a single substrate. With the incorporation of AlGaAs and GaAs opto-electronic circuits and optical waveguides, the multichip module or board, now entirely electronic, could perform more efficiently with less power consumption, move data around faster with less noise, and use less real estate.

An even more attractive benefit is the potential to reconfigure the multichip modules to either perform entirely different operations, or to route signals around inoperative or defective portions of the module. It is an area that the United States Air Force (USAF) and the Advanced Research Projects Agency (ARPA) is very much interested in pursuing. There are several on-going contractual efforts as well as several more planned to develop integrated optical interconnects.<sup>3,42,43,44,151,153,155</sup> The research topic proposed here could directly benefit or reshape such programs.

#### Fredkin Gate and Conservative Logic

Fredkin gate is a term given to a nonlinear dual input/dual output signal processing gate that performs a conditional crossover of the two input

signals via an input control signal<sup>4</sup> (see Fig. 1.1.1). When the input control signal is a logic low, the two input signals cross over as illustrated in Fig. 1.1.2. When the input control signal is a logic high, the two input signals follow a parallel path as shown in Fig. 1.1.3. The logic of the Fredkin gate can, thus, be represented by Table 1.1.1, given originally by Fredkin and Toffoli.<sup>4</sup> Fredkin et al. presented the unit wire and the Fredkin gate to form the elements on which conservative logic is based.<sup>4</sup> Fredkin et al. defined conservative logic as any Boolean function that is invertible and conservative.<sup>4</sup> By invertible, it is argued that invariance under time reversal is not required. By conservative, it is stated that the model for computation is only required to possess at least one additive conserved quantity.<sup>4</sup> Conserved quantities, such as conservation of energy, momentum and angular momentum, are functions of the system's state that remain constant. With conservative logic, it is ideally possible to build sequential circuits that dissipate no internal power.<sup>4</sup> Where the two input NAND gate forms the universal primitive for the set of all Boolean functions, the two input/two output Fredkin gate forms the signal processing universal primitive for the set of all conservative logic functions.<sup>4</sup>

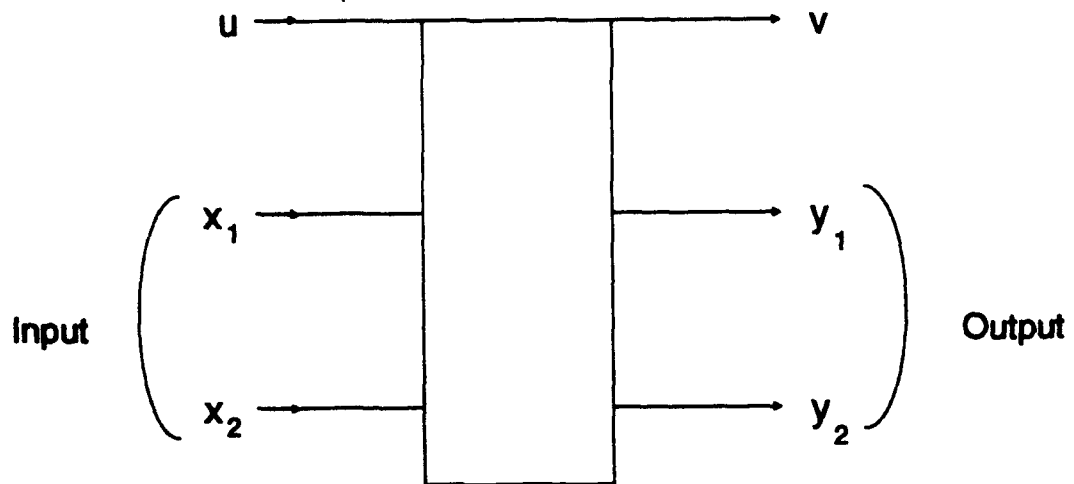


**Figure 1.1.1**  
**Basic Fredkin Gate**

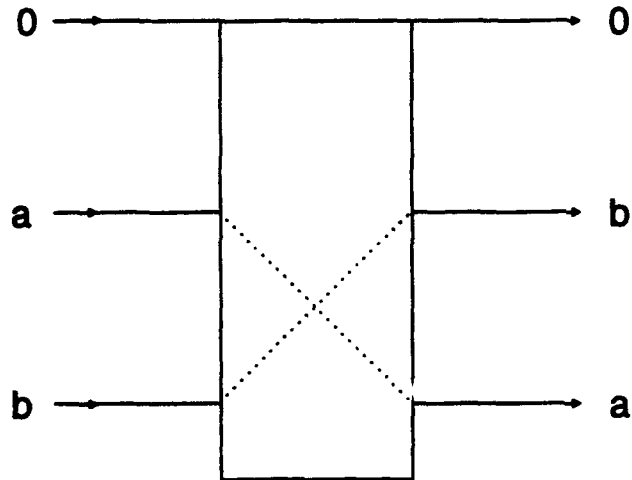


**Figure 1.1.2**  
**Operation of Fredkin Gate with Control Line Low**

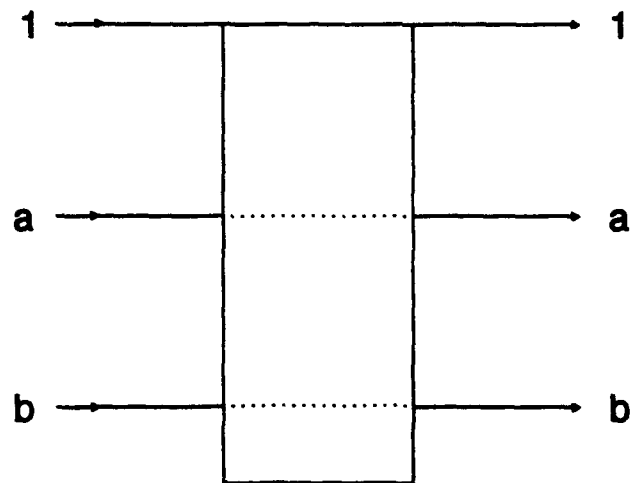


**Figure 1.1.3**  
**Operation of Fredkin Gate with Control Line High**

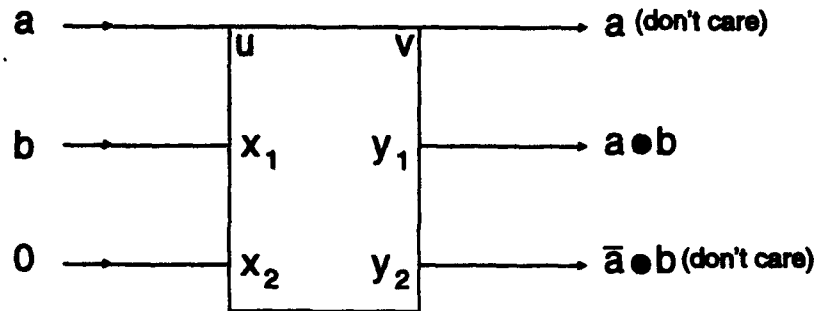


Table 1.1.1  
Representation of Fredkin Gate Logic

u	x <sub>1</sub>	x <sub>2</sub>		v	y <sub>1</sub>	y <sub>2</sub>
0	0	0		0	0	0
0	0	1		0	1	0
0	1	0		0	0	1
0	1	1	→	0	1	1
1	0	0		1	0	0
1	0	1		1	0	1
1	1	0		1	1	0
1	1	1		1	1	1

### Digital Logic and the Fredkin Gate

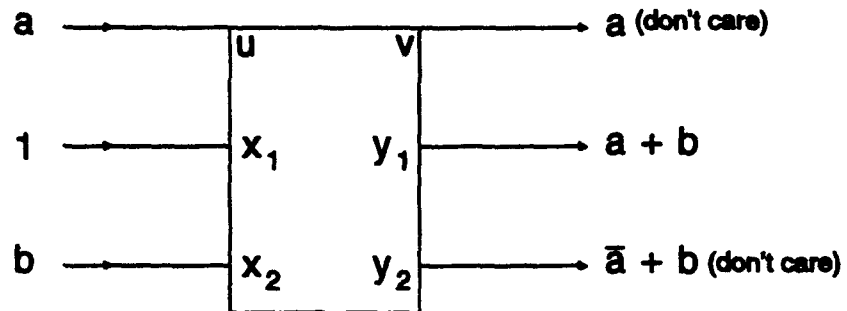
The functions we seek are often non-reversible. These include elementary Boolean functions, such as AND and OR, as well as more complex functions, such as adders and flip flops.<sup>4-11,37</sup> By supplying constants, along with the arguments to one or more Fredkin gates, one can realize many of these non-invertible functions using conservative logic. Figs. 1.2.1 - 1.2.3 show conservative logic realizations of AND, OR and NAND functions. Fig. 1.2.4 illustrates a conservative logic realization of a J-K flip flop. The unit wire, represented in Figs. 1.2.3 and 1.2.4 with a non-inverting buffer symbol, is a conservative storage-transmission primitive. It both stores data and moves data from one point of space-time to another, and it



Truth Table

Inputs			Outputs		
$u$	$x_1$	$x_1$	$v$	$y_1$	$y_1$
0	0	0	0	0	0
0	1	0	0	0	1
1	0	0	1	0	0
1	1	0	1	1	0

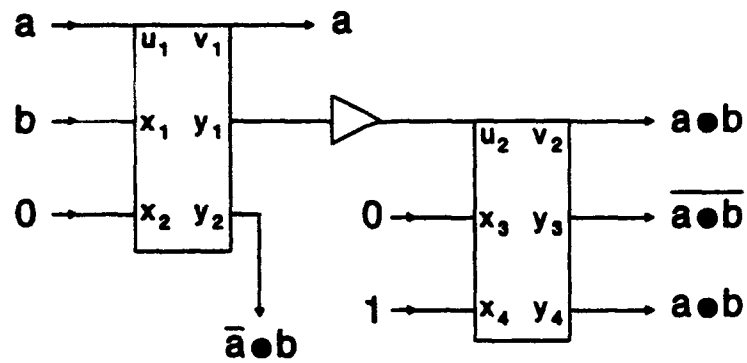
Figure 1.2.1  
AND Operation using Fredkin Gate



Truth Table

Inputs			Outputs		
$u$	$x_1$	$x_1$	$v$	$y_1$	$y_1$
0	1	0	0	0	1
0	1	1	0	1	1
1	1	0	1	1	0
1	1	1	1	1	1

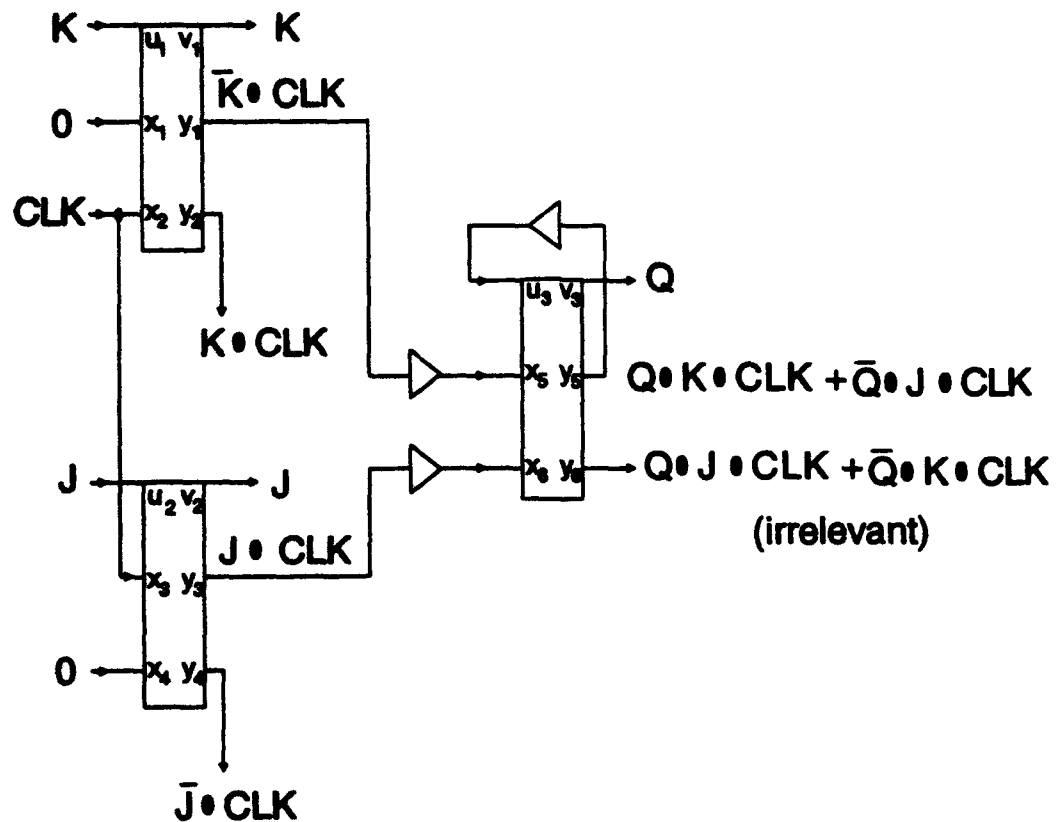
Figure 1.2.2  
OR Operation using Fredkin Gate



Truth Table

Inputs					Outputs		
$u_1$	$x_1$	$x_2$	$x_3$	$x_4$	$y_2$	$y_3$	$y_4$
0	0	0	0	1	0	1	0
0	1	0	0	1	0	1	0
1	0	0	0	1	0	1	0
1	1	0	0	1	1	0	1

Figure 1.2.3  
NAND Operation using Fredkin Gates



Truth Table

Inputs						Output	
$u_1 = K$	$u_2 = J$	$x_1$	$x_4$	$x_2$	$x_3$	$y_2 = Q(t)$	$Q(t+\Delta t)$
0	0	0	0	$\neg$	$\neg$	0	0
				$\neg$	$\neg$	1	1
0	1	0	0	$\neg$	$\neg$	0	1
				$\neg$	$\neg$	1	1
1	0	0	0	$\neg$	$\neg$	0	0
				$\neg$	$\neg$	1	0
1	1	0	0	$\neg$	$\neg$	0	1
				$\neg$	$\neg$	1	0
-	-	0	0	0	0	0	0
						1	1

Figure 1.2.4  
J-K Flip Flop Operation using Fredkin Gates

is separated by one unit of time.<sup>4</sup> The unit wire connects one conservative logic gate to another from the conventional sense that the gate is an instantaneous element and the unit wire is the delay element contained in an interconnection.<sup>4</sup> The output conserves the value present at the input. If, for every new computation, we supply a new set of constants and throw away the "don't cares" present at the output, we will dissipate energy. For almost all Boolean functions, the number of gates increases exponentially with the number of input lines and, thus, the number of "don't cares" at the output also increases exponentially.<sup>4,37</sup> This results in an exponential growth in the dissipated energy. Conservative logic reduces the degree of dissipated energy growth since the number of gates does not depend on the number of inputs. This results in energy dissipation that only has linear growth.<sup>4,11</sup> The reduction in the dissipation of energy is achieved with the introduction of inverse conservative logic.<sup>4</sup>

Inverse conservative logic is attained by replacing the conservative logic gate with its inverse.<sup>4</sup> The Fredkin gate is attractive because it coincides with its inverse. The inverse looks like a mirror image of the original. Fig. 1.2.5 shows a conservative logic realization of a logic function and its inverse using Fredkin gates. Next, by joining the original function with its inverse, and then connecting the outputs of the original Fredkin gate network to the inputs of the inverse Fredkin gate network, one will get back the

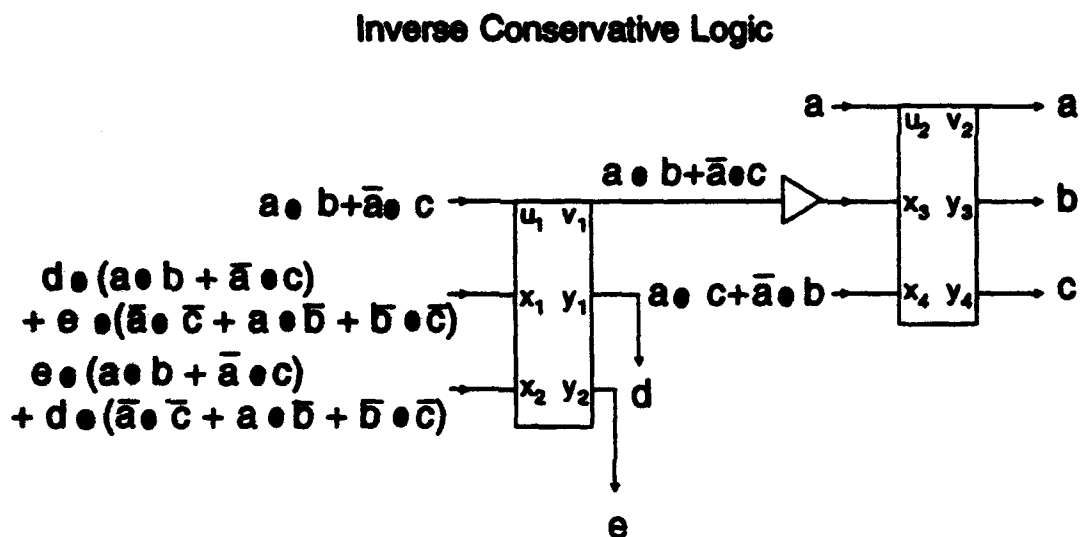
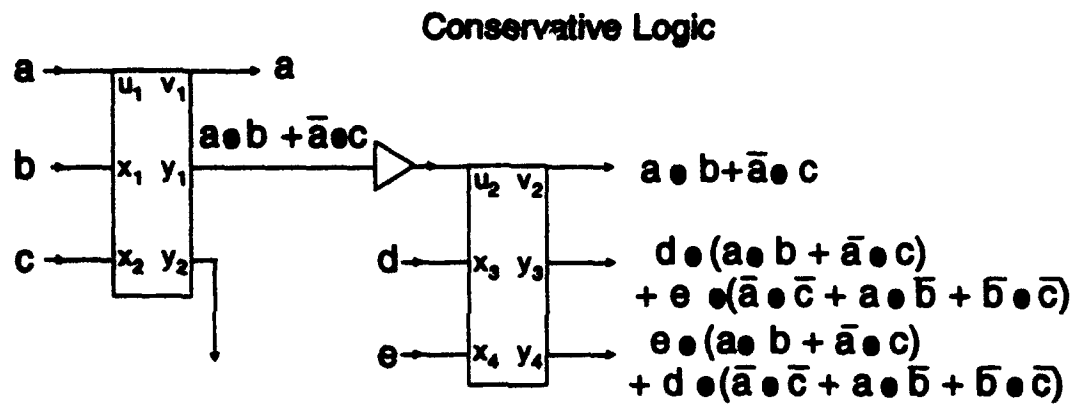


**Figure 1.2.5**  
**Conservative Logic Operation and its Inverse using Fredkin Gates**

original arguments and constants.<sup>4</sup> Fig. 1.2.6 illustrates this property by interfacing a NAND operation with its inverse. As can be seen, the "don't cares", namely  $v_2$  and  $y_4$  in this case, are also used as inputs to the inverse logic gate network in order to help generate the original arguments and constant. One would also like to have the output of the function generated by the first Fredkin gate network because it contains the results of the desired logic function you want to realize in the first place. So, if in addition to feeding the output from the NAND function gating network in Fig. 1.2.6 into the input of its inverted gating network it is also fed to the control input of an additional "Spy" Fredkin gate, one will generate not only the original input arguments and constants at  $v_4$ ,  $y_7$ , and  $y_8$ , but will also output the desired logic function operation at  $y_9$ . This garbageless NAND operation is demonstrated in Fig. 1.2.7. The "Spy" Fredkin gate acts simply as a fan out. So, even though we may not wish to make further use of the original input arguments and constants found at  $v_4$ ,  $y_7$  and  $y_8$ , and therefore let the energy be dissipated as heat, the energy dissipated by these unused lines will grow only as  $3N$ , where  $N$  is the number of output lines.<sup>4</sup> As stated earlier, the number of gates is independent of the number of lines, thus, the energy dissipation grows linearly, not exponentially. This can play a major role for large circuits with many input lines.



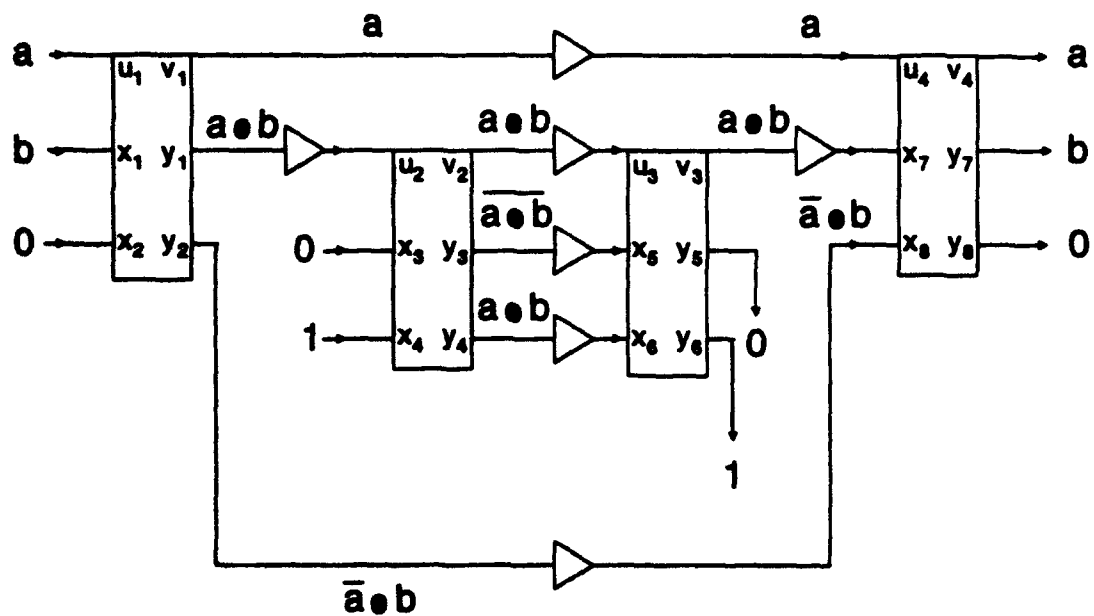
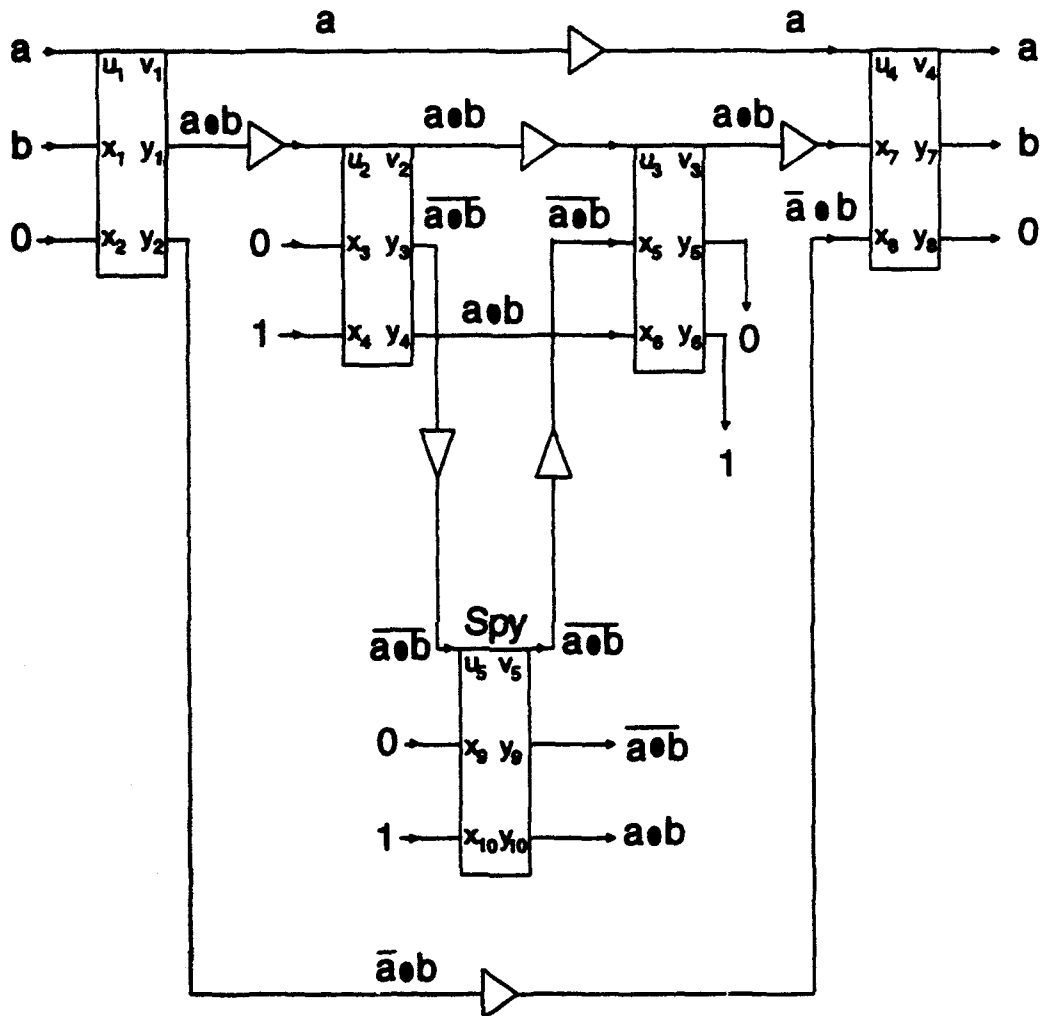


Figure 1.2.6  
NAND Operation Connected to its Inverse using Fredkin Gates



**Figure 1.2.7**  
**Garbageless NAND Operation using Conservative and Inverse**  
**Conservative Logic Fredkin Gates with "Spy" Fredkin Gate**

### Optical Fredkin Gates

An optical Fredkin gate is the optical realization of the Fredkin gate with the use of an optical switch. The argument channels of the optical Fredkin gate are optical. The control channel for these devices, however, can be either optical, electrical, or acoustical. Therefore, the optical Fredkin gate need not be entirely optical. It also does not have to operate exactly as Fredkin proposed. While some of the optical Fredkin gate designs cross the argument channels with a logic low control channel, as Fredkin et al. proposed, other designs cross the argument channels with a logic high control channel. We will designate this second type of gate as a reverse Fredkin gate, which is not the same as an inverse Fredkin gate.

Optical Fredkin gates have been proposed and demonstrated by several researchers utilizing various optical switching designs and materials. Proposed optical implementations of the Fredkin gate include:

1) Polarization switch: The polarizations of the two arguments are orthogonal and are passed through an electro-optic modulator controlled by an applied electric voltage.<sup>5,6,8,9,32,108,154,155</sup> This is a reverse Fredkin gate design. When voltage is applied to the modulator, the polarizations of both arguments rotate by 90° and switching occurs. A similar method has been demonstrated using a polarization color-coded liquid crystal light valve.<sup>10,11</sup>

2) Acousto-optic gate: The arguments are passed through an acousto-

optic deflector and the control line is an acoustic signal applied to the deflector.<sup>8,9,108,154,155</sup> This is also a reverse Fredkin gate design. Switching occurs in the presence of the acoustical signal.

3) **Photorefractive gate:** Based on four wave mixing, the photorefractive gate is an all optical switch where the arguments are signal beams counterpropagated through a photorefractive material. The control line is the pump and it is also counterpropagated through the photorefractive material.<sup>8,9,12,14,16,33,34,108,154,155</sup> This is, again, a reverse Fredkin gate design. When the pump is present, switching occurs via phase conjugation.

4) **Waveguide switch:** The arguments are symmetric coupled channel waveguides in an electro-optically active material. Depending upon the extent of the optical activity of the material, the control channel is either an electrical or optical signal applied across the section of the two argument channels where coupling occurs.<sup>8,9,108,154,155</sup>

Some of the designs for waveguide switches include: directional coupler switch;<sup>16,17,19,28,30,31,39-41,43,89,102,105-107,112,114,115,117,119,142,154,155</sup> zero-gap directional coupler switch, which is a modified version of the directional coupler switch;<sup>3,15,18,20-22,25,28,29,36,154,155</sup> and crossing channel switch or X-switch.<sup>13,18,20,22-24,26,27,36,154,155</sup> The directional coupler and X-switch designs all operate as Fredkin gates. The channel waveguide zero-gap symmetric directional coupler switch, which is the focus of this dissertation, is illustrated in Fig.

1.3.1. Researchers have thoroughly investigated the theory behind channel waveguide directional coupler switches and several of these devices have been demonstrated using lithium niobate ( $\text{LiNbO}_3$ ), indium phosphide (InP), GaAs and AlGaAs as the waveguiding medium.<sup>3,15-31,38-41,43,89,102,105-107,112,114,115,117,119,142,154,155</sup>

### Directional Coupler Switch

The directional coupler switch is a device consisting of parallel channel waveguides separated by a finite distance. The coupling between the modes of the parallel waveguides results in an exchange of power between guided modes of adjacent waveguides.<sup>16</sup> This is referred to as directional coupling. The eigenmodes of the coupling region consist of one symmetric and one antisymmetric mode.<sup>16,17,19,61-63,67,102,105</sup> Treatment of waveguide coupling can be performed by coupled-mode theory.<sup>16,17,102,105</sup> Consider  $P_{i1}$  as the input power to waveguide 1,  $P_{i2}$  as the input power to waveguide 2,  $P_{o1}$  as the output power from waveguide 1 and  $P_{o2}$  as the output power from waveguide 2. Let waveguide 1 propagate through the symmetric mode and waveguide 2 propagate through the antisymmetric mode. Assume that the waveguides are not too close so that the overlap integral of the mode functions will be small.<sup>16,17,102,105</sup> With a single input to waveguide 1,  $P_{i1} = 1$  then  $P_{i2} = 0$ . The output power from waveguides 1 and 2 are given

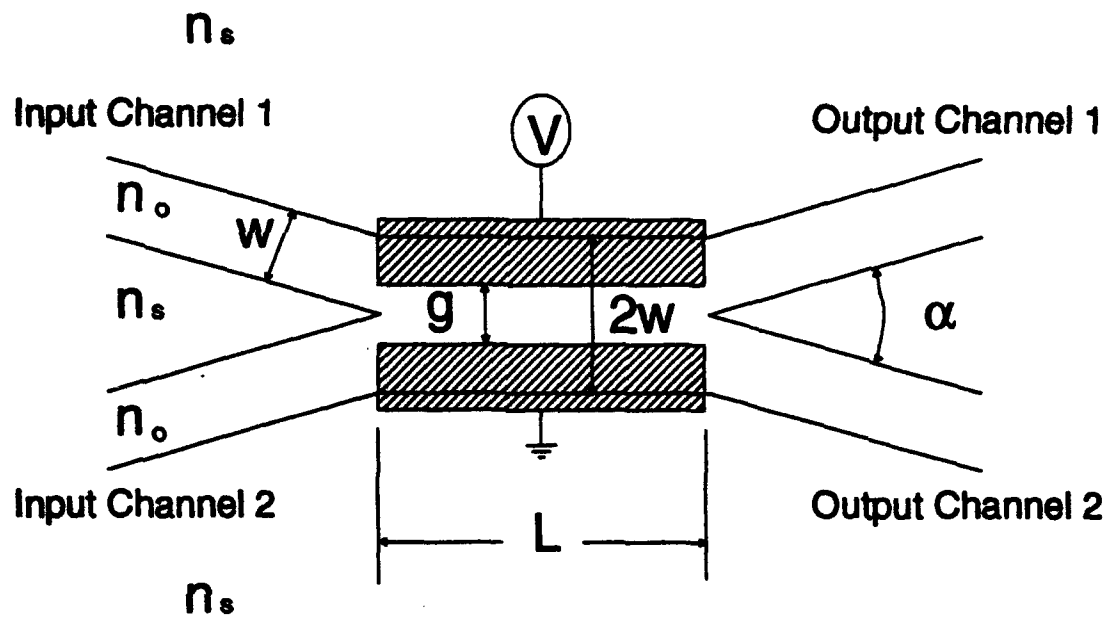


Figure 1.3.1  
Schematic of a Zero-Gap Directional Coupler

as<sup>16,17,19,102,105</sup>

$$\begin{aligned}
 P_{o_1}(\ell) &= P_{i_1} - P_{o_2}(\ell) \\
 &= P_{i_1}(1 - (\kappa^2/(\kappa^2 + \delta^2))(1 - \cos^2[(\kappa^2 + \delta^2)^{1/2}(\ell)]))
 \end{aligned}
 \tag{1.4.1}$$

and

$$P_{o_2}(\ell) = P_{i_1}((\kappa^2/(\kappa^2 + \delta^2))(\sin^2[(\kappa^2 + \delta^2)^{1/2}(\ell)])), \tag{1.4.2}$$

where  $2\delta = \beta_1 - \beta_2$  is the difference in the propagation constants between two adjacent uncoupled waveguides 1 and 2,  $\kappa$  is the coupling constant between the two adjacent waveguides and  $\ell$  is the interaction length over which the two waveguides are coupled. By definition,  $\kappa = \pi/2L$ , where  $L$  is the length required for complete coupling of the power from one waveguide to the other.<sup>16,17,19,38,39,40,41,61,62,63,67,91,102,105</sup>

For symmetric waveguides, the phase velocities in the two modes are equal (i.e.,  $\beta_1 = \beta_2$  or  $\delta = 0$ ). For complete coupling, Eqs. 1.4.1 and 1.4.2 become<sup>16,17,19,102,105</sup>

$$P_{o_1}(L) = P_{i_1}(1 - (1 - \cos^2[\pi/2])) = 0 \tag{1.4.3}$$

and

$$P_{o_2}(L) = P_{i_1}(\sin^2[\pi/2]) = P_{i_1}. \tag{1.4.4}$$

From Eqs. 1.4.3 and 1.4.4, one can see that the input power  $P_{i_1}$  into waveguide 1 will exit waveguide 2 as  $P_{o_2}$  at a distance  $L$ . Using Eqs. 1.4.3 and 1.4.4 complete coupling occurs when  $L = \pi/2\kappa$ .

Applying an electric field to either waveguide 1 or waveguide 2, over the distance  $L$ , where the waveguides are coupled, will change that particular waveguide's propagation constant  $\beta$ . Total switching occurs when  $\delta = \sqrt{3}\pi/2L$ .<sup>16,17,19</sup> This can be verified by the substitution of  $\delta = \sqrt{3}\pi/2L$  into Eqs. 1.4.1 and 1.4.2. By doing this we get<sup>16,17,19,102,105</sup>

$$P_{o_1}(L) = P_{i_1}(1 - (1/4)(1 - \cos^2[\pi])) = P_{i_1} \quad 1.4.5$$

and

$$P_{o_2}(L) = P_{i_1}((1/4)(\sin^2[\pi])) = 0. \quad 1.4.6$$

Using the definitions for  $\delta$  and  $\kappa$  given above, one gets total switching to occur when<sup>16,17,102,105</sup>

$$(\beta_1 - \beta_2) = \sqrt{3}\pi/L. \quad 1.4.7$$

If we apply an electric field ( $E$ ) over waveguide 2, for instance, this will induce a change in the refractive index of waveguide 2 by an amount proportional to  $E$ . Mathematically this is given by<sup>16,17,102,105,106</sup>



$$\Delta n_2 = (n_2^3/2)rE,$$

1.4.8

where  $n_2$  is the refractive index of waveguide 2 and  $r$  is defined as the electro-optic coefficient of the waveguiding material. To apply an electric field to one of the waveguides, we place electrodes on the top and bottom of the waveguide over the coupling length ( $L$ ) and apply a voltage ( $V$ ) to the top electrode. The electric field is then related to the applied voltage by  $V = Ed$ , where  $d$  is the distance between the top and bottom electrode. The total index ( $n_2'$ ) of the waveguide 2 region between the electrodes can be defined by

$$n_2' = n_2 + \Delta n_2 = n_2 + (n_2^3/2)rV/d.$$

1.4.9

By definition,  $\beta = 2\pi/\lambda$ , where  $\lambda$  is the wavelength of the source.<sup>16,17,102,105</sup>

If we let waveguide 1 and waveguide 2 be identical ( $n_1 = n_2 = n$ ) and substitute Eq. 1.4.9 into 1.4.7, along with the definition for  $\beta$ , this yields<sup>16,17,102,105</sup>

$$(2\pi/\lambda)(n' - n)(n^3/2)(rV/d) = (2\pi/\lambda)(n^3/2)(rV/d) = \sqrt{3}\pi/L.$$

1.4.10

We can now find the voltage required to completely switch the coupling. By

rewriting Eq. 1.4.10, we get

$$V = (\sqrt{3}\lambda d)/(n_2^3 rL). \quad 1.4.11$$

The operation of a directional coupler switch is illustrated in Fig. 1.4.1.

### Zero-Gap Directional Coupler Switch

As with directional couplers, the interaction region of a zero-gap directional coupler will support two guided symmetric modes and two guided antisymmetric modes.<sup>3,18,21,22,28,29,38</sup> The difference between them, however, results from the fact that we have zero spacing between the two symmetric waveguides in a zero-gap directional coupler. These modes will now be propagating in a single waveguide. We will again have a voltage independent phase difference that accumulates over the interaction length (the two mode section), due to the difference in the phase velocities of the two orthogonal modes, and a phase difference over the two mode section, brought about by the voltage induced change in refractive index (electro-optic (EO) effect).<sup>16,97-100</sup>

The electro-optic dependent phase difference will be denoted by  $(\beta_s - \beta_{as})/2 = \Delta\beta/2$ , where  $\beta_s$  and  $\beta_{as}$  are the propagation constants of the symmetric and antisymmetric modes, respectively.<sup>21</sup> The value of  $\Delta\beta$

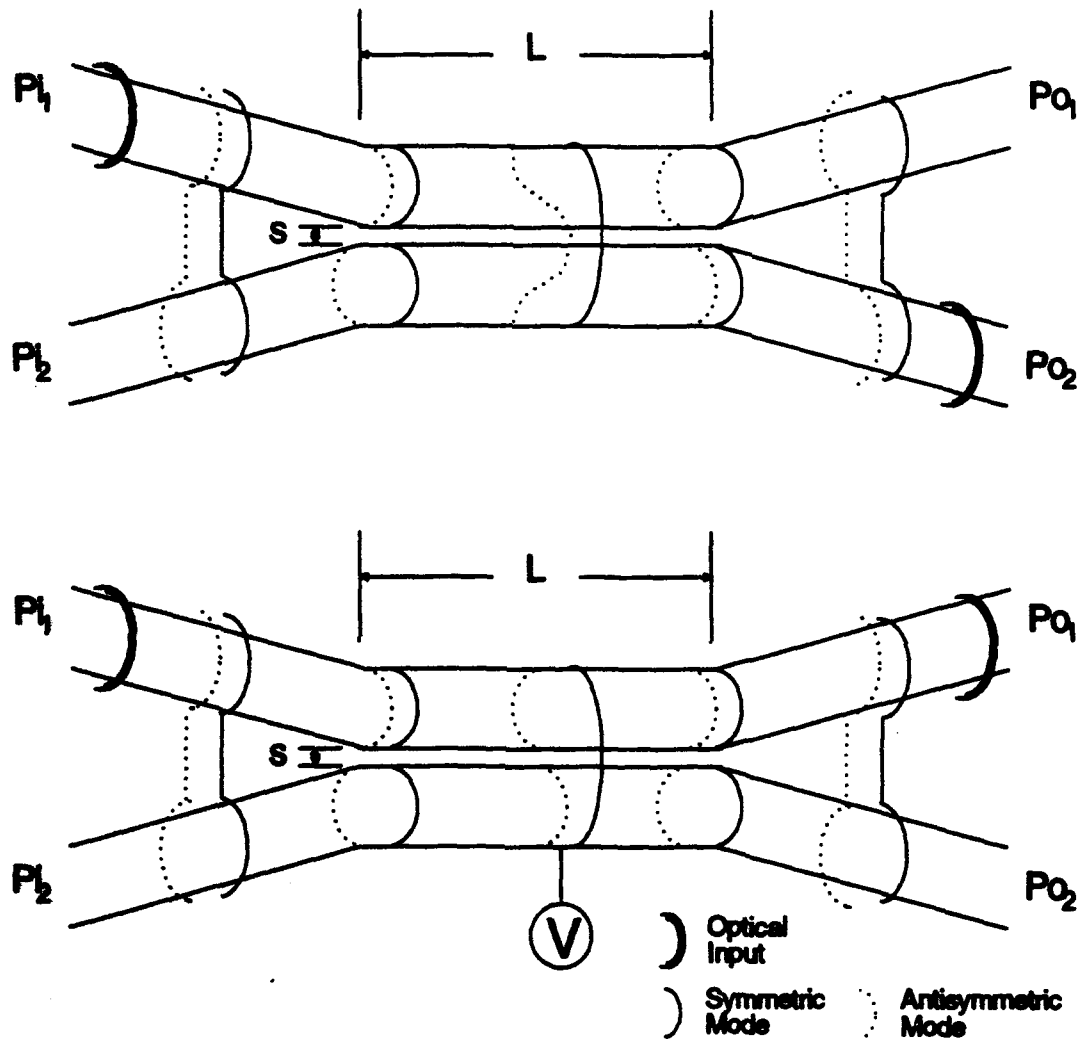


Figure 1.4.1  
Operation of a Directional Coupler

required for complete coupling of energy from the top half of the two mode waveguide to the bottom is given by<sup>21</sup>

$$\Delta\beta = \pi/L. \quad 1.5.1$$

$\Delta\beta$  is varied by changing the index of refraction of the waveguiding material in the two-mode section. We will denote the refractive index change, as we did in the last section, by  $\Delta n$ . The change in the difference between the propagation constants of the two modes can then be written as<sup>21</sup>

$$\Delta(\Delta\beta) = \Delta n (\partial\Delta\beta/\partial n). \quad 1.5.2$$

Equating Eqs. 1.5.1 and 1.5.2 yields<sup>21</sup>

$$\Delta n = (\pi/L)(\partial\Delta\beta/\partial n)^{-1}. \quad 1.5.3$$

It was shown in the last section that for linear EO materials, the refractive index changes proportionally to the applied voltage. With this relation, it can be seen from Eq. 1.5.3 that  $\partial\Delta\beta/\partial n$  is inversely proportional to the applied voltage.  $\partial\Delta\beta/\partial n$  is also strongly dependent on the waveguide separation  $s$  for the directional coupler.<sup>21</sup> Papuchon and Roy<sup>21</sup> showed that as  $s$

decreases,  $\partial(\Delta\beta)/\partial n$  increases, and as the value of  $\partial\Delta\beta/\partial n$  increases, the voltage required for switching decreases. Therefore, the maximum value of  $\partial\Delta\beta/\partial n$  and, thus, the minimum voltage required to switch the coupling guides, occurs when  $s = 0$ . When  $s = 0$ , we have a zero-gap directional coupler.<sup>21</sup> Experiments have shown that the value  $\partial\Delta\beta/\partial n$  varies by an order of magnitude between the conventional directional coupler and the zero-gap directional coupler.<sup>21</sup> This verifies that zero-gap directional couplers require less voltage to switch the coupling than conventional directional couplers.

Expressions for the power coupling in zero-gap directional couplers are similar to those for conventional directional couplers. They are given by<sup>23-25</sup>

$$P_{o_1}(l) = P_{i_1} \cos^2[(\Delta\beta/2 + \Phi_0)l] \quad 1.5.4$$

and

$$P_{o_2}(l) = P_{i_1} \sin^2[(\Delta\beta/2 + \Phi_0)l], \quad 1.5.5$$

where  $\Phi_0$  is the accumulated, voltage independent phase difference in the phase velocities of the symmetric and antisymmetric modes. With no voltage applied (i.e.,  $\Delta\beta = 0$ ) coupling occurs when  $\Phi_0 = \pi/2L$ . When enough voltage is applied so that  $\Delta\beta = \pi/L$ , then complete switching occurs. Equating  $\Delta\beta$  with Eq. 1.4.9 yields

$$(2\pi/\lambda)(n^3/2)(rV/d) = \pi/L.$$

1.5.6

The voltage required for complete switching is then given by

$$V = (\lambda d)/(n^3 r L),$$

1.5.7

where  $n$  is the refractive index of the interaction region. By comparing Eq. 1.5.7 with Eq. 1.4.11, one can see that the voltage required to completely switch the optical input from one channel to the other is less for the zero-gap directional coupler. The zero-gap allows us to approximately treat the center interaction region as one waveguide. It will be shown in Chapter IV that Eq. 1.5.7 is the same expression derived for an electro-optic modulator. Operation of the zero-gap directional coupler switch is illustrated in Fig. 1.5.1. Another advantage of zero-gap directional couplers, in addition to operating with less voltage, is that the interaction length is much shorter than the interaction length of conventional directional couplers.<sup>61-63</sup> This results in the reduction of real estate required. Interaction length dependence on waveguide separation will be treated in Chapter III.

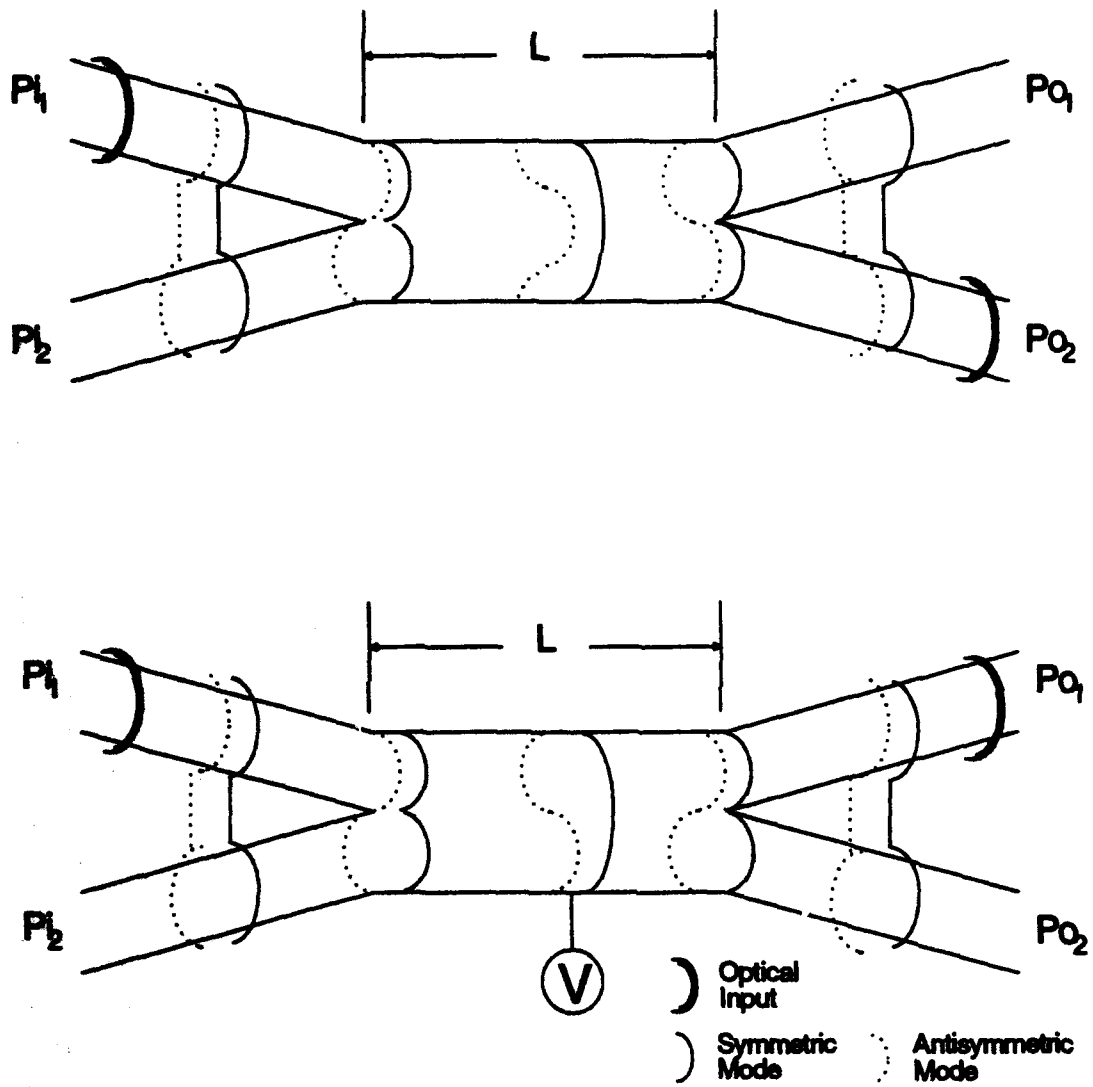


Figure 1.5.1  
Operation of a Zero-Gap Directional Coupler

### Wavefront Tilt

An additional parameter that needs to be considered for both conventional and zero-gap directional couplers is wavefront tilt and its affect on waveguide coupling in the branching section. The larger the tilt angle  $\alpha$  of the branching section, the less the waveguide coupling<sup>18</sup> (see Fig. 1.3.1). Tilt introduces phase differences that decrease waveguide interaction in the branching section of waveguide coupling. The maximum allowable tilt angle can be obtained by forcing the branching region of waveguide coupling to be within a single lobe of the standing wave generated by the two waves propagating along the tilted waveguide portions. This gives the limit<sup>18</sup>

$$\sin(\alpha/2) < \lambda/4nw, \quad 1.6.1$$

where  $w$  is the width of the waveguides.

### Electrode Separation

The separation gap  $g$  between the electrodes over the coupling regions of waveguides 1 and 2, even though not being part of the equations above, plays a major role in switch operation (see Fig. 1.3.1). It has been found that the wider the gap, the lower the electric field strength and induced refractive index change. The narrower the gap, the higher the electric field



strength and induced refractive index change.<sup>20</sup> It has also been presented that the electrode separation gap depends on the waveguide width. It should be much less than  $w$ , so that only the propagation constant of the fundamental mode is strongly modified.<sup>20,27</sup> There are limitations, however, on how narrow or wide  $g$  can be. This is due to the physical reason that variations in the electrode gap can only be partially compensated by applied voltage.<sup>20</sup> Complete compensation is not possible. Overlap of the applied electric field with the optical electric field within the waveguide, is a factor that affects the behavior of the index change.<sup>20</sup> It is brought about by the electrode separation gap versus the applied voltage. This leads to the need to determine an optimum  $g$  versus waveguide width.

### Thesis Organization

Now that the Fredkin gate and zero-gap directional coupler have been introduced, the theory and background references necessary for completing this research will be reviewed in Chapters II, III and IV. Chapters II and IV of the dissertation will describe the optical and electro-optical properties of AlGaAs. The characteristics of conventional and zero-gap directional couplers will be presented in Chapter III. Chapter V will detail the experimental procedures, observations and recorded data of this work. This includes material growth, device fabrication and operation. Results are then

presented in Chapter VI and conclusions, along with recommendations, are given in Chapter VII.

## CHAPTER II

### OPTICAL PROPERTIES OF ALUMINUM GALLIUM ARSENIDE

By convention, the nomenclature for aluminum gallium arsenide is generally given as  $\text{Al}_x\text{Ga}_{1-x}\text{As}$ , where  $x$  is the fraction of aluminum atoms present in the material and  $1-x$  is the fraction of gallium atoms present for each atom of arsenic in the material. Research has demonstrated that the optical properties of  $\text{Al}_x\text{Ga}_{1-x}\text{As}$  have a strong dependence on  $x$  and the optical wavelength ( $\lambda$ ). In this chapter, we will quantitatively investigate the refractive index ( $n$ ) as a function of both  $x$  and  $\lambda$ , and then determine these parameters for the specific  $\text{Al}_x\text{Ga}_{1-x}\text{As}$  structure and wavelength to be used for this experiment.

#### Refractive Index

A literature search was conducted for references investigating the refractive index of  $\text{Al}_x\text{Ga}_{1-x}\text{As}$ . Three of the sources found<sup>46,47,52</sup> were ones in which the index had actually been measured as a function of both  $x$  and  $\lambda$  and that these three sources are the most widely referenced among

$\text{Al}_x\text{Ga}_{1-x}\text{As}$  integrated optics researchers.<sup>3,38-42,45,48,49,53-56,58-60</sup> The literature search also uncovered a few sources that fit these experimental data to analytical models to interpolate the refractive index of various  $\text{Al}_x\text{Ga}_{1-x}\text{As}$  compositions for which the index had not been measured. Sections 2.1 - 2.3 will outline all of the pertinent sources. These sources will be used, along with information gathered through conversations with several researchers in the technical area, listed in the bibliography, to determine the refractive index for the specific  $x$  and  $\lambda$  used for this experiment.

Before going onto the modelling sections, the wavelength and the Al concentration of the waveguide devices to be fabricated for this experiment need to be chosen. It is desirable to have an  $x$  and  $\lambda$  that will yield as low a propagation loss as possible. Selection of  $\lambda$  was based on the type of laser diode used in the experiment. Since the absorption is inversely proportional to  $\lambda$ ,<sup>38</sup> the higher the  $\lambda$ , the lower the loss.

Among the commercially sold laser diodes with as high a  $\lambda$  as possible,  $\text{Al}_x\text{Ga}_{1-x}\text{As}$  laser diodes in the 760 - 850 nm range are readily available as well as inexpensive.  $\text{Al}_x\text{Ga}_{1-x}\text{As}$  laser diodes with  $\lambda > 850$  nm are usually more expensive and not as readily available. For  $\lambda > 900$  nm, the material used for the laser structure included either indium or phosphorus, depending on the desired  $\lambda$ .

Relevant and complementary United States Air Force interests include:

(a) Three Terminal Opto-electronic Arrays (TTOA) for which a laser, photodetector, and amplifier structure are all being fabricated into a single pixel area in  $\text{Al}_x\text{Ga}_{1-x}\text{As}$  material;<sup>42</sup> (b) Integrated Optical Organic Devices (IOOD), for which polymer based optical waveguides are being developed for operation within the 700 - 900 nm wavelength range;<sup>43</sup> and (c) Optical Interconnect Technology (OIT), for which integration of laser source, optical organic waveguide, photodetector and electronics are all being integrated together to realize a complete multichip module optical interconnect operating in the 700 - 900 nm wavelength range.<sup>44,151</sup> These research programs dictated the use of an  $\text{Al}_x\text{Ga}_{1-x}\text{As}$  laser diode with an operating  $\lambda$  somewhere between 700 and 900 nm.

After considering compatibility with the TTOA, IOOD and OIT programs along with price, availability, and monolithic integration of the laser, waveguide and detector, a Sharp Model LT015MD0 40 mW index guided laser diode, operating at  $\lambda = 827$  nm, was selected. A spectrometric measurement of the laser diode was taken with an input current of 81.0 mA and maintained at a temperature of 25.0°C to verify  $\lambda$ .

With  $\lambda$  chosen, the Al concentration to be used for the core of the waveguide, that would yield as low a propagation loss as possible, needed to be determined. At a given  $\lambda$  the absorption is inversely proportional to the fraction of Al atoms.<sup>38</sup> The higher the x value, the lower the loss. In

addition, the required waveguide thickness for a given  $\lambda$  is inversely proportional to  $x$ . These criteria would suggest a large Al concentration. For  $x > 0.350$ , however, the bandgap level becomes indirect, resulting in diminished optical activity, due to the fact that both a photon and phonon are required for an indirect transition.<sup>36</sup> This dictates that  $x \leq 0.350$ . It has also been reported<sup>3</sup> that at wavelengths in the 800 - 850 nm range, the modal attenuations increase markedly for a waveguide core layer when Al concentrations are above 0.310. Accordingly, an  $x$  value of 0.300 was chosen for the waveguide core.

Based on the findings given above, the Al concentration is constrained to the range  $0.200 \leq x \leq 0.400$  when  $0.7 \mu\text{m} \leq \lambda \leq 1.0 \mu\text{m}$  for the  $\text{Al}_x\text{Ga}_{1-x}\text{As}$  refractive index models. In addition, the models were fit to the measured indices by optimizing for an Al concentration  $x = 0.300$  and  $\lambda$  827 nm. This provided better agreement with the measured refractive index in this limited range of  $x$  and  $\lambda$  than when the entire, unlimited, ranges of  $x$  and  $\lambda$  were considered.

## Section 2.1

In 1972, Boyd<sup>45</sup> fit to Sellmeier equation experimental data published by Illegems and Pearson<sup>46</sup>:

$$(n_1)^2 = A + B/(\lambda^2 - C) - D\lambda^2,$$

2.1.1

where  $n_1$  is the index of refraction,  $\lambda$  is the wavelength given in  $\mu\text{m}$  and A, B, C, and D are the Sellmeir coefficients, of which A, C, and D are functions of  $x$ . Ilegems and Pearson used reflectivity measurements to determine the refractive index of  $\text{Al}_x\text{Ga}_{1-x}\text{As}$  for  $x$  values of 0.080, 0.210, 0.380, 0.530, and 0.820, respectively. The accuracy of  $x$  was known to  $\pm 0.020$ ,<sup>46</sup> which is within the tolerance of the various electronic material characterization methods.<sup>161</sup> Numerical values for A, B, C, and D can be found for various Al concentrations by using the equations generated by Boyd as listed in Table 2.1.1.

Table 2.1.1<sup>46</sup>  
Sellmeir Coefficients for  $\text{Al}_x\text{Ga}_{1-x}\text{As}$

A	B	C	D
10.906 - 2.92x	0.97501	$(0.52886 - 0.735x)^2$ $x \leq 0.36$	$[0.002467$ $\cdot (1.41x + 1)]$
		$(0.30386 - 0.105x)^2$ $x \geq 0.36$	

Several of the assumptions used by Boyd were: 1) Linear variation of A with  $x$ ; 2) B independent of  $x$ ; 3) Quadratic variation of C with  $x$  to incorporate the shift in bandgap as a function of  $x$ , which varies linearly with a different

slope in the regions of direct and indirect band transition; 4) D varies linearly with  $x$ .

Thus, Eq. 2.1.1 allows one to determine the refractive index ( $n_1$ ) as a function of both  $x$  and  $\lambda$ . Fig. 2.1.1 shows the plots of the Sellmeir equation for two  $x$  values, 0.200 and 0.400, as a function of  $\lambda$ , between 0.7 and 1.0  $\mu\text{m}$ . It is suggested by Hunsperger,<sup>38</sup> that Eq. 2.1.1, along with the values for A, B, C, and D, can also be used to model the refractive indices measured by Casey, Sell and Panish.<sup>47</sup> When the values for  $x$ , given in that latter work, were substituted into Eq. 2.1.1, however, the modelled index did not fit the experimentally measured index very well. For the indices measured by Casey et al., a second model was found that fit these measurements much better. This model is discussed in the next section.

## Section 2.2

In 1985, Adachi<sup>48</sup> modelled the refractive index data of  $\text{Al}_x\text{Ga}_{1-x}\text{As}$  obtained by Casey, Sell and Panish.<sup>47</sup> These measured indices were determined by reflectivity measurements for  $x$  values of 0.070, 0.100, 0.150, 0.200, 0.240, 0.290 and 0.380 at photon energies ranging from 1.2 to 1.8 electron volts (eV). The accuracy with which  $x$  was known in that experiment was  $\pm 0.020$ .<sup>47</sup> Like the previous index measurements, this accuracy is within the tolerance of the various electronic materials characterization methods.<sup>161</sup>



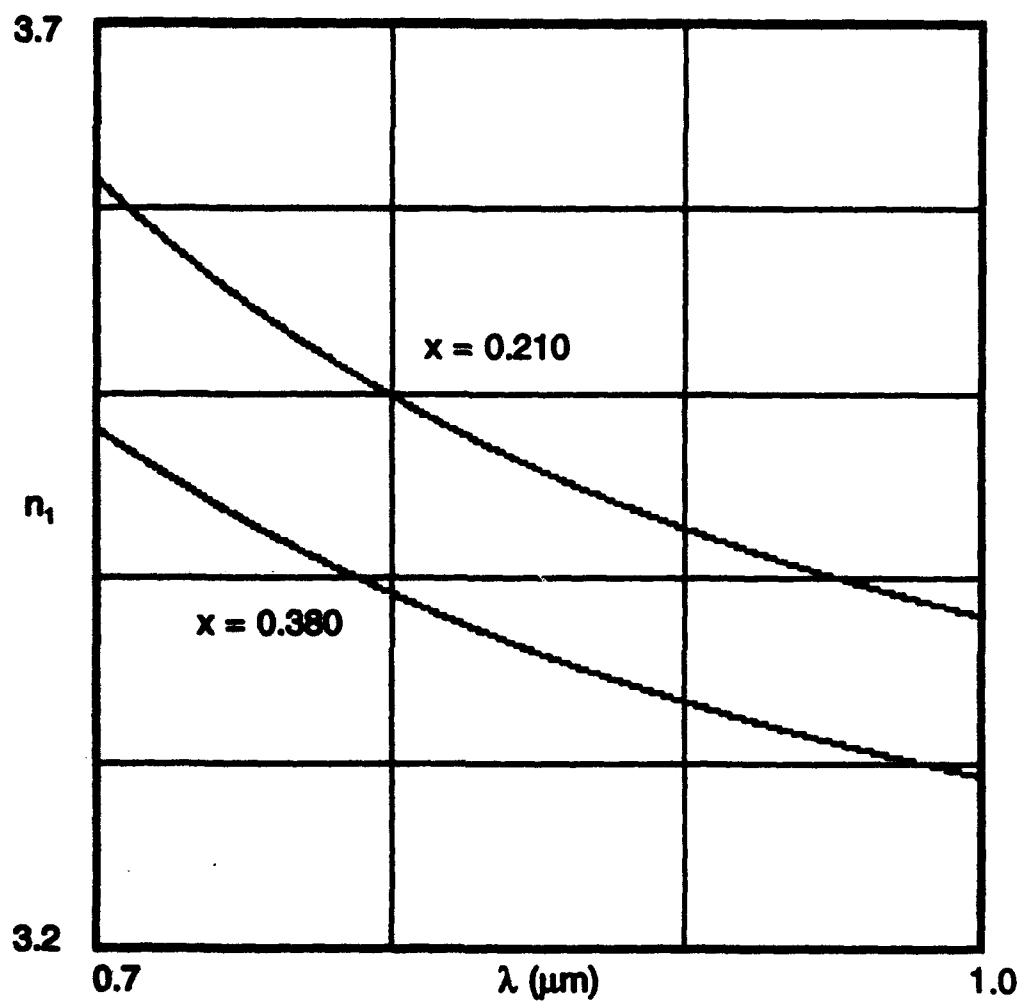


Figure 2.1.1  
Refractive Index of  $\text{Al}_x\text{Ga}_{1-x}\text{As}$  versus Wavelength

Adachi uses the relation<sup>49</sup>

$$(n_2)^2(\omega) = \epsilon_1(\omega) + i\epsilon_2(\omega), \quad 2.2.1$$

to model the refractive index where  $\omega$  is the angular frequency,  $n_2(\omega)$  is the frequency dependent refractive index and  $\epsilon_1(\omega)$  and  $\epsilon_2(\omega)$  are the real and imaginary parts of the frequency dependent dielectric constant, respectively. Adachi's relation, however, is valid for only those energies below the direct band edge. At or near the lowest direct gap ( $E_0$ ), the imaginary part of the dielectric constant ( $\epsilon_2(\omega)$ ) may be taken as zero when Eq. 2.2.1 becomes

$$(n_2)^2(\omega) = \epsilon_1(\omega), \quad 2.2.2$$

where the real part of the dielectric constant ( $\epsilon_1(\omega)$ ) for zincblende materials like  $\text{Al}_x\text{Ga}_{1-x}\text{As}$ , at energies below the  $E_0$  direct gap can be expressed using the well known Kramers-Kronig relation<sup>48</sup>

$$\epsilon_1(\omega) = A_0 \{ f(\chi) + 1/2 [E_0/(E_0 + \Delta_0)]^{3/2} f(\chi_{\infty}) \} + B_0, \quad 2.2.3$$

where

$$f(\chi) = (\chi)^{-2} [2 - (1 + \chi)^{1/2} - (1 - \chi)^{1/2}], \quad 2.2.4$$

$$f(\chi_{\infty}) = (\chi_{\infty})^2 [2 - (1 + \chi_{\infty})^{1/2} - (1 - \chi_{\infty})^{1/2}], \quad 2.2.5$$

$$\chi = \hbar\omega/E_0 \quad 2.2.6$$

and

$$\chi_{\infty} = \hbar\omega/(E_0 + \Delta_0). \quad 2.2.7$$

In Eq. 2.2.3 - 2.2.7,  $E_0$  and  $\Delta_0$  are the lowest direct gap and direct gap splitting energies, or critical point energies, in eV,  $\hbar\omega$  is the photon energy in eV where  $\hbar$  is Plancks constant and  $A_0$  and  $B_0$  are constants used to fit the model to the measured indices. Using the measured values of the critical point energies taken from Berolo and Woolley,<sup>50</sup>  $E_0$  and  $E_0 + \Delta_0$  can be fitted to the parabolic relation<sup>50</sup>

$$E = a + bx + cx^2. \quad 2.2.8$$

The constants a, b and c were determined for  $E_0$  by Lee, Juravel, Woolley and SpringThorpe,<sup>51</sup> by fitting Eq. 2.2.8 to the measured values. Using these values, the equation for  $E_0$  can be given as<sup>51</sup>

$$E_0 = 1.425 + 1.155x + 0.37x^2. \quad 2.2.9$$

Adachi later determined the constants  $a$ ,  $b$  and  $c$  for  $E_0 + \Delta_0$  in the same manner. Using Adachi's values, the equation for  $E_0 + \Delta_0$  is given as<sup>48</sup>

$$E_0 + \Delta_0 = 1.765 + 1.115x + 0.37x^2. \quad 2.2.10$$

$E_0$  and  $E_0 + \Delta_0$  are plotted as a function of  $x$  in Fig. 2.2.1. The fit of the curves generated from Eqs. 2.2.9 and 2.2.10 with Berolo et al. is quite good. By substituting Eqs. 2.2.9 and 2.2.10 into Eqs. 2.2.2 - 2.2.7 and then fitting Eq. 2.2.2 to the indices measured by Casey et al.,  $A_0$  and  $B_0$  can be found. Doing this yields

$$A_0 = 6.34 + 18.39x + 0.78x^2 \quad 2.2.11$$

and

$$B_0 = 9.38 - 10.61x + 0.78x^2. \quad 2.2.12$$

These values for  $A_0$  and  $B_0$  are not the ones used by Adachi<sup>48</sup>, however, they proved to give a better fit to the measured refractive index of Casey et al. than Adachi's values. Figs. 2.2.2 - 2.2.5 show plots of the refractive index ( $n_2$ ), including the  $\pm 0.020$  Al concentration accuracy, for the  $x$  values 0.200, 0.240, 0.290 and 0.380 as a function of  $\hbar\omega$  (between 1.2 and 1.8 eV), which corresponds to, approximately,  $1.0 \mu\text{m} \leq \lambda \leq 0.7 \mu\text{m}$ . Figs. 2.2.2 -

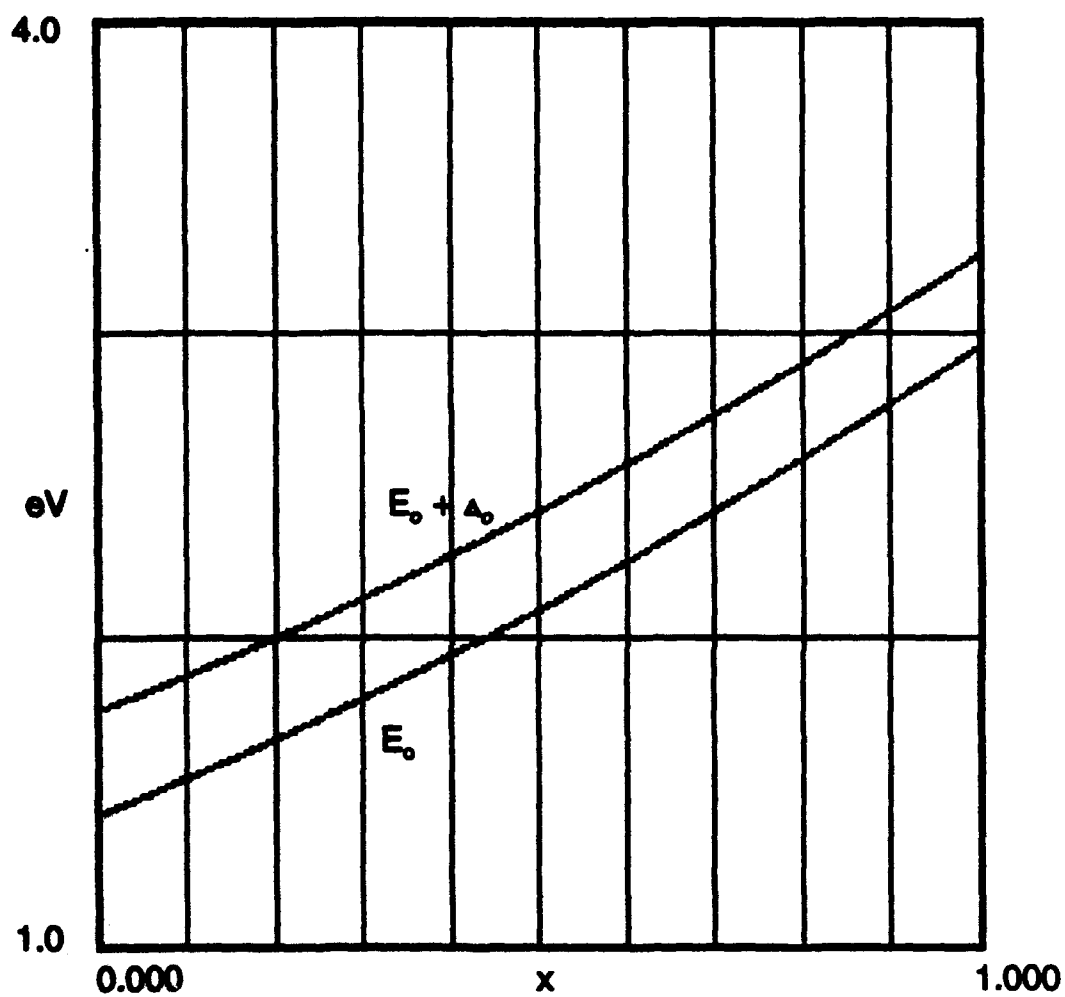


Figure 2.2.1  
Critical Point Energies for  $\text{Al}_x\text{Ga}_{1-x}\text{As}$  versus Al Concentration

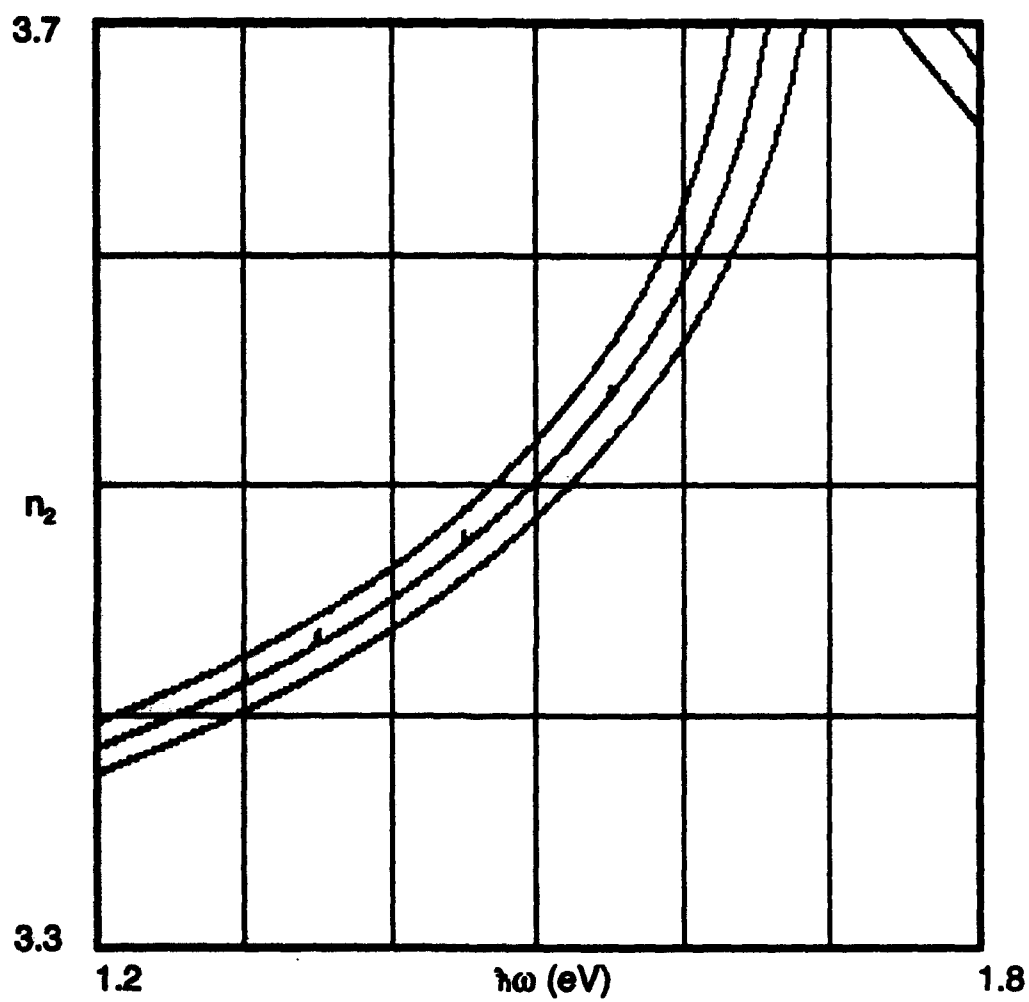


Figure 2.2.2  
Refractive Index of  $\text{Al}_x\text{Ga}_{1-x}\text{As}$  versus  
Photon Energy for  $x = 0.200 \pm 0.020$

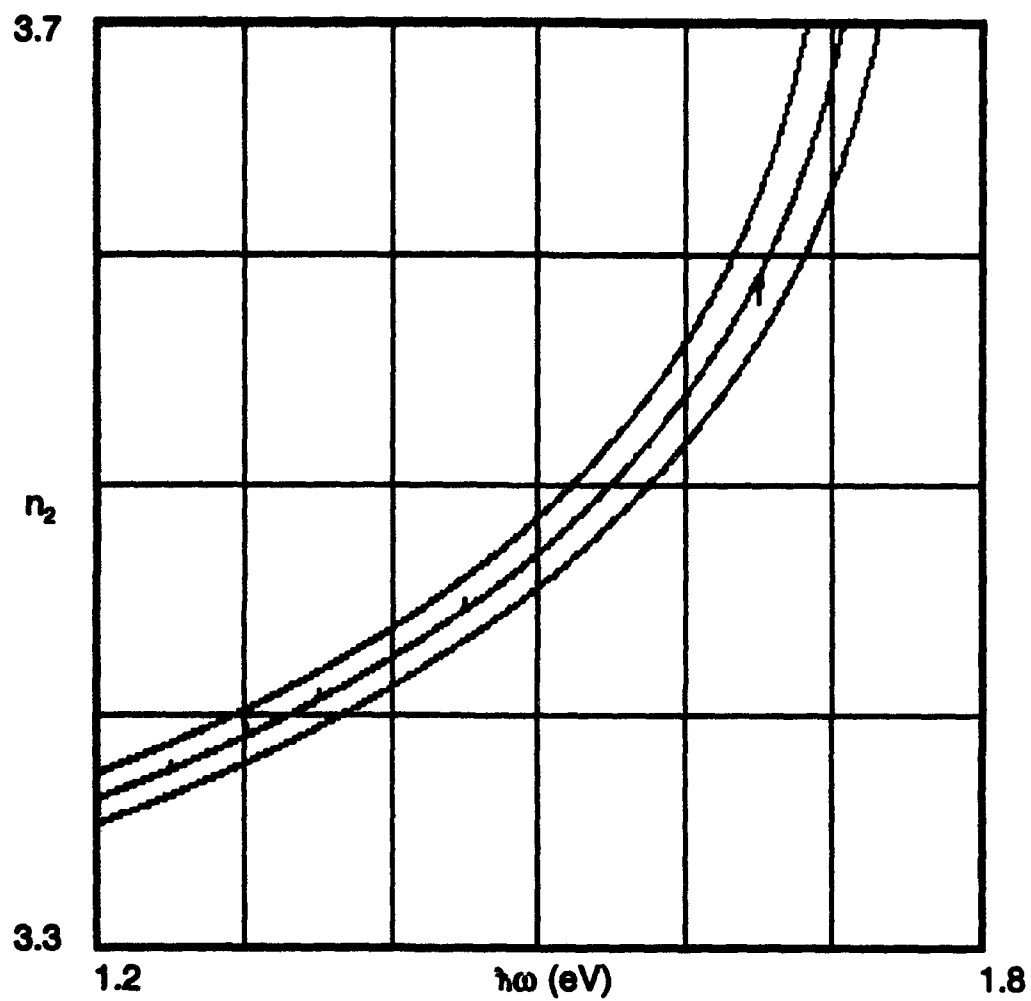


Figure 2.2.3  
Refractive Index of  $\text{Al}_x\text{Ga}_{1-x}\text{As}$  versus  
Photon Energy for  $x = 0.240 \pm 0.020$

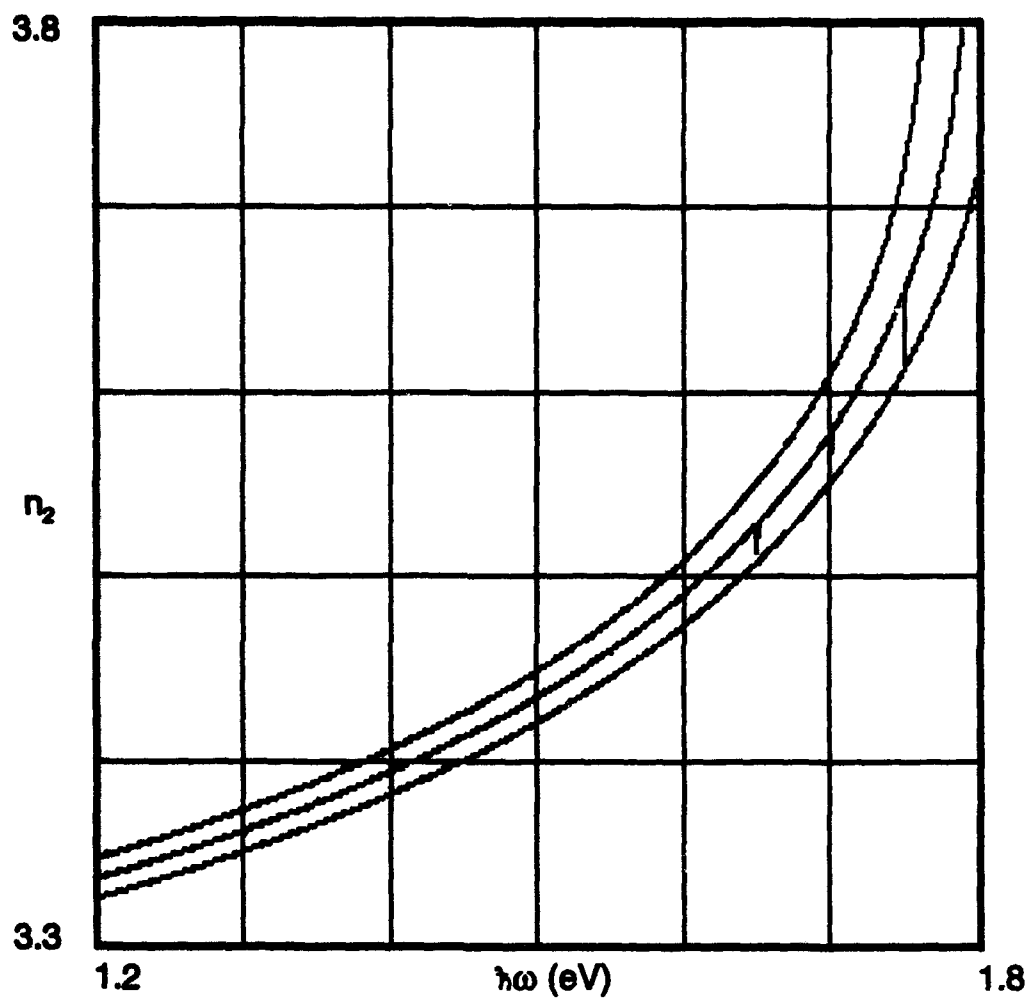


Figure 2.2.4  
Refractive Index of  $\text{Al}_x\text{Ga}_{1-x}\text{As}$  versus  
Photon Energy for  $x = 0.290 \pm 0.020$



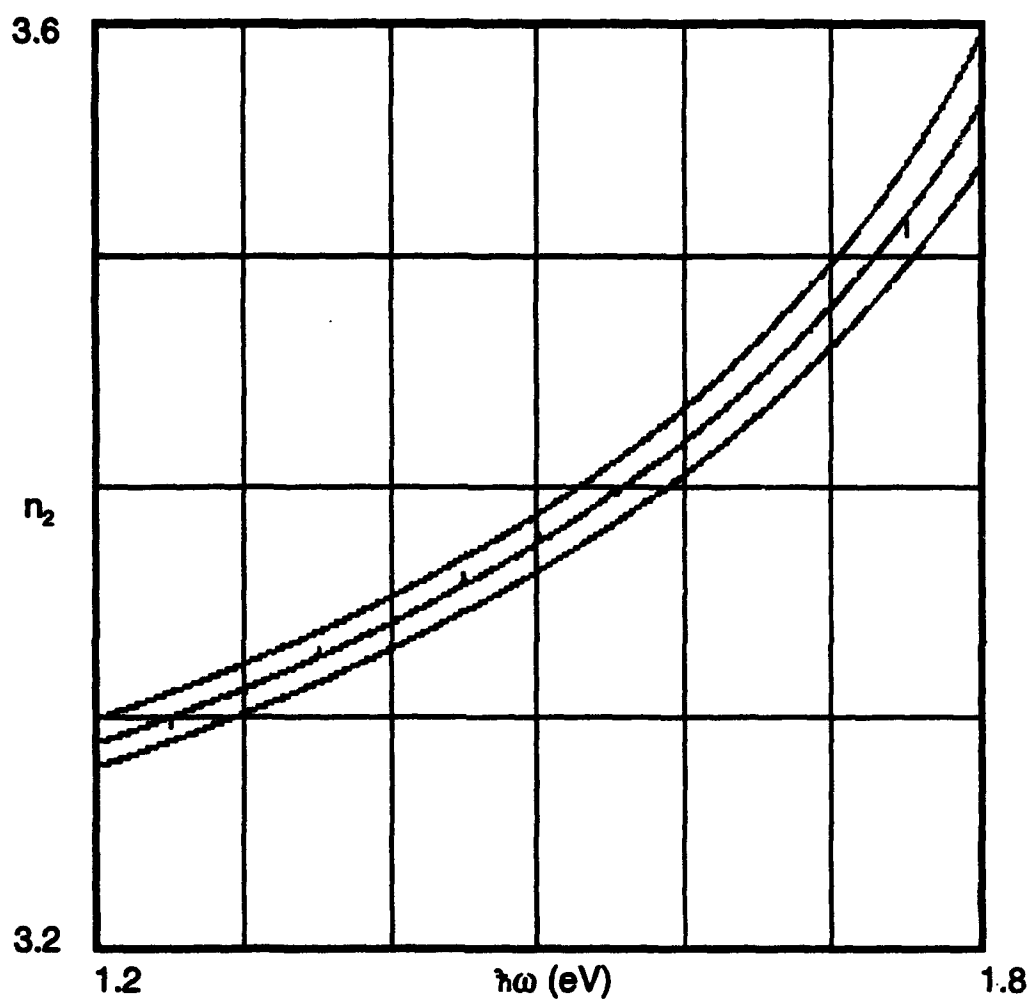


Figure 2.2.5  
Refractive Index of  $\text{Al}_x\text{Ga}_{1-x}\text{As}$  versus  
Photon Energy for  $x = 0.380 \pm 0.020$

2.2.5 also include the refractive indices measured by Casey et al., which were substituted into the model at the specific  $x$  and  $\lambda$  for which the index was actually measured. These substituted values appear as small spikes in an otherwise smooth curve, giving an indication of the accuracy of the model. The refractive indices, using the above model and curve fitting constants, are within the known accuracy of the fraction of Al atoms. It provides a very good fit around the chosen  $x = 0.300$  waveguide core and the 827 nm wavelength,  $\hbar\omega = 1.5$  eV.

### Section 2.3

In 1986, a new set of refractive index measurements were made by Aspnes, Kelso, Logan and Bhat.<sup>52</sup> The indices were measured using a rotating analyzer ellipsometric technique for  $x$  values of 0.099, 0.198, 0.315, 0.419, 0.491, 0.590, 0.700 and 0.804 at photon energies ranging from 1.5 to 6 eV. The accuracy with which  $x$  was known was  $\pm 0.020$ .<sup>52</sup> This accuracy is within the tolerance of the various electronic materials characterization methods.<sup>161</sup> The Adachi model presented in the previous section did not provide a close enough fit to be used to model these measurements taken by Aspnes et al. However, in 1989, Adachi<sup>53</sup> improved his model to better fit these experimental data. This new model includes contributions due to  $E_0$  and  $E_0 + \Delta_0$  as well as the higher critical point

energies  $E_1$ ,  $E_1 + \Delta_1$ ,  $E_2$ ,  $E_0'$ , and  $E_0' + \Delta_0'$ , including nondispersive contributions.

We will determine all the critical point energies and nondispersive terms before presenting the model, since these energies will consequently be used to determine the refractive index. The critical point energies  $E_0$  and  $E_1$  were measured by Aspnes et al.<sup>52</sup> as a function of  $x$ . These measured critical point energies  $E_0$  and  $E_1$ , as well as  $E_0 + \Delta_0$  and  $E_2$ , are given by Adachi.<sup>54</sup> Equations for the critical point energies, fit to the values found in Adachi,<sup>54</sup> are then given as

$$E_0 = 1.42 + 1.195x + 0.315x^2, \quad 2.3.1$$

$$E_0 + \Delta_0 = 1.77 + 1.079x + 0.420x^2, \quad 2.3.2$$

$$E_1 = 2.96 + 0.456x + 0.136x^2 + 0.213x^3 + 0.067x^4 \quad 2.3.3$$

and

$$E_2 = 4.70. \quad 2.3.4$$

The critical point energy  $E_0'$  and the direct gap splitting energies  $\Delta_1$  and  $\Delta_0'$  are not listed by Adachi. The only measurements found for  $E_1 + \Delta_1$ ,  $E_0'$  and  $E_0' + \Delta_0'$  were taken by Berolo et al.<sup>50</sup> Therefore,  $E_0'$  and  $E_0' + \Delta_0'$  were

fitted directly to Berolo et al. giving

$$E_o' = 4.49 + 0.095x \quad 2.3.5$$

and

$$E_o' + \Delta_o' = 4.65 + 0.090x. \quad 2.3.6$$

The  $E_1 + \Delta_1$  critical point energy was determined in a different way. Only Berolo et al. and Aspnes et al. measured  $E_1$ . The critical point energies  $E_1$  and  $E_1 + \Delta_1$ , measured by Berolo et al., appear to have the same basic shape, separated only by a constant eV. Using the critical point energy measurements for  $E_1$  and  $E_1 + \Delta_1$  (from Berolo et al.) and the critical point energy measurement for  $E_1$  (from Aspnes et al.), an approximation for the critical point energy  $E_1 + \Delta_1$ , to be used for this new model, was found by taking the difference between  $E_1$  and  $E_1 + \Delta_1$  from Berolo et al. and then shifting  $E_1$  from Aspnes et al. by the same eV.  $E_1 + \Delta_1$  was then approximated by

$$E_1 + \Delta_1 = 3.19 + 0.456x + 0.136x^2 + 0.210x^3 + 0.048x^4. \quad 2.3.7$$

The critical point energies given by Eqs. 2.3.1 - 2.3.7 are plotted as a function of  $x$  in Fig. 2.3.1.

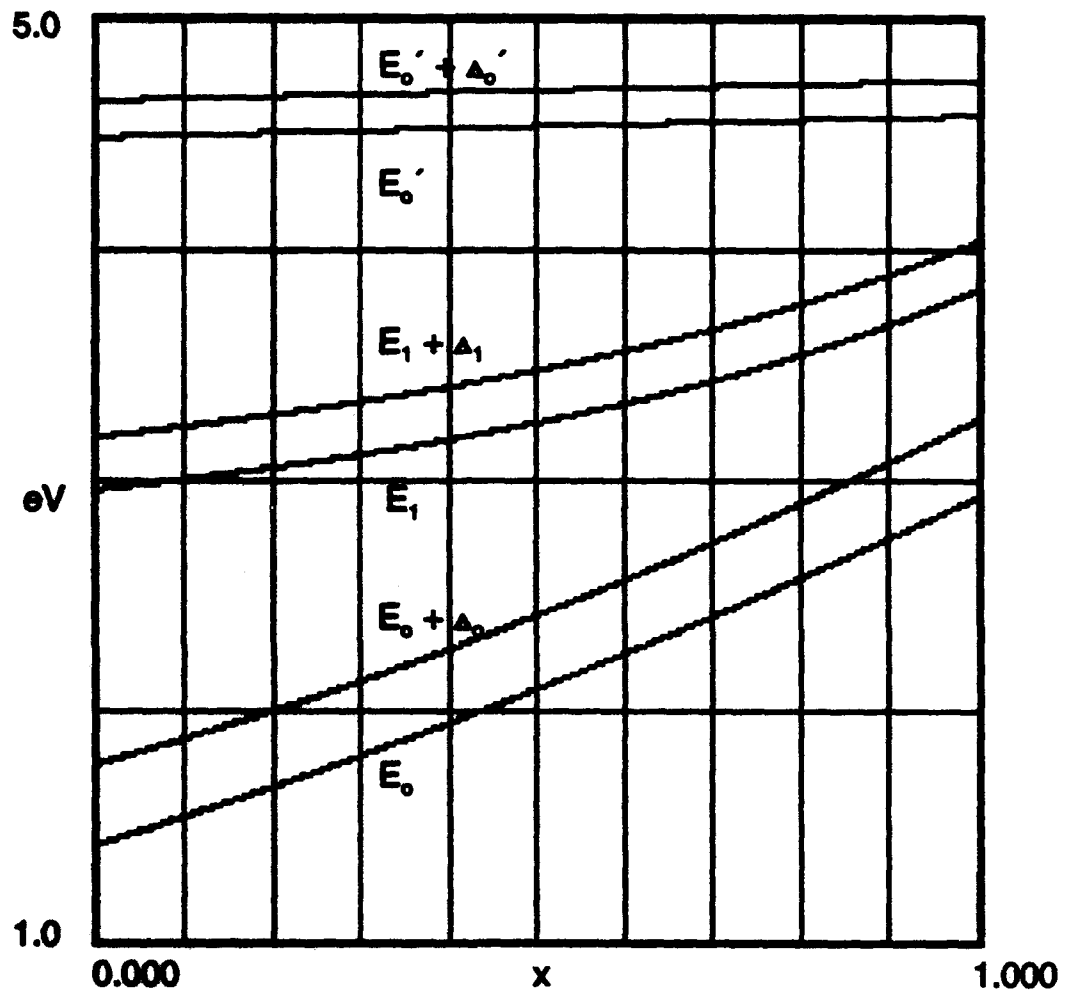


Figure 2.3.1  
Critical Point Energies for  $\text{Al}_x\text{Ga}_{1-x}\text{As}$  versus Al Concentration

Taken from Section 2.2, the refractive index is found here by using the relation:

$$(n_3)^2(\omega) = \epsilon_1(\omega), \quad 2.3.8$$

where  $n_3$ , the refractive index, and the real part of the dielectric constant ( $\epsilon_1(\omega)$ ) now include contributions from the higher transition energies. The value of the real part of the dielectric constant due to the  $E_0$  and  $E_0 + \Delta_0$  transitions<sup>54</sup> is given by the Kramers-Kronig relation<sup>53</sup>

$$\epsilon_{10}(\omega) = A(E_0)^{3/2} \{ f(\chi_0) + 1/2[E_0/(E_0 + \Delta_0)]^{3/2} f(\chi_{00}) \}, \quad 2.3.9$$

where

$$f(\chi_0) = (\chi_0)^{-2} [2 - (1 + \chi_0)^{1/2} - (1 - \chi_0)^{1/2} H(1 - \chi_0)], \quad 2.3.10$$

$$f(\chi_{00}) = (\chi_{00})^{-2} [2 - (1 + \chi_{00})^{1/2} - (1 - \chi_{00})^{1/2} H(1 - \chi_{00})], \quad 2.3.11$$

$$\chi_0 = \hbar\omega/E_0, \quad 2.3.12$$

$$\chi_{00} = \hbar\omega/(E_0 + \Delta_0) \quad 2.3.13$$

and

$$H(y) = \begin{cases} 1 & \text{for } y \geq 0 \\ 0 & \text{for } y < 0. \end{cases} \quad 2.3.14$$

In Eqs. 2.3.9 - 2.3.14,  $E_0$  and  $E_0 + \Delta_0$  are given in eV,  $\hbar\omega$  is the photon energy in eV where  $\hbar$  is Plancks constant and  $A$  is a constant used to fit the model to the experimental data.

The value of the real part of the dielectric constant due to the  $E_1$  transition<sup>54</sup> and  $E_1 + \Delta_1$  transition (Eq. 2.3.7) is given by<sup>53</sup>

$$\epsilon_{11}(\omega) = -B1(\chi_1)^{-2} \ln[1 - (\chi_1)^2] - B2(\chi_{s1})^{-2} \ln[1 - (\chi_{s1})^2], \quad 2.3.15$$

where

$$\chi_1 = \hbar\omega/E_1 \quad 2.3.16$$

and

$$\chi_{s1} = \hbar\omega/(E_1 + \Delta_1). \quad 2.3.17$$

In Eqs. 2.3.15 - 2.3.17,  $E_1$  and  $E_1 + \Delta_1$  are given in eV, and  $B1$  and  $B2$  are constants used to fit the model to the experimental data.

The value of the real part of the dielectric constant due to the  $E_2$  transition<sup>54</sup> is given by<sup>53</sup>

$$\varepsilon_{12}(\omega) = C[1 - (\chi_2)^2]/[1 - (\chi_2)^2 + (\chi_2)^2\gamma^2], \quad 2.3.18$$

where

$$\chi_2 = \hbar\omega/E_2. \quad 2.3.19$$

In Eqs. 2.3.18 - 2.3.19,  $E_2$  is given in eV, and  $C$  and  $\gamma$  are constants used to fit the model to the experimental data.

The value of the real part of the dielectric constant due to the  $E_o'$  and  $E_o' + \Delta_o'$  transitions<sup>50</sup> was found by fitting the model to the index measurements. This gives

$$\varepsilon_{10}'(\omega) = D(\chi_o' + \chi_{so}'), \quad 2.3.20$$

where

$$\chi_o' = \hbar\omega/E_o' \quad 2.3.21$$

and

$$\chi_{so}' = \hbar\omega/(E_o' + \Delta_o'). \quad 2.3.22$$

In Eqs. 2.3.20 - 2.3.22,  $E_o'$  and  $E_o' + \Delta_o'$  are given in eV,  $\hbar\omega$  is the photon energy in eV and  $D$  is a constant used to fit the model to the experimental data. The value of the nondispersive elements of the dielectric constant due



to the indirect gap transitions is given by a constant  $\epsilon_{1\infty}$ , which is used to fit the model to the experimental data.<sup>64</sup> The real part of the total dielectric constant due to all of the transition energies is the sum of the dielectric constants for each of the transition energies or

$$\epsilon_1(\omega) = \epsilon_{10}(\omega) + \epsilon_{11}(\omega) + \epsilon_{12}(\omega) + \epsilon_{10}'(\omega) + \epsilon_{1\infty}. \quad 2.3.23$$

The strength parameters A, C,  $\gamma$ , and  $\epsilon_{1\infty}$  were determined as a function of Al concentration by fitting equations to the curves presented by Adachi.<sup>64</sup>

They are given as follows:

$$A = 2.9 + 15.9x + 6.5x^2 + 0.1x^3 + 0.1x^4 + 3x^5 + 13x^6 + 32x^7, \quad 2.3.24$$

$$C = [2.31 - 0.001x - 0.001x^2 - 0.001x^3 - 0.001x^4 - 0.5x^5 - 1.2x^6 + 2.5x^7], \quad 2.3.25$$

$$\gamma = 0.137 - 0.005x - 0.0001x^2 - 0.0001x^3 - 0.02x^4 - 0.16x^5 \quad 2.3.26$$

and

$$\epsilon_{1\infty} = 1.25 - 1.98x - 0.4x^3. \quad 2.3.27$$

The strength parameters B1 and B2 were estimated by using the expressions<sup>66</sup>

$$B1 = 44[E_1 + \Delta_1/3]/[a_0(E_1)^2] \quad 2.3.28$$

and

$$B2 = 44[E_1 + 2\Delta_1/3]/[a_0(E_1 + \Delta_1)^2], \quad 2.3.29$$

where  $a_0$  is the lattice constant in Å given by<sup>48</sup>

$$a_0 = 5.6533 + 0.0078x. \quad 2.3.30$$

The strength parameter D was estimated as a function of x by substituting Eq. 2.3.20 into Eq. 2.3.23, varying D until Eq. 2.3.23 fit the experimental measurements from Aspnes et al.<sup>62</sup> for both x and photon energy. This yields

$$D = 2.535 - 1.075x - 0.65x^2 - 0.7x^3 - 0.8x^4 - 2.8x^5. \quad 2.3.31$$

Substitution of Eq. 2.3.23 into 2.3.8 gives the refractive index for the given x values as a function of  $\hbar\omega$ . Figs. 2.3.2 - 2.3.4 show the plot of the index ( $n_2$ ) as a function of  $\hbar\omega$ , between 1.2 and 1.8 eV, for the x values

0.198, 0.315 and 0.419, respectively, including the  $\pm 0.020$  accuracy of  $x$ . Figs. 2.3.2 - 2.2.4 also include the refractive indices measured by Aspnes et al., which were substituted into the model at the specific  $x$  and  $\lambda$  for which the index was actually measured. These substituted values appear as small spikes in an otherwise smooth curve, giving an indication of the accuracy of the model. As can be seen, the refractive indices, using the above model and curve fitting constants, are well within the known accuracy of  $x$ . The spikes, representing the measured values, are nearly undetectable. This model provides an excellent fit, not only around the chosen  $x = 0.300$  waveguide core and 827 nm wavelength, but also for the range of  $x$  from 0.200 - 0.400 and the range of  $\lambda$  from 0.700 - 1.0  $\mu\text{m}$ .

### Refractive Index of the Waveguide Core

Using the models from Sections 2.1 - 2.3, the refractive index of  $\text{Al}_x\text{Ga}_{1-x}\text{As}$  can be determined at fractions of Al atoms for which the index was not measured. As stated above, the target Al concentration chosen for the waveguide core in this experiment was  $x = 0.300$ . Fig. 2.4.1 is a plot of the indices versus wavelength for  $x = 0.300$  using the models outlined in Sections 2.1 - 2.3. As can be seen in Fig. 2.4.1, there is a significant difference between the three curves. The curves generated by Adachi's models ( $n_2$  and  $n_3$ ) based on Casey et al. and Aspnes et al., respectively,

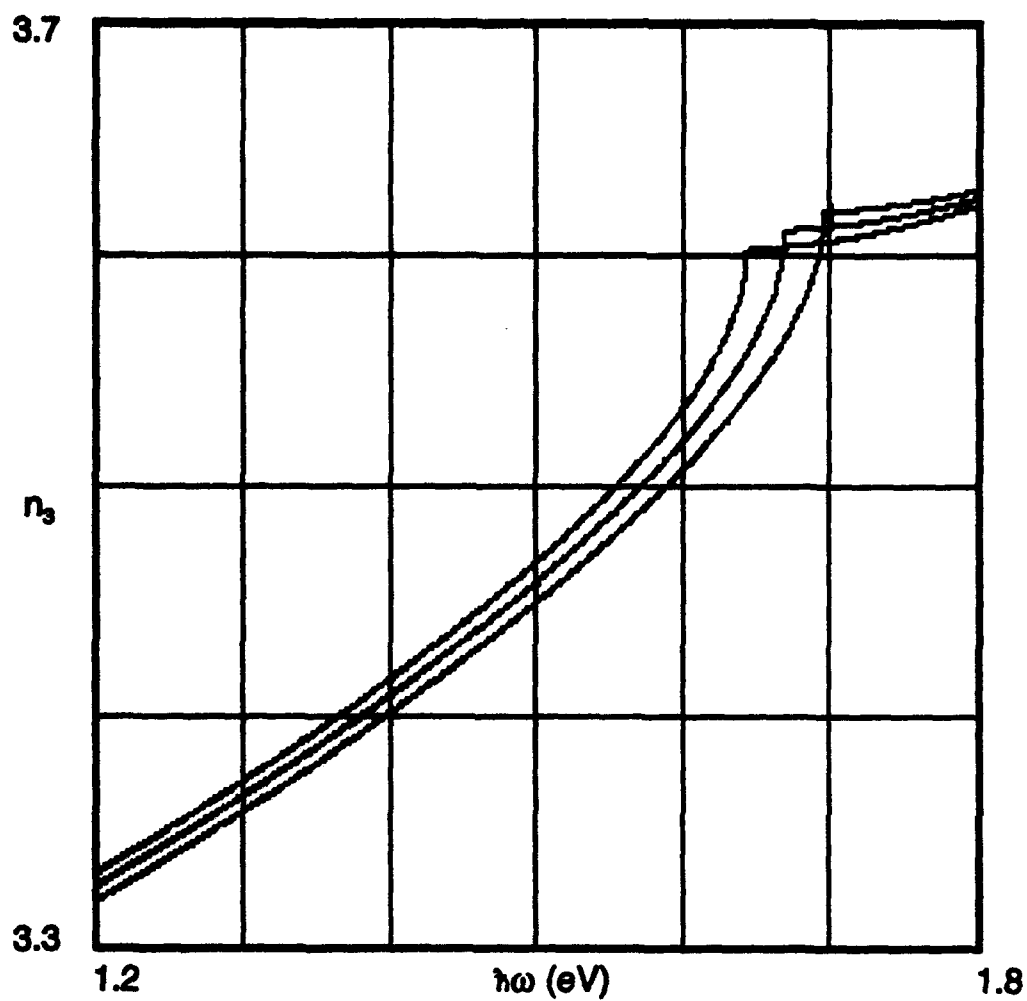


Figure 2.3.2  
Refractive Index of  $\text{Al}_x\text{Ga}_{1-x}\text{As}$  versus  
Photon Energy for  $x = 0.198 \pm 0.020$

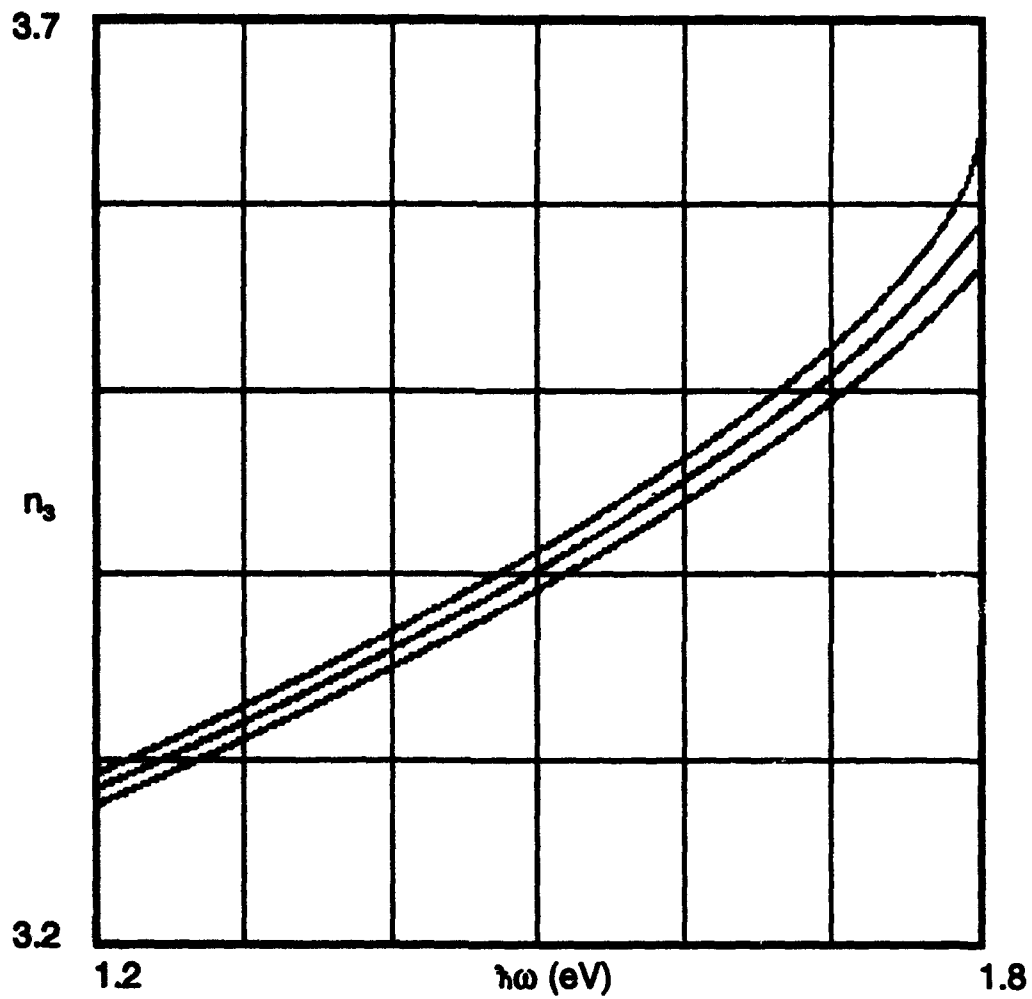


Figure 2.3.3  
Refractive Index of  $\text{Al}_x\text{Ga}_{1-x}\text{As}$  versus  
Photon Energy for  $x = 0.315 \pm 0.020$

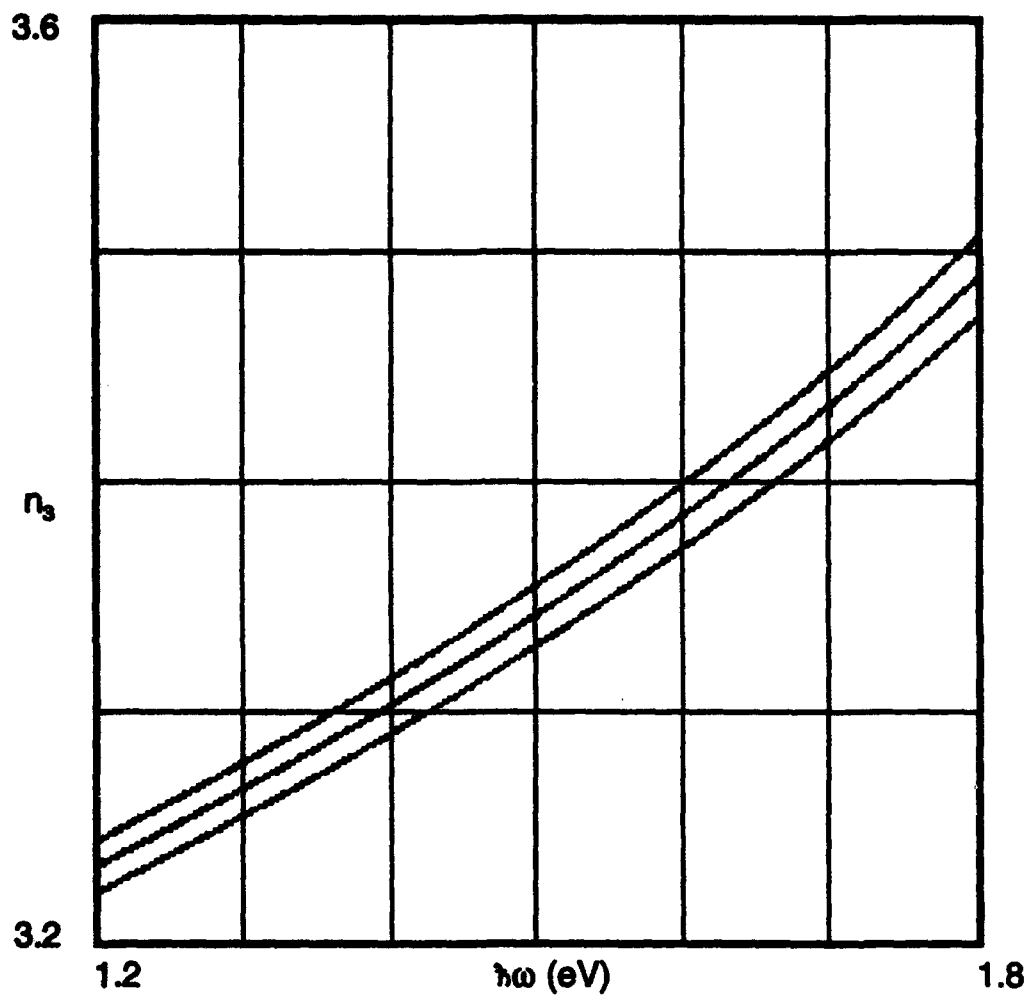


Figure 2.3.4  
Refractive Index of  $\text{Al}_x\text{Ga}_{1-x}\text{As}$  versus  
Photon Energy for  $x = 0.419 \pm 0.020$

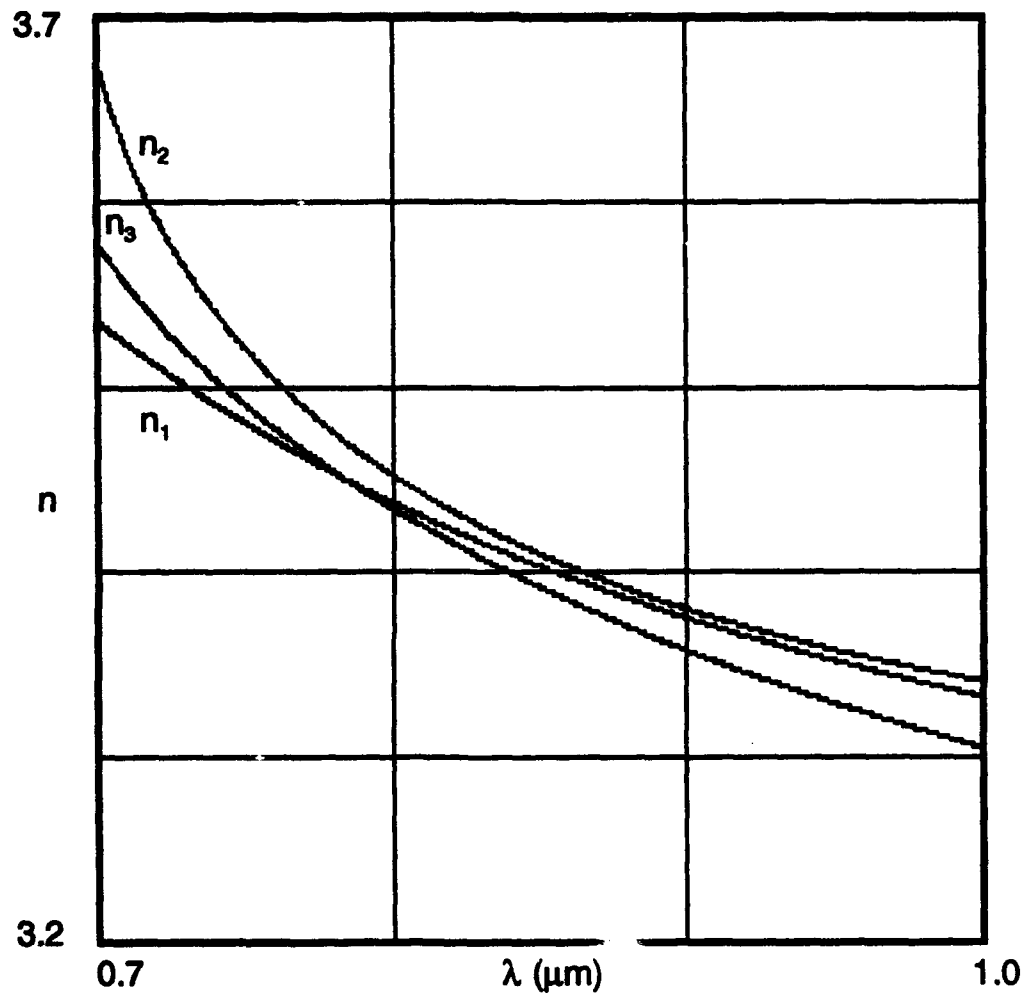


Figure 2.4.1  
Refractive Index of  $\text{Al}_x\text{Ga}_{1-x}\text{As}$   
versus Wavelength for  $x = 0.300$

are offset  $\Delta n$  from one another, but they possess the same basic shape. The slope of  $n_3$ , above  $\lambda = 0.9 \mu\text{m}$ , appears to be steeper than that of  $n_2$ . Modelling the refractive index for  $x = 0.300$  along with the  $\pm 0.020$  Al concentration accuracy, incorporating Adachi's models, shows that the difference between the two index models is barely within this  $\pm 0.020$  Al concentration accuracy. The minimum index value ( $x = 0.320$ ) for Adachi<sup>48</sup>, based on Casey et al., just overlaps the maximum index value ( $x = 0.280$ ) for Adachi,<sup>53</sup> based on Aspnes et al. (see Fig. 2.4.2). In Fig. 2.4.1, the curve for  $n_1$ , generated by Boyd's Sellmeir equation,<sup>45</sup> based on Ilegems et al., lies between the other two curves with a slope that follows the other two curves, as long as  $\lambda > 780 \text{ nm}$ . Below  $780 \text{ nm}$ , the slope of  $n_1$  falls off considerably, no longer following the other two. The correct curve is virtually impossible to determine at this time and, as mentioned above, all three curves are used almost equally by researchers. Based on Figs. 2.4.1 and 2.4.2, along with the wavelength of the laser diode used, and the fact that the indices measured by Aspnes et al. were not recorded above  $\lambda > 827 \text{ nm}$ , it was decided to further restrict the wavelength range to  $0.8 \mu\text{m} \leq \lambda \leq 0.9 \mu\text{m}$  for determination of the refractive index of  $\text{Al}_x\text{Ga}_{1-x}\text{As}$ . For this range of  $\lambda$  and the  $0.200 \leq x \leq 0.400$  given earlier, the three individual models follow their measured values quite well, offset from each other only by an amount  $\Delta n$  which is within the accuracy of the known Al concentration. Taking all three models into account, it was decided that the refractive index used in this



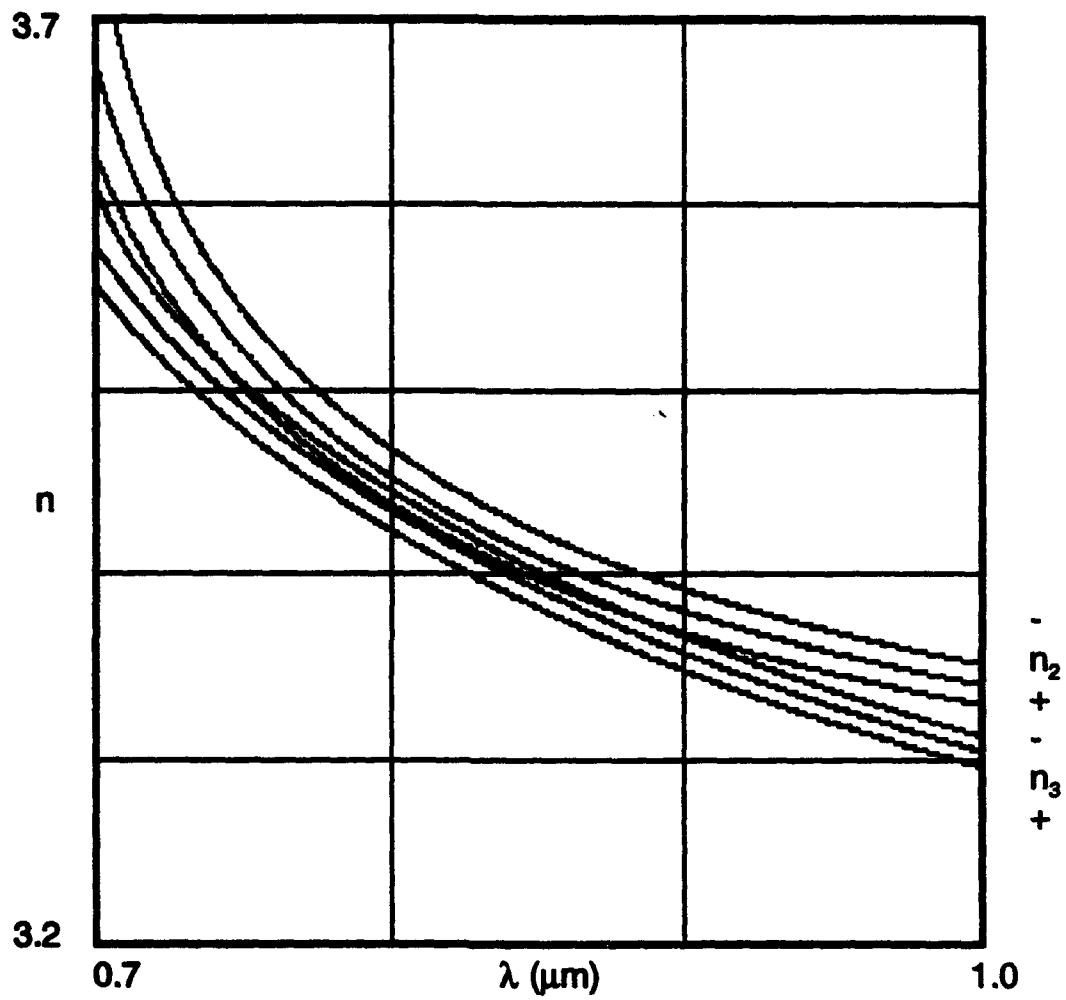


Figure 2.4.2  
Refractive Index of  $\text{Al}_x\text{Ga}_{1-x}\text{As}$   
versus Wavelength for  $x = 0.300 \pm 0.020$

dissertation would be the average of the three modelled indices, designated here as  $n_{avg}$ . The upper limit of accuracy was chosen to be  $n_2$  at  $x = 0.280$  (Adachi<sup>46</sup>), since it gave the maximum index of all the curves, and the lower limit of accuracy was chosen to be  $n_3$  at  $x = 0.320$  (Adachi<sup>53</sup>), since it gave the minimum index. Fig. 2.4.3 shows the plot of  $n_{avg}$  of  $Al_{0.30}Ga_{0.70}As$  versus wavelength, including the upper and lower limits of accuracy,  $n_2$  at 0.280 and  $n_3$  at 0.320. The  $n_{avg}$  value of the  $Al_{0.30}Ga_{0.70}As$  composition will be given the designation  $n_{core}$ , the refractive index of the core layer of the waveguide. Calculating the average index of refraction, at  $\lambda = 827$  nm, for  $x = 0.300$ , yields the refractive index of the core that will be used for this experiment. This is given as

$$n_{core} = n_{avg} = 3.419. \quad 2.4.1$$

The "plus" accuracy, as stated above, will be  $n_2$  while the "minus" accuracy will be  $n_3$ . Calculating index  $n_2$ , at  $\lambda = 827$  nm, for  $x = 0.280$ , and index  $n_3$  at  $\lambda = 827$  nm, for  $x = 0.320$ , gives

$$n_{core} = 3.419 \pm 0.023. \quad 2.4.2$$

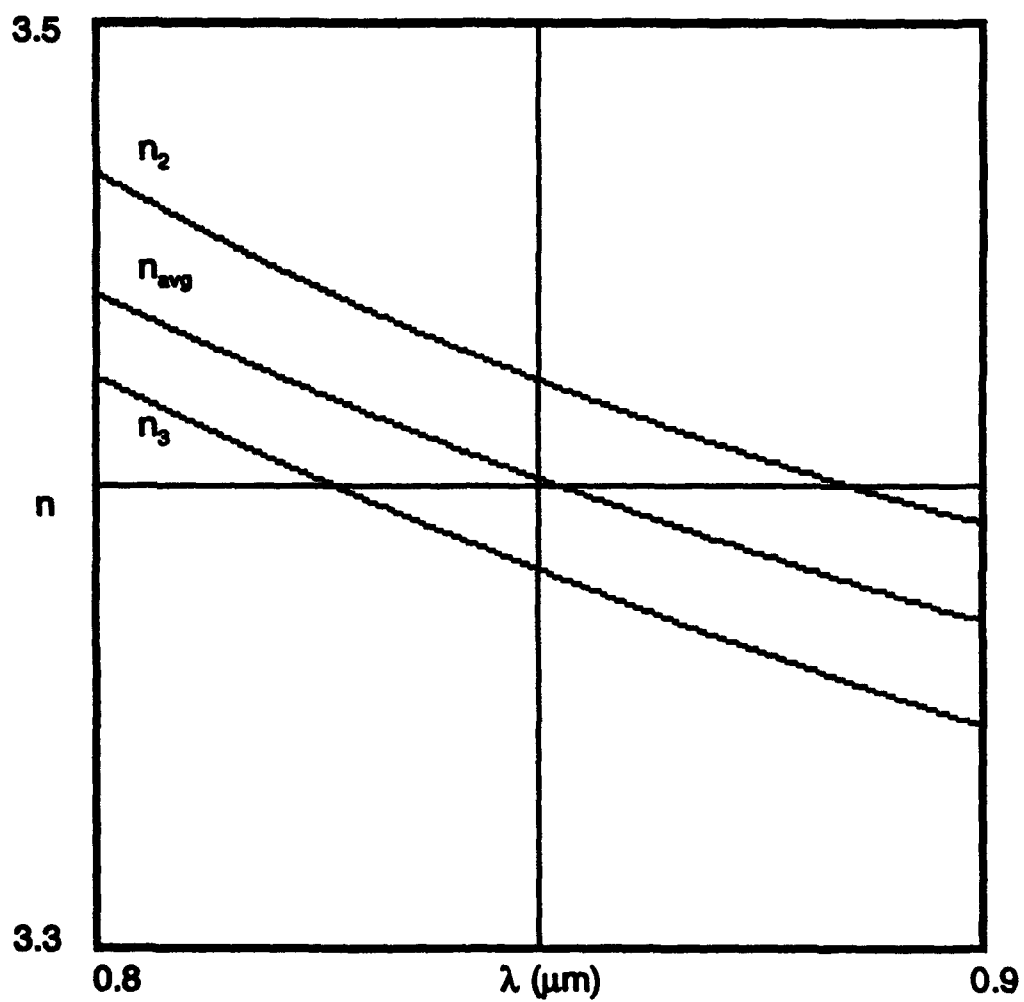


Figure 2.4.3  
Refractive Index of  $\text{Al}_x\text{Ga}_{1-x}\text{As}$   
versus Wavelength for  $x = 0.300 \pm 0.020$

### Refractive Index of the Waveguide Clad

Based on work done by Honeywell for the Air Force, the optimum thickness ( $t_g$ ) for the waveguide core layer of an  $\text{Al}_{0.30}\text{Ga}_{0.70}\text{As}$  composition was determined to be  $t_g = 1 \mu\text{m}$ .<sup>3</sup> Assuming a single mode ( $m = 0$ ) optical waveguide, with  $t_g = 1 \mu\text{m}$ ,  $\lambda = 827 \text{ nm}$ ,  $n_{\text{core}}$  given in the previous section and the relation<sup>38</sup>

$$n_{\text{core}} - n_{\text{clad}} > m^2 \lambda^2 / [4(t_g)^2 (n_{\text{core}} + n_{\text{clad}})], \quad 2.5.1$$

the index of the cladding layer can be found as

$$n_{\text{clad}} > [(n_{\text{core}})^2 - \lambda^2 / [4(t_g)^2]]^{1/2}. \quad 2.5.2$$

The Al concentration of the cladding can then be determined by using Eq. 2.5.2 along with  $n_{\text{avg}}$  for various  $x$  values until an index above the cutoff is found. Choosing  $x = 0.350$ , at  $\lambda = 827 \text{ nm}$ , one gets a refractive index for the clad slightly less than the cutoff index (see Fig. 2.5.1). The refractive index for a cladding composition of  $\text{Al}_{0.35}\text{Ga}_{0.65}\text{As}$ , at  $\lambda = 827 \text{ nm}$ , is determined by calculating  $n_{\text{avg}}$  for  $x = 0.350$ . This gives

$$n_{\text{clad}} = 3.389. \quad 2.5.3$$

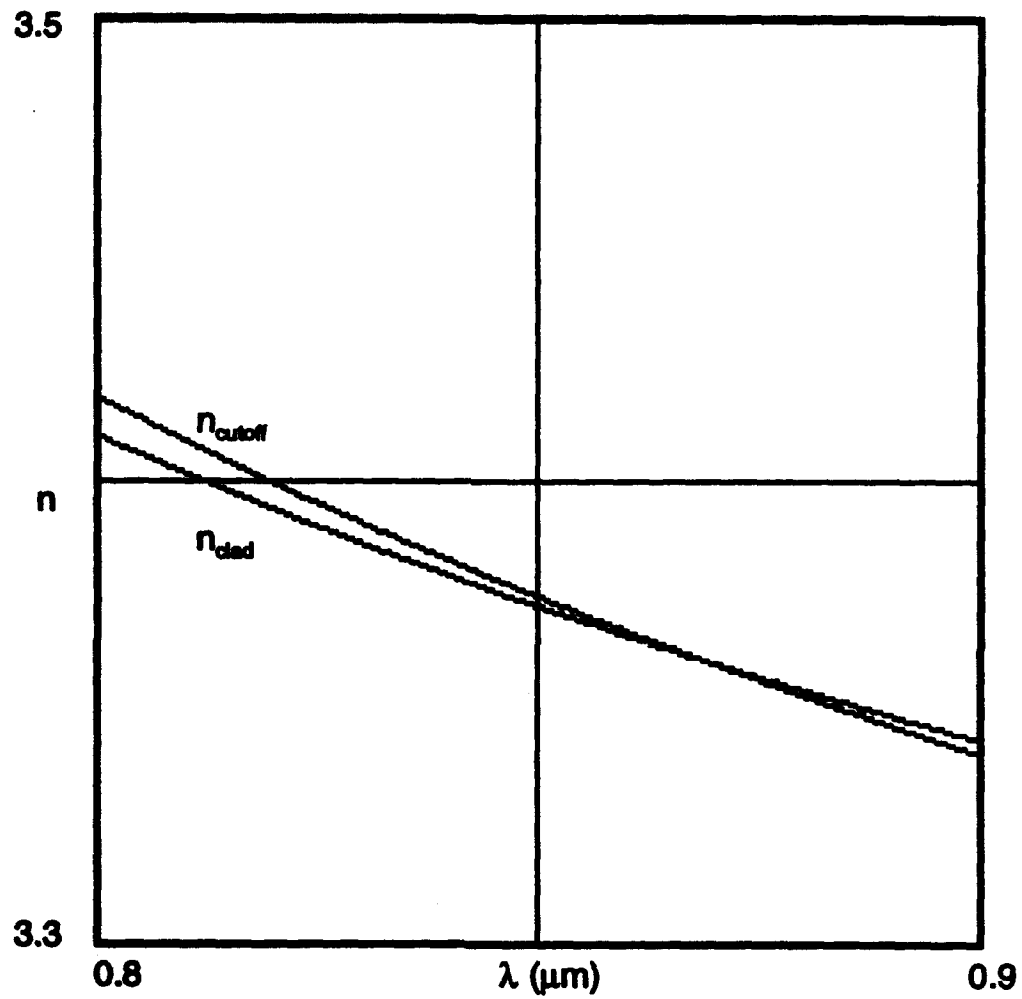


Figure 2.5.1  
Single Mode  $n_{\text{core}}$  for  $\text{Al}_{0.30}\text{Ga}_{0.70}\text{As}$  Core and  
 $n_{\text{clad}}$  for  $\text{Al}_{0.35}\text{Ga}_{0.65}\text{As}$  Clad versus Wavelength

A TE/TM mode analysis computer program, acquired from Honeywell<sup>9</sup> and based on a paper by Ghatak, Thyagarajan and Shenoy,<sup>56</sup> was run on a waveguide structure with a core composition of  $\text{Al}_{0.30}\text{Ga}_{0.70}\text{As}$  and a clad composition of  $\text{Al}_{0.35}\text{Ga}_{0.65}\text{As}$  at  $\lambda = 827$  nm to assess the losses for the various waveguide modes. The program predicted a 0.00007 dB/cm TE mode loss and a 0.00009 dB/cm TM mode loss for the "0th order" mode, and a 13.22 dB/cm TE mode loss and a 16.54 dB/cm TM mode loss for the "1st order" mode. This suggests that even though  $n_{\text{clad}}$  does not quite meet the criteria of Eq. 2.5.2, the losses of the higher order modes, predicted by the TE/TM mode analysis, are sufficient to ensure single mode propagation at  $\lambda = 827$  nm.

The molecular beam epitaxy (MBE) growth facility, located in the Solid State Electronics Directorate at Wright-Patterson Air Force Base, and the metal-organic chemical vapor deposition (MOCVD) growth facility, located at Honeywell, should be able to control the Al concentration, over a range of 0.300 - 0.350, to within  $\pm 0.005$  of the target composition for both the first layer and the difference in  $x$  between successive layers.<sup>57,159</sup> This will provide excellent repeatability. Both MBE and MOCVD machines will be used for this dissertation. The claim of the accuracy of the control of  $x$  is a valid one since this level of control has also been demonstrated on the TTOA program<sup>42</sup> as well as on the III-V Optical Waveguide Technology

program.<sup>3</sup> With this accuracy, the Al concentration of the waveguide core could be as low as  $x = 0.295$  and the Al concentration of the waveguide clad could be as high as 0.355. Fig. 2.5.2 is a plot of  $n_{\text{clad}}$ , for  $x = 0.355$ , and  $n_{\text{cutoff}}$ , calculated from Eq. 2.5.2, using  $n_{\text{core}}$  for  $x = 0.295$ . As can be seen,  $n_{\text{clad}}$  is slightly less than  $n_{\text{cutoff}}$  at  $\lambda = 827$  nm, indicating the possible presence of higher order modes. The TE/TM mode analysis program, run on this waveguide structure at  $\lambda = 827$  nm, predicted 0.00001 dB/cm TE/TM mode losses for the "0th order" mode and a 2.21 dB/cm TE mode loss and 2.86 dB/cm TM mode loss for the "1st order" mode. Based on these results, which also indicate that one might not be able to ensure against the presence of higher order modes, the target Al concentration for the clad will be slightly less than 35%. Trying to grow a clad with  $x < 0.350$  while maintaining  $x = 0.300$  for the core is difficult.<sup>57,169</sup> Waveguide structures using a target  $\text{Al}_{0.30}\text{Ga}_{0.70}\text{As}$  core composition along with a target  $\text{Al}_{0.35}\text{Ga}_{0.65}\text{As}$  clad composition will be investigated next.

### AlGa<sub>1-x</sub>As Waveguide Structure

As stated in the previous section, the accuracy of the Al concentration can be controlled to within  $\pm 0.005$  for this experiment. Using this accuracy when determining  $n_{\text{avg}}$  for  $x = 0.300$  at  $\lambda = 827$  nm gives a core index of

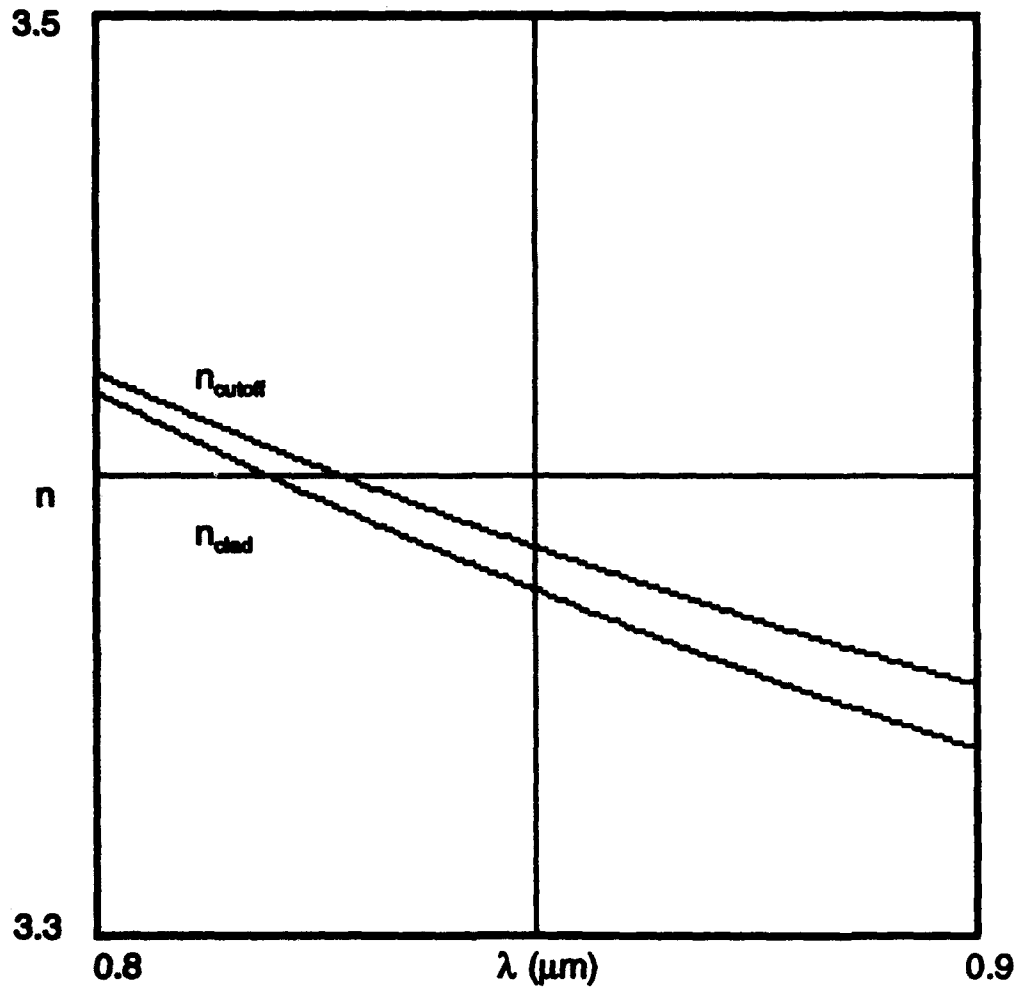


Figure 2.5.2  
Single Mode  $n_{\text{cutoff}}$  for  $\text{Al}_{0.295}\text{Ga}_{0.705}\text{As}$  Core and  
 $n_{\text{clad}}$  for  $\text{Al}_{0.365}\text{Ga}_{0.635}\text{As}$  Clad versus Wavelength



$$n_{\text{core}} = 3.419 \pm 0.003.$$

2.5.5

Using the same accuracy to determine  $n_{\text{avg}}$  for  $x = 0.350$  at  $\lambda = 827$  nm gives a clad index of

$$n_{\text{clad}} = 3.389 \pm 0.003.$$

2.5.6

One also needs to take into account the difference in the refractive index measurements taken by Ilegems et al., Casey et al. and Aspnes et al. This will be done by designating three configurations of waveguide structures using  $n_{\text{avg}}$  along with the "plus" and "minus" accuracies ( $n_2$  and  $n_3$ ) for the core and clad layers. First, the average refractive indices ( $n_{\text{avg}}$ ) for the core and clad will make up Waveguide Structure 1. Next, the "plus" accuracy indices ( $n_2$ ) for the core and clad, modelled by Adachi<sup>48</sup>, based on Casey et al., will make up Waveguide Structure 2. Last, the "minus" accuracy indices ( $n_3$ ) for the core and clad, modelled by Adachi<sup>53</sup>, based on Aspnes et al., will make up Waveguide Structure 3. This gives the possibility of three waveguide structures. The three waveguide structures, along with the indices of refraction, are presented below.

Each of the three waveguide structures will be used for determining the interaction length of the optical directional coupler switches that will model

the optical Fredkin gates. Comparing the three structures should then provide a more thorough analysis than using only one of the models or one set of measurements for the refractive index.

### Waveguide Structure 1

$$(n_{\text{avg}}, x_{\text{core1}} = 0.300 \pm 0.005, x_{\text{clad1}} = 0.350 \pm 0.005)$$

$$\text{core}_1 = \text{Al}_{0.300}\text{Ga}_{0.700}\text{As} \quad \text{clad}_1 = \text{Al}_{0.350}\text{Ga}_{0.650}\text{As}$$

$$n_{\text{core1}} = 3.419 \pm 0.003 \quad n_{\text{clad1}} = 3.389 \pm 0.003$$

### Waveguide Structure 2

$$(n_2, x_{\text{core2}} = 0.315 \pm 0.005, x_{\text{clad2}} = 0.365 \pm 0.005)$$

$$\text{core}_2 = \text{Al}_{0.315}\text{Ga}_{0.685}\text{As} \quad \text{clad}_2 = \text{Al}_{0.365}\text{Ga}_{0.635}\text{As}$$

$$n_{\text{core2}} = 3.403 \pm 0.003 \quad n_{\text{clad2}} = 3.375 \pm 0.003$$

### Waveguide Structure 3

$$(n_3, x_{\text{core3}} = 0.285 \pm 0.005, x_{\text{clad3}} = 0.335 \pm 0.005)$$

$$\text{core}_3 = \text{Al}_{0.285}\text{Ga}_{0.715}\text{As} \quad \text{clad}_3 = \text{Al}_{0.335}\text{Ga}_{0.665}\text{As}$$

$$n_{\text{core3}} = 3.438 \pm 0.003 \quad n_{\text{clad3}} = 3.404 \pm 0.003$$

### CHAPTER III

#### DETERMINATION OF THE INTERACTION LENGTH OF THE ZERO-GAP DIRECTIONAL COUPLER

In this chapter, the interaction length of an  $\text{Al}_x\text{Ga}_{1-x}\text{As}$  zero-gap directional coupler is determined by substituting the refractive index of  $\text{Al}_x\text{Ga}_{1-x}\text{As}$  into several dielectric strip waveguide directional coupler models, driving the separation between the waveguides to zero.

Directional coupling is the exchange of power between the guided modes in adjacent parallel waveguides separated by a finite distance. Fig. 3.0.1 is a schematic of a conventional directional coupler device. The index of refraction of the core region is  $n$  while that of the clad regions is  $n(1 - \Delta)$ , which is less than the index of the core region by an amount  $\Delta$ . The dimensions  $a$ ,  $b$  and  $c$  are, respectively, the width, thickness and separation of the waveguides. The interaction length, or distance required for total exchange of power from one guide to the other is  $L$ .<sup>61</sup> The wave is considered to propagate along the  $z$  axis.

Extensive treatment of optical waveguide and directional coupler theory has been addressed by many researchers for both continuous two-

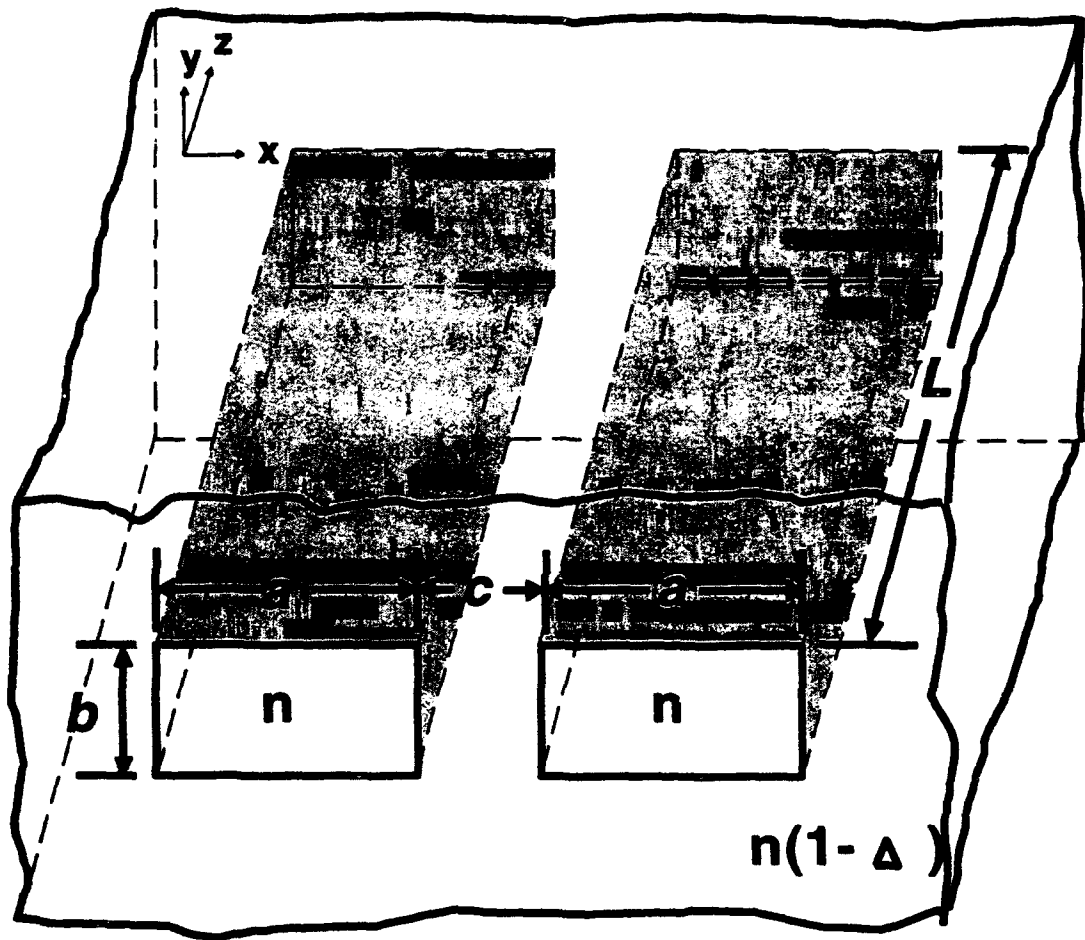


Figure 3.0.1  
Rectangular Waveguide Directional Coupler

dimensional film waveguides and dielectric strip waveguides. Various methods, such as dielectric waveguide, coupled mode theory, effective index, beam propagation method and finite-element analysis have been used.<sup>16,17,28,61-60</sup> Analysis of these methods shows good agreement between all of the different models provided that we are far from cutoff. This means that the normalized frequency, defined as

$$B = (bk/\pi)[n - n(1 - \Delta)]^{1/2}, \quad 3.0.1$$

is greater than or equal to 1.6 for single mode operation.<sup>79,80</sup> In Eq. 3.0.1 the free-space propagation constant of plane waves is defined as  $k = 2\pi/\lambda$  or wave number, where  $\lambda$  is the wavelength. Since the waveguides fabricated for this experiment will be rectangular ridge type structures, we will use several of the dielectric strip waveguide methods to model the devices for this experiment.<sup>61,62,66-74</sup>

### Marcatili Rectangular Dielectric Waveguide Model

In 1969, Marcatili<sup>61</sup> presented an analytical model for integrated optical rectangular dielectric waveguides and directional couplers. Fig. 3.1.1 illustrates a directional coupler with the following parameters:  $n_1$  and  $n_2$  are the refractive indices of the core and top clad, respectively;  $n_3$  is the

refractive index of the outside clad;  $n_4$  is the refractive index of the bottom clad;  $n_5$  is the refractive index of the center clad; the width and thickness of the individual waveguides are  $a$  and  $b$ , respectively; the distance of separation between the two waveguides is  $c$ . The modes of the dielectric waveguide are classified as transverse electric ( $TE_{pq}$ ) and transverse magnetic ( $TM_{pq}$ ) modes. The variables,  $p = (0,1,2,...)$  and  $q = (0,1,2,...)$ , indicate the number of extrema of the electric or magnetic field along the  $x$  and  $y$  directions, respectively. This gives the order of the mode. For the fundamental "0th order"  $TE_{pq}$  mode,  $p = q = 0$ , and the transverse electric mode is given the designation  $TE_{00}$ .  $TE_{pq}$  ( $TM_{pq}$ ) modes have the electric field component polarized predominantly in the  $y$  ( $x$ ) direction and the magnetic field component polarized predominantly in the  $x$  ( $y$ ) direction. The amplitudes of the fields have only one maximum in each direction.

For well-guided modes, the field decays exponentially in the  $n_2$ ,  $n_3$ ,  $n_4$  and  $n_5$  regions of the directional coupler waveguide structure. Most of the power travels in the  $n_1$  regions while only a small part of the power travels in the  $n_2$ ,  $n_3$ ,  $n_4$  and  $n_5$  regions. An even smaller portion of the power travels in the shaded areas. Marcatili found that very little error was introduced when the fields along the edges of the shaded regions were not properly matched when calculating the fields in the  $n_1$  regions. This allowed him to neglect the shaded areas from consideration, thus, simplifying the boundary

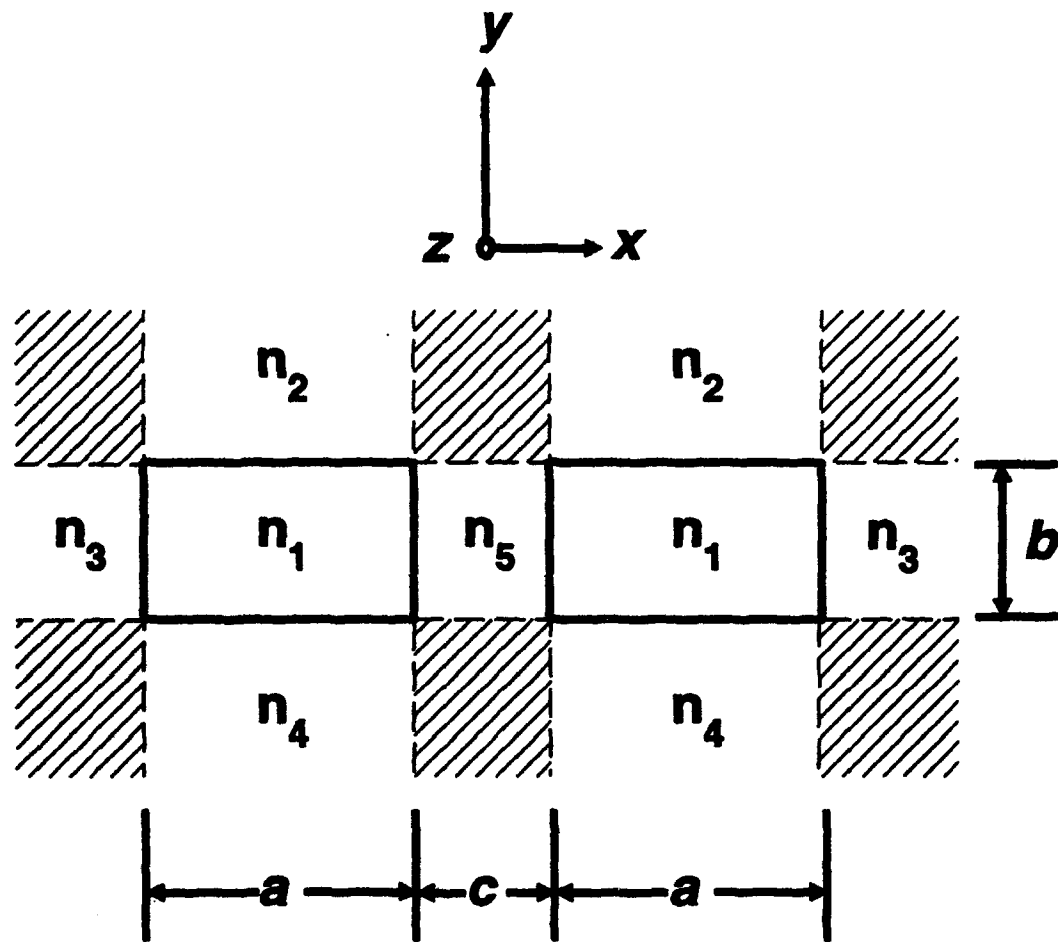


Figure 3.1.1  
Rectangular Waveguide Directional Coupler Cross Section

value problem by solving only along the four sides of the core region  $n_1$ .

### TE<sub>pq</sub> Modes

For the rectangular dielectric waveguide, illustrated in Fig. 3.1.1, the electric and magnetic field components in the five areas are given by<sup>61</sup>

$$H_{x1} = M_1 \cos(k_x x + \alpha) \cos(k_y y + \delta) \exp(-ik_z z + i\omega t), \quad 3.1.1$$

$$H_{x2} = M_2 \cos(k_x x + \alpha) \exp[-(ik_y y + ik_z z - i\omega t)], \quad 3.1.2$$

$$H_{x3} = M_3 \cos(k_y y + \delta) \exp[-(ik_x x + ik_z z - i\omega t)], \quad 3.1.3$$

$$H_{x4} = M_4 \cos(k_x x + \alpha) \exp(ik_y y - ik_z z + i\omega t), \quad 3.1.4$$

$$H_{x5} = M_5 \cos(k_y y + \delta) \sin(k_{x5} x + \gamma) \exp(-ik_z z + i\omega t), \quad 3.1.5$$

$$H_{y1} = H_{y2} = H_{y3} = H_{y4} = H_{y5} = 0, \quad 3.1.6$$

$$H_{z1} = -[(i/k_z) \partial^2 H_{x1} / \partial x \partial y], \quad 3.1.7$$

$$H_{z2} = -[(i/k_z) \partial^2 H_{x2} / \partial x \partial y], \quad 3.1.8$$



$$H_{x3} = -[(1/k_2)\partial^2 H_{x3}/\partial x \partial y], \quad 3.1.9$$

$$H_{x4} = -[(1/k_2)\partial^2 H_{x4}/\partial x \partial y], \quad 3.1.10$$

$$H_{x5} = -[(1/k_2)\partial^2 H_{x5}/\partial x \partial y], \quad 3.1.11$$

$$E_{x1} = -[(1/(\omega n_1^2 k_2))\partial^2 H_{x1}/\partial x \partial y], \quad 3.1.12$$

$$E_{x2} = -[(1/(\omega n_2^2 k_2))\partial^2 H_{x2}/\partial x \partial y], \quad 3.1.13$$

$$E_{x3} = -[(1/(\omega n_3^2 k_2))\partial^2 H_{x3}/\partial x \partial y], \quad 3.1.14$$

$$E_{x4} = -[(1/(\omega n_4^2 k_2))\partial^2 H_{x4}/\partial x \partial y], \quad 3.1.15$$

$$E_{x5} = -[(1/(\omega n_5^2 k_2))\partial^2 H_{x5}/\partial x \partial y], \quad 3.1.16$$

$$E_{y1} = H_{x1}[(k^2 n_1^2 - k_{y1}^2)/\omega n_1^2 k_2], \quad 3.1.17$$

$$E_{y2} = H_{x2}[(k^2 n_2^2 - k_{y2}^2)/\omega n_2^2 k_2], \quad 3.1.18$$

$$E_{y3} = H_{x3}[(k^2 n_3^2 - k_{y3}^2)/\omega n_3^2 k_2], \quad 3.1.19$$

$$E_{y4} = H_{x4}[(k^2 n_4^2 - k_{y4}^2)/\omega \epsilon n_4^2 k_2], \quad 3.1.20$$

$$E_{y5} = H_{x5}[(k^2 n_5^2 - k_{y5}^2)/\omega \epsilon n_5^2 k_2], \quad 3.1.21$$

$$E_{x1} = [(i/\omega \epsilon n_1^2) \partial H_{x1} / \partial y], \quad 3.1.22$$

$$E_{x2} = [(i/\omega \epsilon n_2^2) \partial H_{x2} / \partial y], \quad 3.1.23$$

$$E_{x3} = [(i/\omega \epsilon n_3^2) \partial H_{x3} / \partial y], \quad 3.1.24$$

$$E_{x4} = [(i/\omega \epsilon n_4^2) \partial H_{x4} / \partial y], \quad 3.1.25$$

$$E_{x5} = [(i/\omega \epsilon n_5^2) \partial H_{x5} / \partial y], \quad 3.1.26$$

where  $M_{1,2,3,4,5}$  are the amplitudes of the field in each respective medium,  $\alpha$  locates the field maxima in the core region  $n_1$ ,  $\delta$  locates the field minima in the core region  $n_1$ ,  $\omega$  is the angular frequency and  $\epsilon$  is the permittivity of free space. The  $\gamma$  term is necessary because single mode operation of a directional coupler will guide two kinds of  $TE_{00}$  modes. One is symmetric when  $\gamma = 90^\circ$ , and the other is antisymmetric when  $\gamma = 0^\circ$ .<sup>61</sup> Both are TEM modes with main field components  $E_y$  and  $H_x$ . For a symmetric mode, the

plane  $x = 0$  is a magnetic short circuit. For an antisymmetric mode, the plane  $x = 0$  is an electric short circuit. The electric and magnetic field components for both symmetric and antisymmetric modes are depicted in Fig. 3.1.2.

The propagation constants  $k_{xv}$ ,  $k_{yv}$  and  $k_z$  in each of the five regions are related by<sup>81</sup>

$$k_{xv}^2 + k_{yv}^2 + k_z^2 = \omega^2 \epsilon \mu n_v^2 = k_v^2, \quad 3.1.27$$

where  $v = 1, 2, 3, 4, 5$  indicates the region and  $\mu$  is the permeability of free space. In order to match the fields along the boundaries between the core region  $n_1$  and the top and bottom clad regions ( $n_2$  and  $n_4$ ) and between the core region  $n_1$  and the outside and center clad regions ( $n_3$  and  $n_5$ ), Marcatili assumed the following:

$$k_{x1} = k_{x2} = k_{x4} = k_x \quad 3.1.28$$

and

$$k_{y1} = k_{y3} = k_{y5} = k_y \quad 3.1.29$$

Since the refractive index of the core region  $n_1$  is larger than the refractive indices of the cladding regions, only modes of plane wavelets

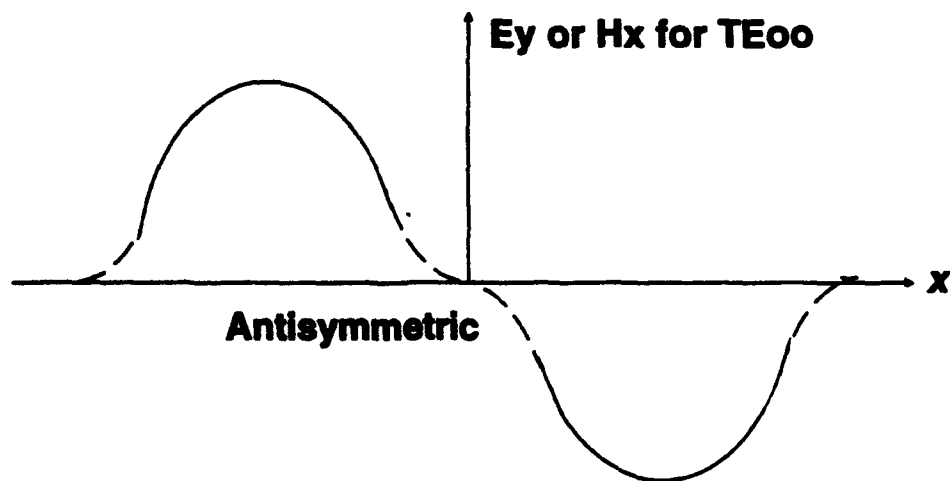
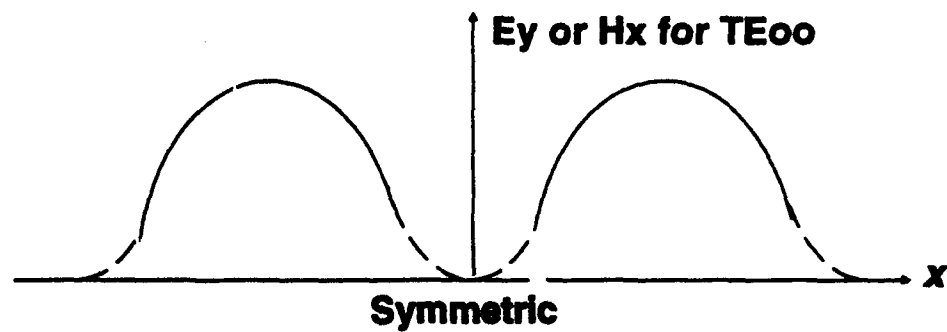
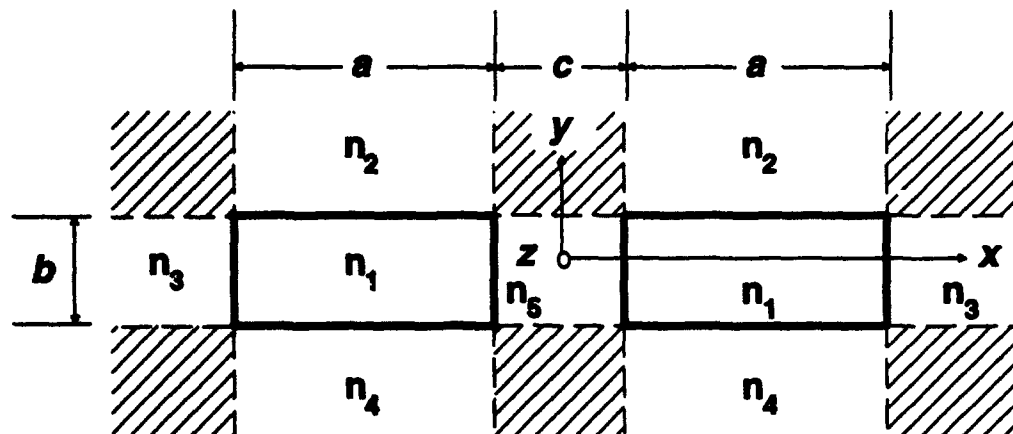


**Figure 3.1.2**  
**Field Intensity Profiles of the Symmetric and**  
**Antisymmetric Modes in a Rectangular Directional Coupler**

impinging at grazing angles on the surface of the core region  $n_1$  are guided. This implies that  $k_x \ll k_z$  and  $k_y \ll k_z$  and, therefore, the electric field components  $E_{x1}$ ,  $E_{x2}$ ,  $E_{x3}$ ,  $E_{x4}$  and  $E_{x5}$  can be neglected. Matching the remaining field components,  $H_x$  and  $E_y$ , along the boundaries of the core region  $n_1$  gives the transcendental equations<sup>61</sup>

$$k_x a = k_{x0} a [1 + (2\xi_{35}/a) \exp(-\alpha \xi_{35} - 2\gamma) / (1 + k_{x0}^2 \xi_{35}^2)] \quad 3.1.30$$

and

$$k_y b = (q + 1)\pi - \tan^{-1}[(n_2^2/n_1^2)(k_y \eta_{24})] - \tan^{-1}[(n_4^2/n_1^2)(k_y \eta_{44})], \quad 3.1.31$$

where the transverse propagation constants  $k_x$  and  $k_y$  are solutions to Eqs. 3.1.30 and 3.1.31, respectively.  $k_{x0}$  is the solution to<sup>61</sup>

$$k_{x0} a = (p + 1)\pi - \tan^{-1}(k_{x0} \xi_{33}) - \tan^{-1}(k_{x0} \xi_{55}). \quad 3.1.32$$

A measure of the penetration depths of the field components in the various media are given by<sup>61</sup>

$$\xi_{3,5} = 1/[(\pi/A_{3,5})^2 - k_{x0}^2]^{1/2} \quad 3.1.33$$

and

$$\eta_{2,4} = 1/[(\pi/A_{2,4})^2 - k_y^2]^{1/2} \quad 3.1.34$$

where

$$A_{2,3,4,5} = \lambda[2(n_1^2 - n_{2,3,4,5}^2)^{1/2}] \quad 3.1.35$$

are the maximum thicknesses of the media for which the slab supports only the fundamental  $TE_{00}$  mode.

From Eqs. 3.1.27, 3.1.28 and 3.1.29 the axial propagation constant for each mode of the coupler is determined by<sup>61</sup>

$$k_z = (k_1^2 - k_x^2 - k_y^2)^{1/2}, \quad 3.1.36$$

where  $k_1 = kn_1$  is the propagation constant of a plane wave through a medium with a refractive index  $n_1$  at a free-space wavelength  $\lambda$ , and  $k_x$  and  $k_y$  are obtained from Eqs. 3.1.30 and 3.1.31.

Substituting  $\gamma$  into Eq. 3.1.30 gives slightly different axial propagation constants for the symmetric ( $\gamma = 90^\circ$ ) modes and antisymmetric ( $\gamma = 0^\circ$ ) modes.<sup>61</sup>

$$k_{za} = k_{zo}[1 + 2(k_{zo}^2/k_{zo}^2)(\xi_s/a)\exp(-d\xi_s)/(1 + k_{zo}^2\xi_s^2)] \quad 3.1.37$$

and

$$k_{zs} = k_{zo}[1 - 2(k_{zo}^2/k_{zo}^2)(\xi_s/a)\exp(-d\xi_s)/(1 + k_{zo}^2\xi_s^2)], \quad 3.1.38$$

where

$$k_{x0} = (k_1^2 - k_{x0}^2 - k_y^2)^{1/2} \quad 3.1.39$$

is the axial propagation constant of the TE mode of a single dielectric waveguide ( $c \rightarrow \infty$ ) (see Fig. 3.1.2.).

The interaction length  $L$  for total power transfer from one waveguide to the other and the coupling coefficient  $K$  between the two waveguides can then be related to  $k_{zs}$  and  $k_{ze}$  by<sup>61</sup>

$$\begin{aligned} -iK = \pi/(2L) &= (k_{zs} - k_{ze})/2 \\ &= 2(k_{x0}^2/k_{z0})(\xi_s/a)\exp(-d\xi_s)/(1 + k_{x0}^2\xi_s^2). \end{aligned} \quad 3.1.40$$

The interaction length and coupling coefficient for the zero-gap directional coupler are obtained by driving the separation between the two adjacent waveguides to zero, which yields

$$-iK = \pi/(2L) = 2(k_{x0}^2/k_{z0})(\xi_s/a)/(1 + k_{x0}^2\xi_s^2). \quad 3.1.41$$

### TM<sub>pq</sub> Modes

The analysis for the TM<sub>pq</sub> modes is very similar to that for the TE<sub>pq</sub> modes. The electric and magnetic field components for TM<sub>pq</sub> modes are

found by substituting  $E$  for  $H$ ,  $H$  for  $E$ ,  $-\epsilon$  for  $\mu$  and  $-\mu$  for  $\epsilon$  into Eqs. 3.1.1 - 3.1.26. Following Eqs. 3.1.28 and 3.1.29, the field components  $E_y$  and  $H_x$  can be neglected for the  $TM_{pq}$  analysis.

Matching the field components,  $E_x$  and  $H_y$ , along the boundaries of the core region  $n_1$  in the same way as was done to match the field components  $H_x$  and  $E_y$  for the  $TE_{pq}$  analysis gives the transcendental equations<sup>61</sup>

$$k_x a = k_{x0} a [1 + (2\xi_3/a) \exp(-\alpha\xi_3 - 2\eta)] / (1 + k_{x0}^2 \xi_3^2) \quad 3.1.42$$

and

$$k_y b = (q + 1)\pi - \tan^{-1}(k_y \eta_2) - \tan^{-1}(k_y \eta_4), \quad 3.1.43$$

where the transverse propagation constants  $k_x$  and  $k_y$  are solutions to Eqs. 3.1.42 and 3.1.43, respectively,  $k_{x0}$  is the solution to

$$k_{x0} a = (p + 1)\pi - \tan^{-1}[(n_3^2/n_1^2)(k_{x0} \xi_3)] - \tan^{-1}[(n_5^2/n_1^2)(k_{x0} \xi_5)], \quad 3.1.44$$

and  $\eta_2$ ,  $\eta_4$ ,  $\xi_3$  and  $\xi_5$  are obtained from Eqs. 3.1.33, 3.1.34 and 3.1.35.

The interaction length  $L$  for total power transfer from one waveguide to the other and the coupling coefficient  $K$  between the two waveguides are determined by Eq. 3.1.40 using  $k_{x0}$ ,  $k_y$  and  $k_{x0}$  obtained from Eqs. 3.1.39, 3.1.43 and 3.1.44, respectively. The interaction length and coupling



coefficient for the zero-gap directional coupler are obtained by substituting  $k_{x0}$ ,  $k_y$  and  $k_{x0}$  obtained from Eqs. 3.1.39, 3.1.43 and 3.1.44, into Eq. 3.1.41.

### Marcuse Rectangular Dielectric Waveguide Model

Marcuse<sup>62</sup> has derived a rectangular dielectric waveguide model following the approach developed by Marcatili. Like the preceding analysis, the four shaded regions, (see Fig. 3.1.1), are neglected. The analysis presented by Marcuse starts with the Maxwell equations:

$$\nabla \times \mathbf{H} = \epsilon_0 n^2 \partial \mathbf{E} / \partial t \quad 3.2.1$$

and

$$\nabla \times \mathbf{E} = -\mu_0 \partial \mathbf{H} / \partial t, \quad 3.2.2$$

where  $\mathbf{H}$  is the magnetic field vector,  $\mathbf{E}$  is the electric field vector,  $\epsilon_0$  is the dielectric permittivity of vacuum,  $\mu_0$  is the magnetic permeability of vacuum,  $n$  is the refractive index of the medium and  $t$  is the time variable. The time and  $z$  dependence equation for the time harmonic and mode fields is given by<sup>62</sup>

$$\exp[i(\omega t - \beta z)], \quad 3.2.3$$

where  $\omega$  is the radian frequency and the eigenvalue  $\beta$  is the  $z$  component of the propagation vector of plane waves traveling in the waveguide core. The variable  $\beta$  is designated as the propagation constant of the guided waveguide modes and is expressed by<sup>86</sup>

$$\beta = n_1 k \cos \theta_1, \quad 3.2.4$$

where  $k = 2\pi/\lambda$  is the wave number,  $n_1$  is the refractive index of the waveguide core and  $\theta_1$  is the angle at which the wave propagates through the waveguide core with respect to the waveguide clad  $n_2$  (see Fig. 3.2.1). For the wave to propagate through the core medium with a refractive index of  $n_1$ ,  $\theta_1$  must not exceed the critical angle for total internal reflection given by<sup>86</sup>

$$\cos \theta_{1c} = n_2/n_1. \quad 3.2.5$$

Using the equations above, the transverse electric and magnetic field components for the  $TE_{pq}$  and  $TM_{pq}$  modes can be given in terms of the longitudinal field components by<sup>82</sup>

$$E_x = -(1/K_1^2)[(\beta \partial E_z / \partial x) + (\omega \mu_0 \partial H_z / \partial y)], \quad 3.2.6$$

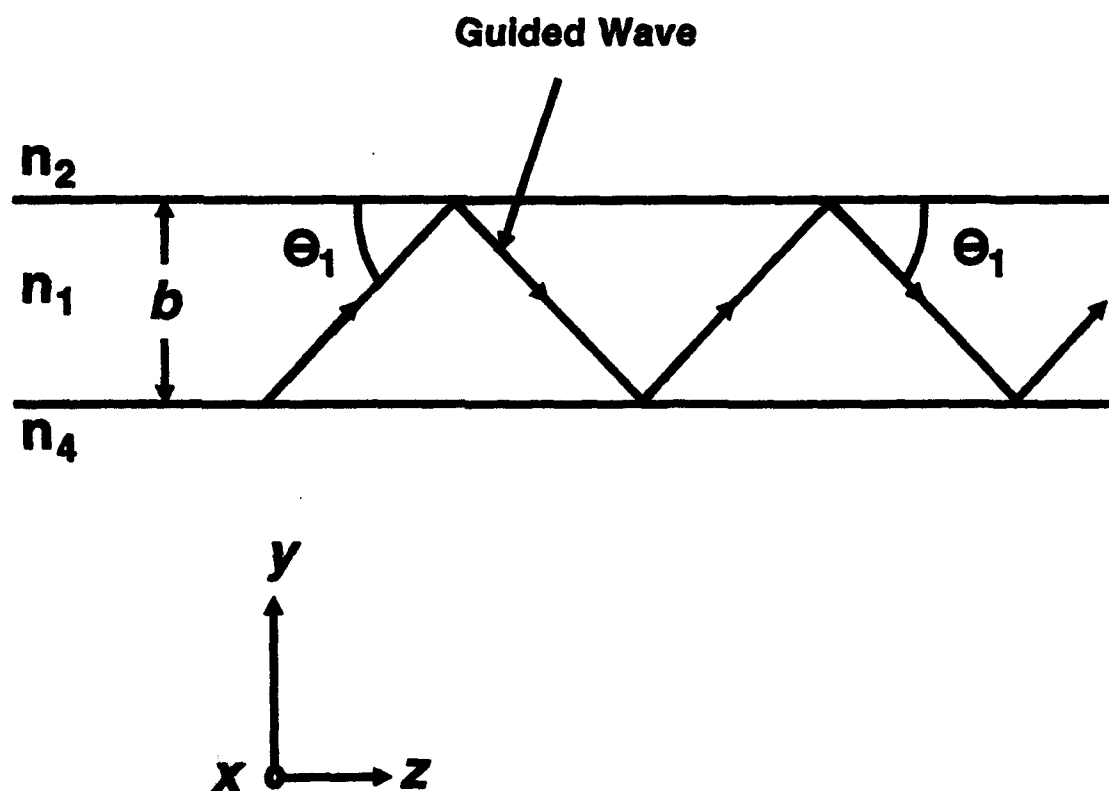


Figure 3.2.1  
Trajectory of a Guided Wave in a Slab Waveguide

$$E_y = -(i/K_j^2)[(\beta \partial E_z / \partial y) - (\omega \mu_0 \partial H_z / \partial x)], \quad 3.2.7$$

$$H_x = -(i/K_j^2)[(\beta \partial H_z / \partial x) - (\omega n_j^2 \epsilon_0 \partial E_z / \partial y)] \quad 3.2.8$$

and

$$H_y = -(i/K_j^2)[(\beta \partial H_z / \partial y) + (\omega n_j^2 \epsilon_0 \partial E_z / \partial x)], \quad 3.2.9$$

where

$$K_j = (n_j^2 k^2 - \beta^2)^{1/2} \quad 3.2.10$$

and  $j = 1, 2, 3, 4, 5$  corresponds to the values for the fields in the five regions of the waveguide. The longitudinal field components  $E_z$  and  $H_z$  must then satisfy the wave equation<sup>62</sup>

$$(\partial^2 \psi / \partial x^2) + (\partial^2 \psi / \partial y^2) + K_j^2 \psi = 0. \quad 3.2.11$$

### TE<sub>pq</sub> Modes

For TE<sub>pq</sub> modes, the electric field component is polarized predominantly in the  $y$  direction. The amplitude coefficients of  $E_z$  and  $H_z$  are adjusted so that one of the transverse field components vanishes. The following set of longitudinal field components satisfies the wave equation (Eq. 3.2.11) and the transverse field component equations (Eqs. 3.2.6 - 3.2.9). They describe

a TE<sub>pq</sub> mode in the core region  $n_1$ :<sup>62</sup>

$$E_z = A \cos[k_y(y+\eta)] \cos[k_x(x+\xi)] \quad 3.2.12$$

and

$$H_z = -A(\epsilon_0/\mu_0)^{1/2} n_1^2 (k k_x / \beta k_y) \sin[k_y(y+\eta)] \sin[k_x(x+\xi)], \quad 3.2.13$$

with

$$K_1^2 = n_1^2 k^2 - \beta^2 = k_x^2 + k_y^2; \quad 3.2.14$$

and that to the top clad region  $n_2$  yields<sup>62</sup>

$$E_z = A \cos[k_y \eta] \cos[k_x(x + \xi)] \exp(-\gamma_2 y) \quad 3.2.15$$

and

$$H_z = A(\epsilon_0/\mu_0)^{1/2} n_2^2 (k k_x / \beta \gamma_2) \cos[k_y \eta] \sin[k_x(x+\xi)] \exp(-\gamma_2 y), \quad 3.2.16$$

with

$$K_2^2 = n_2^2 k^2 - \beta^2 = k_x^2 - \gamma_2^2; \quad 3.2.17$$

and that to the outside clad region  $n_3$  yields<sup>62</sup>

$$E_z = A(n_1^2/n_3^2) \cos[k_x(a+\xi)] \cos[k_y(y+\eta)] \exp[-\gamma_3(x-a)] \quad 3.2.18$$

and

$$H_z = -[A(\epsilon_0/\mu_0)^{1/2}n_1^2(k\gamma_3/\beta k_y)\cos[k_x(a+\xi)] \\ \cdot \sin[k_y(y+\eta)]\exp[-\gamma_3(x-a)]], \quad 3.2.19$$

with

$$K_3^2 = n_3^2 k^2 - \beta^2 = k_y^2 - \gamma_3^2; \quad 3.2.20$$

and that to the bottom clad region  $n_4$  yields<sup>62</sup>

$$E_z = A\cos[k_y(\eta-b)]\cos[k_x(x+\xi)]\exp[\gamma_4(y+b)] \quad 3.2.21$$

and

$$H_z = -[A(\epsilon_0/\mu_0)^{1/2}n_4^2(kk_x/\beta\gamma_4)\cos[k_y(\eta-b)] \\ \cdot \sin[k_x(x+\xi)]\exp[\gamma_4(y+b)]], \quad 3.2.22$$

with

$$K_4^2 = n_4^2 k^2 - \beta^2 = k_x^2 - \gamma_4^2; \quad 3.2.23$$

and that to the center clad region  $n_5$  yields<sup>62</sup>

$$E_z = A(n_1^2/n_5^2)\cos(k_x\xi)\cos[k_y(y+\eta)]\exp(\gamma_5 x) \quad 3.2.24$$

and

$$H_z = A(\epsilon_0/\mu_0)^{1/2} n_1^2 (k\gamma_5/\beta k_y) \cos(k_x \xi) \sin[k_y(y+\eta)] \exp(\gamma_5 x), \quad 3.2.25$$

with

$$K_5^2 = n_5^2 k^2 - \beta^2 = k_y^2 - \gamma_5^2. \quad 3.2.26$$

In Eqs. 3.2.12, 3.2.13, 3.2.15, 3.2.16, 3.2.18, 3.2.19, 3.2.21, 3.2.22, 3.2.24 and 3.2.25, variable A is the amplitude of the field.

The transverse electric field component  $E_y$  can satisfy one of the boundary conditions by using the proper field amplitudes. The other boundary conditions can be matched by forcing the longitudinal magnetic field component  $H_z$  in the top and bottom clad regions ( $n_2$  and  $n_4$ ) to pass continuously through the core boundary at  $y = 0$  and  $y = -b$ , dictating that  $H_x$  be continuous. Note that  $E_x$  can be neglected since it is small compared to the other field components. These conditions lead to the equations<sup>62</sup>

$$(n_1^2/k_y) \sin[k_y(\eta - b)] - (n_4^2/\gamma_4) \cos[k_y(\eta - b)] = 0 \quad 3.2.27$$

and

$$(n_1^2/k_y) \sin(k_y \eta) + (n_2^2/\gamma_2) \cos(k_y \eta) = 0. \quad 3.2.28$$

Expansion of the sine and cosine functions in the above equations yields the eigenvalue equation<sup>62</sup>

$$\tan(k_y b) = n_1^2 k_y (n_2^2 \gamma_4 + n_4^2 \gamma_2) / (n_2^2 n_4^2 k_y^2 - n_1^4 \gamma_2 \gamma_4). \quad 3.2.29$$

This is the eigenvalue equation of  $TM_{pq}$  modes in an infinite slab waveguide for which the transverse electric field  $E_y$  is normal to the core boundaries at  $y=0$  and  $y=-b$ . Using Eqs. 3.2.17 and 3.2.23 to express  $\gamma_2$  and  $\gamma_4$  in terms of  $k_y$ ,

$$\gamma_2 = [(n_1^2 - n_2^2)k^2 - k_y^2]^{1/2} \quad 3.2.30$$

and

$$\gamma_4 = [(n_1^2 - n_4^2)k^2 - k_y^2]^{1/2}, \quad 3.2.31$$

one can determine  $k_y$  using Eq. 3.2.29.

At the waveguide core boundaries in the outside and center clad regions ( $n_3$  and  $n_5$ ),  $H_z$  must be equal and continuous on both sides of the dielectric interface at  $x=a$  and  $x=0$ . The transverse electric field component  $E_y$  is already continuous by the choice of field amplitudes. This leads to the following equations:<sup>62</sup>

$$k_x \sin[k_x(a+\xi)] - \gamma_3 \cos[k_x(a+\xi)] = 0 \quad 3.3.32$$

and

$$k_x \sin(k_x \xi) - \gamma_5 \cos(k_x \xi) = 0. \quad 3.2.33$$



Expansion of the sine and cosine functions in the above equations yields the eigenvalue equation<sup>62</sup>

$$\tan(k_x a) = k_x(\gamma_3 + \gamma_5)/(k_x^2 - \gamma_3\gamma_5), \quad 3.2.34$$

for  $TE_{pq}$  modes in an infinite slab waveguide. Since  $E_y$  is the dominant electric field component the field appears as a  $TE_{pq}$  mode with respect to the outside and center clad regions  $n_3$  and  $n_5$ .

Using Eqs. 3.2.20 and 3.2.26 to express  $\gamma_3$  and  $\gamma_5$  in terms of  $k_x$ ,

$$\gamma_3 = [(n_1^2 - n_3^2)k^2 - k_x^2]^{1/2} \quad 3.2.35$$

and

$$\gamma_5 = [(n_1^2 - n_5^2)k^2 - k_x^2]^{1/2}, \quad 3.2.36$$

one can determine  $k_x$  using Eq. 3.2.34.

The propagation constant  $\beta$  can be obtained for  $TE_{pq}$  mode propagation using Eq. 3.2.14, with the values for  $k_y$  and  $k_x$  determined from Eqs. 3.2.29 and 3.2.34, respectively.<sup>62</sup>

$$\beta = [n_1^2 k^2 - (k_x^2 + k_y^2)]^{1/2}. \quad 3.2.37$$

The interaction length  $L$  for total power transfer from one waveguide to the other and the coupling coefficient  $K$  between the two waveguides are then found by substituting  $\beta$  for  $k_{x0}$ ,  $k_x$  for  $k_{x0}$  and  $1/\gamma_s$  for  $\xi_s$  in Eq. 3.1.40. This yields<sup>62</sup>

$$-iK = \pi/(2L) = 2(k_x^2/\beta)[(1/\alpha\gamma_s)]\exp(-c\gamma_s)/(1 + k_x^2\gamma_s^2). \quad 3.2.38$$

The interaction length and coupling coefficient for the zero-gap directional coupler are obtained by driving the separation between the two adjacent waveguides to zero which yields,

$$-iK = \pi/(2L) = 2(k_x^2/\beta)(1/\alpha\gamma_s)/(1 + k_x^2\gamma_s^2). \quad 3.2.39$$

### TM<sub>pq</sub> Modes

The TM<sub>pq</sub> modes are derived in a similar manner to the TE<sub>pq</sub> modes, with the electric field component polarized predominantly in the  $x$  direction. The following set of longitudinal field components satisfies the wave equation (Eq. 3.2.11) and the transverse field component equations (Eqs. 3.2.6 - 3.2.9). They describe a TM<sub>pq</sub> mode in the core region  $n_1$ .<sup>62</sup>

$$E_z = B\cos[k_y(y+\eta)]\cos[k_x(x+\xi)] \quad 3.2.40$$

and

$$H_z = B(\epsilon_0/\mu_0)^{1/2} n_1^2 (k k_y / \beta k_y) \sin[k_y(y+\eta)] \sin[k_x(x+\xi)]; \quad 3.2.41$$

and that to the top clad region  $n_2$  yields<sup>62</sup>

$$E_z = B(n_1^2/n_2^2) \cos[k_y \eta] \cos[k_x(x+\xi)] \exp(-\gamma_2 y) \quad 3.2.42$$

and

$$H_z = B(\epsilon_0/\mu_0)^{1/2} n_1^2 (k \gamma_2 / \beta k_y) \cos[k_y \eta] \sin[k_x(x+\xi)] \exp(-\gamma_2 y); \quad 3.2.43$$

and that to the outside clad region  $n_3$  yields<sup>62</sup>

$$E_z = B \cos[k_x(a+\xi)] \cos[k_y(y+\eta)] \exp[-\gamma_3(x-a)] \quad 3.2.44$$

and

$$H_z = -[B(\epsilon_0/\mu_0)^{1/2} n_3^2 (k k_y / \beta \gamma_3) \cos[k_x(a+\xi)] \cdot \sin[k_y(y+\eta)] \exp[-\gamma_3(x-a)]]; \quad 3.2.45$$

and that to the bottom clad region  $n_4$  yields<sup>62</sup>

$$E_z = B(n_1^2/n_2^2) \cos[k_y(\eta-b)] \cos[k_x(x+\xi)] \exp[\gamma_4(y+b)] \quad 3.2.46$$

and

$$H_z = -[B(\epsilon_0/\mu_0)^{1/2}n_1^2(k\gamma_4/\beta k_2)\cos[k_2(\eta-b)] \cdot \sin[k_2(x+\xi)]\exp[\gamma_4(y+b)]]; \quad 3.2.47$$

and that to the center clad region  $n_5$  yields<sup>62</sup>

$$E_x = B\cos(k_x\xi)\cos[k_2(y+\eta)]\exp(\gamma_5x) \quad 3.2.48$$

and

$$H_z = B(\epsilon_0/\mu_0)^{1/2}n_5^2(kk_2/\beta\gamma_5)\cos(k_x\xi)\sin[k_2(y+\eta)]\exp(\gamma_5x). \quad 3.2.49$$

In Eqs. 3.2.40 - 3.2.49, variable  $B$  is the amplitude of the field. The values for  $K_1^2$ ,  $K_2^2$ ,  $K_3^2$ ,  $K_4^2$  and  $K_5^2$  are obtained by using Eqs. 3.2.14, 3.2.17, 3.2.20, 3.2.23 and 3.2.26, respectively.

The transverse electric field component  $E_x$  can satisfy one of the boundary conditions by the proper choice of the field amplitudes. The other boundary conditions can be matched by forcing the longitudinal magnetic field component  $H_z$  in the top and bottom clad regions ( $n_2$  and  $n_4$ ) to pass continuously through the core boundary at  $y = 0$  and  $y = -b$ , dictating that  $H_y$  be continuous. Note that  $E_y$  can be neglected since it is small compared to the other field components. These conditions lead to the equations<sup>62</sup>

$$k_2\sin[k_2(b + \eta)] - \gamma_4\cos[k_2(b + \eta)] = 0 \quad 3.2.50$$

and

$$k_y \sin(k_y \eta) + \gamma_2 \cos(k_y \eta) = 0. \quad 3.2.51$$

Expansion of the sine and cosine functions in the equations above yields the eigenvalue equation<sup>62</sup>

$$\tan(k_y b) = k_y (\gamma_2 + \gamma_4) / (k_y^2 - \gamma_2 \gamma_4), \quad 3.2.52$$

for TE<sub>pq</sub> modes in an infinite slab waveguide. Using Eqs. 3.2.30 and 3.2.31, which express  $\gamma_2$  and  $\gamma_4$  in terms of  $k_y$ , one can determine  $k_y$  using Eq. 3.2.52.

At the waveguide core boundaries in the outside and center clad regions ( $n_3$  and  $n_5$ ),  $H_z$  must be equal and continuous on both sides of the dielectric interface at  $x = a$  and  $x = 0$ . The transverse electric field component  $E_x$  is already continuous by the choice of field amplitudes. This leads to the following equations:<sup>62</sup>

$$(n_1^2/k_x) \sin[k_x(\xi - a)] - (n_3^2/\gamma_3) \cos[k_x(\xi - a)] = 0 \quad 3.2.53$$

and

$$(n_1^2/k_x) \sin(k_x \xi) + (n_5^2/\gamma_5) \cos(k_x \xi) = 0. \quad 3.2.54$$

Expansion of the sine and cosine functions in the equations above yields the eigenvalue equation<sup>62</sup>

$$\tan(k_x a) = n_1^2 k_x (n_3^2 \gamma_5 + n_5^2 \gamma_3) / (n_3^2 n_5^2 k_x^2 - n_1^4 \gamma_3 \gamma_5), \quad 3.2.55$$

for the  $TM_{pq}$  modes in an infinite slab waveguide. Thus, the field appears as a  $TM_{pq}$  mode with respect to the outside and center clad regions ( $n_3$  and  $n_5$ ). Using Eqs. 3.2.35 and 3.2.36, which express  $\gamma_3$  and  $\gamma_5$  in terms of  $k_x$ , one can determine  $k_x$  using Eq. 3.2.55. The propagation constant  $\beta$  can be obtained for  $TM_{pq}$  mode propagation by substituting  $k_x$  and  $k_y$ , obtained by Eqs. 3.2.52 and 3.2.55, into Eq. 3.2.37.

The interaction length  $L$  for total power transfer from one waveguide to the other and the coupling coefficient  $K$  between the two waveguides are then found by substitution of the above  $TM_{pq}$  mode variables into Eq. 3.2.38. The interaction length and coupling coefficient for the zero-gap directional coupler are obtained by using Eq. 3.2.39.

### Burns and Milton Effective Index Method

In a 1975 paper, Burns and Milton discussed mode conversion in planar dielectric separating waveguides.<sup>66</sup> This has since become known as the effective index method, and is treated in detail by Nishihara, Haruna and

Suhara for both two and three dimensional dielectric waveguide structures.<sup>67</sup>

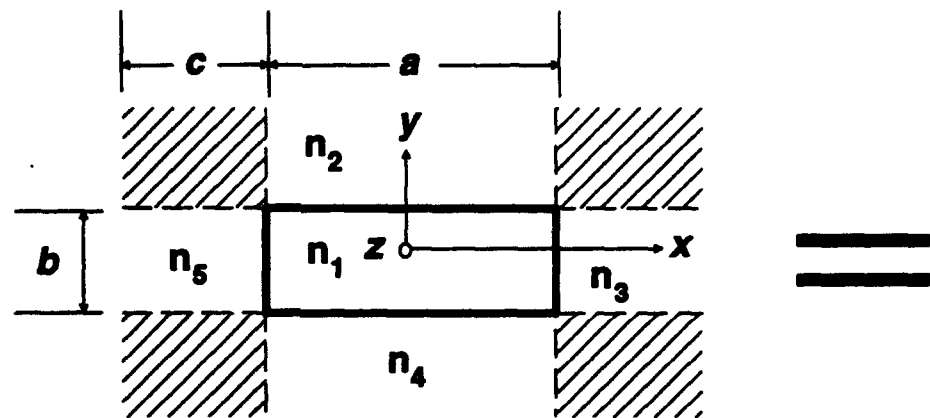
The effective index method is based on the concept of the effective index of the guided mode. The guided mode propagating along the  $z$  axis sees the effective index ( $N$ ) defined by<sup>67,86</sup>

$$\beta = kN, \quad 3.3.1$$

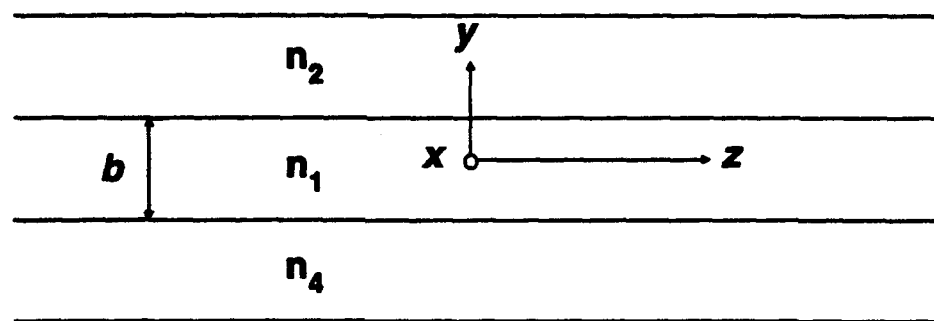
where  $\beta$  is the axial propagation constant,  $k$  is the free space propagation constant (defined in the first section of this chapter) and  $N = n_1 \cos \theta_1$  (see Fig. 3.2.1 and Eq. 3.2.4.).

The effective index method for the dielectric waveguide structure to be fabricated for this experiment (illustrated in Fig. 3.1.1) is performed by dividing the three dimensional waveguide into two two-dimensional waveguides. One is 2-D Waveguide 1, with light confinement in the  $y$  direction and the second is 2-D Waveguide 2, with light confinement in the  $x$  direction (see Fig. 3.3.1). The axial propagation constant for the  $TE_{pq}$  modes of a three dimensional waveguide structure is determined by the following procedure:

The effective index  $N_1$  of 2-D Waveguide 1 is found first by applying  $TM_{pq}$  mode analysis to the top and bottom clad regions ( $n_2$  and  $n_4$ ) with waveguide thickness  $b$ . Effective index  $N_1$  is then used to find the effective

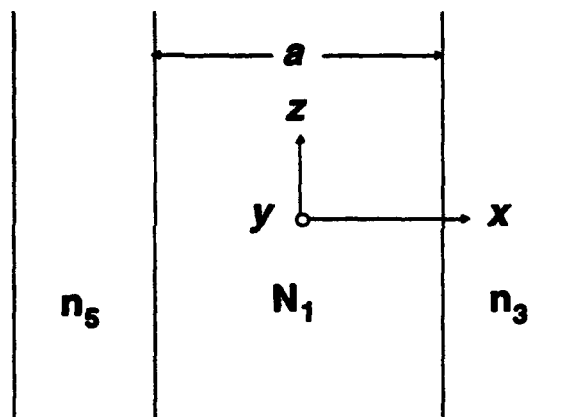


**Three-Dimensional Dielectric Waveguide**



**Two-Dimensional Waveguide 1**

+



**Two-Dimensional Waveguide 2**

**Figure 3.3.1**  
**Analytical Model for the Effective Index Method for  $TE_{pq}$  Modes**



index  $N_2$  of 2-D Waveguide 2 by applying  $TE_{pq}$  mode analysis to the outside and center clad regions ( $n_3$  and  $n_5$ ) with waveguide width  $a$ . The axial propagation constant is finally obtained by substituting  $N_2$  for  $N$  in Eq. 3.3.1.

The axial propagation constant for the  $TM_{pq}$  modes is determined in a manner similar to the one used for the  $TE_{pq}$  modes. First, effective index  $N_1$  of 2-D Waveguide 1 is found by applying  $TE_{pq}$  mode analysis to the top and bottom clad regions ( $n_2$  and  $n_4$ ) with waveguide thickness  $b$ . Effective index  $N_1$  is then used to find effective index  $N_2$  of 2-D Waveguide 2 by applying  $TM_{pq}$  mode analysis to the outside and center clad regions ( $n_3$  and  $n_5$ ) with waveguide width  $a$ .

### $TE_{pq}$ Modes

As outlined in the preceding section, 2-D Waveguide 1 represents the  $TM_{pq}$  modes in an infinite slab waveguide of thickness  $b$  and 2-D Waveguide 2 represents the  $TE_{pq}$  modes in an infinite slab waveguide of width  $a$ . Since  $E_y$  is the dominant electric field component, the field appears as a  $TE_{pq}$  mode with respect to the outside and center clad regions ( $n_3$  and  $n_5$ ). The analysis can be represented by the following:<sup>79</sup>

$$\beta_2 = k[N_2\{TM^b(n_2|n_1|n_4);TE^a(n_3|N_1|n_5)\}], \quad 3.3.2$$

where  $\beta_2$  is the  $TE_{pq}$  axial propagation constant for the three dimensional dielectric waveguide.

First, we start with the wave equation for the  $TM_{pq}$  modes of 2-D Waveguide 1, given by<sup>67</sup>

$$\partial^2 H_x / \partial y^2 + (k^2 n^2 - \beta_1^2) H_x = 0, \quad 3.3.3$$

where

$$E_y = (\beta_1 / \omega \epsilon_0 n^2) H_x, \quad 3.3.4$$

and

$$E_z = (1 / k \omega \epsilon_0 n^2) \partial H_x / \partial y, \quad 3.3.5$$

where  $\beta_1$  is the  $TM_{pq}$  axial propagation constant for 2-D waveguide 1.

The field solutions can then be written as<sup>67</sup>

$$H_{x1} = H_1 \cos(k_y y + \phi_2), \quad 3.3.6$$

at  $-b < y < 0$  for the core region  $n_1$ ,

$$H_{x2} = H_2 \exp(-\gamma_2 y), \quad 3.3.7$$

at  $y > 0$  for the top clad region  $n_2$ , and

$$H_y = H_4 \exp[\gamma_4(y+b)], \quad 3.3.8$$

at  $y < -b$  for the bottom clad region  $n_4$ . The variables  $\gamma_2$  and  $\gamma_4$  are the transverse propagation constants of a plane wave in the top and bottom cladding regions, respectively, and  $\phi_2$  is the phase shift suffered by a wave polarized with its magnetic field vector parallel to the interface between the core region  $n_1$  and the top clad region  $n_2$ .

In addition to the phase shift due to reflection of the wave from the interface between  $n_1$  and  $n_2$ , there is also a phase shift  $\phi_4$  suffered by the reflection of the wave from the interface between the core region  $n_1$  and the bottom clad region  $n_4$ . Using Eqs. 3.3.3 - 3.3.8, these phase shifts can be defined mathematically by<sup>82</sup>

$$\phi_2 = -2\arctan[(n_1^2/n_2^2)(\beta_1^2 - n_2^2 k^2)^{1/2}/(n_1^2 k^2 - \beta_1^2)^{1/2}] \quad 3.3.9$$

and

$$\phi_4 = -2\arctan[(n_1^2/n_4^2)(\beta_1^2 - n_4^2 k^2)^{1/2}/(n_1^2 k^2 - \beta_1^2)^{1/2}]. \quad 3.3.10$$

Using the differences between the phase fronts, which are due to the reflection of the wave at the two interfaces and given mathematically by<sup>82</sup>

$$s_1 = (b \cos \theta_1) [(1/\tan \theta_1) - \tan \theta_1] = (b/\sin \theta_1) (\cos^2 \theta_1 - \sin^2 \theta_1) \quad 3.3.11$$

and

$$s_2 = b/\sin \theta_1, \quad 3.3.12$$

the condition that both reflected waves contribute to the same plane waves can be expressed by the relation<sup>62</sup>

$$n_1(s_2 - s_1)k + \phi_2 + \phi_4 = 2(q + 1)\pi, \quad 3.3.13$$

where  $q = (0, 1, 2, \dots)$  indicates the number of extrema of the magnetic field in the  $y$  direction.

The eigenvalue equation, obtained from Eqs. 3.3.9 - 3.3.13, can then be written as<sup>67</sup>

$$k_y b = (q + 1)\pi - \tan^{-1}[(n_2^2/n_1^2)(k_y/\gamma_2)] - \tan^{-1}[(n_4^2/n_1^2)(k_y/\gamma_4)], \quad 3.3.14$$

where

$$k_y = (n_1^2 k^2 - \beta_1^2)^{1/2}, \quad 3.3.15$$

$$\gamma_2 = (\beta_1^2 - n_2^2 k^2)^{1/2} \quad 3.3.16$$

and

$$\gamma_4 = (\beta_1^2 - n_4^2 k^2)^{1/2} \quad 3.3.17$$

are the transverse propagation constants.

Using Eq. 3.3.1, the transverse propagation constants, given by Eqs. 3.3.15 - 3.3.17, can be expressed in terms of the effective index of 2-D Waveguide 1:

$$k_y = k(n_1^2 - N_1^2)^{1/2}, \quad 3.3.18$$

$$\gamma_2 = k(N_1^2 - n_2^2)^{1/2} \quad 3.3.19$$

and

$$\gamma_4 = (N_1^2 - n_4^2)^{1/2}. \quad 3.3.20$$

Next, the wave equation for the  $TE_{pq}$  modes of 2-D Waveguide 2 is given by<sup>87</sup>

$$\partial^2 E_y / \partial x^2 + (k^2 \pi^2 - \beta_2^2) E_y = 0, \quad 3.3.21$$

where

$$H_x = -(\beta_2 / \omega \mu_0) E_y \quad 3.3.22$$

and

$$H_z = -(1/k\mu_0)\partial E/\partial x. \quad 3.3.23$$

The field solutions can be written as<sup>67</sup>

$$E_{y1} = E_1 \cos(k_x x + \phi_3), \quad 3.3.24$$

at  $0 < x < a$  for the core region now defined as  $N_1$ ,

$$E_{y3} = E_2 \exp(-\gamma_3 x), \quad 3.3.25$$

at  $x < 0$  for the outside clad region  $n_3$ , and

$$E_{y5} = E_5 \exp[\gamma_5(x+a)], \quad 3.3.26$$

at  $x > a$  for the center clad region  $n_5$ . The variables  $\gamma_3$  and  $\gamma_5$  are the transverse propagation constants of a plane wave in the outside and center cladding regions, respectively, and  $\phi_3$  is the phase shift suffered by a wave polarized with its electric field vector parallel to the interface between the core region  $N_1$  and the outside clad region  $n_3$ .

In addition to the phase shift due to reflection of the wave from the interface between  $N_1$  and  $n_3$ , there is also a phase shift  $\phi_5$  suffered by the

reflection of the wave from the interface between the core region  $N_1$  and the center clad region  $n_3$ . Using Eqs. 3.3.21 - 3.3.26, these phase shifts can be defined mathematically by<sup>62</sup>

$$\phi_3 = -2\arctan[(\beta_2^2 - n_3^2 k^2)^{1/2}/(n_1^2 k^2 - \beta_2^2)^{1/2}] \quad 3.3.27$$

and

$$\phi_5 = -2\arctan[(\beta_2^2 - n_5^2 k^2)^{1/2}/(n_1^2 k^2 - \beta_2^2)^{1/2}]. \quad 3.3.28$$

Using the differences between the phase fronts, which are due to the reflection of the wave at the two interfaces and given mathematically by<sup>62</sup>

$$s_1 = (a \cos \theta_1)[(1/\tan \theta_1) - \tan \theta_1] = (a/\sin \theta_1)(\cos^2 \theta_1 - \sin^2 \theta_1) \quad 3.3.29$$

and

$$s_2 = a/\sin \theta_1, \quad 3.3.30$$

the condition that both reflected waves contribute to the same plane waves can be expressed with the relation<sup>62</sup>

$$n_1(s_2 - s_1)k + \phi_3 + \phi_5 = 2(p + 1)\pi, \quad 3.3.31$$

where  $p = (0, 1, 2, \dots)$  indicates the number of extrema of the electric field in

the  $x$  direction.

The eigenvalue equation, obtained from Eqs. 3.3.27 - 3.3.31, can then be written as<sup>67</sup>

$$k_x a = (p + 1)\pi - \tan^{-1}(k_x/\gamma_3) - \tan^{-1}(k_x/\gamma_6), \quad 3.3.32$$

where

$$k_x = (N_1^2 k^2 - \beta_2^2)^{1/2}, \quad 3.3.33$$

$$\gamma_3 = (\beta_2^2 - n_3^2 k^2)^{1/2} \quad 3.3.34$$

and

$$\gamma_6 = (\beta_2^2 - n_6^2 k^2)^{1/2} \quad 3.3.35$$

are the transverse propagation constants.

Using Eq. 3.3.1, the transverse propagation constants, given by Eqs. 3.3.33 - 3.3.35, can be expressed in terms of the effective index of 2-D

Waveguide 2:

$$k_y = k(N_1^2 - N_2^2)^{1/2}, \quad 3.3.36$$

$$\gamma_3 = k(N_2^2 - n_3^2)^{1/2} \quad 3.3.37$$



and

$$\gamma_s = (N_2^2 - n_s^2)^{1/2}. \quad 3.3.38$$

Having solved for  $\beta_2$  and  $k_x$ , the symmetric propagation constant  $\beta_s$  and antisymmetric propagation constant  $\beta_a$ , corresponding to the symmetric and antisymmetric  $TE_{00}$  modes of the directional coupler, respectively, are found by<sup>61</sup>

$$\beta_s = \beta_2[1 + 2(k_x^2/\beta_2^2)(1/\alpha\gamma_s)\exp(-c\gamma_s)/(1 + k_x^2/\gamma_s^2)] \quad 3.3.39$$

and

$$\beta_a = \beta_2[1 - 2(k_x^2/\beta_2^2)(1/\alpha\gamma_s)\exp(-c\gamma_s)/(1 + k_x^2/\gamma_s^2)], \quad 3.1.40$$

where  $c$  is the distance of separation between the two waveguides.

The interaction length  $L$  for total power transfer from one waveguide to the other and the coupling coefficient  $K$  between the two waveguides can then be related to  $\beta_s$  and  $\beta_a$  by<sup>67</sup>

$$-iK = \pi/(2L) = (\beta_s - \beta_a)/2. \quad 3.3.41$$

The interaction length and coupling coefficient for the zero-gap directional coupler are obtained by driving the separation between the two

adjacent waveguides to zero. This yields,

$$\beta_s = \beta_2[1 + 2(k_x^2/\beta_2^2)(1/\alpha\gamma_s)(1/(1 + k_x^2/\gamma_s^2))] \quad 3.3.42$$

and

$$\beta_s = \beta_2[1 - 2(k_x^2/\beta_2^2)(1/\alpha\gamma_s)(1/(1 + k_x^2/\gamma_s^2))], \quad 3.3.43$$

which are then substituted back into Eq. 3.3.41.

### TM<sub>pq</sub> Modes

For TM<sub>pq</sub> mode analysis, 2-D Waveguide 1 represents the TE<sub>pq</sub> modes in an infinite slab waveguide of thickness  $b$  and 2-D Waveguide 2 represents the TM<sub>pq</sub> modes in an infinite slab waveguide of width  $a$ . With  $H_y$  as the dominant magnetic field component, the field appears as a TM<sub>pq</sub> mode with respect to the outside and center clad regions ( $n_3$  and  $n_5$ ). The analysis can be represented by the following:<sup>79</sup>

$$\beta_2 = K[N_2[TE^b(n_2|n_1|n_4); TM^a(n_3|N_1|n_5)]], \quad 3.3.44$$

where  $\beta_2$  is the TM<sub>pq</sub> axial propagation constant for the three dimensional dielectric waveguide. Following the same procedure as was presented in the previous section, the eigenvalue equation for the TE<sub>pq</sub> modes of 2-D

Waveguide 1 can be written as<sup>67</sup>

$$k_x a = (p + 1)\pi - \tan^{-1}[(n_3^2/n_1^2)(k_x/\gamma_3)] - \tan^{-1}[(n_5^2/n_1^2)(k_x/\gamma_5)], \quad 3.3.45$$

where

$$k_x = (n_1^2 k^2 - \beta_1^2)^{1/2}, \quad 3.3.46$$

$$\gamma_3 = (\beta_1^2 - n_3^2 k^2)^{1/2} \quad 3.3.47$$

and

$$\gamma_5 = (\beta_1^2 - n_5^2 k^2)^{1/2}. \quad 3.3.48$$

Using Eq. 3.3.1, the transverse propagation constants, given by Eqs. 3.3.46 - 3.3.48, can be expressed in terms of the effective index of 2-D Waveguide 1:

$$k_y = k(n_1^2 - N_1^2)^{1/2}, \quad 3.3.49$$

$$\gamma_3 = k(N_1^2 - n_3^2)^{1/2} \quad 3.3.50$$

and

$$\gamma_5 = (N_1^2 - n_5^2)^{1/2}. \quad 3.3.51$$

The eigenvalue equation for the  $TM_{pq}$  modes of 2-D Waveguide 2 can be written as<sup>67</sup>

$$k_y b = (q + 1)\pi - \tan^{-1}(k/\gamma_2) - \tan^{-1}(k/\gamma_4), \quad 3.3.52$$

where

$$k_y = (N_1^2 k^2 - \beta_2^2)^{1/2}, \quad 3.3.53$$

$$\gamma_2 = (\beta_2^2 - n_2^2 k^2)^{1/2} \quad 3.3.54$$

and

$$\gamma_4 = (\beta_2^2 - n_4^2 k^2)^{1/2}. \quad 3.3.55$$

Using Eq. 3.3.1, the transverse propagation constants, given by Eqs. 3.3.53 - 3.3.55, can be expressed in terms of the effective index of 2-D Waveguide 2:

$$k_y = k(N_1^2 - N_2^2)^{1/2}, \quad 3.3.56$$

$$\gamma_2 = k(N_2^2 - n_2^2)^{1/2} \quad 3.3.57$$

and

$$\gamma_4 = (N_2^2 - n_4^2)^{1/2}. \quad 3.3.58$$

Having solved for  $\beta_2$  and  $k_x$ , the symmetric propagation constant  $\beta_s$  and antisymmetric propagation constant  $\beta_a$  for the  $TM_{00}$  modes of the directional coupler are found by substituting  $\beta_2$  and  $k_x$ , determined here, into Eqs. 3.3.39 and 3.3.40.

The interaction length  $L$  for total power transfer from one waveguide to the other and the coupling coefficient  $K$  between the two waveguides, can then be related to  $\beta_s$  and  $\beta_a$  by Eq. 3.3.41. The interaction length and coupling coefficient for the zero-gap directional coupler are obtained using Eqs. 3.3.42 and 3.3.43, which are then substituted back into the equation for the zero-gap directional coupler, Eq. 3.3.41.

#### Fleck, Morris and Feit Beam Propagation Method

Fleck, Morris and Feit proposed, in 1976, a propagating beam method for computing fields of an optical beam passing through a medium.<sup>68</sup> The method calculates the characteristics of an input beam as it propagates through a medium over a small distance  $z$ , and then corrects for the variations of the refractive index as seen by the beam over this distance  $z$ . It has already been applied to several optical fiber and integrated optic applications.<sup>69-75,82,88,89</sup>

The beam propagation method is derived for a scalar field. The theory is restricted to small changes in the refractive index. The first part of the

derivation assumes the propagation of a high frequency beam through an inhomogeneous medium. It begins with the wave equation<sup>74</sup>

$$\nabla^2 \phi + k^2 n^2(r) \phi = 0, \quad 3.4.1$$

where  $\phi$  represents the scalar field,  $k$  is the free space wave number defined at the beginning of this chapter and  $n(r) = n_0(r)^2 + \Delta n^2(r)$  is the refractive index of the medium consisting of an unperturbed part ( $n_0(r)^2$ ) and a perturbation ( $\Delta n^2(r)$ ). Splitting  $n^2(r)$  into its respective parts, Eq. 3.4.1 takes the form<sup>74</sup>

$$\nabla^2 \phi + k^2 n_0^2(r) \phi = -k^2 \Delta n^2(r) \phi = s(r), \quad 3.4.2$$

where the right hand side of the equation, designated as  $s(r)$ , is considered a source function. Next, the unperturbed part of the index is chosen so that the new wave equation<sup>74</sup>

$$\nabla^2 \psi + k^2 n_0^2(r) \psi = 0, \quad 3.4.3$$

along with the radiation conditions at  $z = \infty$ , has a solution. If  $\psi$  is known for  $z = z_0$ , where  $z_0$  is the position  $z = 0$ , then  $\psi$  and its derivative, with respect

to  $z$ , can be solved for all values of  $z$  by use of an operator ( $\hat{a}$ ).  $\hat{a}$  acts with respect to only the transverse coordinates ( $x, y$ ). This leads to<sup>74</sup>

$$\partial\psi/\partial z = \hat{a}\psi(x, y, z_0). \quad 3.4.4$$

For  $n_0 = \text{constant}$ , the scalar field can be represented in the angular spectrum domain by<sup>74,93</sup>

$$\Psi(k_x, k_y, z) = \iint_{-\infty}^{+\infty} \psi(x, y, z) \exp[-i(k_x x + k_y y)] dx dy, \quad 3.4.5$$

where  $\Psi(k_x, k_y, z)$  is the Fourier transform of the scalar field ( $\psi(x, y, z)$ ), and  $k_x$  and  $k_y$  are the transverse propagation constants. Taking the derivative of Eq. 3.4.5, with respect to  $z$ , yields<sup>74,93</sup>

$$\partial\Psi/\partial z(k_x, k_y, z) = -ik_z\Psi(k_x, k_y, z), \quad 3.4.6$$

where  $k_z = (k^2 n_0^2 - k_x^2 - k_y^2)^{1/2}$  is the axial propagation constant. Using Eq. 3.4.6, the integral operator  $\hat{a}$  can be derived.

For a given coordinate ( $z$ ), the field ( $\phi$ ) is split into two parts. The first part ( $\phi_1$ ) is generated by the sources in the region where  $z' < z$ , and the second part ( $\phi_2$ ) is generated by the sources where  $z' > z$ . Using the

function:<sup>74</sup>

$$\{e_1(r|r') = 0 \text{ for } z < z'\}$$

$$e_1(r|r') = 1/2 \text{ for } z = z'$$

$$e_1(r|r') = 1 \text{ for } z > z'\},$$

3.4.7

an explicit expression for  $\phi_1$  and  $\phi_2$  can be obtained. Defining  $G$  as Greens function of Eq. 3.3.3, the wave equation ( $\phi_1$ ) can be expressed by<sup>74</sup>

$$\phi_1(r) = \iiint_{-\infty}^{+\infty} G(r|r') e_1(r|r') s(r') dV'.$$

3.4.8

Taking the derivative of  $\phi_1$ , with respect to  $z$ , yields<sup>74</sup>

$$\begin{aligned} \partial\phi_1/\partial z(r) = & \iiint_{-\infty}^{+\infty} \partial G/\partial z(r|r') e_1(r|r') s(r') dV' \\ & + \iiint_{-\infty}^{+\infty} G(r|r') \delta(z - z') s(r') dV', \end{aligned}$$

3.4.9

where  $\delta(z - z')$  is the step size. The first integral of equation 3.4.9 represents the unperturbed medium. It can be expressed in terms of  $\hat{a}$  using Eq. 3.4.4.<sup>74</sup>

$$\hat{a}\phi_1(r).$$

3.4.10



The second integral of Eq. 3.4.9 includes both the unperturbed medium and the perturbation. With the help of Eq. 3.4.2, the second integral in Eq. 3.4.9 can be written as<sup>74</sup>

$$\iint_{-\infty}^{+\infty} G(x,y,z|x',y',z)(-k^2)\Delta n^2(x',y',z)\phi(x',y',z)dx'dy'. \quad 3.4.11$$

Equation 3.4.11 can then be expressed in terms of an operator ( $\hat{U}$ ) acting on  $\phi$  by<sup>74</sup>

$$\hat{U}\phi(x',y',z), \quad 3.4.12$$

where, like  $\hat{A}$ , operator  $\hat{U}$  acts with respect to only the transverse coordinates  $(x,y)$ . Substitution of Eqs. 3.4.10 and 3.4.12 into Eq. 3.4.9 yields<sup>74</sup>

$$\partial\phi_1/\partial z(x',y',z) = \hat{A}\phi_1(x',y',z) + \hat{U}\phi_1(x',y',z). \quad 3.4.13$$

Neglecting the influence of the reflected field ( $\phi_2$ ) on  $\phi_1$ ,  $\phi_1$  can be substituted for  $\phi$  in Eq. 3.4.13. The first-order differential equation for  $\phi_1$  then becomes<sup>74</sup>

$$\partial\phi_1/\partial z(x',y',z) = \hat{A}\phi_1(x',y',z) + \hat{U}\phi_1(x',y',z) \quad 3.4.14$$

where  $\hat{0}\phi_1$  is the correction term.

From Eq. 3.4.14, the propagation of field  $(\phi_1)$  is given by two terms. One describes propagation in an unperturbed medium  $(\hat{a}\phi_1)$  while the other describes a correction term  $(\hat{0}\phi_1)$  representing the influence of  $\Delta n$ . Using Fourier transforms and convolution along with the assumption that the unperturbed media is homogeneous, the correction term in Eq. 3.4.14 can be simplified.<sup>74</sup>

$$\hat{0}\phi_1(x', y', z) = -(ik/2n_0)\Delta n^2\phi_1(x', y', z). \quad 3.4.15$$

By combining Eqs. 3.4.14 and 3.4.15, the first-order differential equation for  $\phi_1$  becomes<sup>74</sup>

$$\partial\phi_1/\partial z(x', y', z) = \hat{a}\phi_1(x', y', z) - (ik/2n_0)\Delta n^2\phi_1(x', y', z). \quad 3.4.16$$

In order to solve Eq. 3.4.16, it will be assumed that  $\phi_1$  is known at position  $z = z_0$ . If  $\Delta n^2 = 0$ , Eq. 3.4.16 reduces to<sup>74</sup>

$$\partial\epsilon/\partial z(x, y, z_0) = \hat{a}\epsilon(x, y, z_0), \quad 3.4.17$$

where  $\epsilon(x, y, z_0) = \phi_1(x, y, z_0)$  is given. Therefore,  $\epsilon$  represents the field as it

propagates through a medium with refractive index ( $n_0(r)$ ). Introducing a correction factor ( $\exp(\Gamma)$ ) leads to an approximate solution to the differential Eq. 3.4.16. This solution is derived by<sup>74</sup>

$$\phi_1(r) = \exp[\Gamma(r)]\epsilon(r), \quad 3.4.18$$

with  $\Gamma(x, y, z_0) = 0$ . Combining Eqs. 3.4.16 and 3.4.18 yields<sup>74</sup>

$$\partial\Gamma/\partial z = -(\#d^2n_0)\Delta n^2 + [\hat{A}(\exp(\Gamma)\epsilon) - \exp(\Gamma)\hat{A}(\epsilon)]/\exp(\Gamma)\epsilon. \quad 3.4.19$$

It has been demonstrated that the second term in Eq. 3.4.19 can be neglected, provided Eq. 3.4.19 is integrated over a small distance ( $z - z_0$ ).<sup>74</sup>

This yields

$$\Gamma = -(\#d^2n_0)\Delta n^2(z - z_0), \quad 3.4.20$$

for ( $z - z_0$ ) small. Combining Eqs. 3.4.18 and 3.4.20 yields<sup>74</sup>

$$\phi_1(x, y, z_0 + \Delta z) = \epsilon(x, y, z_0 + \Delta z)\exp[-(\#d^2n_0)\Delta n^2\Delta z], \quad 3.4.21$$

which is the equation for the correction term.

For  $n_0(r)$  independent of  $z$ , the eigenmode of Eq. 3.4.3 can be determined. This allows one to calculate the propagation of  $\epsilon$ .<sup>74</sup>

$$\epsilon(x, y, z_0 + \Delta z) = \sum_n A_n \psi_n(x, y) \exp[-(ik_n \Delta z)] \quad 3.4.22$$

where

$$A_n = \iint_{-\infty}^{+\infty} \epsilon(x, y, z_0) \psi_n(x, y) dx dy. \quad 3.4.23$$

Using Eq. 3.4.22 and multiplication with the correction term, defined by Eq. 3.4.21, allows the propagation of light in small steps.

Application of the beam propagation method to media with small refractive index variations allows one to analyze beam propagation through integrated waveguide structures. For this case, the operator  $\hat{a}$  can be expressed in terms of Fourier transforms (see Eqs. 3.4.5 and 3.4.6). The propagation step defined by Eq. 3.4.22 can, thus, be calculated using fast Fourier transforms (FFT's). Performing a two dimensional FFT extends the beam propagation method to three dimensions, allowing one to analyze the dielectric waveguide structure illustrated in Fig. 3.1.1.

The beam propagation method for integrated optical waveguide applications has been programmed into a SUN Sparc station by A. Ticknor, of Lockheed Missiles and Space Company.<sup>94</sup> Although it does not generate

hard numbers for the interaction length of directional couplers, the way the dielectric waveguide and effective index methods do, the beam propagation method does provide an excellent prediction of device performance. It calculates the amplitudes of the fields as they propagate through the medium. As an example, the beam propagation method computer program acquired from Lockheed was used to generate Fig. 3.4.1 which gives a visual prediction of the behavior of a light wave propagating through an  $\text{Al}_x\text{Ga}_{1-x}\text{As}$  waveguide with an S-bend. The following parameters were substituted into the beam propagation method using the indices from Waveguide Structure 1 (Chapter II): the waveguide width  $a = 3 \mu\text{m}$ , the waveguide core thickness  $b = 1 \mu\text{m}$ , the operating wavelength  $\lambda = 827 \text{ nm}$ , the refractive index of the core  $n_1 = 3.419$ , the refractive index of the top and bottom clad regions  $n_2 = n_4 = 3.389$ , the refractive index of the outside clad regions  $n_3 = n_5 = 1.000$ . Zero propagation loss was assumed for the straight guides. A step size of  $0.5 \mu\text{m}$  was used to calculate the propagating field amplitudes. The S-bend was designed using the formula<sup>95</sup>

$$x(z) = (h/l)z - (h/2\pi)\sin[(2\pi/l)z], \quad 3.4.24$$

where  $l$  is the longitudinal separation in the  $z$  direction and  $h$  is the lateral offset in the  $x$  direction. Eq. 3.4.24 allows one to minimize the radiative loss

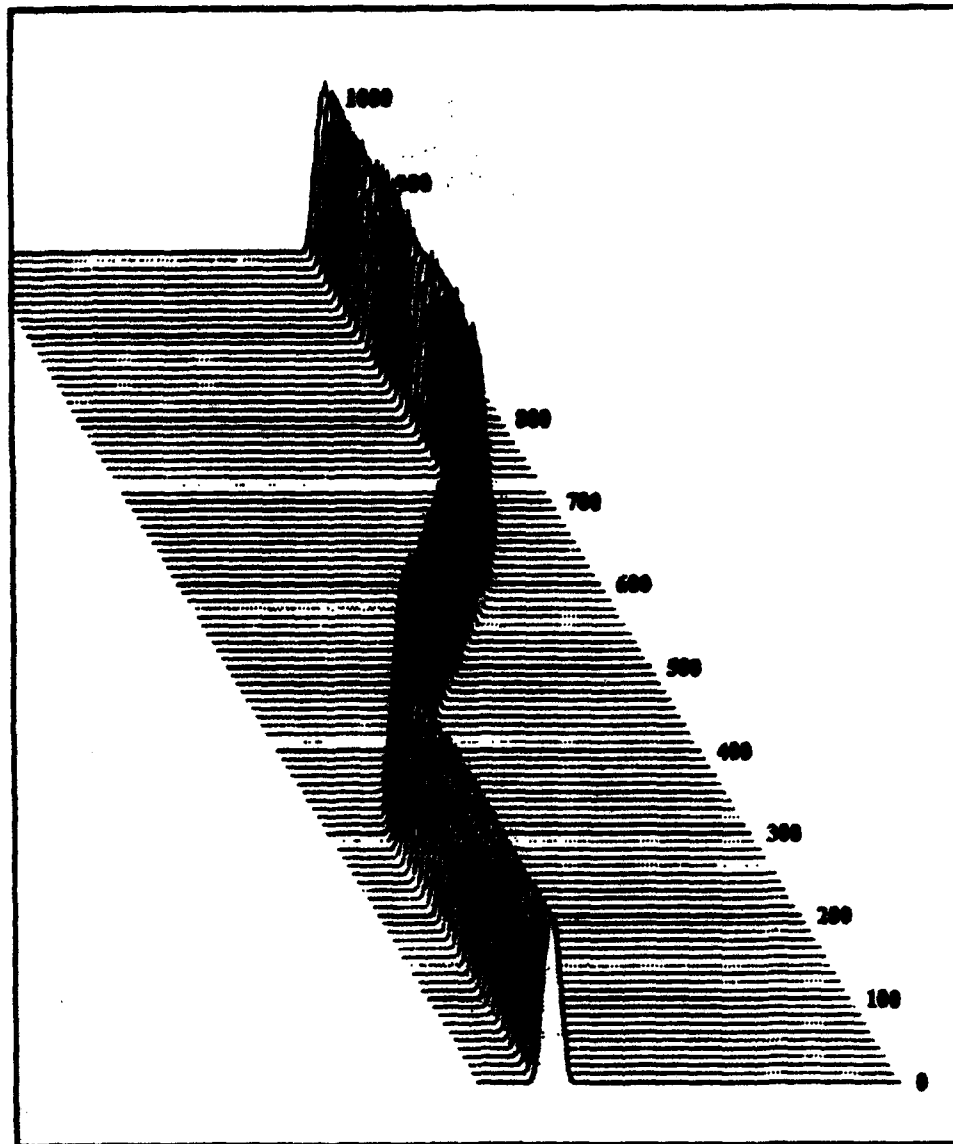


Figure 3.4.1  
Amplitudes of the Propagating Fields in an  
 $\text{Al}_x\text{Ga}_{1-x}\text{As}$  Waveguide with an S-Bend

and maximize the mode confinement. For the S-bend structure illustrated in Fig. 3.4.1,  $h = 20 \mu\text{m}$  and  $l = 500 \mu\text{m}$ .

## CHAPTER IV

### ELECTRO-OPTIC PROPERTIES OF ALUMINUM GALLIUM ARSENIDE

$\text{Al}_x\text{Ga}_{1-x}\text{As}$  is an optically isotropic crystal belonging to the cubic  $\bar{4}3m$  symmetry class known as zincblende.<sup>96</sup> Certain isotropic crystals, including  $\text{Al}_x\text{Ga}_{1-x}\text{As}$ , possess electro-optic (EO) properties in which a polarization and, hence, a birefringence can be induced when an electric field ( $E$ ) is applied to the crystal (Pockels effect).<sup>97,106</sup> The Pockels effect is a linear EO effect; the induced birefringence is directly proportional to the first power of the applied electric field. Thus,  $\text{Al}_x\text{Ga}_{1-x}\text{As}$  exhibits anisotropic behavior.

In an anisotropic crystal the polarization induced by  $E$  is dependent on the direction of  $E$ .<sup>97,106</sup> Therefore, the speed at which light travels through an anisotropic crystal is dependent on the direction of propagation. A light beam propagating through an anisotropic crystal along the optic axis ( $O$ ) is defined as an ordinary ray.<sup>97,106</sup> The refractive index seen by this propagating beam is defined as the ordinary refractive index ( $n_{||}$  or  $n_o$ ).  $n_{||}$  is independent of the direction of the polarization.<sup>97,106</sup> A light beam



propagating through an anisotropic crystal at any other direction to  $O$  is defined as an extraordinary ray.<sup>106</sup> The refractive index seen by this propagating beam is defined as the extraordinary refractive index ( $n_{\perp}$  or  $n_o$ ).  $n_{\perp}$  is dependent on the direction of polarization.<sup>97,106</sup> Hence,  $n_{\perp}$  is dependent on the direction  $E$ . Since  $\text{Al}_x\text{Ga}_{1-x}\text{As}$  has one optic axis it behaves like a specific group of anisotropic crystals known as uniaxial crystals.<sup>100,106</sup> If we define the  $z$  axis as the optic axis then  $n_z = n_{\parallel}$  and  $n_x = n_y = n_{\perp}$ . The index surfaces can, therefore, be represented by a sphere with radius  $n_{\parallel}$  and an ellipsoid with radius  $n_{\parallel}$  parallel to  $O$  and radius  $n_{\perp}$  normal to the  $O$  (see Fig 4.0.1).<sup>106</sup> For  $n_{\perp} > n_{\parallel}$  the uniaxial crystal is known as a positive type and for  $n_{\perp} < n_{\parallel}$  the uniaxial crystal is known as a negative type.<sup>106</sup> As can be seen, the sphere and ellipse are tangent to each other only at the points along the optic axis. The amount of induced birefringence is defined as the difference between these two refractive indices and, as stated above, is linearly proportional to  $E$ .<sup>97,106</sup> Pockels effect is given mathematically by<sup>97,106</sup>

$$n_{\parallel} - n_{\perp} = mE,$$

4.0.1

where  $m$  is a proportionality constant. Modulating the electric field allows one to modulate the input signal and provide the basis for building an electro-optic switch.

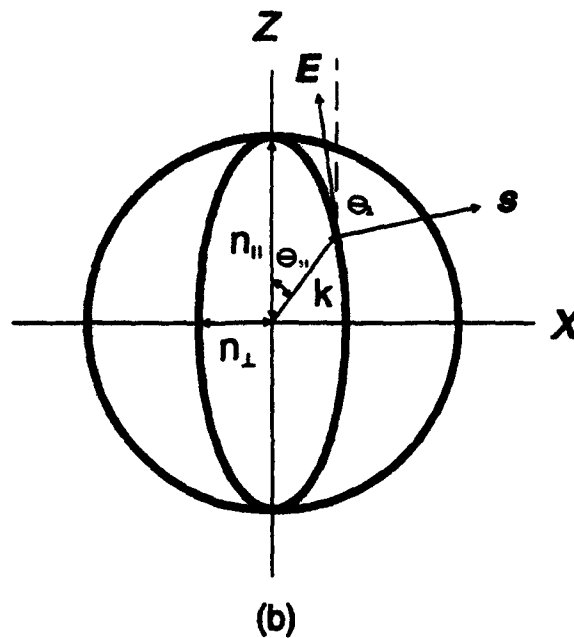
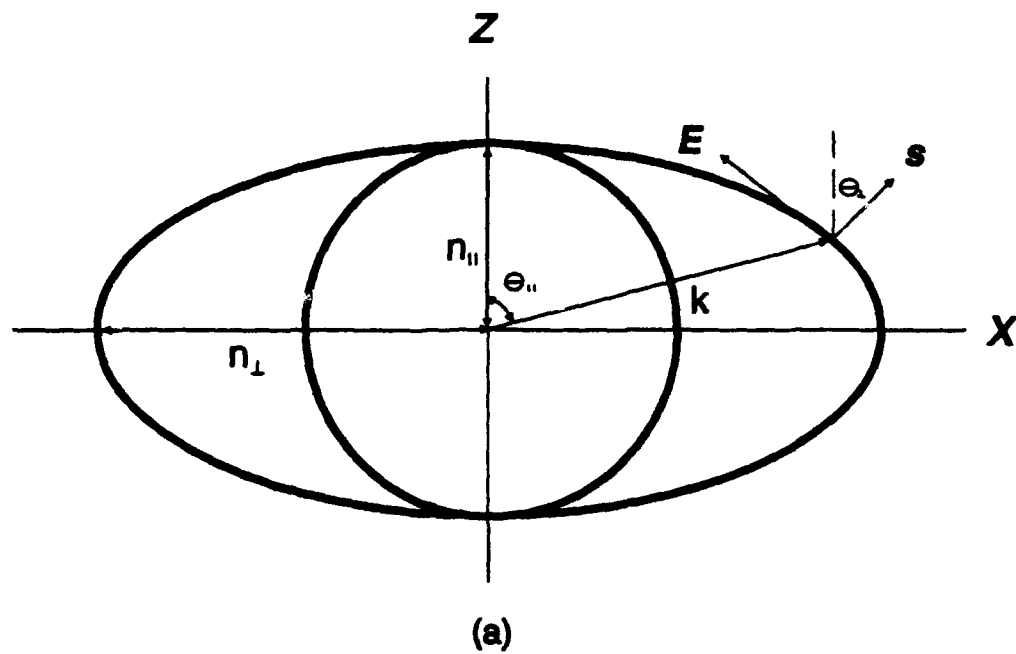


Figure 4.0.1<sup>106</sup>  
 Index Surfaces for (a) a Positive Uniaxial Crystal  
 and (b) a Negative Uniaxial Crystal

In this chapter we will determine the induced birefringence and derive an expression for electro-optic modulation using the EO properties of the specific  $\text{Al}_x\text{Ga}_{1-x}\text{As}$  structure to be fabricated for this experiment.

### Linear Electro-Optic Effect

We will begin our analysis with the constitutive equation<sup>98,99</sup>

$$\mathbf{D} = \epsilon_0 \mathbf{E} + \mathbf{P}. \quad 4.1.1$$

In Eq. 4.1.1,  $\mathbf{D}$  is the electric displacement or electric flux density vector,  $\mathbf{E}$  is the electric field vector,  $\mathbf{P}$  is the electric polarization vector and  $\epsilon_0$  is the permittivity of vacuum. In many isotropic materials the induced polarization is directly proportional to the applied field strength, except for the case of very high fields. We can write:<sup>100</sup>

$$\mathbf{P} = \epsilon_0 \chi \mathbf{E}, \quad 4.1.2$$

where  $\chi$  is the dielectric susceptibility of the medium. Combining Eqs. 4.1.1 and 4.1.2 yields<sup>100,106</sup>

$$\mathbf{D} = \epsilon \mathbf{E}, \quad 4.1.3$$

where  $\epsilon = \epsilon_0(1 + \chi)$  is the permittivity of the medium.

The analysis is similar in anisotropic materials. Eq. 4.1.2 can be expressed in its tensor form as<sup>16,100</sup>

$$P_x = \epsilon_0(\chi_{11}E_x + \chi_{12}E_y + \chi_{13}E_z), \quad 4.1.4$$

$$P_y = \epsilon_0(\chi_{21}E_x + \chi_{22}E_y + \chi_{23}E_z) \quad 4.1.5$$

and

$$P_z = \epsilon_0(\chi_{31}E_x + \chi_{32}E_y + \chi_{33}E_z), \quad 4.1.6$$

where  $\chi_{ij}$  are the coefficients of a 3x3 array called the dielectric susceptibility tensor of the medium for which  $i = 1, 2$  or  $3$  and  $j = 1, 2$  or  $3$ . The suffixes  $i$  and  $j$  designate which axes the coefficients correspond to since 1 represents  $x$ , 2 represents  $y$  and 3 represents  $z$ . Choosing  $x$ ,  $y$  and  $z$  so that the diagonal terms vanish gives the principal dielectric axes of the crystal:<sup>16</sup>

$$P_x = \epsilon_0\chi_{11}E_x \quad 4.1.7$$

$$P_y = \epsilon_0\chi_{22}E_y \quad 4.1.8$$

and

$$P_z = \epsilon_0 \chi_{33} E_z \quad 4.1.9$$

Combining Eq. 4.1.1 with Eqs. 4.1.7 - 4.1.9 yields<sup>16,100,106</sup>

$$D_x = \epsilon_{11} E_x \quad 4.1.10$$

$$D_y = \epsilon_{22} E_y \quad 4.1.11$$

and

$$D_z = \epsilon_{33} E_z \quad 4.1.12$$

where

$$\epsilon_{11} = \epsilon_0 (1 + \chi_{11}), \quad 4.1.13$$

$$\epsilon_{22} = \epsilon_0 (1 + \chi_{22}) \quad 4.1.14$$

and

$$\epsilon_{33} = \epsilon_0 (1 + \chi_{33}) \quad 4.1.15$$

are the diagonal coefficients of a  $3 \times 3$  array  $\epsilon_i$  which is referred to as the permittivity tensor of the medium.

If we introduce the phase velocity ( $v = (\mu\epsilon)^{-1/2}$ ), where  $\mu$  is the permeability of the medium, it becomes evident that for anisotropic crystals,

$v$  depends on the direction of the applied field. Thus we have<sup>16,98,99</sup>

$$v_x = (\mu\epsilon_{11})^{-1/2}, \quad 4.1.16$$

$$v_y = (\mu\epsilon_{22})^{-1/2} \quad 4.1.17$$

and

$$v_z = (\mu\epsilon_{33})^{-1/2}. \quad 4.1.18$$

For an anisotropic crystal, at least one of the permittivity coefficients is not equal to the other two (i.e.,  $\epsilon_{11} \neq \epsilon_{22}$  or  $\epsilon_{33}$ ). Only the polarization parallel to the applied electric field and, hence, the permittivity parallel to  $E$ , will contribute to the phase velocity. For example, if an input beam is propagating along the  $z$  axis and  $E$  is applied parallel to the  $y$  axis,  $\epsilon_{22}$  will be the permittivity, a polarization ( $P_y$ ) will be induced and the phase velocity will be  $v_y$  (see Eq. 4.1.17).

The index of refraction is defined as the reciprocal of the relative phase velocity.<sup>98,99,106</sup>

$$n = c/v, \quad 4.1.19$$

where  $c$  is the speed of light in vacuum. Going to tensor form, we can write

the principal refractive indices as<sup>16,99</sup>

$$n_x = c/v_x = (\mu_r \epsilon_{r11})^{1/2}, \quad 4.1.20$$

$$n_y = c/v_y = (\mu_r \epsilon_{r22})^{1/2} \quad 4.1.21$$

and

$$n_z = c/v_z = (\mu_r \epsilon_{r33})^{1/2}. \quad 4.1.22$$

In Eqs. 4.1.21 - 4.1.22,  $\mu_r = \mu/\mu_0$  is the relative permeability of the medium,  $\mu_0$  is the permeability of vacuum and  $\epsilon_{rj} = \epsilon_j/\epsilon_0$  are the coefficients of a 3x3 array called the relative permittivity tensor of the medium. For nonconductive media the relative permeability ( $\mu_r$ ) can be assumed unity<sup>99</sup> and the principal refractive indices then become<sup>16,99</sup>

$$n_x = (\epsilon_{11}/\epsilon_0)^{1/2}, \quad 4.1.23$$

$$n_y = (\epsilon_{22}/\epsilon_0)^{1/2} \quad 4.1.24$$

and

$$n_z = (\epsilon_{33}/\epsilon_0)^{1/2}. \quad 4.1.25$$

Using the definition for the refractive index along with the analysis for

anisotropic crystals given above, it becomes evident that one can induce a change in the refractive index with an applied electric field. This change will, in turn, induce birefringence, a phenomenon known as the Pockels or linear electro-optic effect.

### Index Ellipsoid

Because  $\text{Al}_x\text{Ga}_{1-x}\text{As}$  has been shown to exhibit Pockels effect,<sup>3,101</sup> we can use the anisotropic analysis to determine the induced birefringence. We will start with the general index ellipsoid for a crystal in its simplest form. This will allow us to determine the direction of polarization as well as the corresponding refractive indices of the crystal. The index ellipsoid is given in the principal coordinate system as<sup>98,102,106</sup>

$$x^2/n_x^2 + y^2/n_y^2 + z^2/n_z^2 = 1. \quad 4.2.1$$

In Eq. 4.2.1,  $x$ ,  $y$  and  $z$  are the principal axes (the direction in the crystal along which the electric field vector ( $E$ ) and the electric displacement vector ( $D$ ) are parallel) and  $1/n_x^2$ ,  $1/n_y^2$  and  $1/n_z^2$  are the principal refractive indices along their respective axes. The lengths of the major axes of the index ellipsoid, represented by Eq. 4.2.1, are  $2n_x$ ,  $2n_y$  and  $2n_z$ , parallel to directions  $x$ ,  $y$  and  $z$ , respectively.<sup>16,98</sup> The index ellipsoid is used to find the two



refractive indices and two corresponding directions of  $D$  associated with the two independent plane waves propagating along an arbitrary direction  $s$  in the crystal. These indices are determined using Eq. 4.2.1. Visually depicted in Fig. 4.2.1, the major and minor axes of the ellipsoid are in the directions  $D_1$  and  $D_2$ , respectively, with the length of  $D_1$  equal to  $2n_1$  and the length of  $D_2$  equal to  $2n_2$ .

Next we will introduce the optical dielectric impermeability tensor of a crystal. The coefficients ( $\eta_i$ ) of this tensor depend on the distribution of bond charges in the material.<sup>16,100</sup>  $\eta_i$  are found by taking the reciprocal of the relative permittivity or dielectric constant.<sup>100</sup>  $\eta_i$  has been defined in terms of the refractive index of the crystal as<sup>100</sup>

$$\eta_i = \epsilon_0/\epsilon_i = 1/n_i^2 \quad 4.2.2$$

(see Eqs. 4.1.23 - 4.1.25). Application of an electric field  $E$  to the crystal results in a redistribution of the bond charges of the crystal and a possible deformation of the ion lattice. This causes a change in the optical impermeability tensor and, hence, a change the refractive index of the crystal. This allows us to write the index ellipsoid in the presence of an electric field:<sup>16</sup>

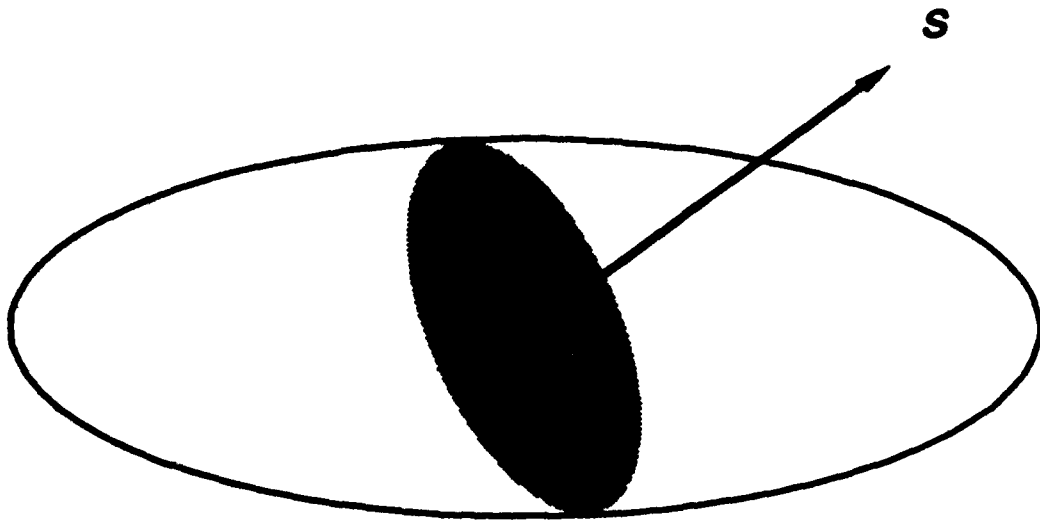


**Figure 4.2.1<sup>16</sup>**  
**Inner Ellipse is the Intersection of the Index Ellipsoid**  
**with the Plane Perpendicular to  $s$**

$$\begin{aligned}
 (1/n_x^2)x^2 + (1/n_y^2)y^2 + (1/n_z^2)z^2 + A_1x^2 + A_2y^2 + A_3z^2 + A_4yz \\
 + A_5zx + A_6xy + A_7zy + A_8xz + A_9yx = 1.
 \end{aligned}
 \tag{4.2.3}$$

For  $E = 0$ ,  $A_1$  through  $A_9 = 0$ , and Eq. 4.2.3 reduces to Eq. 4.2.1.

Introducing the notations

$$\begin{aligned}
 x^2 &= xx = (11) \rightarrow 1 \\
 y^2 &= yy = (22) \rightarrow 2 \\
 z^2 &= zz = (33) \rightarrow 3 \\
 yz &= (23) \rightarrow 4 \\
 zx &= (31) \rightarrow 5 \\
 xy &= (12) \rightarrow 6 \\
 zy &= (32) \rightarrow 7 \\
 xz &= (13) \rightarrow 8 \\
 yx &= (21) \rightarrow 9,
 \end{aligned}
 \tag{4.2.4}$$

along with

$$\begin{aligned}
 (1/n^2)_1 &= 1/n_x^2 = A_1 \\
 (1/n^2)_2 &= 1/n_y^2 = A_2 \\
 (1/n^2)_3 &= 1/n_z^2 = A_3 \\
 (1/n^2)_4 &= 1/n_y n_z = A_4 \\
 (1/n^2)_5 &= 1/n_z n_x = A_5
 \end{aligned}
 \tag{4.2.5}$$

$$(1/n^2)_6 = 1/n_x n_y = A_6$$

$$(1/n^2)_7 = 1/n_z n_y = A_7$$

$$(1/n^2)_8 = 1/n_x n_z = A_8$$

$$(1/n^2)_9 = 1/n_y n_x = A_9$$

Eq. 4.2.3 becomes

$$\begin{aligned} & [1/n_x^2 + (1/n^2)_1]x^2 + [1/n_y^2 + (1/n^2)_2]y^2 + [1/n_z^2 + (1/n^2)_3]z^2 \\ & + [(1/n^2)_4]yz + [(1/n^2)_5]zx + [(1/n^2)_6]xy + [(1/n^2)_7]zy \\ & + [(1/n^2)_8]xz + [(1/n^2)_9]yx = 1. \end{aligned} \quad 4.2.6$$

It has been shown that  $\eta_{ij}$  is symmetric, provided that the medium is lossless and optically active.<sup>16</sup> This allows the permutation of  $i$  and  $j$ , and the notation presented in Eq. 4.2.5 and Eq. 4.2.6 reduces to

$$\begin{aligned} x^2 &= xx = (11) \rightarrow 1 \\ y^2 &= yy = (22) \rightarrow 2 \\ z^2 &= zz = (33) \rightarrow 3 \\ yz &= zy = (23) = (32) \rightarrow 4 \\ zx &= xz = (31) = (13) \rightarrow 5 \\ xy &= yx = (12) = (21) \rightarrow 6, \end{aligned} \quad 4.2.7$$

with

$$\begin{aligned}
 (1/n^2)_1 &= 1/n_x^2 \\
 (1/n^2)_2 &= 1/n_y^2 \\
 (1/n^2)_3 &= 1/n_z^2 \\
 (1/n^2)_4 &= 1/n_y n_z = 1/n_z n_y \\
 (1/n^2)_5 &= 1/n_z n_x = 1/n_x n_z \\
 (1/n^2)_6 &= 1/n_x n_y = 1/n_y n_x
 \end{aligned}
 \tag{4.2.8}$$

Substituting Eq. 4.2.7 and Eq. 4.2.8 into Eq. 4.2.6 yields<sup>102</sup>

$$\begin{aligned}
 &[1/n_x^2 + (1/n^2)_1]x^2 + [1/n_y^2 + (1/n^2)_2]y^2 + [1/n_z^2 + (1/n^2)_3]z^2 \\
 &+ 2[(1/n^2)_4]yz + 2[(1/n^2)_5]xz + 2[(1/n^2)_6]xy = 1.
 \end{aligned}
 \tag{4.2.9}$$

### Electro-Optic Coefficients

The electro-optic (EO) coefficients are traditionally defined as<sup>18,108</sup>

$$\eta_i(E) - \eta_i(0) \equiv \Delta\eta_i = r_{jk}E_k + s_{ijk}E_kE_j
 \tag{4.3.1}$$

In Eq. 4.3.1,  $E$  is the applied electric field,  $r_{jk}$  are the coefficients of a  $3 \times 9$  array called the linear electro-optic (Pockels) tensor of the medium and  $s_{ijk}$  are the coefficients of a  $6 \times 6$  array called the quadratic electro-optic (Kerr)

tensor of the medium for which  $k = 1, 2$ , or  $3$  and  $l = 1, 2$ , or  $3$ . In the equation above, we have omitted terms higher than the quadratic. These higher order effects are so weak compared with the linear and quadratic effects, that they can be neglected for most applications.<sup>16,106</sup> For centrosymmetric crystals (crystals possessing inversion symmetry for all physical properties<sup>100</sup>), the linear EO effect vanishes (i.e.,  $r_{ijk} = 0$ ). This is caused by the spatial inversion symmetry of such crystals. Therefore, the quadratic EO effect will dominate.<sup>16</sup> For noncentrosymmetric crystals (crystals that do not possess inversion symmetry for all physical properties<sup>100</sup>), both the linear and quadratic effects will be present.<sup>16</sup> From the section above, the EO effects will depend on the ratio of the applied electric field ( $E$ ) to the intra-atomic electric field ( $E_u$ ) binding the charged particles. This ratio can be estimated by finding the magnitude of  $E_u$  at a position ( $T$ ) arising from a point charge ( $q$ ) located at a distance ( $u$ ) from  $T$ .  $E_u$  at  $T$  is given by<sup>98,99</sup>

$$E_u = (1/4\pi\epsilon_0)q/u^2.$$

4.3.2

The minimum field inside the atom  $E_u$  can be determined by substituting the lattice constant  $a_0$  of the crystal for  $u$  and the elementary electron charge for  $q$ . In this experiment,  $\text{Al}_{0.30}\text{Ga}_{0.70}\text{As}$  was used for the core. The lattice

constant for  $\text{Al}_x\text{Ga}_{1-x}\text{As}$  is given by Eq. 2.3.30. For  $x = 0.300$ ,  $\epsilon_0 = 8.85418782 \times 10^{-12} \text{ F/m}$  and  $e = 1.6021892 \times 10^{-19} \text{ C}$ ,<sup>103</sup> the minimum electric field inside the atom is found to be  $E_u = 4.5 \times 10^7 \text{ V/cm}$ . This is expected to be far greater than the applied field. As a result, the quadratic EO effect should be small enough, when compared to the linear EO effect, to allow us to neglect the  $s_{jk}$  terms. Eq. 4.3.1 becomes

$$\eta_i(E) - \eta_i(0) = \Delta\eta_i = r_{ik}E_k \quad 4.3.3$$

The permutation property along with Eqs. 4.2.2, 4.2.7, 4.2.8 and 4.3.3 yields<sup>97,106</sup>

$$\Delta(1/n^2)_i = \sum_{k=1}^3 r_{ik}E_k \quad 4.3.4$$

where, for example,  $\Delta(1/n^2)_4 = r_{41}E_1 + r_{42}E_2 + r_{43}E_3$ . Substitution of Eq. 4.3.4 into Eq. 4.2.9 gives the general index ellipsoid in the presence of an electric field in terms of  $r_{ik}$ .<sup>16</sup>

$$\begin{aligned} & [1/n_x^2 + r_{1k}E_k]x^2 + [1/n_y^2 + r_{2k}E_k]y^2 + [1/n_z^2 + r_{3k}E_k]z^2 \\ & + 2[r_{4k}E_k]yz + 2[r_{5k}E_k]xz + 2[r_{6k}E_k]xy = 1. \end{aligned} \quad 4.3.5$$

In order to determine the EO tensor for crystals belonging to the cubic  $\bar{4}3m$  class we will start with the EO tensor for the triclinic 1 crystal group in matrix form:<sup>102</sup>

$$r_{ik} = \begin{bmatrix} r_{11} & r_{12} & r_{13} \\ r_{21} & r_{22} & r_{23} \\ r_{31} & r_{32} & r_{33} \\ r_{41} & r_{42} & r_{43} \\ r_{51} & r_{52} & r_{53} \\ r_{61} & r_{62} & r_{63} \end{bmatrix} \quad 4.3.6$$

Neglecting the permutation property for the moment, Eq. 4.3.6 expands to

$$r_{ijk} = \begin{bmatrix} r_{111} & r_{112} & r_{113} \\ r_{221} & r_{222} & r_{223} \\ r_{331} & r_{332} & r_{333} \\ r_{231} & r_{232} & r_{233} \\ r_{321} & r_{322} & r_{323} \\ r_{131} & r_{132} & r_{133} \\ r_{311} & r_{312} & r_{313} \\ r_{121} & r_{122} & r_{123} \\ r_{211} & r_{212} & r_{213} \end{bmatrix} \quad 4.3.7$$



Since zincblende crystals have axes of fourfold symmetry along the cube edges, we can let  $z$  be the axis of two fold rotation which can be represented by the matrix<sup>16</sup>

$$a_j = \begin{bmatrix} -1 & 0 & 0 \\ 0 & -1 & 0 \\ 0 & 0 & 1 \end{bmatrix} \quad 4.3.8$$

Eq. 4.3.8 dictates that the suffixes of the EO coefficients change as follows:

$1 \rightarrow -1, 2 \rightarrow -2$  and  $3 \rightarrow 3$ .<sup>100</sup> Substituting this property into Eq. 4.3.7 yields

$$r_{ijk} = \begin{bmatrix} -r_{111} & -r_{112} & r_{113} \\ -r_{221} & -r_{222} & r_{223} \\ -r_{331} & -r_{332} & r_{333} \\ r_{231} & r_{232} & -r_{233} \\ r_{321} & r_{322} & -r_{323} \\ r_{131} & r_{132} & -r_{133} \\ r_{311} & r_{312} & -r_{313} \\ -r_{121} & -r_{122} & r_{123} \\ -r_{211} & -r_{212} & r_{213} \end{bmatrix} \quad 4.3.9$$

where

$$r_{ijk} = r_{111} \rightarrow r_{(-1)(-1)(-1)} = -r_{111},$$

$$r_{ijk} = r_{123} \rightarrow r_{(-1)(-2)(3)} = r_{123},$$

$$r_{jk} = r_{223} \rightarrow r_{(-2)(-2)(3)} = r_{223},$$

etc. Setting  $r_{jk} = \pm r_{jk}$  leads to the following condition:  $r_{jk} = -r_{jk}$ , only if  $r_{jk} = 0$ .<sup>16</sup> Equating Eqs. 4.3.7 and 4.3.9 with this condition yields

$$r_{jk} = \begin{bmatrix} 0 & 0 & r_{113} \\ 0 & 0 & r_{223} \\ 0 & 0 & r_{333} \\ r_{231} & r_{232} & 0 \\ r_{321} & r_{322} & 0 \\ r_{131} & r_{132} & 0 \\ r_{311} & r_{312} & 0 \\ 0 & 0 & r_{123} \\ 0 & 0 & r_{213} \end{bmatrix} \quad 4.3.10$$

Since cubic  $\bar{4}3m$  class crystals also have axes of fourfold symmetry, which includes three mutually perpendicular twofold axes  $x$ ,  $y$  and  $z$ , this allows us to perform a triple product:

$$i(j \times k) = k(i \times j) = j(k \times i). \quad 4.3.11$$

Performing this triple product with the coefficients in Eq. 4.3.10 yields

$$r_{jk} = \begin{bmatrix} 0 & 0 & 0 \\ 0 & 0 & 0 \\ 0 & 0 & 0 \\ r_{231} & 0 & 0 \\ 0 & 0 & 0 \\ 0 & 0 & 0 \\ 0 & r_{312} & 0 \\ 0 & 0 & r_{123} \\ 0 & 0 & 0 \end{bmatrix}, \quad 4.3.12$$

where

$$r_{jk} = r_{113} \rightarrow i \cdot (i \times k) = 0,$$

$$r_{jk} = r_{321} \rightarrow k \cdot (j \times i) = -r_{321} = 0,$$

$$r_{jk} = r_{231} \rightarrow j \cdot (k \times i) = r_{231},$$

etc. Finally, we need to take into account the axes of threefold symmetry.

The simplest threefold symmetry operation is  $x \rightarrow y$ ,  $y \rightarrow z$  and  $z \rightarrow x$ . This

is represented by the matrix<sup>16</sup>

$$a_j = \begin{bmatrix} 0 & 1 & 0 \\ 0 & 0 & 1 \\ 1 & 0 & 0 \end{bmatrix}. \quad 4.3.13$$

Eq. 4.3.13 dictates that the suffixes of the EO coefficients change as follows:

$1 \rightarrow 2, 2 \rightarrow 3$  and  $3 \rightarrow 1$ .<sup>16</sup> Using the threefold symmetry operation gives

$$r_{ijk} = r_{123} \rightarrow r_{(2)(3)(1)} = r_{231} \quad 4.3.14$$

and

$$r_{ijk} = r_{231} \rightarrow r_{(3)(1)(2)} = r_{312}. \quad 4.3.15$$

This proves that

$$r_{123} = r_{231} = r_{312}. \quad 4.2.16$$

Going back to contracted notation, the electro-optic tensor ( $r_k$ ) for crystals belonging to the cubic  $\bar{4}3m$  group can be represented by the well known matrix<sup>16</sup>

$$r_k = \begin{bmatrix} 0 & 0 & 0 \\ 0 & 0 & 0 \\ 0 & 0 & 0 \\ r_{41} & 0 & 0 \\ 0 & r_{41} & 0 \\ 0 & 0 & r_{41} \end{bmatrix} \quad 4.3.17$$

Substituting the EO tensor for zincblende crystals back into the index ellipsoid (Eq. 4.3.5) gives<sup>16</sup>

$$\begin{aligned} & [1/n_x^2]x^2 + [1/n_y^2]y^2 + [1/n_z^2]z^2 \\ & + 2yzr_{41}E_x + 2xzr_{41}E_y + 2xyr_{41}E_z = 1. \end{aligned} \quad 4.2.18$$

Taking into account that cubic  $\bar{4}3m$  crystals are optically isotropic allows us to further simplify the index ellipsoid. This yields<sup>96</sup>

$$(1/n^2)[x^2 + y^2 + z^2] + 2yzr_{41}E_x + 2xzr_{41}E_y + 2xyr_{41}E_z = 1. \quad 4.2.19$$

### Induced Refractive Indices and Birefringence

We need to determine the direction and magnitude of the principal axes of the new ellipsoid represented by Eq. 4.3.19 since they may not coincide with  $x$ ,  $y$ ,  $z$ . For this experiment, we are fabricating an EO directional coupler switch. This dictates that the electrodes be placed parallel to the waveguides along the optic axis. Therefore, propagation of the input beam will be along the  $\langle 011 \rangle$  (i.e.,  $z$ ) direction through the directional coupler of length  $L$ , and the electrodes will be placed on the top and bottom of the coupler running along  $z$  and separated by a distance  $d$ . The electric field  $E$  will be applied along the  $\langle 100 \rangle$  (i.e.,  $y$ ) direction. With  $E$  applied normal to

the direction of the input beam, we have what is defined as transverse modulation.<sup>16</sup> A transverse modulator using a zincblende crystal in the orientation used for this experiment is illustrated in Fig. 4.4.1. Since the electric field is in the  $y$  direction, we have

$$E_x = E_z = 0$$

and

$$E_y = E. \quad 4.4.1$$

This is similar to one of the three cases presented by Namba<sup>86</sup> with  $E$  along the  $\langle 001 \rangle$  direction and the input beam propagating along the  $\langle 100 \rangle$  direction. These were defined by Namba as the  $x$  and  $y$  directions, respectively. Scribe and break experiments performed on GaAs wafers have demonstrated, however, that the preferential cleave planes for GaAs are  $(011)$ ,  $(0\bar{1}1)$ ,  $(01\bar{1})$ ,  $(0\bar{1}\bar{1})$ ,  $(101)$ ,  $(10\bar{1})$ ,  $(\bar{1}01)$ ,  $(\bar{1}0\bar{1})$ ,  $(110)$ ,  $(1\bar{1}0)$ ,  $(\bar{1}10)$  and  $(\bar{1}\bar{1}0)$  as shown in Fig. 4.4.2.<sup>104</sup> This suggests that even though Namba's case can be solved theoretically, it cannot practically be demonstrated. This is the argument used for the crystal orientation chosen for this experiment. Substituting Eq. 4.4.1 into Eq. 4.3.19 yields the index ellipsoid

$$(1/n^2)[x^2 + y^2 + z^2] + 2xzr_{41}E = 1. \quad 4.4.2$$

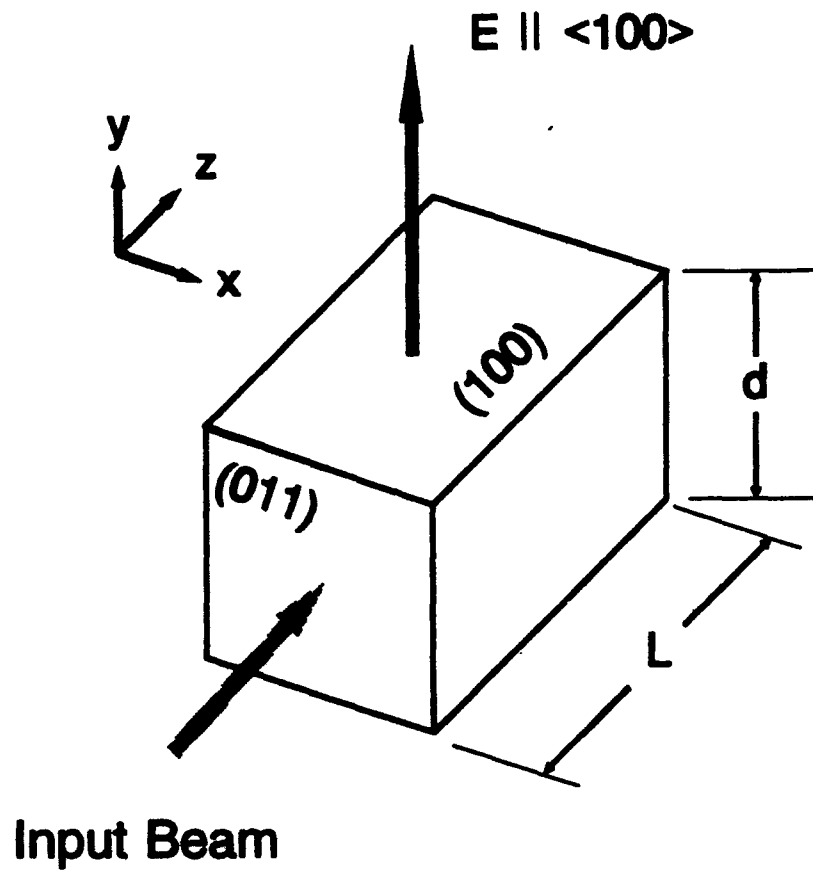


Figure 4.4.1  
Transverse Electro-Optic Modulator using a Cubic  $\bar{4}3m$  Group Crystal

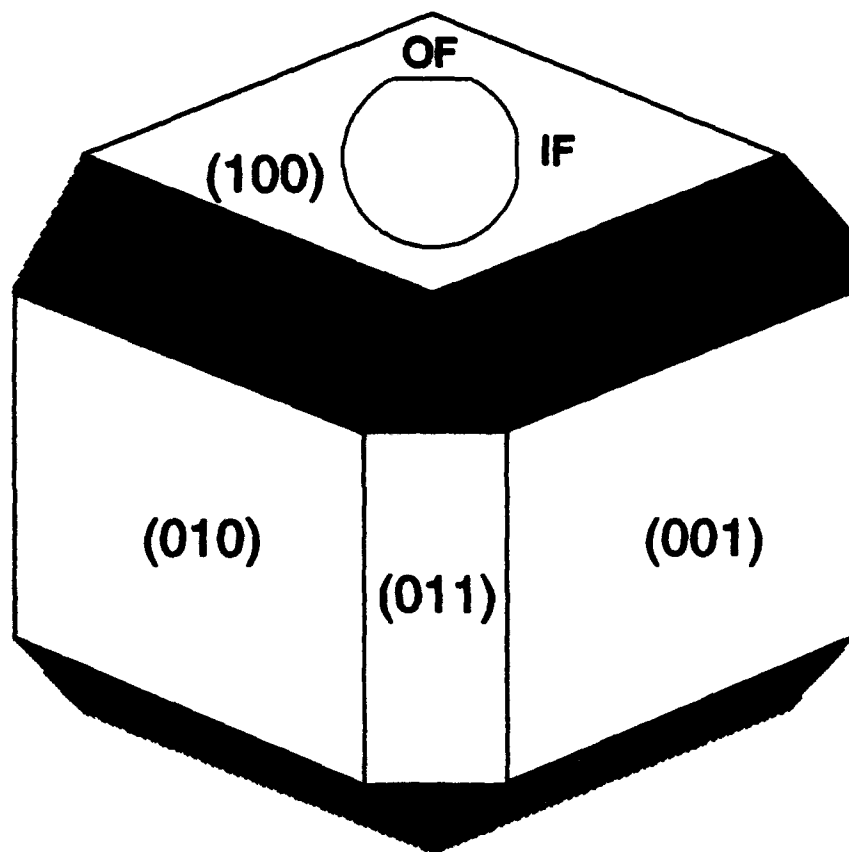


Figure 4.4.2  
Representation of a GaAs Crystal



In order to determine the direction and magnitude of the principal axes of the new ellipsoid, we first need to convert Eq. 4.4.2 into its diagonal form by transforming the coordinate system  $(x,y,z)$  into a new coordinate system  $(x',y',z')$ . This is done by rotating the axes perpendicular to the applied electric field by  $45^\circ$ .<sup>16,106</sup> For this experiment we will rotate the  $x$  and  $z$  axes, which gives

$$x = x' \cos(45^\circ) - z' \sin(45^\circ), \quad 4.4.3$$

$$y = y' \quad 4.4.4$$

and

$$z = x' \sin(45^\circ) + z' \cos(45^\circ). \quad 4.4.5$$

Substituting Eqs. 4.4.3, 4.4.4 and 4.4.5 into Eq. 4.4.2 yields

$$[(1/n^2) + r_{41}E]x'^2 + [1/n^2]y'^2 + [(1/n^2) - r_{41}E]z'^2 = 1. \quad 4.4.6$$

Using Eq. 4.3.4, we have

$$[(1/n^2) + \Delta(1/n^2)]x'^2 + [1/n^2]y'^2 + [(1/n^2) - \Delta(1/n^2)]z'^2 = 1. \quad 4.4.7$$

From Eq. 4.4.7 we can write

$$1/(n_x)^2 = 1/n^2 + \Delta(1/n^2), \quad 4.4.8$$

$$1/(n_y)^2 = 1/n^2 \quad 4.4.9$$

and

$$1/(n_z)^2 = 1/n^2 - \Delta(1/n^2). \quad 4.4.10$$

Using Eq. 4.0.1 for Pockels effect along with Eqs. 4.2.2, 4.3.3 and 4.3.4 yields the induced change in the refractive index

$$\Delta n = m' r_{41} E = m' \Delta(1/n^2), \quad 4.4.11$$

where  $m'$  is a proportionality factor we will use to equate  $\Delta n$  and  $\Delta(1/n^2)$ . If we assume  $r_{41} E \ll 1/n^2$ , (i.e.,  $\Delta(1/n^2)$  sufficiently small), this allows us to use the relation<sup>16</sup>

$$\Delta(1/n^2) \approx \partial(1/n^2) = -(2/n^3) \partial n. \quad 4.4.12$$

Multiplying both sides by  $-(n^3/2)$  yields

$$\partial n = -(n^3/2)\partial(1/n^2). \quad 4.4.13$$

Equating Eqs. 4.2.11 and 4.2.13 leads to<sup>16</sup>

$$\Delta n = m' = -(n^3/2)\Delta(1/n^2). \quad 4.4.14$$

Using Eq. 4.3.4 once again, we can write

$$\Delta n = -(n^3/2)r_{41}E. \quad 4.4.15$$

This leads to the new indices<sup>16</sup>

$$n_x = n + \Delta n = n - (n^3/2)r_{41}E, \quad 4.4.16$$

$$n_y = n \quad 4.4.17$$

and

$$n_z = n - \Delta n = n + (n^3/2)r_{41}E. \quad 4.4.18$$

The induced birefringence for the new axes with the input beam propagating perpendicular to the applied electric field (i.e., for transverse modulation) can now be given by<sup>16,97</sup>

$$n_y - n_x = (n^3/2)r_{41}E. \quad 4.4.19$$

Eq. 4.4.19 is the definition for the induced birefringence that we will use to describe the phase retardation experienced by the input beam as it propagates through the crystal.

### Electro-Optic Modulation

For our experiment we will consider an optical field that is incident and normal to the  $x'y'$  plane propagating along the  $z$  axis with  $E$  parallel to the  $y$  axis. At the input plane  $z = 0$  the optical field can be resolved into two mutually orthogonal components polarized along  $x'$  and  $y'$ . The  $x'$  component propagates as<sup>102,106</sup>

$$E_x = A \exp[i(\omega t - (\omega/c)n_x z)], \quad 4.5.1$$

where  $\omega$  is the angular frequency,  $t$  is time and  $A$  is a constant. The  $y'$  component propagates as<sup>102,106</sup>

$$E_y = A \exp[i(\omega t - (\omega/c)n_y z)]. \quad 4.5.2$$

The difference in phase between these two components at the output plane

$z = L$  is called the phase retardation.<sup>102,106</sup> It is given by the difference of the exponential terms in Eqs. 4.5.1 and 4.5.2. Performing the subtraction yields

$$\Gamma_{xy} = (\omega/c)[n_y - n_x]L, \quad 4.5.3$$

where  $[n_y - n_x]$  is the induced birefringence found in the previous section. Substituting for the induced birefringence using Eq. 4.4.19 gives<sup>102,106</sup>

$$\Gamma_{xy} = (\omega/c)[(n^3/2)r_{41}E]L. \quad 4.5.4$$

Using the relation  $\omega/c = 2\pi/\lambda$  with  $\lambda$  defined as the wavelength, the phase retardation becomes<sup>98,106</sup>

$$\Gamma_{xy} = (\pi n^3 r_{41} VL)/(\lambda d), \quad 4.5.5$$

where  $V$  is the voltage applied between electrodes separated by a distance  $d$ . For this experiment, we want a phase retardation of  $180^\circ$  or  $\Gamma_{xy} = \pi$ . The voltage necessary to realize a  $\pi$  phase change is defined as half wave voltage.<sup>102,106</sup> Setting the left side of Eq. 4.5.5 equal to  $\pi$  gives us

$$V_\pi = (\lambda d)/(n^3 r_{41} L). \quad 4.5.6$$

$V_{\pi}$  is the voltage necessary to realize half wave polarization in zincblende crystals. Eq. 4.5.6 is also the same relation that was given for complete switching using a zero-gap directional coupler (see Eq. 1.5.7). For conventional directional coupler switches the voltage required for switching the input beam completely from one channel to the other, requires a phase change of  $\sqrt{3}\pi$ . Substituting  $\Gamma_{xy} = \sqrt{3}\pi$  into Eq. 4.5.5 yields

$$V_{\sqrt{3}\pi} = (\sqrt{3}\lambda d)/(n^3 r_{41} L). \quad 4.5.7$$

Eq. 4.5.7 is the same relation that was given for complete switching using a conventional directional coupler (see Eq. 1.4.11). Since we are fabricating zero-gap directional couplers, Eq. 4.5.6 is the relation we will use for the switching voltage in this experiment.

Electro-optic modulators and directional couplers using GaAs have been modelled, fabricated and/or analyzed extensively over the years by many researchers.<sup>16,19,39-41,89,98,101,102,105-107,111-121</sup> The EO coefficient for GaAs has been measured or modelled by several researchers as well.<sup>116,120-137</sup> Conducting an exhaustive search of the open literature for  $\text{Al}_x\text{Ga}_{1-x}\text{As}$  waveguide modulators and directional couplers, however, has turned up only a few papers.<sup>3,138-144</sup> For the EO coefficient for  $\text{Al}_x\text{Ga}_{1-x}\text{As}$ , only one paper was found that gives a measured value of  $r_{41}$ .<sup>145</sup> This was for a specific Al

concentration ( $x = 0.17$ ) and at a specific wavelength ( $\lambda = 1.1523 \mu\text{m}$ ). In addition, no models for the determining the EO coefficient for  $\text{Al}_x\text{Ga}_{1-x}\text{As}$  were discovered. Therefore,  $r_{41}$  for the  $\text{Al}_x\text{Ga}_{1-x}\text{As}$  composition used in this experiment will have to be estimated. This was also the case for those previous works on  $\text{Al}_x\text{Ga}_{1-x}\text{As}$  modulators.<sup>3,138-144</sup> What is different from those earlier papers, however, is the fact that we have a measured value of  $r_{41}$  for  $\text{Al}_{0.17}\text{Ga}_{0.83}\text{As}$ .<sup>145</sup> This will allow us to model  $r_{41}$  for other concentrations of  $\text{Al}_x\text{Ga}_{1-x}\text{As}$  and should provide a closer estimate.

## CHAPTER V

### EXPERIMENTAL PROCEDURES AND DEVICE CHARACTERIZATION

In the preceding chapters, the theory behind optical Fredkin gates and zero-gap directional couplers was presented. In this chapter, the actual experimental procedures used to fabricate and evaluate these devices will be detailed.  $\text{Al}_x\text{Ga}_{1-x}\text{As}$  material growth and characterization as well as waveguide and device fabrication and performance will be addressed. Optical digital logic will also be demonstrated. In addition, a method to determine the linear electro-optic coefficient for  $\text{Al}_x\text{Ga}_{1-x}\text{As}$  will be developed.

#### Material Growth

The  $\text{Al}_x\text{Ga}_{1-x}\text{As}$  structure used to fabricate Fredkin gates for this experiment was grown using both molecular beam epitaxy (MBE) and metal-organic chemical vapor deposition (MOCVD).

MBE is an epitaxial growth technique that utilizes the reaction of one or more thermal beams of atoms or molecules that have a crystalline surface



under ultra-high vacuum (i.e.,  $< 10^{-10}$  Torr). Molecular beams are generated from thermal effusion cells known as Knudsen sources.<sup>149</sup> The molecules interact on a heated crystalline substrate producing a single-crystal layer. Each of the constituent elements and dopants required for making up the composition of the grown film is emitted from its own Knudsen source. Fig. 5.1.1 is a schematic diagram of the MBE process for  $\text{Al}_x\text{Ga}_{1-x}\text{As}$  growth. Each source is independently temperature controlled and arranged around the substrate in such a way as to ensure that the uniformity of both film composition and thickness is optimized.<sup>149</sup> The addition of mechanical shutters for each source as well as rotating the substrate, further optimizes the growth.<sup>57,149</sup> Growth using MBE enhances the electrical and optical properties of the grown films.<sup>149</sup> The growth rate for MBE is typically  $1 \mu\text{m}/\text{hour}$ .<sup>57,149</sup> Growth temperatures using MBE range from  $550 - 650^\circ\text{C}$  for  $\text{Al}_x\text{Ga}_{1-x}\text{As}$  deposition.<sup>57,149</sup>

MOCVD growth of III-V materials utilizes a liquid source of the group III components (Al and Ga) that are vaporized in a temperature controlled stainless steel bubbler.<sup>149,150</sup> The group III vapor is transported to a process tube by a hydrogen ( $\text{H}_2$ ) carrier gas and pyrolyzed with the group V component (As).<sup>149</sup> This forms an epitaxial layer on the substrate. Fig. 5.1.2 is a schematic diagram of an MOCVD reactor for  $\text{Al}_x\text{Ga}_{1-x}\text{As}$  growth. Growth rates using MOCVD are controlled by adjusting the  $\text{H}_2$  flow through the

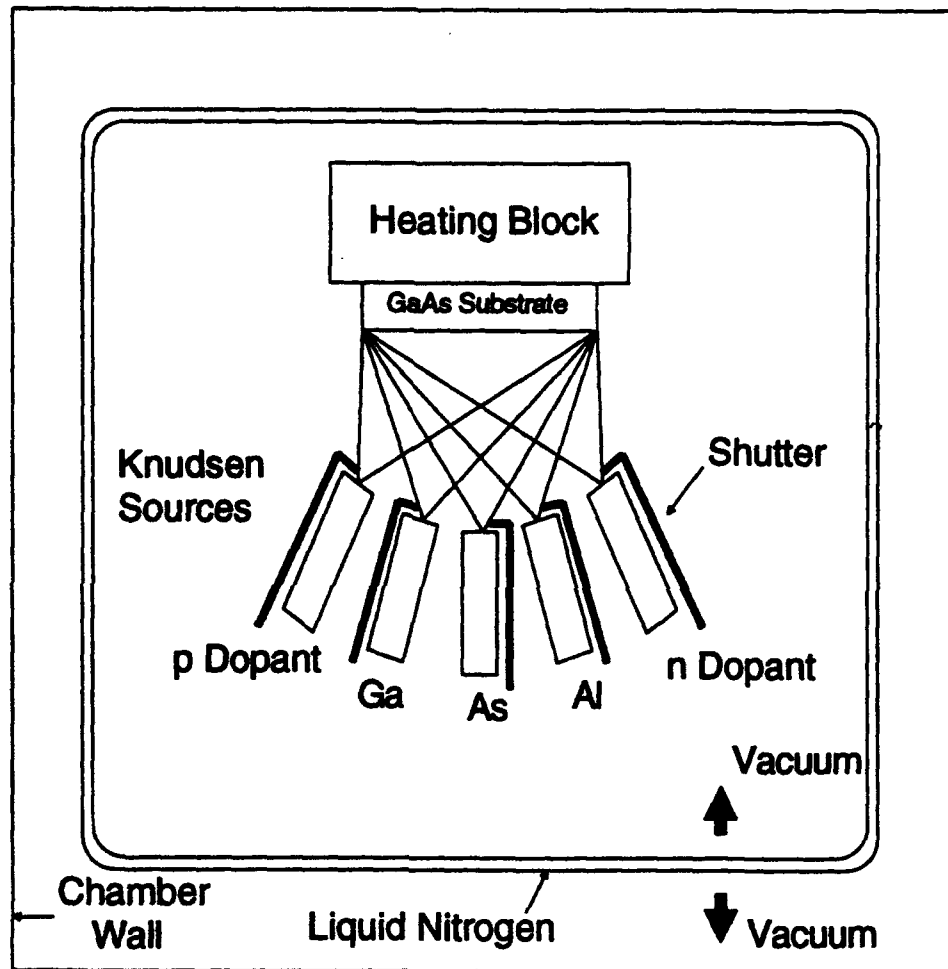


Figure 5.1.1<sup>149</sup>  
MBE Growth Process for  $\text{Al}_x\text{Ga}_{1-x}\text{As}$

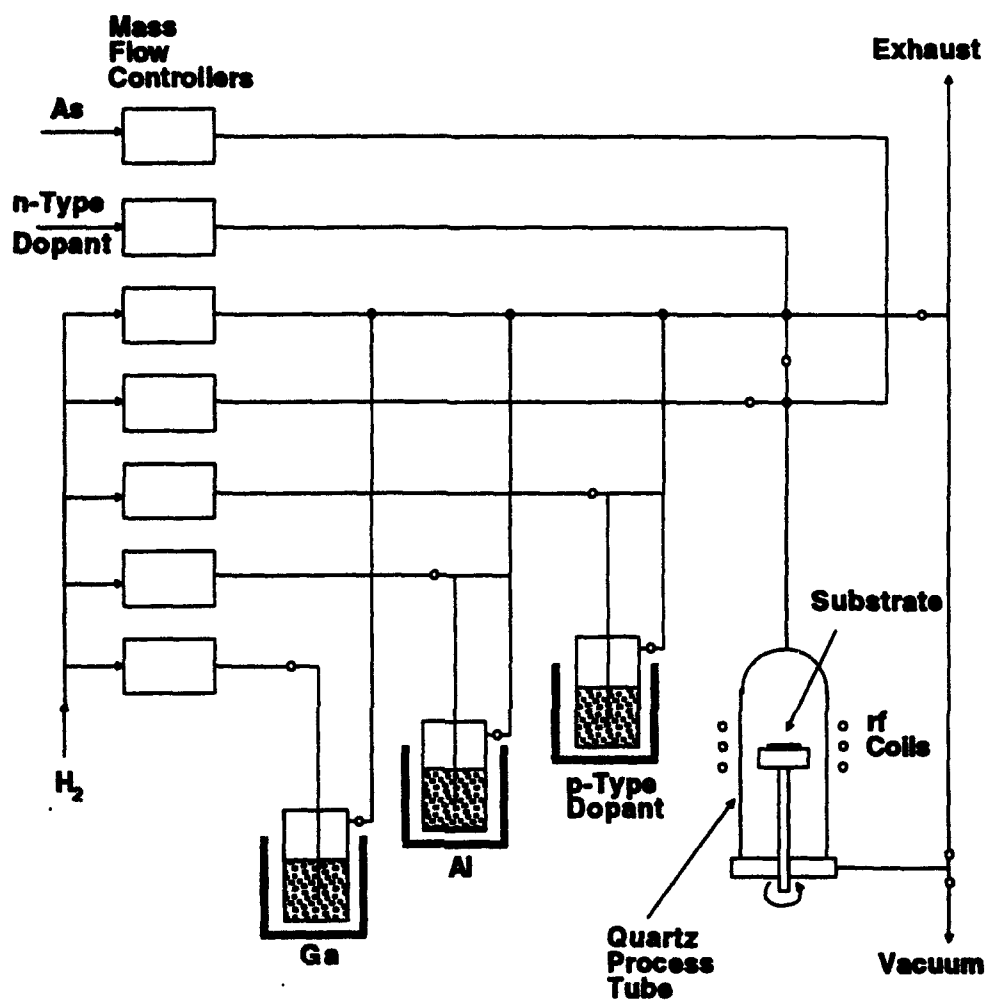


Figure 5.1.2<sup>149</sup>  
MOCVD Growth Process for  $\text{Al}_x\text{Ga}_{1-x}\text{As}$

bubbler and typically range from 1 - 10  $\mu\text{m}/\text{hour}$ .<sup>149,150</sup> Film layers as thin as 25 Å can be deposited.<sup>149,150</sup> Growth temperatures using MOCVD range from 550 - 750°C for  $\text{Al}_x\text{Ga}_{1-x}\text{As}$  deposition.<sup>149,150</sup> P-type dopants are introduced using zinc (Zn) and n-type dopants are introduced using tellurium (Te).<sup>149</sup>

The  $\text{Al}_x\text{Ga}_{1-x}\text{As}$  waveguide structure showing the target Al concentrations and layer thicknesses is illustrated in Fig. 5.1.3. The target thickness of the  $\text{Al}_{0.30}\text{Ga}_{0.70}\text{As}$  core region grown was 1  $\mu\text{m}$  in order to provide single mode operation at 827 nm (see Chapter II). The target thickness for the top  $\text{Al}_{0.35}\text{Ga}_{0.65}\text{As}$  clad layer grown was 1  $\mu\text{m}$  in order to provide low modal attenuation.<sup>3</sup> The target thickness of the bottom  $\text{Al}_{0.35}\text{Ga}_{0.65}\text{As}$  clad layer grown ranged from 2 - 4  $\mu\text{m}$  in order to provide isolation between the device and the substrate. It has been shown that a thicker bottom clad lowers the propagation loss.<sup>3</sup> The alternating  $\text{Al}_{0.28}\text{Ga}_{0.72}\text{As}$  and GaAs super lattice buffer layers grown between the GaAs substrate and the bottom clad layer have been shown to provide improved surface morphology of the subsequently grown layers.<sup>3,58,150</sup>

The MBE chambers used for the  $\text{Al}_x\text{Ga}_{1-x}\text{As}$  growth were a Varian 360, a Varian GEN 1.5 and a Varian GEN 2. All three MBE's had 40 cc oven sizes. They were capable of processing a single 2" wafer. An Al concentration uniformity of 6.5% had been measured over a 1" radius for all three machines.<sup>57</sup> Samples 562 and 563 were grown on Nippon Mining 2"

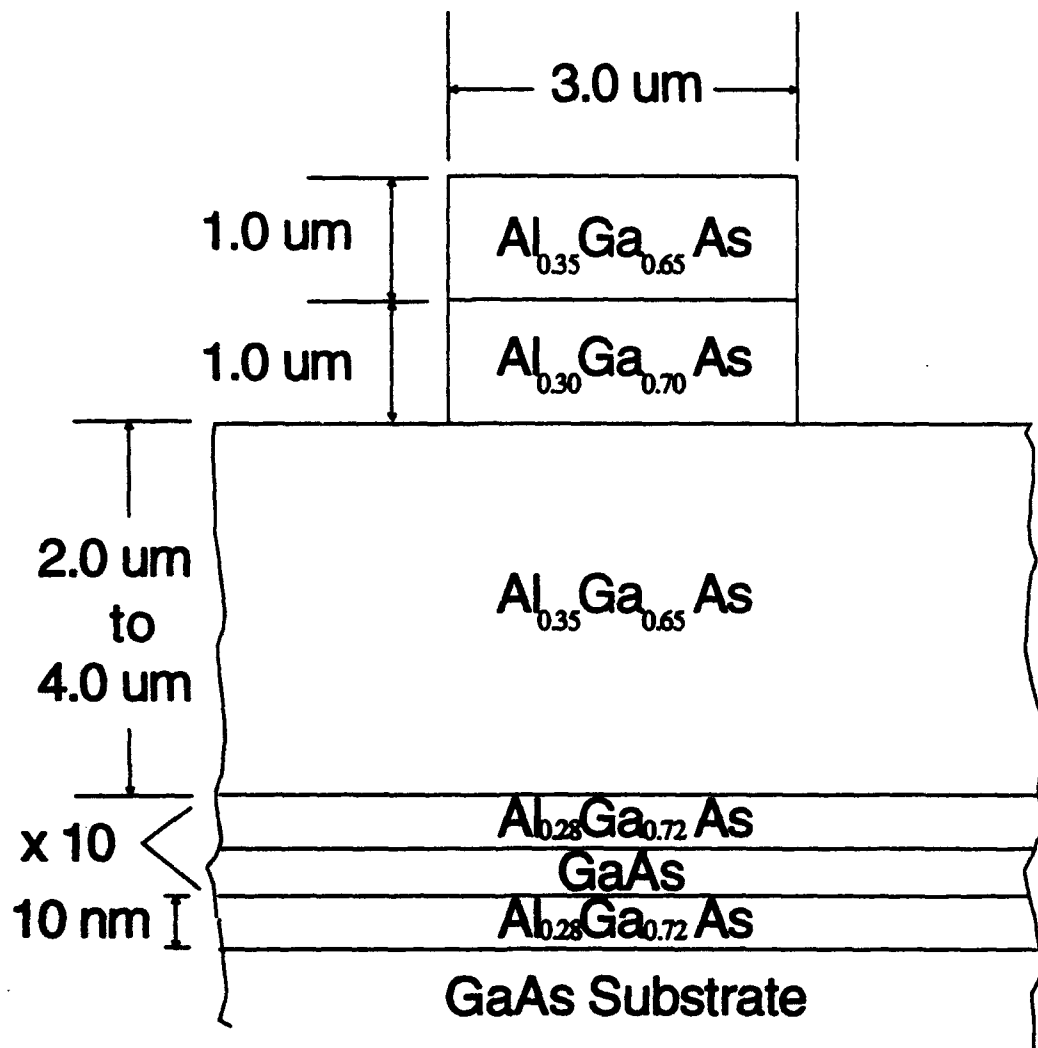


Figure 5.1.3  
Target  $\text{Al}_x\text{Ga}_{1-x}\text{As}$  Structure

GaAs substrates using the GEN 1.5. Samples 571 and 572 were grown on Outokumpu Semitronic 2" GaAs substrates using the GEN 1.5. Sample I79 was grown on a Spectrum Technology 2" GaAs substrate using the Varian 360. Samples 1108 and 1109 were grown on Sumitomo Electric 2" GaAs substrates using the GEN 2. The substrates for samples 562, 563, 571, 572 and I79 were liquid encapsulated (LEC) type semi-insulating with no dopants. The substrates for samples 1108 and 1111 were LEC type semi-insulating doped with indium (In). The substrates for samples 562, 563, 571 and 572 had (100) orientation tilted 6° off toward the nearest <110> direction. The substrates for samples 1108, 1111 and I79 had (100) orientation tilted 2° off toward the nearest <110> direction. The etch pit density of the substrates for samples 1108 and 1111 was  $\leq 1 \times 10^3$  defects/cm<sup>2</sup>. The etch pit density of the substrates for samples 562, 563, 571, 572 and I79 was  $\leq 1 \times 10^5$  defects/cm<sup>2</sup>. The substrates were all polished on both sides. The thickness of all substrates was  $450 \mu\text{m} \pm 10 \mu\text{m}$ . The target thickness for the bottom clad grown was 2  $\mu\text{m}$  for samples 562, 563, 571, 572, 1108 and 1111, and 3  $\mu\text{m}$  for I79. Table 5.1.1 lists the MBE growth parameters. During growth, the substrates were rotated at 15 rpm. The Arsenic source used was cracked As at a pressure of  $6.5 \times 10^{-6}$  Torr. The  $\text{Al}_x\text{Ga}_{1-x}\text{As}$  samples were grown on top of the (100) plane for all substrates.

**Table 5.1.1**  
**Growth Parameters for  $\text{Al}_x\text{Ga}_{1-x}\text{As}$  Structure using**  
**the Varian 360, GEN 1.5 and GEN 2 MBE**

Sample Number	Substrate Temperature (°C)	Growth Rate (monolayers/sec)		
		$\text{Ga}_1$	$\text{Ga}_2$	Al
562	675	0.70	0.56	0.30
563	675	0.70	0.56	0.30
571	630	0.70	0.56	0.30
572	630	0.70	0.60	0.30
1108	617	0.70	0.55	0.30
1111	593	0.70	0.55	0.30
179	630	0.49	0.39	0.21

The MOCVD chamber used for the growth was an Aixtron AIX 200. The AIX 200 was capable of processing a single 3" wafer. An Al concentration uniformity of 0.5% has been measured over a 3" diameter using the AIX 200.<sup>180</sup> Samples 121 and 128 were grown on Mitsubishi Monsanto Kasei 3" GaAs substrates. Both substrates were LEC type semi-insulating with no dopants. The substrates for samples 121 and 128 had (100) orientation. The etch pit density of both the substrates was  $\leq 1 \times 10^5$  defects/cm<sup>2</sup>. The substrates were polished on the (100) plane (front side) only. The backsides were lapped and briefly etched. The thickness of both substrates was 600  $\mu\text{m} \pm 20 \mu\text{m}$ . The  $\text{Al}_x\text{Ga}_{1-x}\text{As}$  samples were grown on top of the (100) plane

for both substrates. In addition to the structure shown in Fig. 5.1.3, a 0.1  $\mu\text{m}$  layer of GaAs was grown between the core and each clad layer of samples 121 and 128 to provide better lattice matching between the various  $\text{Al}_x\text{Ga}_{1-x}\text{As}$  layers.<sup>150</sup> Table 5.1.2 lists the MOCVD growth parameters.

Table 5.1.2  
Growth Parameters for  $\text{Al}_x\text{Ga}_{1-x}\text{As}$  Structure using  
the AIX 200 MOCVD

Sample Number	Substrate Temperature (°C)	Flow Rate (sccm/sec)			
		$\text{Al}_{0.35}$	$\text{Al}_{0.30}$	Ga	$\text{AsH}_3$
121	760	17.80	13.90	8.00	95/75°
128	740	17.80	13.90	8.00	80/60°

°(clad/core)

Photoluminescence (PL) measurements were taken to determine the aluminum concentration present in the core and clad layers of the samples. For samples 562, 563, 571, 572, 1108, 1111 and 179, PL measurements were taken at 3°K. For samples 121 and 128, PL measurements were taken at both 300°K and 3°K. Selected plots of these PL measurements can be seen in Appendix A. At 300°K, the Al concentration (x) can be calculated by equating the band-gap energy  $E_g$ <sup>163</sup> at 300°K and the measured photon energy  $E_{\text{PL}}$  where the peak intensity levels occur on the PL curve:



$$E_{PL} = E_{g(300K)} = 1.424 + 1.247x. \quad 5.1.1$$

At 3°K, x can be calculated by equating  $E_g^{160}$  at 3°K and  $E_{PL}^{160}$

$$E_{PL} = E_{g(3K)} = 1.518 + 1.228x. \quad 5.1.2$$

Table 5.1.3 lists the Al concentrations determined from the PL measurements taken on the various samples using Eqs. 5.1.1 and 5.1.2. From Table 5.1.3, one can see good agreement between the Al concentrations calculated from the PL measurements taken at the two temperatures. The difference between the two measurements is within the known accuracy of other electronic materials characterization techniques.<sup>161</sup> The Al concentrations for samples 121 and 128 appear very close to the target core and clad values. Hence, these samples were chosen as the ones used to fabricate the actual waveguides and devices. The Al concentrations of samples 562, 563, 571, 572, 1108, 1111 and 179 were far from the target and not acceptable for device fabrication. These samples were used to formulate the processing techniques. The multiple peaks measured on samples 562, 563, 571, 572 and 179 (see Table 5.1.3 and Appendix A) were most likely due to antimony (Sb) contamination.<sup>57</sup> Contamination occurred because the MBE growth machines were used by

**Table 5.1.3**  
**Al Concentration Determined from**  
**Photoluminescence Measurements**

PL						
Sample Number	Temperature (°K)	x	x	x	x	x
121	300	0.298	0.351			
121	3	0.277	0.332			
128	300	0.296	0.348			
128	3	0.274	0.327			
562	3	0.361	0.381	0.402	0.413	0.438
563	3	0.324	0.354	0.383	0.404	
571	3	0.356	0.376	0.392	0.437	
572	3	0.360	0.382	0.427		
1108	3	0.225	0.337			
1111	3	0.370				
179	3	0.242	0.260	0.284	0.300	

several researchers growing many different materials.

Using the values for  $x$  derived from the PL measurements, the refractive index of the core and cladding layers of samples 121 and 128 were calculated with the models from Chapter II. Taking into account the  $\pm 2\%$  accuracy of the known Al concentration along with the two different PL measurements produced, the possible waveguide structures are given below:

Waveguide Structure 121-300°K-1

$$(x_{\text{core1}} = 0.298 \pm 0.005, x_{\text{clad1}} = 0.351 \pm 0.005)$$

$$\text{core}_1 = \text{Al}_{0.298}\text{Ga}_{0.702}\text{As} \quad \text{clad}_1 = \text{Al}_{0.351}\text{Ga}_{0.649}\text{As}$$

$$n_{\text{core1}} = 3.420 \pm 0.003 \quad n_{\text{clad1}} = 3.388 \pm 0.003$$

Waveguide Structure 121-300°K-2

$$(x_{\text{core2}} = 0.313 \pm 0.005, x_{\text{clad2}} = 0.366 \pm 0.005)$$

$$\text{core}_2 = \text{Al}_{0.313}\text{Ga}_{0.687}\text{As} \quad \text{clad}_2 = \text{Al}_{0.366}\text{Ga}_{0.634}\text{As}$$

$$n_{\text{core2}} = 3.404 \pm 0.003 \quad n_{\text{clad2}} = 3.374 \pm 0.003$$

Waveguide Structure 121-300°K-3

$$(x_{\text{core3}} = 0.283 \pm 0.005, x_{\text{clad3}} = 0.336 \pm 0.005)$$

$$\text{core}_3 = \text{Al}_{0.283}\text{Ga}_{0.717}\text{As} \quad \text{clad}_3 = \text{Al}_{0.336}\text{Ga}_{0.664}\text{As}$$

$$n_{\text{core3}} = 3.439 \pm 0.004 \quad n_{\text{clad3}} = 3.403 \pm 0.003$$

Waveguide Structure 121-3°K-1

$$(x_{\text{core1}} = 0.277 \pm 0.005, x_{\text{clad1}} = 0.332 \pm 0.005)$$

$$\text{core}_1 = \text{Al}_{0.277}\text{Ga}_{0.723}\text{As} \quad \text{clad}_1 = \text{Al}_{0.332}\text{Ga}_{0.668}\text{As}$$

$$n_{\text{core1}} = 3.433 \pm 0.003 \quad n_{\text{clad1}} = 3.399 \pm 0.003$$

Waveguide Structure 121-3°K-2

$$(x_{\text{core2}} = 0.292 \pm 0.005, x_{\text{clad2}} = 0.347 \pm 0.005)$$

$$\text{core}_2 = \text{Al}_{0.292}\text{Ga}_{0.708}\text{As} \quad \text{clad}_2 = \text{Al}_{0.347}\text{Ga}_{0.653}\text{As}$$

$$n_{\text{core2}} = 3.414 \pm 0.003 \quad n_{\text{clad2}} = 3.385 \pm 0.003$$

Waveguide Structure 121-3°K-3

$$(x_{\text{core3}} = 0.262 \pm 0.005, x_{\text{clad3}} = 0.317 \pm 0.005)$$

$$\text{core}_3 = \text{Al}_{0.262}\text{Ga}_{0.738}\text{As} \quad \text{clad}_3 = \text{Al}_{0.317}\text{Ga}_{0.683}\text{As}$$

$$n_{\text{core3}} = 3.454 \pm 0.004 \quad n_{\text{clad3}} = 3.416 \pm 0.003$$

Waveguide Structure 128-300°K-1

$$(x_{\text{core1}} = 0.296 \pm 0.005, x_{\text{clad1}} = 0.348 \pm 0.005)$$

$$\text{core}_1 = \text{Al}_{0.296}\text{Ga}_{0.704}\text{As} \quad \text{clad}_1 = \text{Al}_{0.348}\text{Ga}_{0.652}\text{As}$$

$$n_{\text{core1}} = 3.421 \pm 0.003 \quad n_{\text{clad1}} = 3.390 \pm 0.003$$

Waveguide Structure 128-300°K-2

$$(x_{\text{core2}} = 0.311 \pm 0.005, x_{\text{clad2}} = 0.363 \pm 0.005)$$

$$\text{core}_2 = \text{Al}_{0.311}\text{Ga}_{0.689}\text{As} \quad \text{clad}_2 = \text{Al}_{0.363}\text{Ga}_{0.637}\text{As}$$

$$n_{\text{core2}} = 3.405 \pm 0.003 \quad n_{\text{clad2}} = 3.376 \pm 0.003$$

Waveguide Structure 128-300°K-3

$$(x_{\text{core3}} = 0.281 \pm 0.005, x_{\text{clad3}} = 0.333 \pm 0.005)$$

$$\text{core}_3 = \text{Al}_{0.281}\text{Ga}_{0.719}\text{As} \quad \text{clad}_3 = \text{Al}_{0.333}\text{Ga}_{0.667}\text{As}$$

$$n_{\text{core3}} = 3.441 \pm 0.004 \quad n_{\text{clad3}} = 3.405 \pm 0.003$$

Waveguide Structure 128-3°K-1

$$(x_{\text{core1}} = 0.274 \pm 0.005, x_{\text{clad1}} = 0.327 \pm 0.005)$$

$$\text{core}_1 = \text{Al}_{0.274}\text{Ga}_{0.726}\text{As} \quad \text{clad}_1 = \text{Al}_{0.327}\text{Ga}_{0.673}\text{As}$$

$$n_{\text{core1}} = 3.434 \pm 0.003 \quad n_{\text{clad1}} = 3.402 \pm 0.003$$

Waveguide Structure 128-3°K-2

$$(x_{\text{core2}} = 0.289 \pm 0.005, x_{\text{clad2}} = 0.342 \pm 0.005)$$

$$\text{core}_2 = \text{Al}_{0.289}\text{Ga}_{0.711}\text{As} \quad \text{clad}_2 = \text{Al}_{0.342}\text{Ga}_{0.658}\text{As}$$

$$n_{\text{core2}} = 3.416 \pm 0.003 \quad n_{\text{clad2}} = 3.388 \pm 0.003$$

Waveguide Structure 128-3°K-3

$$(x_{\text{core3}} = 0.259 \pm 0.005, x_{\text{clad3}} = 0.312 \pm 0.005)$$

$$\text{core}_3 = \text{Al}_{0.259}\text{Ga}_{0.741}\text{As} \quad \text{clad}_3 = \text{Al}_{0.312}\text{Ga}_{0.688}\text{As}$$

$$n_{\text{core3}} = 3.456 \pm 0.004 \quad n_{\text{clad3}} = 3.419 \pm 0.003$$

The measured thickness of the core and cladding layers of samples 121 and 128 are given in Table 5.1.4. They were inferred during MOCVD growth based on the growth rates.<sup>159</sup>

Table 5.1.4  
Core and Clad Thickness for  $\text{Al}_x\text{Ga}_{1-x}\text{As}$   
Samples 121 and 128

Sample Number	core ( $\mu\text{m}$ )	Top Clad ( $\mu\text{m}$ )	Bottom Clad ( $\mu\text{m}$ )
121	$0.90 \pm 0.04$	$0.95 \pm 0.04$	$3.95 \pm 0.04$
128	$0.90 \pm 0.04$	$0.95 \pm 0.04$	$3.95 \pm 0.04$

#### Determination of $r_{41}$

The EO coefficient  $r_{41}$  is generally defined as the unclamped or constant stress EO coefficient ( $r_{41}^T$ ).<sup>123</sup>  $r_{41}^T$  is a value that can and has been measured. It is referred to as the unclamped coefficient because it is often measured at low frequencies in comparison to acoustic resonator frequencies.  $r_{41}^T$  is broken down into two parts: a constant strain or clamped value ( $r_{41}^S$ ) and a piezoelectric induced value ( $r_{41}^P$ ).<sup>122,124,134,137</sup>

$$r_{41}^T = r_{41}^S + r_{41}^P.$$

5.2.1

$r_{41}^T$ ,  $r_{41}^S$  and  $r_{41}^P$  are given in  $10^{-12}$  m/V. In particular,  $r_{41}^T$  for GaAs has been measured at several different wavelengths.<sup>116,120,125,129,130,132,137</sup>

The linear photoelastic constant ( $\alpha_{44}$ ), given in  $10^{-11}$  cm<sup>2</sup>/dyne, is a measure of the internal stress due to epitaxial growth. It has been recorded for GaAs at several wavelengths.<sup>125,129,146</sup> This provides the data necessary to model  $r_{41}^T$ ,  $r_{41}^S$  and  $r_{41}^P$  for GaAs as a function of wavelength.<sup>48,49,121,123,125,129,136,137,146</sup>  $\alpha_{44}$  has also been measured for  $\text{Al}_{0.48}\text{Ga}_{0.52}\text{As}$ .<sup>101</sup> This allows  $r_{41}^P$  to be modelled for  $\text{Al}_x\text{Ga}_{1-x}\text{As}$  as a function of both wavelength and Al concentration.<sup>48,49,137</sup> Since  $r_{41}^T$  has been measured for  $\text{Al}_{0.17}\text{Ga}_{0.83}\text{As}$ ,<sup>146</sup> this allows us to model  $r_{41}^S$  for  $\text{Al}_x\text{Ga}_{1-x}\text{As}$  as a function of both  $\lambda$  and  $x$  and, hence, determine  $r_{41}^T$  for  $\text{Al}_x\text{Ga}_{1-x}\text{As}$  as a function of both  $\lambda$  and  $x$ .

We will start with a model for  $r_{41}^P$  for GaAs presented by Higginbotham, Cardona and Pollak<sup>148</sup> and Adachi.<sup>48,49,123,137</sup> The photoelastic effect can be expressed as<sup>48,49,137</sup>

$$\alpha_i = \Delta \epsilon_i / X = -\sum_{mn} \epsilon_i \epsilon_j \rho_{ij} S_{ikmn} \quad 5.2.2$$

where  $X$  is the stress in  $10^{11}$  dyne/cm<sup>2</sup>,  $\epsilon_i = \epsilon_j$  is the component of the dielectric constant in the absence of stress (see Chapter II),  $\rho_{ij}$  is the component of the fourth-rank photoelastic tensor (constants) and  $S_{ikmn}$  is the

component of the elastic compliance tensor in  $10^{-12}$  cm<sup>2</sup>/dyne.  $\Delta\epsilon_i$  is the change in the real part of the dielectric constants parallel and perpendicular to the stress given by<sup>137</sup>

$$\Delta\epsilon_i = \epsilon_{111} - \epsilon_{11}.$$

5.2.3

The linear photoelastic tensor in a cubic  $\bar{4}3m$  class crystal can be written as<sup>100</sup>

$$[p] = \begin{bmatrix} p_{11} & p_{12} & p_{12} & 0 & 0 & 0 \\ p_{12} & p_{11} & p_{12} & 0 & 0 & 0 \\ p_{12} & p_{12} & p_{11} & 0 & 0 & 0 \\ 0 & 0 & 0 & p_{44} & 0 & 0 \\ 0 & 0 & 0 & 0 & p_{44} & 0 \\ 0 & 0 & 0 & 0 & 0 & p_{44} \end{bmatrix}. \quad 5.2.4$$

Similarly, the elastic compliance tensor in a cubic  $\bar{4}3m$  class crystal can be written as<sup>100</sup>



$$[S] = \begin{bmatrix} S_{11} & S_{12} & S_{12} & 0 & 0 & 0 \\ S_{12} & S_{11} & S_{12} & 0 & 0 & 0 \\ S_{12} & S_{12} & S_{11} & 0 & 0 & 0 \\ 0 & 0 & 0 & S_{44} & 0 & 0 \\ 0 & 0 & 0 & 0 & S_{44} & 0 \\ 0 & 0 & 0 & 0 & 0 & S_{44} \end{bmatrix} \quad 5.2.5$$

From Eqs. 4.3.18, 5.2.4 and 5.2.5, one can see that  $p_{44}$  and  $S_{44}$  are the only components that will contribute to the EO coefficients ( $r_{41}^S$  and  $r_{41}^T$ ). We can write<sup>134</sup>

$$r_{41}^P = p_{44} S_{44} e_{14}, \quad 5.2.6$$

where  $e_{14} = S_{44} X_{14}$  is the strain component connected with the stress.<sup>137</sup>  $p_{44}$  can also be defined using the inverse dielectric constant<sup>137</sup>

$$\Delta(1/\epsilon_1(\omega))_i = -\Delta\epsilon_i/(\epsilon_i\epsilon_j) = \sum_k p_{ijk} e_{jk}, \quad 5.2.7$$

where  $\epsilon_1(\omega)$  is the real part of the dielectric constant given by Eq. 2.2.3.

Substitution of Eqs. 5.2.4 - 5.2.7 into Eq. 5.2.2 leads to<sup>137</sup>

$$\alpha_{44}(\omega) = -\epsilon_1(\omega)^2 \rho_{44} S_{44}. \quad 5.2.8$$

The first-order change in  $\epsilon_1(\omega)$  due to applied stress is given by<sup>137</sup>

$$\Delta \epsilon_1(\omega) = \sum_i [(\partial \epsilon_1 / \partial M_i) \Delta M_i + (\partial \epsilon_1 / \partial E_{gi}) \Delta E_{gi}], \quad 5.2.9$$

where  $E_{gi}$  is the interband transition or gap energy of the  $i$ th transition (i.e.,  $E_0$ ,  $E_0 + \Delta_0$ ,  $E_1$ , etc.) and  $M_i$  is a strength parameter used to fit the measured data. Substituting Eq. 2.2.3 into Eq. 5.2.9, Adachi obtained the expression for the photoelastic coefficient:<sup>49</sup>

$$\alpha_{44}(\omega) = C_0 \{ -g(\chi) + (4E_g/\Delta_0) [f(\chi) - (E_g/(E_0 + \Delta_0))^{3/2} \cdot f(\chi_{\infty})] \} + D_0, \quad 5.2.10$$

where

$$g(\chi) = (\chi)^{-2} [2 - (1 + \chi)^{-1/2} - (1 - \chi)^{-1/2}]. \quad 5.2.11$$

$E_0$ ,  $E_0 + \Delta_0$ ,  $f(\chi)$  and  $f(\chi_{\infty})$  are determined using Eqs. 2.2.4 - 2.2.10.  $C_0$  and  $D_0$  are strength parameters found by fitting Eq. 5.2.10 to the elasto-optic measurements recorded by Higginbotham et al. for GaAs.<sup>147</sup> With the measurements taken by van der Ziel et al.<sup>101</sup> for  $\text{Al}_{0.48}\text{Ga}_{0.52}\text{As}$ , we have been

able to determine  $C_0$  and  $D_0$  as a function of Al concentration ( $x$ ).<sup>101</sup> Doing that yields

$$C_0 = -0.21 + 0.19x \quad 5.2.12$$

and

$$D_0 = 2.03 - 1.95x, \quad 5.2.13$$

where  $C_0$  and  $D_0$  are in  $10^{-11}$  cm<sup>2</sup>/dyne. With  $S_{44}$  given by<sup>48</sup>

$$S_{44} = (1.68 + 0.02x) \times 10^{-12} \text{ cm}^2/\text{dyne} \quad 5.2.14$$

and  $e_{14}$  given by<sup>48</sup>

$$e_{14} = -(0.160 - 0.065x) \text{ C/m}^2, \quad 5.2.15$$

we can calculate  $r_{41}^P$  as a function of both wavelength and Al concentration. Figs. 5.2.1 and 5.2.2 show plots of  $r_{41}^P$  versus  $x$  (at  $\lambda = 827$  nm) and  $\lambda$  (for  $x = 0.300$ ), respectively.

Using Eq. 4.3.5 and the definition for the refractive index, the linear EO effect can be defined by

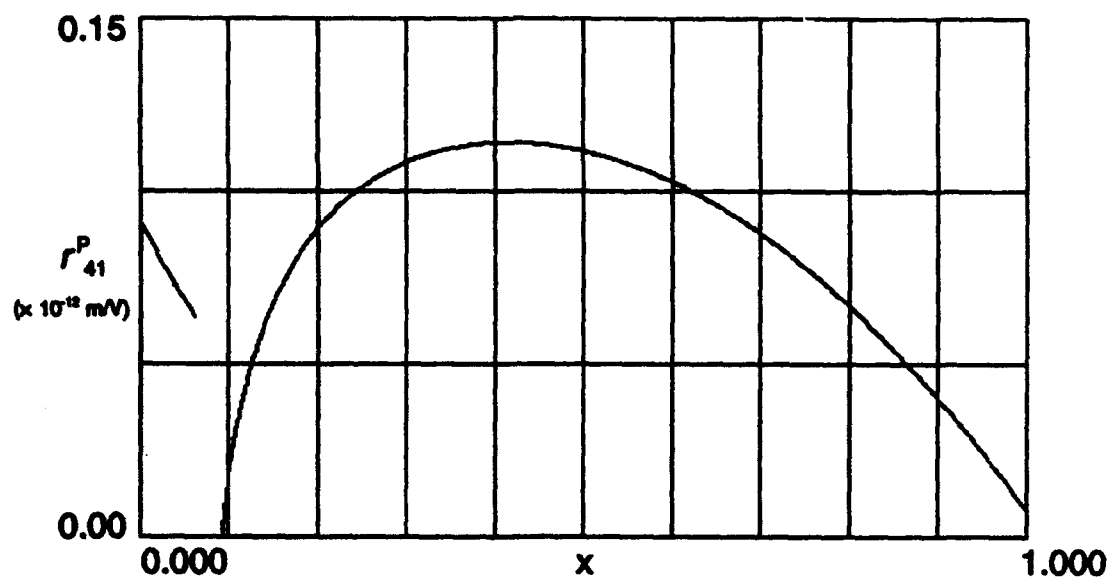


Figure 5.2.1  
Piezoelectric Coefficient for  $\text{Al}_x\text{Ga}_{1-x}\text{As}$  versus  
Al Concentration at  $\lambda = 827$  nm

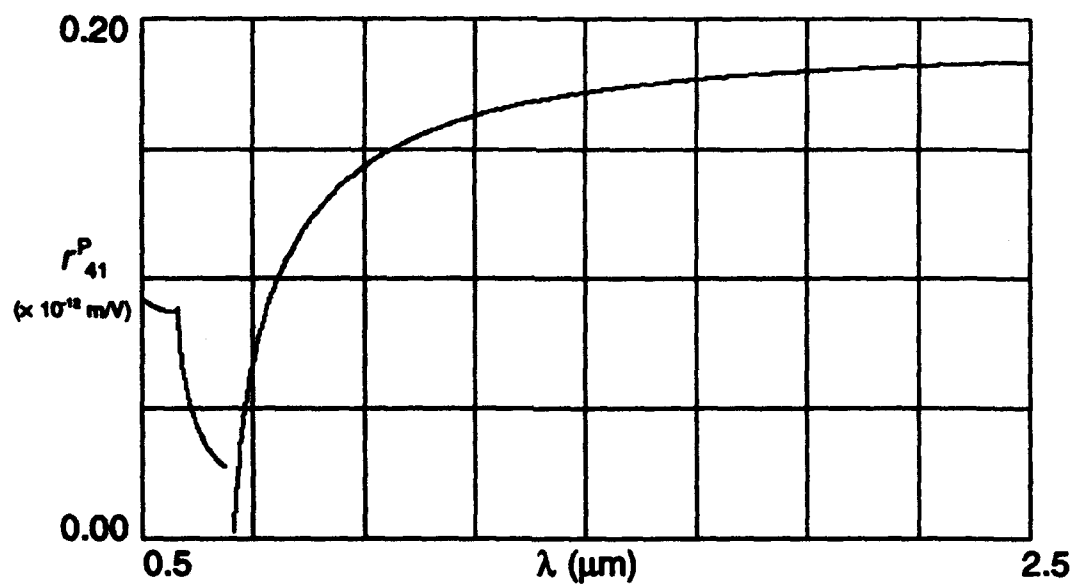


Figure 5.2.2  
Piezoelectric Coefficient for  $\text{Al}_x\text{Ga}_{1-x}\text{As}$   
versus Wavelength for  $x = 0.300$

$$\Delta(1/\epsilon)_I = r_{\#}^S E_K \quad 5.2.16$$

Substituting Eq. 5.2.7 into Eq. 5.2.16 yields<sup>137</sup>

$$r_{41}^S = \Delta(1/\epsilon_1)/E = -\Delta\epsilon_1(1/\epsilon_1^2). \quad 5.2.17$$

It should be noted that  $\Delta\epsilon_1$  in Eq. 5.2.17, used to calculate  $r_{41}^S$ , is not the same one used to calculate  $r_{41}^P$ .  $\Delta\epsilon_1$ , used to calculate  $r_{41}^S$ , defined hereafter as  $\epsilon_1^S$ , can be obtained by taking into account the changes in the lowest direct gap energies:<sup>123,137</sup>

$$\begin{aligned} \Delta\epsilon_1^S = & (\partial\epsilon_1/\partial E_0)\Delta E_0 + (\partial\epsilon_1/\partial A_0)\Delta A_0 + (\partial^2\epsilon_1/\partial E_0^2)(\Delta E_0)^2 \\ & + (\partial^2\epsilon_1/\partial A_0^2)(\Delta A_0)^2 + [\partial^2\epsilon_1/(\partial E_0\partial A_0)](\Delta E_0\Delta A_0) + \dots; \end{aligned} \quad 5.2.18$$

where  $E_0$  is given by Eq. 2.2.9,  $A_0$  is given by Eq. 2.2.11 and  $\Delta E_0$  and  $\Delta A_0$  are the electric field induced changes in  $E_0$  and  $A_0$ , respectively. Considering only the linear EO effects allows us to neglect the higher order terms. Eq. 5.2.18 can be reduced to<sup>123,137</sup>

$$\epsilon_1^S = (\partial\epsilon_1/\partial E_0) E_0 + (\partial\epsilon_1/\partial A_0) A_0. \quad 5.2.19$$

Adachi conveyed that the changes in the band parameters can be written in terms of the first-order Stark-like effect as<sup>123,137</sup>

$$\Delta E_o = a_1 E \quad 5.2.20$$

and

$$\Delta A_o = b_1 E, \quad 5.2.21$$

where  $a_1$  and  $b_1$  are strength parameters. Substituting Eqs. 5.2.20 and 5.2.21 into Eq. 5.2.19 yields<sup>123,137</sup>

$$\Delta \epsilon_1^s(\omega)_{E_o} = (\partial \epsilon_1 / \partial E_o) \Delta E_o = (a_1/2) [A_o/E_o] E g(\chi) \quad 5.2.22$$

and

$$\Delta \epsilon_1^s(\omega)_{A_o} = (\partial \epsilon_1 / \partial A_o) \Delta A_o = b_1 E f(\chi), \quad 5.2.23$$

where  $g(\chi)$  and  $f(\chi)$  are defined by Eqs. 5.2.11 and 2.2.4, respectively.

Substituting Eqs. 5.2.22 and 5.2.23 into Eq. 5.2.17 gives<sup>123,137</sup>

$$r_{41}^s(\omega) = -[1/(\epsilon_1(\omega))^2] [(a_1/2) [A_o/E_o] g(\chi) + b_1 f(\chi) + F_o], \quad 5.2.24$$

where  $F_o$  is a strength parameter that accounts for the nondispersive, higher gap energies. Adachi pointed out<sup>137</sup> that  $g(\chi)$  shows a very sharp dispersion

near  $E_0$  compared with  $f(\chi)$ . Therefore,  $\Delta \epsilon_1^s(\omega)_{A_0}$  can be included in the contribution of the higher gap energies. Doing this yields<sup>137</sup>

$$r_{41}^s(\omega) = -[1/(\epsilon_1(\omega))^2]E_0^*g(\chi) + F_0^*], \quad 5.2.25$$

with

$$E_0^* = (a_1/2)[A_0/E_0]. \quad 5.2.26$$

The parameters  $E_0^*$  and  $F_0^*$  were adjusted to fit the experimental data.  $r_{41}^T$  for GaAs, measured by Faist and Reinhart,<sup>116</sup> and  $r_{41}^T$  for  $Al_{0.17}Ga_{0.83}As$ , measured by Glick, Reinhart and Martin,<sup>145</sup> were the coefficients chosen to fit Eq. 5.2.25.  $r_{41}^T$  measured by Faist et al. was used (instead of those measured by Sugie and Tada<sup>129</sup> and Suzuki and Tada<sup>125</sup>) primarily because the Sugie et al. and Suzuki et al. measurements were taken on heavily Cr-doped GaAs crystals. The Faist et al. measurements were taken on undoped GaAs grown on a Si-doped GaAs substrate. The  $Al_{0.17}Ga_{0.83}As$  layer investigated by Glick et al. was also grown on a Si-doped GaAs substrate. In addition, one of the researchers who measured  $r_{41}^T$  for GaAs also measured  $r_{41}^T$  for  $Al_{0.17}Ga_{0.83}As$ . We are looking for comparisons between the EO coefficient for GaAs and  $Al_xGa_{1-x}As$ . It is believed that more consistent results could be achieved using measurements taken on both GaAs and  $Al_xGa_{1-x}As$  by the same researcher, using substrates doped with



the same material. Substituting the measured data,  $r_{41}^T = -1.68 \times 10^{-12}$  m/V at  $\lambda = 1.15 \mu\text{m}$  for  $x = 0.00$ ,  $r_{41}^T = -1.72 \times 10^{-12}$  m/V at  $\lambda = 1.09 \mu\text{m}$  for  $x = 0.00$  and  $r_{41}^T = -1.43 \times 10^{-12}$  m/V at  $\lambda = 1.1523 \mu\text{m}$  for  $x = 0.17$ , into Eqs. 5.2.1 and 5.2.25, the strength parameters were found to be

$$E_o^* = -1.375[A_o/E_o] \quad 5.2.27$$

and

$$F_o^* = 18.15 - 38.5x, \quad 5.2.28$$

with  $E_o^*$  and  $F_o^*$  in  $10^{-12}$  m/V.

The model presented above is valid only for those energies below the direct band edge. Therefore, we will limit the Al concentration for this model to include only those values that ensure that we are below the band edge. For this experiment, where  $\lambda = 827$  nm,  $x$  must be greater than 0.10 in order to use this model. Fig. 5.2.3 plots  $r_{41}^S$  and  $r_{41}^T$  versus  $x$  at  $\lambda = 827$  nm. Fig. 5.2.4 plots  $r_{41}^S$  and  $r_{41}^T$  versus  $\lambda$  for  $x = 0.300$ . The PL measured  $x$  values for the core layers of Samples 121 and 128 were substituted into the model to determine the linear EO coefficient to be used for this experiment. The  $r_{41}^T$  values at  $\lambda = 827$  nm using these four Al concentrations are given in Table 5.2.1. Also included in the table is the estimated  $\pm 5\%$  accuracy for the measured EO coefficients.<sup>118,145</sup> Table 5.2.1 provides the values of the

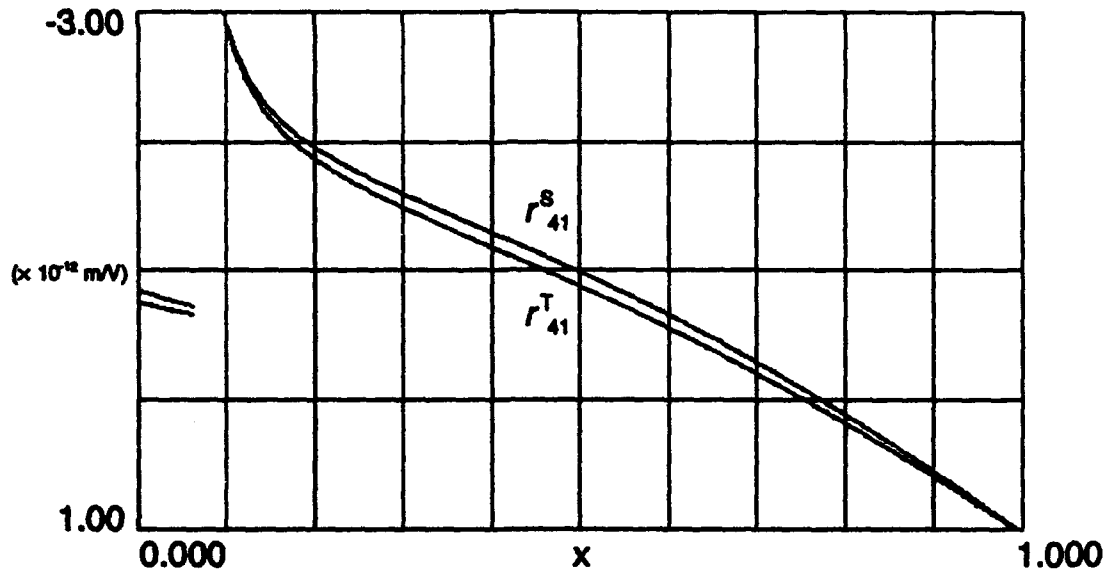


Figure 5.2.3  
Linear Electro-Optic Coefficients for  $\text{Al}_x\text{Ga}_{1-x}\text{As}$   
versus Al Concentration at  $\lambda = 827$  nm

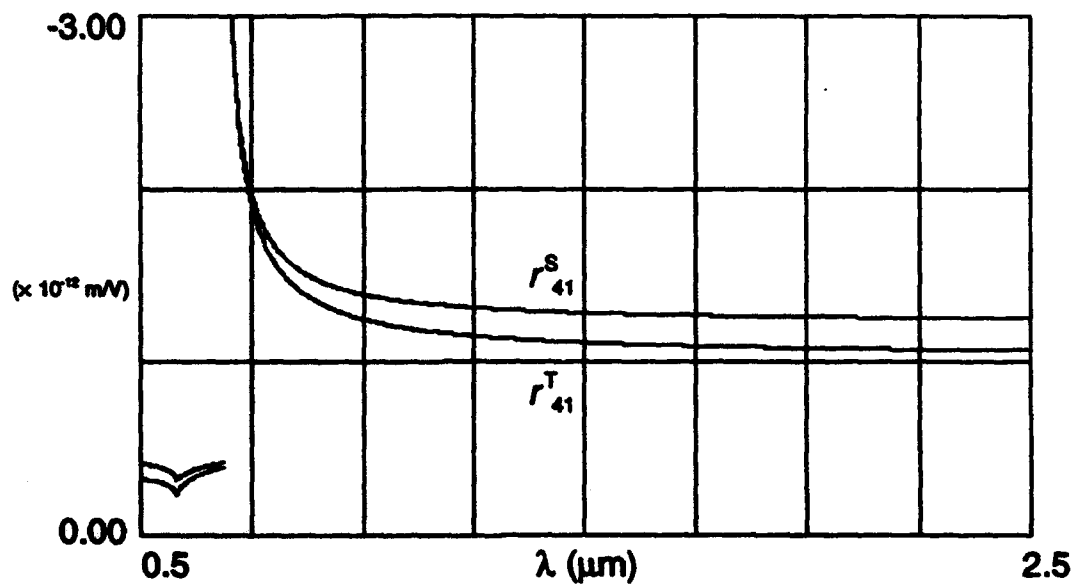


Figure 5.2.4  
Linear Electro-Optic Coefficients for  $\text{Al}_x\text{Ga}_{1-x}\text{As}$   
versus Wavelength for  $x = 0.300$

Table 5.2.1  
Linear Electro-Optic Coefficients for  $\text{Al}_x\text{Ga}_{1-x}\text{As}$   
Samples 121 and 128 at  $\lambda = 827 \text{ nm}$

Sample Number	PL Temperature ( $^{\circ}\text{K}$ )	x	$r_{41}^T$ ( $\times 10^{-12} \text{ m/V}$ )
121	300	298	$-1.49 \pm 0.08$
121	3	277	$-1.56 \pm 0.08$
128	300	296	$-1.50 \pm 0.08$
128	3	274	$-1.57 \pm 0.08$

linear EO coefficient that can be used in Eqs. 4.5.4 and 4.5.5 to calculate the phase change.

### $\text{Al}_x\text{Ga}_{1-x}\text{As}$ Device Fabrication and Characterization

This section details the techniques used to fabricate the  $\text{Al}_x\text{Ga}_{1-x}\text{As}$  waveguides and directional couplers for this experiment as well as the testing methods used to characterize the devices.

#### Straight and Crossthrough Waveguides

Integrated  $\text{Al}_x\text{Ga}_{1-x}\text{As}$  optical waveguides and crossthroughs were fabricated in sample 121 using processes compatible to those for electronics. The mask used to pattern the waveguide devices was a clear field type designed using an Omni-Dex Design Workshop 2000 graphics

programming environment CAD system. A chrome-on-glass mask was generated from this layout using a Jeol JBX-5DII electron beam fine lithography system. This type mask was used to pattern the waveguides and devices in positive photoresist deposited on top of the wafer using a Karl Suss MJB-3 mask aligner and 505 optical energy controller. The waveguides were then formed by etching the material not protected with photoresist using a Plasma-Therm Series 700 reactive ion etch (RIE) machine. RIE is a dry etch technique that uses directional ion bombardment of the material to be etched.<sup>160</sup> The reactive species generated from a plasma are used to etch the material.<sup>160</sup> RIE is anisotropic (i.e., the vertical etch rate is much faster than the lateral rate).<sup>160</sup> This leads to very straight vertical sidewalls. The step-by-step procedures for the waveguide fabrication are outlined in Appendix B.

The target width of the straight and crossthrough waveguides was 3  $\mu\text{m}$ , and the target etch depth was 2  $\mu\text{m}$  (see Fig. 5.1.3). The actual parameters realized after fabrication were measured using a Cambridge Stereoscan 250 Mk2 scanning electron microscope (SEM), a Jeol JSM-IC845A SEM and a Tencor Alpha-Step 250 surface profiler. The actual width of the waveguides measured 2.7  $\mu\text{m}$  - 2.8  $\mu\text{m}$  (see Fig 5.3.1). The actual etch depth measured 1.9  $\mu\text{m}$  - 2.1  $\mu\text{m}$ . Fig. 5.3.2 illustrates the sidewall morphology that was achieved using RIE. The waveguides were characterized using a Cohu

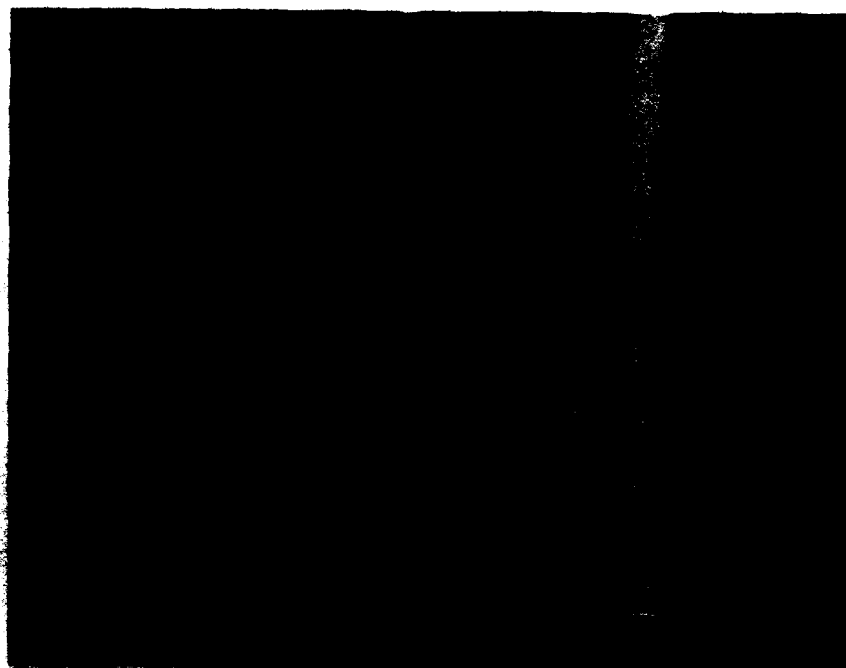


**Figure 5.3.1**  
**SEM Aerial View of an  $\text{Al}_x\text{Ga}_{1-x}\text{As}$  Straight Waveguide**

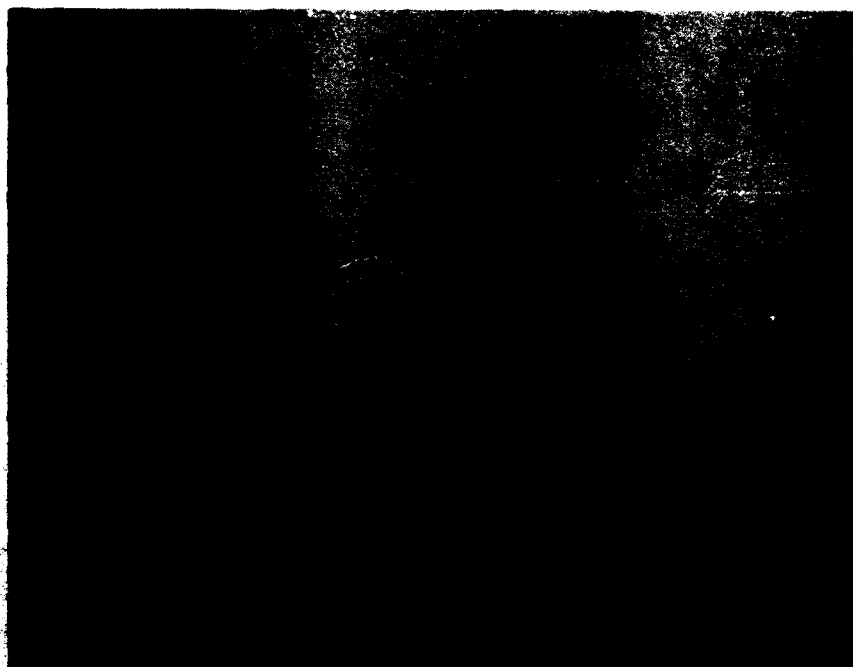


**Figure 5.3.2**  
**Sidewall Morphology of an  $\text{Al}_x\text{Ga}_{1-x}\text{As}$  Waveguide using RIE**

6315 CCD video camera and a Data Translation DT3852 frame processor. The 827 nm Sharp LT015MDO laser diode was collimated using a 14.5 mm focal length (FL) lens and passed through a 3X anamorphic prism pair to transform the elliptical beam to circular. It was focused into the waveguide with an 8.0 mm FL lens. This produced a  $1\text{ }\mu\text{m}$  spot size at the waveguide input. The numerical aperture (NA) of the 8.0 mm FL lens was 0.50, giving a possible coupling efficiency of 84%.<sup>106</sup> The beam was viewed with the CCD camera from above as it propagated through the waveguide. The image was captured using a frame processor. Fig. 5.3.3 is a photograph of the waveguide characterization system. A captured image of the laser propagating through a straight waveguide using this system can be seen in Fig. 5.3.4. Images of the propagating signal were captured at the input, center and output of the waveguide. The average pixel intensities of these images were then analyzed with Data Translation GLOBAL LAB image processing software. Since the coordinates of each image were known, the pixel intensities could be translated into propagation loss.<sup>106</sup> This frame processor system was capable of detecting 256 shades of gray. The field of view of the CCD camera was  $700\text{ }\mu\text{m}$ . Therefore, losses as small as 0.2 dB/cm could be detected. Using this method, the typical propagation loss of the straight waveguides measured between 0.5 dB/cm and 1.0 dB/cm. The coupling efficiency for end fire coupling of the laser into the waveguides



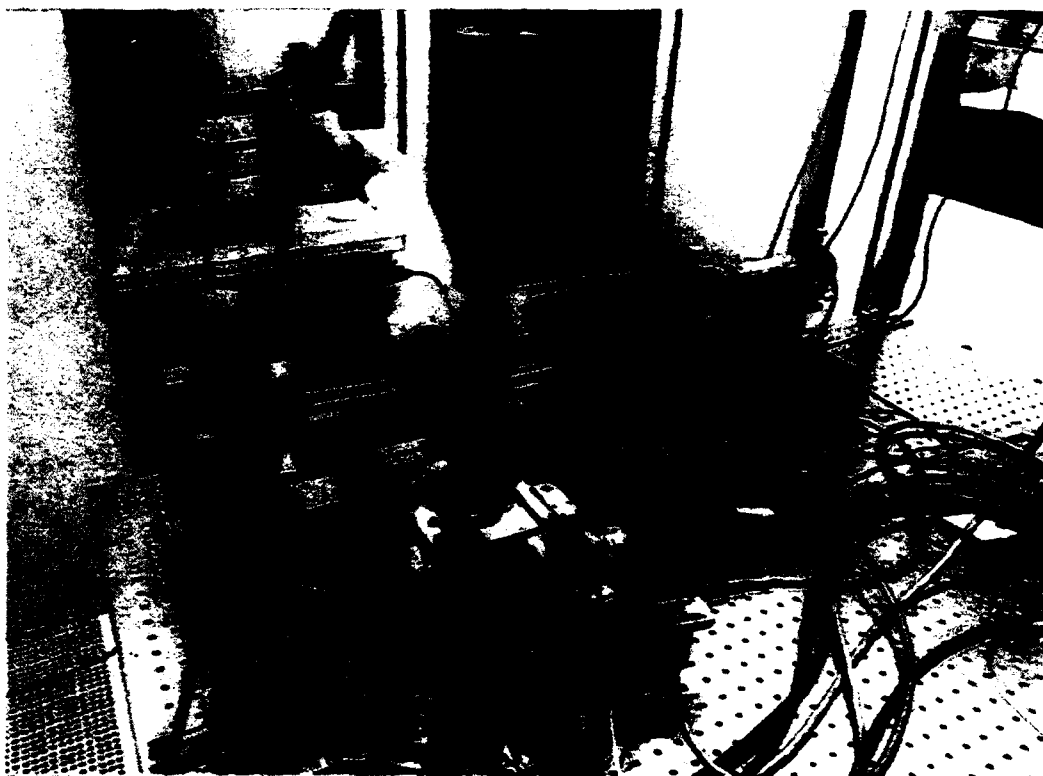


**Figure 5.3.3**  
**Waveguide Characterization System**

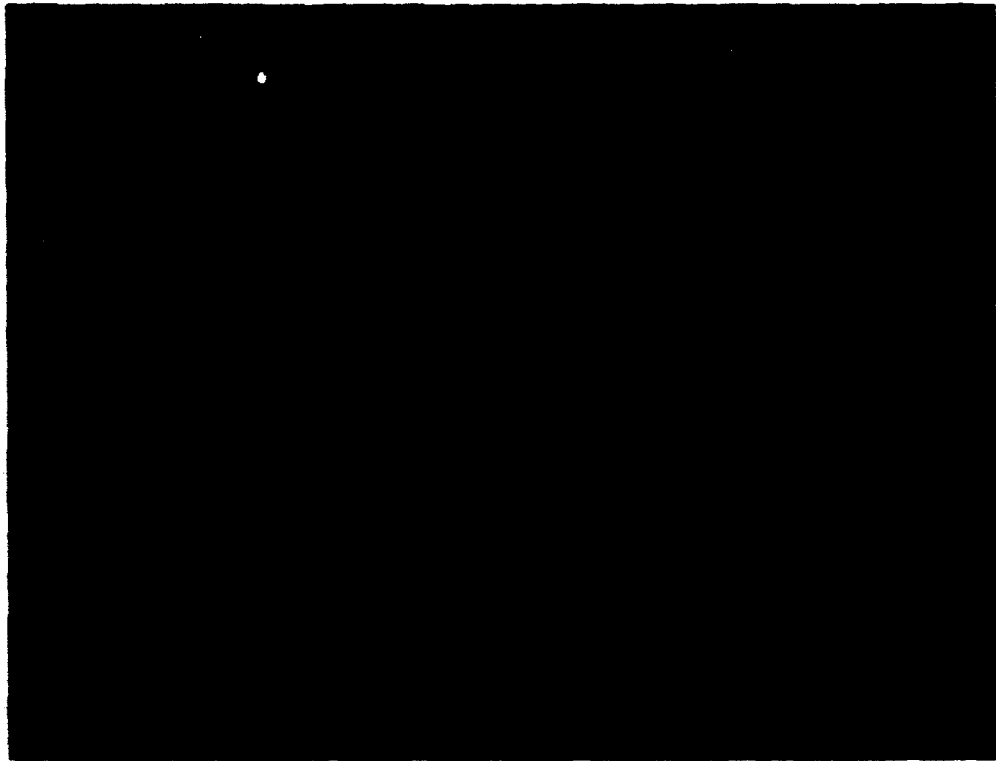


**Figure 5.3.4**  
**CCD Image of Laser Beam Propagating through**  
**an  $\text{Al}_x\text{Ga}_{1-x}\text{As}$  Straight Waveguide**

was also measured. It was found that a 75% coupling efficiency could be attained with careful alignment.

Waveguide crossthroughs were tested using the methods described above. Fig. 5.3.5 is an aerial photomicrograph of a crossthrough taken using a Carl Zeiss Axioplan MC80 microscope. Fig. 5.3.6 is a captured CCD image of a crossthrough with the laser beam propagating in one of the waveguides. The second waveguide was normal to the first. Comparing light intensities in both waveguides, no crossover from the first waveguide to the second was observed. With the limitation of gray scale, an exact measure of the crossover could not be performed using the DT3852 frame processor. The minimum signal that could be detected was -24 dB. Since no intensity in the perpendicular waveguide was detected, the maximum crossover for these crossthrough structures was  $\geq -24$  dB.

### Passive Zero-Gap Directional Couplers

Passive (minus switching electrodes)  $\text{Al}_x\text{Ga}_{1-x}\text{As}$  zero-gap directional couplers (ZGDC's) were fabricated in sample 121 using the same techniques presented in the preceding section and Appendix B. The target width of the input and output guides was  $3\text{ }\mu\text{m}$ , while the target width of the interaction section was  $6\text{ }\mu\text{m}$ . To experimentally determine the interaction length for complete coupling of the ZGDC's, several structures were fabricated with



**Figure 5.3.5**  
**Photomicrographic Aerial View of an**  
 **$\text{Al}_x\text{Ga}_{1-x}\text{As}$  Crosshatch**



**Figure 5.3.6**  
**CCD Image of Laser Beam Propagating through**  
**an  $\text{Al}_x\text{Ga}_{1-x}\text{As}$  Crossthrough Waveguide**

various interaction channel lengths. The interaction channel lengths ranged from 100  $\mu\text{m}$  - 1000  $\mu\text{m}$  in increments of 100  $\mu\text{m}$ . Fig. 5.4.1 is a schematic of the section of the mask for a passive ZGDC with a 200  $\mu\text{m}$  interaction channel length. As can be seen by the dimensions, a wavefront tilt angle of  $\alpha = 0.91^\circ$  was chosen (see Eq. 1.6.1). Fig. 5.4.2 is a photomicrograph of fabricated passive ZGDC's with 200  $\mu\text{m}$  interaction channel lengths taken with the Zeiss Axioplan. The actual width of the input and output channels of the devices measured 2.7  $\mu\text{m}$  - 2.8  $\mu\text{m}$  (see Fig. 5.4.3). The actual width of the interaction channel measured 5.5  $\mu\text{m}$  - 5.6  $\mu\text{m}$  (see Fig. 5.4.4). The etch depth measured 1.9  $\mu\text{m}$  - 2.1  $\mu\text{m}$ . The processing equipment used for this experiment could not resolve separations less than 0.5  $\mu\text{m}$ . The two input channels joined together below 0.5  $\mu\text{m}$  of separation. The same was true for the two output channels. The channels did not converge to a point. This added 60  $\mu\text{m}$  to the length of the interaction channel. To account for this, the length of the interaction channels of the ZGDC's on the mask were reduced by 60  $\mu\text{m}$ . The actual lengths were verified by measuring the separation between Input Channel 1 and Input Channel 2 where they joined the interaction channel (see Fig. 5.4.5).

To characterize the structures, the laser diode was launched into one of the input channels of the couplers and the intensity of the beam was measured at both output channels. Figs. 5.4.6 and 5.4.7 are captured images of the laser beam propagating through passive ZGDC's with 200  $\mu\text{m}$

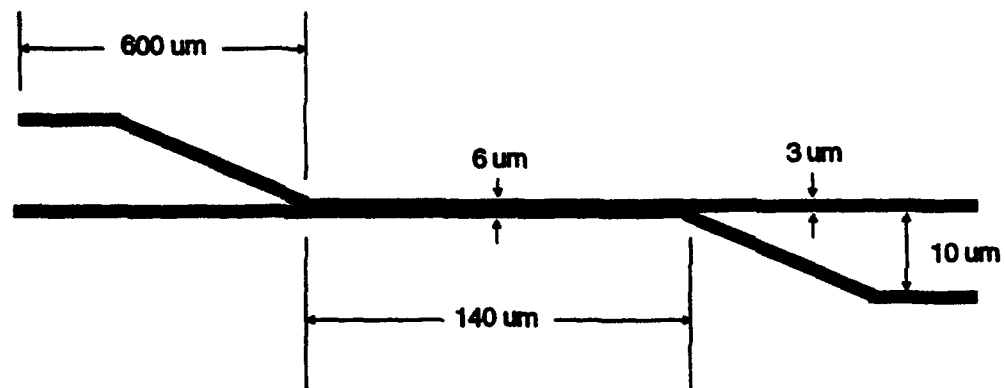


**Figure 5.4.1**  
**Schematic of Mask Layout for a Passive  $\text{AlGa}_{1-x}\text{As}$  Zero-Gap**  
**Directional Coupler with a 200  $\mu\text{m}$  Interaction Length**

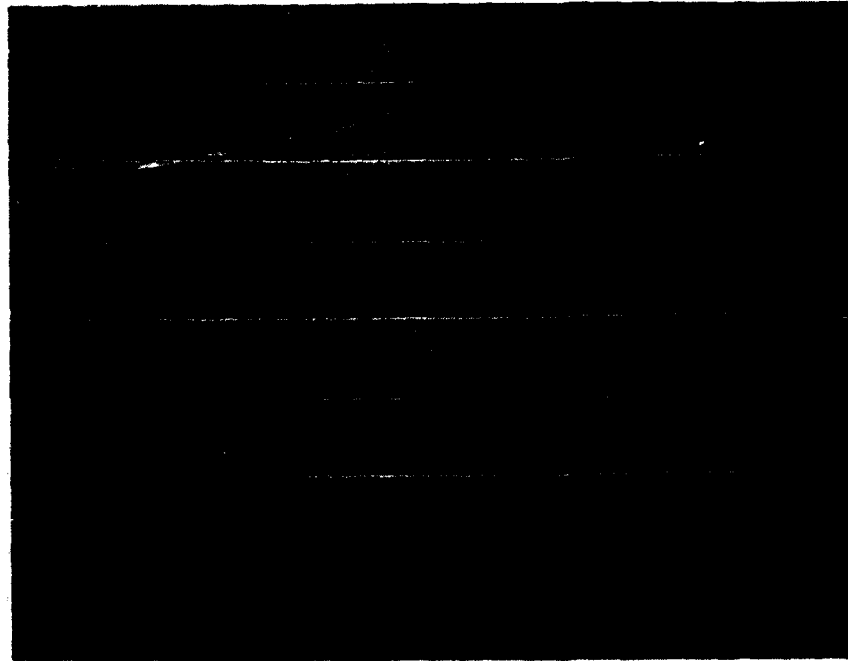


**Figure 5.4.2**  
**Photomicrograph Aerial View of Passive  $\text{Al}_x\text{Ga}_{1-x}\text{As}$  Zero-Gap**  
**Directional Couplers with 200  $\mu\text{m}$  Interaction Lengths**



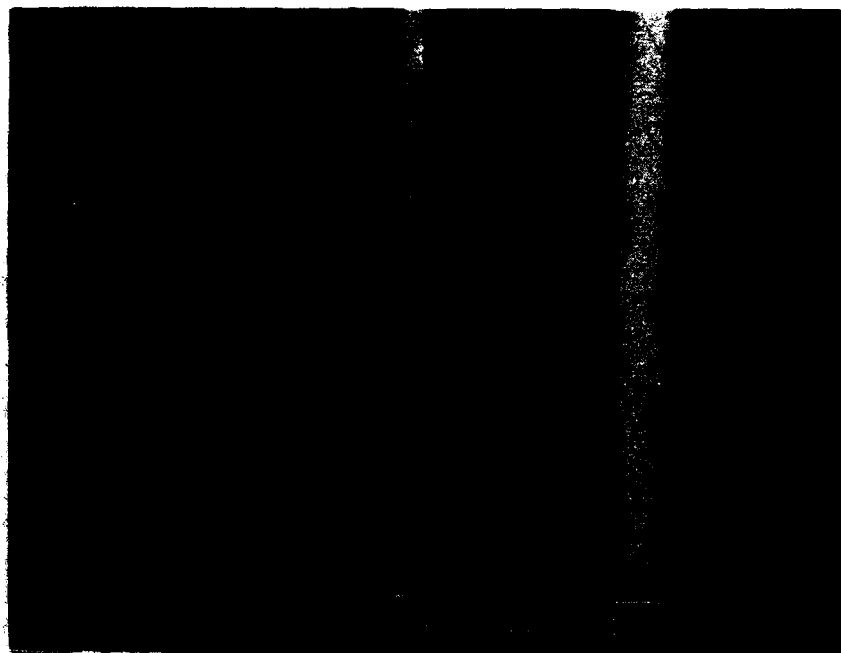
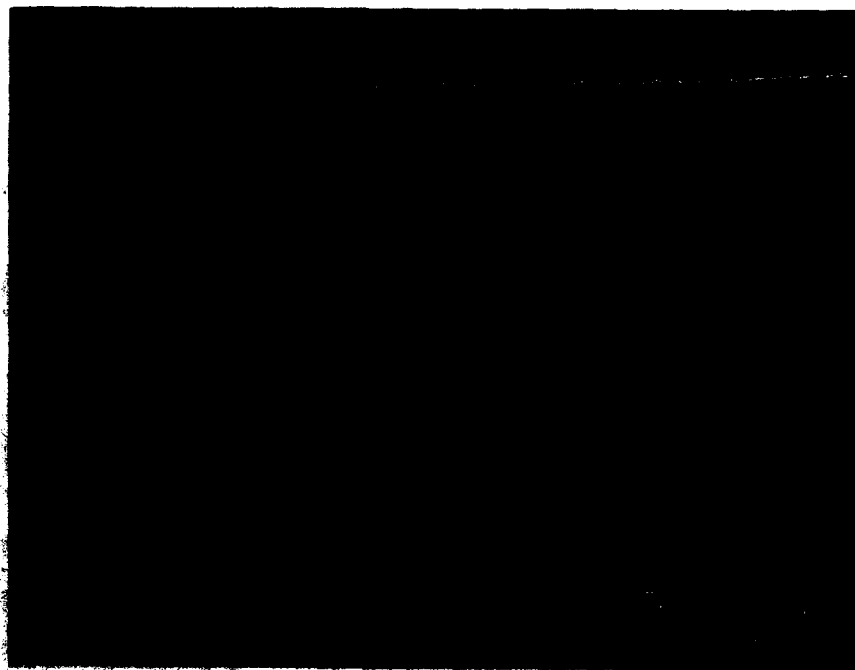


Figure 5.4.3  
SEM Aerial View of the Input Channel of a Passive  
AlGa<sub>1-x</sub>As Zero-Gap Directional Coupler



**Figure 5.4.4**  
**SEM Aerial View of the Interaction Channel Section of a Passive**  
 **$\text{AlGa}_{1-x}\text{As}$  Zero-Gap Directional Coupler**



**Figure 5.4.5**  
**SEM Aerial View of the Intersection of the Input Channels**  
**and the Interaction Channel of a Passive  $\text{Al}_x\text{Ga}_{1-x}\text{As}$**   
**Zero-Gap Directional Coupler**

and 400  $\mu\text{m}$  interaction channel lengths, respectively. For the ZGDC with a 200  $\mu\text{m}$  interaction channel length, the beam enters Input Channel 2 and exits Output Channel 1. For the ZGDC with a 400  $\mu\text{m}$  interaction channel length, the beam enters Input Channel 1 and exits Output Channel 1. Output intensity measurements were taken of all the various interaction channel length passive ZGDC's. These measurements were then normalized and fit to the  $\sin^2(\Phi_0 L)$  curve corresponding to Eq. 1.5.5 by varying  $L$ . By doing this, it was observed that an optimum fit occurred at an interaction length of  $L = 196 \mu\text{m} \pm 3 \mu\text{m}$  (see Fig. 5.4.8). This experimentally inferred interaction length for complete coupling will be compared to the model in the next chapter. In addition to determining the interaction length, the total device loss was measured by comparing the input and output intensities of the various passive ZGDC's. Including the waveguide propagation loss, the total loss of these devices was found to range between -3 dB and -7 dB.

### Active Zero-Gap Directional Couplers

Active ZGDC's (switching electrodes present) were fabricated in sample 121 using the process presented in Appendix B. The target width of the input and output channels was 3  $\mu\text{m}$ , and the target width of the center interaction channel was 6  $\mu\text{m}$ . An initial calculation using the data from the



**Figure 5.4.6**  
**CCD Image of Laser Beam Propagating through a Passive  $\text{Al}_x\text{Ga}_{1-x}\text{As}$**   
**Zero-Gap Directional Coupler with a 200  $\mu\text{m}$  Interaction Length**



**Figure 5.4.7**  
**CCD Image of Laser Beam Propagating through a Passive  $\text{Al}_x\text{Ga}_{1-x}\text{As}$**   
**Zero-Gap Directional Coupler with a 400  $\mu\text{m}$  Interaction Length**

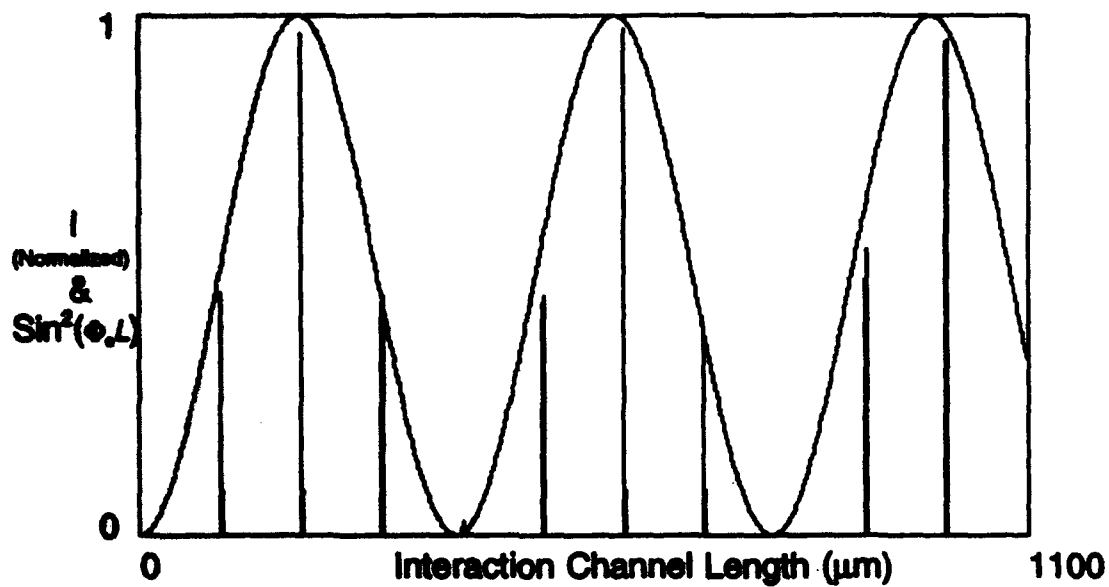


**Figure 5.4.8**  
**Normalized Intensity Plotted Against  $\text{Sin}^2(\Phi_0 L)$  with  $L = 196 \mu\text{m}$  versus**  
**Interaction Channel Length for Passive  $\text{Al}_x\text{Ga}_{1-x}\text{As}$**   
**Zero-Gap Directional Coupler**

previous sections suggested that a very high switching voltage would be required if a 196  $\mu\text{m}$  interaction length was used. To keep voltages low and prevent device breakdown, the length of the interaction channel was extended to 5000  $\mu\text{m}$ . In addition, the placement of the voltage and ground electrodes had to be different from that for the EO modulator presented in Chapter IV, or for the active ZGDC's presented in Chapter I. This was due to the fact that the electrodes could not be placed on the top and the bottom of the core layer because of the cladding layers. Also, if the electrodes were placed on top of the top clad and the bottom of the wafer, the separation  $d$  between the electrodes would be too large, requiring an excessive voltage for modulation even for a device 5000  $\mu\text{m}$  in length (see Eq. 4.5.6). This would result in device breakdown. The electrodes would need to be placed on top of the top clad over the interaction channel similar to that shown in Fig. 1.3.1. This scheme would have to be modified, however, since there was an air interface on the outside walls of the ZGDC's fabricated for this experiment. It was decided to place the voltage electrode over the interaction channel, as one would for an EO modulator, and the ground electrode beside the interaction channel on top of a mesa. Fig. 5.5.1 is a schematic of the mask layout for an active ZGDC with an interaction length of 5000  $\mu\text{m}$  showing the electrode placement. The target dimensions for the voltage electrode were 2  $\mu\text{m}$  wide  $\times$  4996  $\mu\text{m}$  long centered above the 6  $\mu\text{m}$



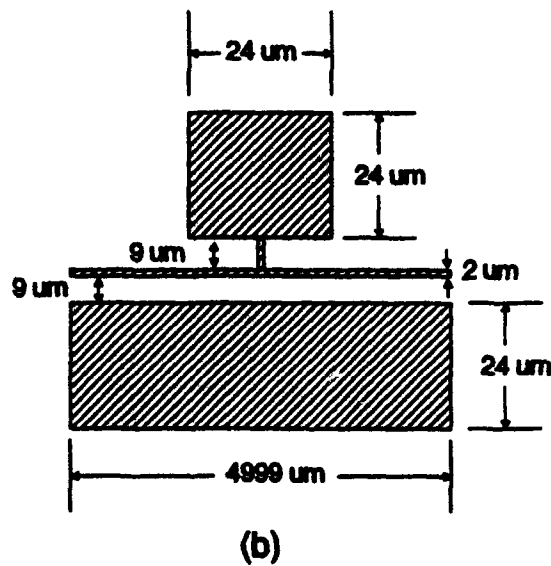
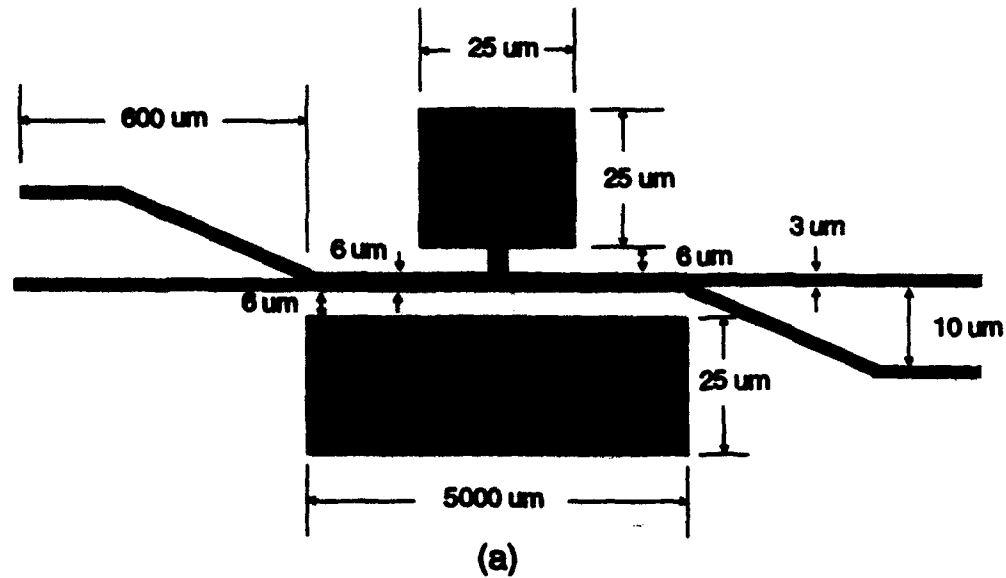


**Figure 5.5.1**  
**Schematic of Mask Layout for (a) the Waveguide Pattern and (b) the**  
**Electrode Pattern for an Active  $\text{Al}_x\text{Ga}_{1-x}\text{As}$  Zero-Gap Directional**  
**Coupler with a 5000  $\mu\text{m}$  Interaction Length**

$\times 5000 \mu\text{m}$  interaction channel. This was done to give a  $2 \mu\text{m}$  space from the edge of the metal to the edge of the waveguide, and to ensure that the metal would not touch the sides of the waveguides. A contact pad for the voltage electrode was fabricated with target dimensions of  $24 \mu\text{m} \times 24 \mu\text{m}$  centered above a  $25 \mu\text{m} \times 25 \mu\text{m}$  mesa. In the last section, it was shown that there is little if any crossover between waveguides normal to each other, so it was decided to attach the voltage electrode to the pad via an electrode strip centered above a mesa intersecting the interaction channel normal to the channel (see Fig. 5.5.1). The target width of the intersecting electrode was the same as that for the voltage electrode, and the target width of the intersecting mesa was the same as that for the ZGDC interaction channel. The target dimensions for the ground electrode were  $24 \mu\text{m}$  wide  $\times 4999 \mu\text{m}$  long centered above a  $25 \mu\text{m} \times 5000 \mu\text{m}$  mesa. The contact pad for the voltage electrode and the ground electrode were both designed to be  $1 \mu\text{m}$  narrower than the mesas that they were above. Metal on the sides of the voltage pad and ground electrode mesas was not as critical. This would give a lateral electrode separation of  $9 \mu\text{m}$  and prevent any possible shorts from metal whiskers that might be left after fabrication. The contact pad for the voltage electrode and the ground electrode were made large to ease the task of placement of the Alessi micropositioner probe tips. The mask generated for the electrodes was a dark field type. The mask generated for the ZGDC was a clear field type. The metal used for the electrodes

consisted of a trilayer of 300 Å of Titanium (Ti)/400 Å platinum (Pt)/3500 Å of gold (Au) deposited in that order using a Temescal FC-1800 electron beam evaporator. Figure 5.5.2 is an aerial view of the center section of the fabricated device showing the voltage and ground electrodes, including the pad for the voltage electrode and the intersecting electrode.

The actual width of the input and output channels measured 2.2  $\mu\text{m}$  - 2.3  $\mu\text{m}$  (see Fig. 5.5.3). The actual width of the interaction channel measured 4.6  $\mu\text{m}$  - 4.7  $\mu\text{m}$  (see Fig 5.5.4). The actual width of the voltage electrode above the interaction channel measured 1.5  $\mu\text{m}$  centered above the interaction channel (see Fig. 5.5.4). The etch depth measured 1.9  $\mu\text{m}$  - 2.1  $\mu\text{m}$ .

These devices were tested by launching the LT015MDO laser diode into one of the input channels, applying a DC voltage, and observing the two output channels. Fig. 5.5.5 is an image showing the output of the device with the laser launched into Input Channel 2 with no voltage applied. As in the last section, the intensities at Outputs 1 and 2 were normalized and fit to the  $\sin^2(\Phi_0 L)$ . In doing this, it was found that an optimum fit occurred at  $L = 123 \mu\text{m} \pm 0.1 \mu\text{m}$ . The fit was much more sensitive to small changes in  $L$  with an interaction channel length of 5000  $\mu\text{m}$  than it was when the length of the interaction channel was closer to  $L$ .

A small voltage was then applied to the voltage electrode and increased gradually to 19 VDC, making observations of any changes at the outputs.



**Figure 5.5.2**  
**Photomicrographic Aerial View of the Center Region of an Active**  
**Al<sub>x</sub>Ga<sub>1-x</sub>As Zero-Gap Directional Coupler**



**Figure 5.5.3**  
**SEM Aerial View of the Input Channel Section of an Active**  
 **$\text{Al}_x\text{Ga}_{1-x}\text{As}$  Zero-Gap Directional Coupler**



**Figure 5.5.4**  
**SEM Aerial View of the Interaction Channel Section of an**  
**Active  $\text{Al}_x\text{Ga}_{1-x}\text{As}$  Zero-Gap Directional Coupler**

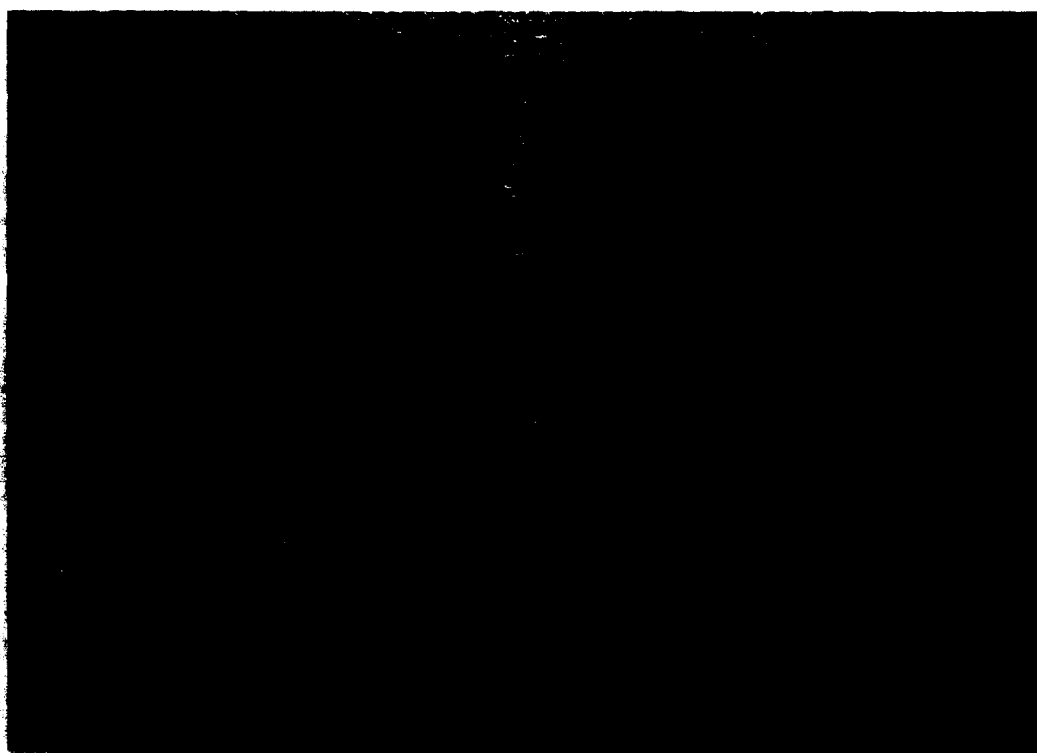


**Figure 5.5.5**  
**CCD Image of Laser Beam at the Output of an Active  $\text{Al}_x\text{Ga}_{1-x}\text{As}$  Zero-Gap**  
**Directional Coupler with Input at Channel 2 (no Voltage Applied)**

The intensity at Output Channel 1 did not appear to change until the voltage level reached 3 VDC. Above 3 VDC, the intensity at Output Channel 1 began to drop off, reaching a minimum at  $V = 10$  VDC. The intensity at Output Channel 1 stayed at a minimum up to  $V = 16$  VDC and then increased slightly up to  $V = 19$  VDC. The intensity at Output Channel 2 did not appear to change until the voltage level reached 10 VDC. Above 10 VDC, the intensity at Output Channel 2 began to increase, reaching a maximum at  $V = 18$  VDC. Fig. 5.5.6 is a CCD image showing the output with 18 VDC applied. Since the waveguide characterization system could not compensate for the polarization rotation induced by the applied voltage, the switching voltage could not be measured directly. Therefore, the intensities observed at Output Channels 1 and 2 were fit to the corresponding  $\sin^2$  and  $\cos^2$  curves (see Eqs. 1.5.5 and 1.5.4), taking into account the polarization rotation induced by the applied voltage. The switching voltage was determined for the  $TE_{00}$  mode. This is illustrated in Figs. 5.5.7 and 5.5.8. A switching voltage of  $10.5 \text{ VDC} \pm 0.3 \text{ VDC}$  was inferred using this method. The loss of the active ZGDC's measured -3 dB to -7 dB, which is comparable to that for the passive devices. In Chapter VI, the measured switching voltage will be compared to the predicted voltage derived by using the models.



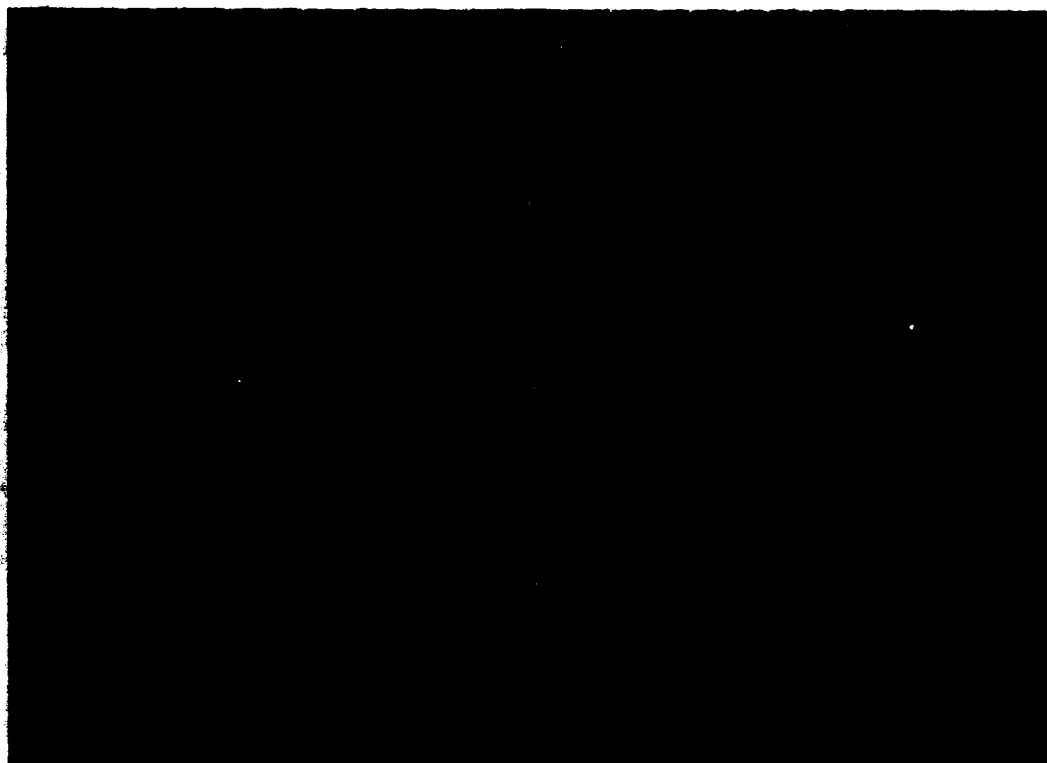


**Figure 5.5.6**  
**CCD Image of Laser Beam at the Output of an Active  $\text{Al}_x\text{Ga}_{1-x}\text{As}$  Zero-Gap**  
**Directional Coupler with Input at Channel 2 (18 VDC Applied)**

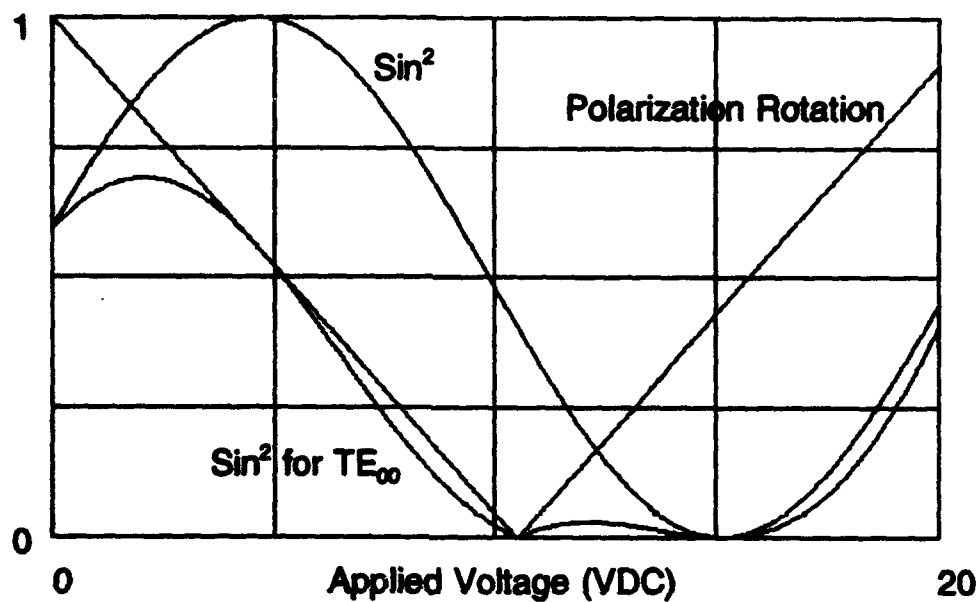


**Figure 5.5.7**  
 $\text{Sin}^2(\Phi_o L)$  of  $\text{TE}_{00}$  Mode Plotted Against  $\text{Sin}^2(\Phi_o L)$  and  
 Polarization Rotation versus Applied Voltage  
 for Output Channel 1

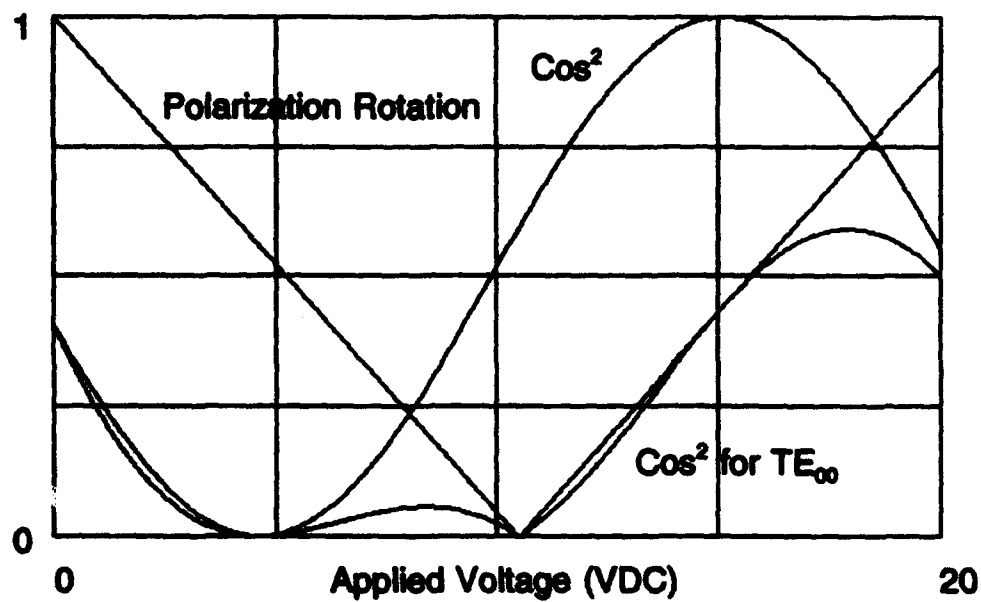


**Figure 5.5.8**  
 $\text{Cos}^2(\Phi_0 L)$  of  $\text{TE}_{00}$  Mode Plotted Against  $\text{Cos}^2(\Phi_0 L)$  and  
 Polarization Rotation versus Applied Voltage  
 for Output Channel 2

Optical Digital Logic

An AND gate was realized using an active zero-gap directional coupler by letting Input Channel 2 represent AND input "a" and the control electrode represent AND input "b" (see Fig. 1.2.1). Input Channel 1 was held low (no input beam). Light into the waveguide channel was defined as a logic 1. Absence of light was defined as a logic 0. The voltage that allowed complete switching of the active ZGDC represented a logic 1. Absence of voltage represented a logic 0. Fig. 5.6.1 shows the CCD images captured at Output Channels 1 and 2 with various combinations of input. If we define Output Channel 2 as the output of the logic function and let the presence of light represent a logic 1 and the absence of light represent a logic 0 then, as can be seen in Fig. 5.6.1, a digital AND function is realized. In Chapter VI, more complicated digital functions and reconfigurable interconnects using active zero-gap directional couplers will be addressed.

AND Input "b"  
Applied Voltage

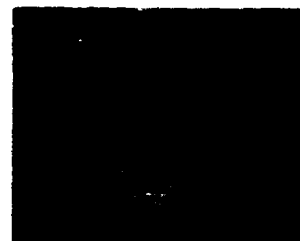
AND Input "a"  
Input Channel 2

AND Output  
Output Channel 2

0 VDC



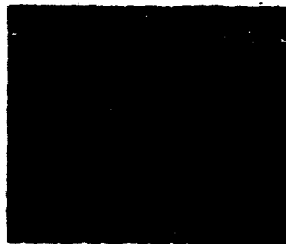
0 VDC



1 2

1 2

18 VDC



18 VDC



1 2

1 2

Figure 5.6.1  
AND Gate Realized with an Active  $\text{Al}_x\text{Ga}_{1-x}\text{As}$   
Zero-Gap Directional Coupler

## CHAPTER VI

### RESULTS

In this chapter, the characteristics of the zero-gap directional couplers measured in Chapter V are compared with those predicted using the models presented in Chapters II - IV. The first section equates the interaction length versus refractive index and waveguide width. The second section compares the measured and modelled switching voltage. The last section deals with digital logic and reconfigurable interconnects.

#### Interaction Length

It has been shown that if we ensure we are far from cutoff, then all of the various models predicting interaction length presented in Chapter III show good agreement.<sup>79,80</sup> To determine that we are far from cutoff, we will substitute the various core and clad indices for sample 121, the measured width for the input and output channels of both the passive and active zero-gap directional coupler and  $\lambda = 827$  nm into Eq. 3.0.1 to confirm that the normalized frequency  $B \geq 1.6$ . In doing this, we find  $B = 1.6 - 2.6$ . Hence, the Marcatili model<sup>61</sup> will be used to predict the interaction length of the

ZGDC's, and the beam propagation method (BPM)<sup>68</sup> will be used to model their behavior.

### Passive Zero-Gap Directional Coupler

As the separation between the two waveguides of a conventional directional coupler approaches zero, the effective index of the region between the two waveguides approaches the index of the core region. After substituting the various measured parameters (i.e., refractive index, waveguide width and core thickness) and driving the waveguide separation to zero, the Marcatili model was fit to the measured interaction length. Choosing a center index of  $n_5 = 1.0$  and driving the gap to zero resulted in a predicted interaction length much longer than the measured length. Choosing  $n_5$  close to the core index and driving the separation to zero, resulted in a predicted interaction length significantly smaller than the measured length. The best fit occurred when the refractive index of the center region was set equal to the index of the top and bottom clad. Fig. 6.1.1 is a plot of the interaction length versus the waveguide separation for Waveguide Structure 121-300°K-1 with  $n_5 = n_2 = n_4$ . For this plot the  $\pm$  values for the refractive index were not included. The core index used was  $n_1 = 3.420$ , the top, bottom, and center clad indices used were  $n_2 = n_4 = n_5 = 3.388$  and the side clad index used was  $n_3 = 1.0$ . The width used for the

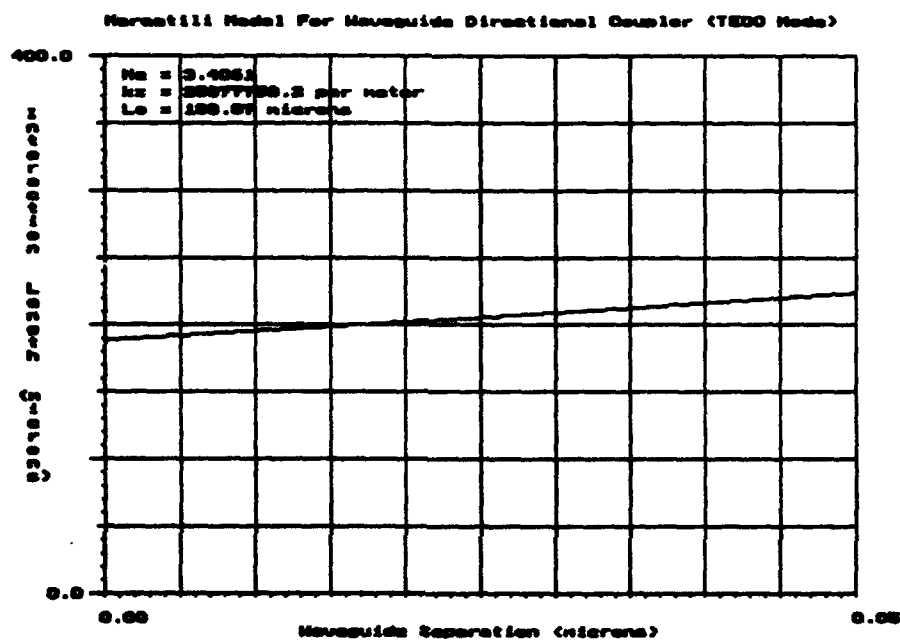


Figure 6.1.1  
Interaction Length versus Waveguide Separation  
using the Marcatili Model



input and output channels was  $b = 2.7 \mu\text{m}$ , the core thickness used was  $t = 0.9 \mu\text{m}$  and the wavelength used was  $\lambda = 827 \text{ nm}$ . Fig. 6.1.2 is a BPM plot of the amplitudes of the propagating fields of the ZGDC structure using the same parameters along with the Marcatili modelled interaction length and a  $0.1 \mu\text{m}$  step size. This illustrates the predicted behavior of the device. As can be seen, there is good agreement between the two models. The interaction length was also modelled for a ZGDC using Waveguide Structure 121-300°K-1 with  $b = 2.8 \mu\text{m}$  and all other parameters remaining the same as for the previous case. The interaction length modelled with these parameters was  $208 \mu\text{m}$ . Taking the mean of the two values gives an interaction length of  $199 \mu\text{m} \pm 10 \mu\text{m}$ , which is not far from the measured value. Comparisons were made of all of the waveguide structures from Chapter V for sample 121, including the  $\pm$  values of the refractive indices. Table 6.1.1 lists the results of these comparisons. As can be seen, the modelled value that best fits the measured interaction length is that using  $n_{\text{avg}}$  for the Al concentration determined with the 300°K PL measurements. Most importantly, though, Table 6.1.1 shows that a change in the width of the input and output channels by as little as  $0.1 \mu\text{m}$  can lead to as much as a  $20 \mu\text{m}$  change in the interaction length. A change in the Al concentration by as little as 0.5% can lead to as much as a  $20 \mu\text{m}$  change in the interaction length. This could result in a total change in the interaction length of  $\pm 40 \mu\text{m}$ . The voltage independent phase change could then vary

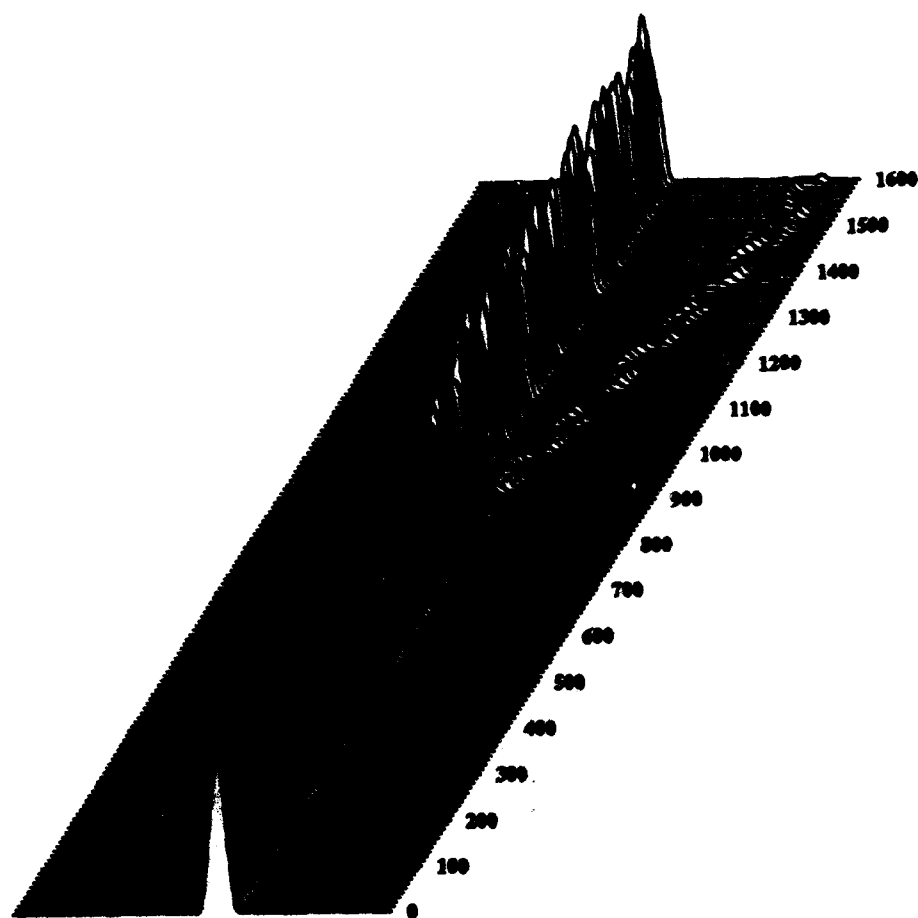


Figure 6.1.2  
Amplitudes of the Propagating Fields in a Passive  $\text{Al}_{0.298}\text{Ga}_{0.351}\text{As}$   
Zero-Gap Directional Coupler with a  $189\text{ }\mu\text{m}$  Interaction Length

Table 6.1.1  
Interaction Length versus the Various Waveguide  
Structures and Channel Widths

Waveguide Structure	$n_1$	$n_2, n_4, n_5$	$n_3$	$\lambda$ (nm)	$t$ ( $\mu\text{m}$ )	$b$ ( $\mu\text{m}$ )	$L$ ( $\mu\text{m}$ )
121-300°K-1	$n_{\text{core1}}$	$n_{\text{clad1}}$	1.00	827	0.9	2.7	$189 \pm 13$
121-300°K-1	$n_{\text{core1}}$	$n_{\text{clad1}}$	1.00	827	0.9	2.8	$208 \pm 13$
121-3°K-1	$n_{\text{core1}}$	$n_{\text{clad1}}$	1.00	827	0.9	2.7	$194 \pm 13$
121-3°K-1	$n_{\text{core1}}$	$n_{\text{clad1}}$	1.00	827	0.9	2.8	$214 \pm 15$
121-300°K-2	$n_{\text{core2}}$	$n_{\text{clad2}}$	1.00	827	0.9	2.7	$183 \pm 13$
121-300°K-2	$n_{\text{core2}}$	$n_{\text{clad2}}$	1.00	827	0.9	2.8	$202 \pm 18$
121-3°K-2	$n_{\text{core2}}$	$n_{\text{clad2}}$	1.00	827	0.9	2.7	$182 \pm 14$
121-3°K-2	$n_{\text{core2}}$	$n_{\text{clad2}}$	1.00	827	0.9	2.8	$201 \pm 20$
121-300°K-3	$n_{\text{core3}}$	$n_{\text{clad3}}$	1.00	827	0.9	2.7	$199 \pm 15$
121-300°K-3	$n_{\text{core3}}$	$n_{\text{clad3}}$	1.00	827	0.9	2.8	$219 \pm 17$
121-3°K-3	$n_{\text{core3}}$	$n_{\text{clad3}}$	1.00	827	0.9	2.7	$202 \pm 15$
121-3°K-3	$n_{\text{core3}}$	$n_{\text{clad3}}$	1.00	827	0.9	2.8	$225 \pm 17$

by as much as  $\pm 20\%$ . Even with these large changes in the interaction length and phase, however, the output intensity will only change by  $\pm 10\%$  (see Eq. 1.5.5). This demonstrates a fabrication tolerant device.

### Active Zero-Gap Directional Coupler

Before the switching voltage was analyzed, the measured interaction length of the active  $\text{Al}_x\text{Ga}_{1-x}\text{As}$  ZGDC was compared to the modelled length.

After substituting the measured parameters into the Marcatili model, considering only the accuracy of the known waveguide width, an interaction length of  $117 \mu\text{m} \pm 7 \mu\text{m}$  was calculated. This compares favorably with the measured interaction length within experimental error. When taking the accuracy of the refractive index into account, the interaction length becomes  $117 \mu\text{m} \pm 14 \mu\text{m}$ . The output of these longer devices is much more sensitive to the accuracy of the interaction length than it is for the passive devices. If one could control the interaction length even to within  $1 \mu\text{m}$ , which would hold the voltage independent phase change to within 1%, the output intensity could vary by as much as 45% (see Eq. 1.5.5). This is much less fabrication tolerant than the passive devices. Figs. 6.2.1 and 6.2.2 are BPM plots illustrating the predicted behavior of active ZGDC's having interaction lengths of  $123 \mu\text{m}$  and  $124 \mu\text{m}$ , respectively, with  $5000 \mu\text{m}$  interaction channels and no voltage applied. This was done in order to demonstrate the sensitivity of the output intensity versus interaction length. The step size used for these plots was  $0.1 \mu\text{m}$ . For the active device fabricated for this experiment, the measured output intensity with no voltage applied was 30% less than the optimum with no voltage applied (see Fig. 5.5.7). To achieve maximum coupling for this device, the interaction channel length would have to be  $40 \mu\text{m}$  longer. With the degree of inaccuracies for this experiment, however, it would be very difficult to predict the exact interaction length and extremely difficult to ensure that it could be fabricated

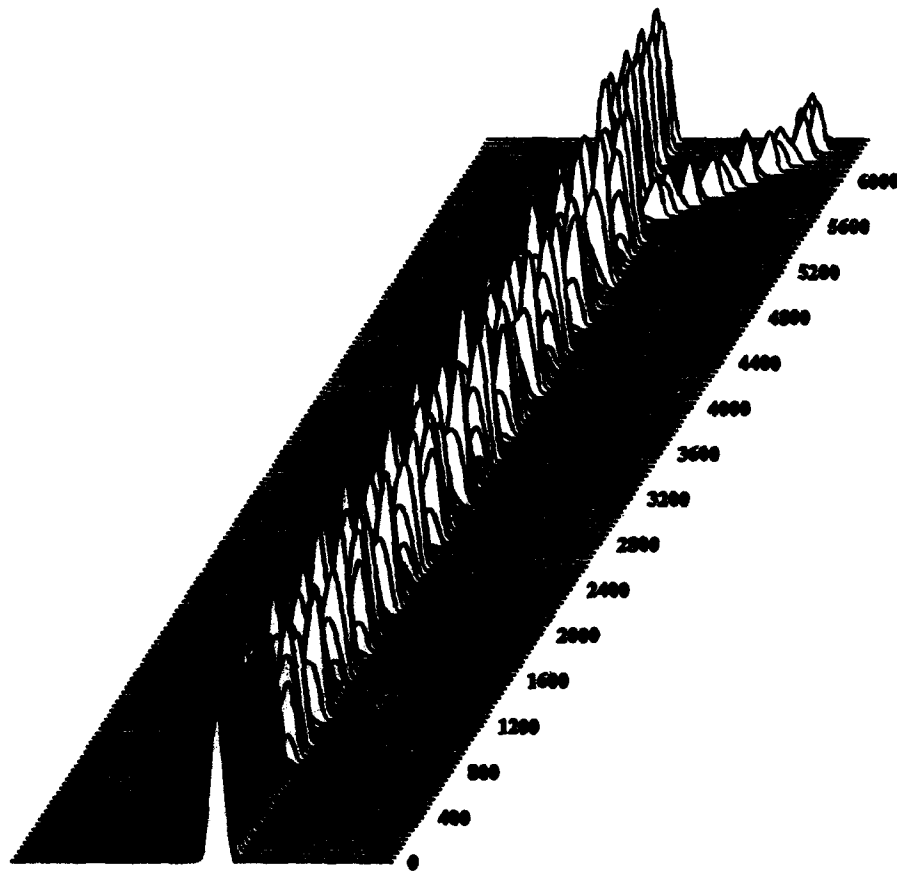


Figure 6.2.1  
Amplitudes of the Propagating Fields in an Active  $\text{Al}_{0.298}\text{Ga}_{0.351}\text{As}$  Zero-Gap  
Directional Coupler with a  $123\text{ }\mu\text{m}$  Interaction Length and  $5000\text{ }\mu\text{m}$   
Interaction Channel (no Voltage Applied)

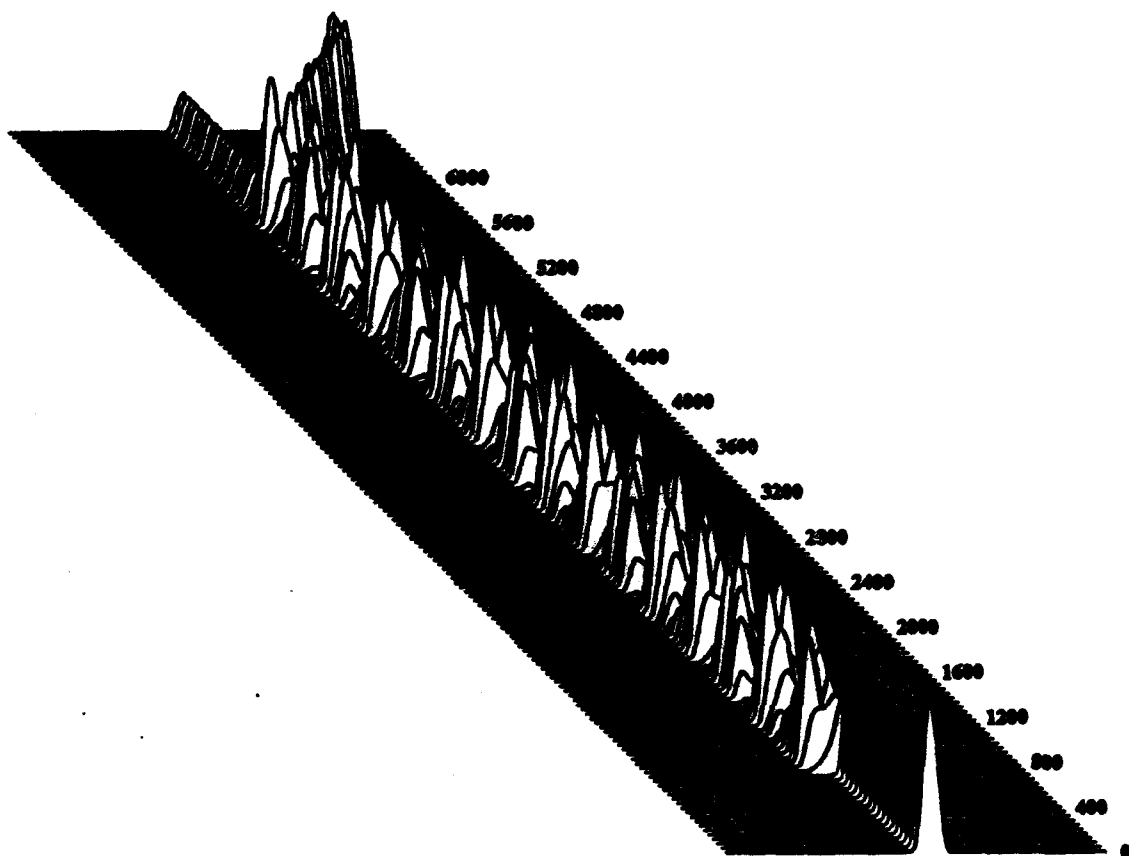


Figure 6.2.2  
Amplitudes of the Propagating Fields in an Active  $\text{Al}_{0.298}\text{Ga}_{0.351}\text{As}$  Zero-Gap  
Directional Coupler with a  $124\text{ }\mu\text{m}$  Interaction Length and  $5000\text{ }\mu\text{m}$   
Interaction Channel (no Voltage Applied)

the same way each time.

### Switching Voltage

The active  $\text{Al}_x\text{Ga}_{1-x}\text{As}$  ZGDC fabricated for this experiment required 30% higher voltage than optimum to achieve switching (see Fig. 5.5.7). This was due to the fact that the interaction channel length was not optimum. Based on the known accuracies for the refractive index and waveguide width, one could end up with a device, after fabrication, requiring as much as twice the optimum switching voltage. Possible solutions to this problem will be addressed in Chapter VII.

To evaluate the actual versus modelled voltage required for complete switching of the active  $\text{Al}_x\text{Ga}_{1-x}\text{As}$  ZGDC, Eq. 4.5.6 was used. Since the electrodes were placed on top of the device, the vertical distance between the top of the top clad to the bottom of the core was substituted for the electrode separation  $d$ . Using Table 5.1.4, and knowing that  $0.1\text{ }\mu\text{m}$  of GaAs was grown between the core and clad layers,  $d = 1.95\text{ }\mu\text{m}$  for sample 121. From electromagnetic theory,<sup>99</sup> the electric field actually reaching the bottom of the core layer would be 5% less than the electric field applied to the electrode. This was determined from the lateral distance between the center of the voltage electrode and the center of ground electrode. Table 6.2.1 presents the predicted switching voltage of the active  $\text{Al}_x\text{Ga}_{1-x}\text{As}$  ZGDC

for the various waveguide structures for sample 121, as well as the linear EO coefficients from Table 5.2.1. Comparing the modelled values for switching voltage with the switching voltage measured in the last chapter, one can see that the measured voltage is approximately  $\sqrt{3}$  greater than the predicted voltage. This is due to the width of the voltage electrode and position of the ground electrode. The voltage electrode was less than half the width of the interaction channel. The ground electrode was on the Channel 2 side of the device. Because the voltage electrode was not over the majority of the interaction channel and the ground electrode was located only on one side of the channel, it can be hypothesized that most of the voltage was concentrated in the Channel 2 side of the interaction channel. The electric field distribution between the voltage and ground electrode is further explained by electromagnetic<sup>69</sup> and transmission line theory<sup>164</sup> and has been analyzed for the region between the gate and drain electrodes in GaAs metal semiconductor field effect transistors (MESFET's).<sup>147</sup> With an unequal distribution of electric field in the two regions of the interaction channel, the voltage induced change in the refractive index would, likewise, be unequal across the width of the channel. The index change would be greater on the Channel 2 side than on the Channel 1 side and the device would behave more like a conventional directional coupler (see Eqs. 1.4.11 and 4.5.7). To test the plausibility of this theory, the BPM was programmed



Table 6.2.1  
Switching Voltage versus the Various Waveguide  
Structures and Electro-Optic Coefficients

Waveguide Structure	$n_i$	$d$ ( $\mu\text{m}$ )	$L$ ( $\mu\text{m}$ )	$\lambda$ (nm)	$r_{41}^T$ (pm/V)	$ V $ VDC
121-300°K-1	$n_{\text{core1}}$	1.95	5000	827	-1.41	$5.72 \pm 0.02$
121-300°K-1	$n_{\text{core1}}$	1.95	5000	827	-1.49	$5.41 \pm 0.02$
121-300°K-1	$n_{\text{core1}}$	1.95	5000	827	-1.57	$5.14 \pm 0.02$
121-3°K-1	$n_{\text{core1}}$	1.95	5000	827	-1.48	$5.39 \pm 0.02$
121-3°K-1	$n_{\text{core1}}$	1.95	5000	827	-1.56	$5.11 \pm 0.01$
121-3°K-1	$n_{\text{core1}}$	1.95	5000	827	-1.64	$4.86 \pm 0.01$
121-300°K-2	$n_{\text{core2}}$	1.95	5000	827	-1.41	$5.80 \pm 0.02$
121-300°K-2	$n_{\text{core2}}$	1.95	5000	827	-1.49	$5.49 \pm 0.02$
121-300°K-2	$n_{\text{core2}}$	1.95	5000	827	-1.57	$5.21 \pm 0.01$
121-3°K-2	$n_{\text{core2}}$	1.95	5000	827	-1.48	$5.48 \pm 0.02$
121-3°K-2	$n_{\text{core2}}$	1.95	5000	827	-1.56	$5.20 \pm 0.02$
121-3°K-2	$n_{\text{core2}}$	1.95	5000	827	-1.64	$4.94 \pm 0.02$
121-300°K-3	$n_{\text{core3}}$	1.95	5000	827	-1.41	$5.62 \pm 0.02$
121-300°K-3	$n_{\text{core3}}$	1.95	5000	827	-1.49	$5.32 \pm 0.02$
121-300°K-3	$n_{\text{core3}}$	1.95	5000	827	-1.57	$5.05 \pm 0.02$
121-3°K-3	$n_{\text{core3}}$	1.95	5000	827	-1.48	$5.29 \pm 0.02$
121-3°K-3	$n_{\text{core3}}$	1.95	5000	827	-1.56	$5.02 \pm 0.02$
121-3°K-3	$n_{\text{core3}}$	1.95	5000	827	-1.64	$4.77 \pm 0.02$

for two conditions. The first condition was to let the voltage induced change in the refractive index occur across the entire width of the interaction channel. The second condition was to let the voltage induced change in the

refractive index occur only across the width of the Channel 2 side of the interaction channel (i.e., only in one half of the width of the channel). The step size used to calculate the propagating field amplitudes for both plots was  $0.1\text{ }\mu\text{m}$ . The BPM model predicted that for complete switching, the change in the refractive index for the case in which the index change occurred only on one half of the interaction channel would have to be approximately  $\sqrt{3}$  higher than for the case in which the index change occurred across the entire width. Since the applied voltage is proportional to the change in the refractive index, this predicts that the voltage would also have to be  $\sqrt{3}$  higher for the second case. Dividing the measured switching voltage by  $\sqrt{3}$ , taking into account the 5% difference between the applied voltage and actual voltage reaching the core, one gets  $5.76\text{ VDC} \pm 0.17\text{ VDC}$ . This is within  $0.35\text{ VDC}$  of the predicted voltage for Sample 121-300°K-1 and well within the experimental accuracies. Figs. 6.2.3 and 6.2.4 are BPM plots illustrating the predicted behavior of the active ZGDC with no voltage applied and with voltage applied, respectively. An interaction channel length of  $5040\text{ }\mu\text{m}$  was chosen for these plots because it allows complete crossing from one channel to the other with no voltage applied. Fig. 6.2.4 was generated for the case in which voltage is applied across the entire width of the interaction channel. For both plots a  $0.1\text{ }\mu\text{m}$  step size was used. By increasing the width of the voltage electrode so that it covers

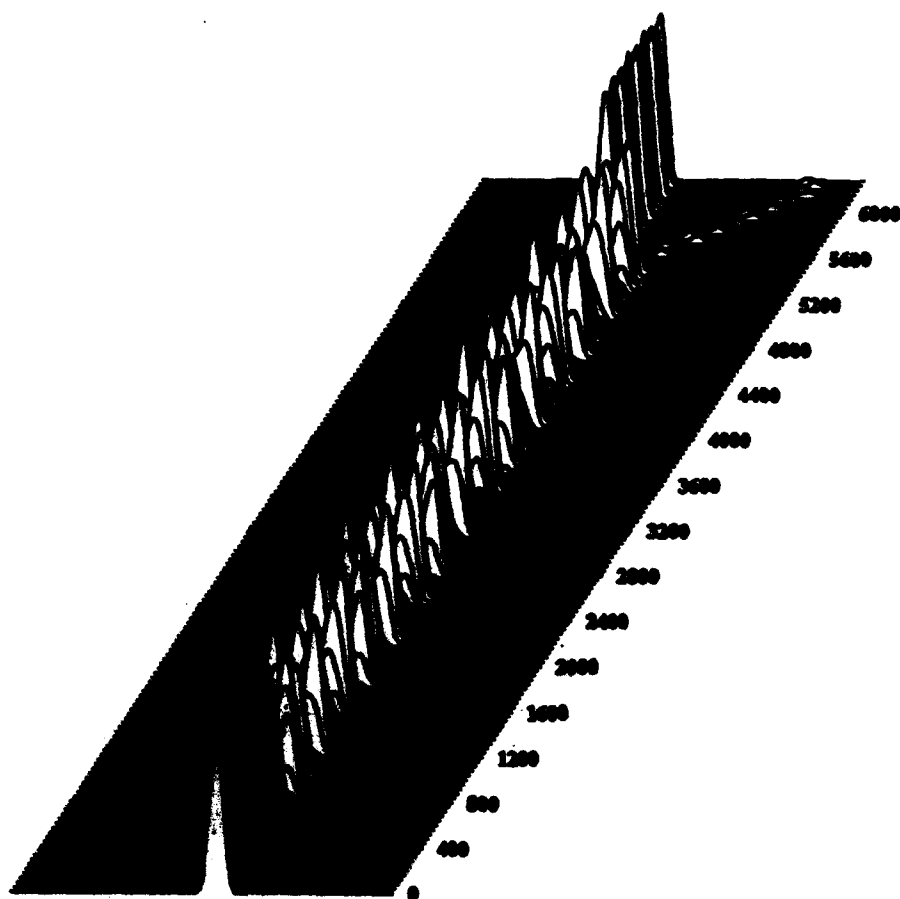


Figure 6.2.3  
Amplitudes of the Propagating Fields in an Active  $\text{Al}_{0.298}\text{Ga}_{0.351}\text{As}$  Zero-Gap  
Directional Coupler with a  $123\text{ }\mu\text{m}$  Interaction Length and  $5040\text{ }\mu\text{m}$   
Interaction Channel (no Voltage Applied)

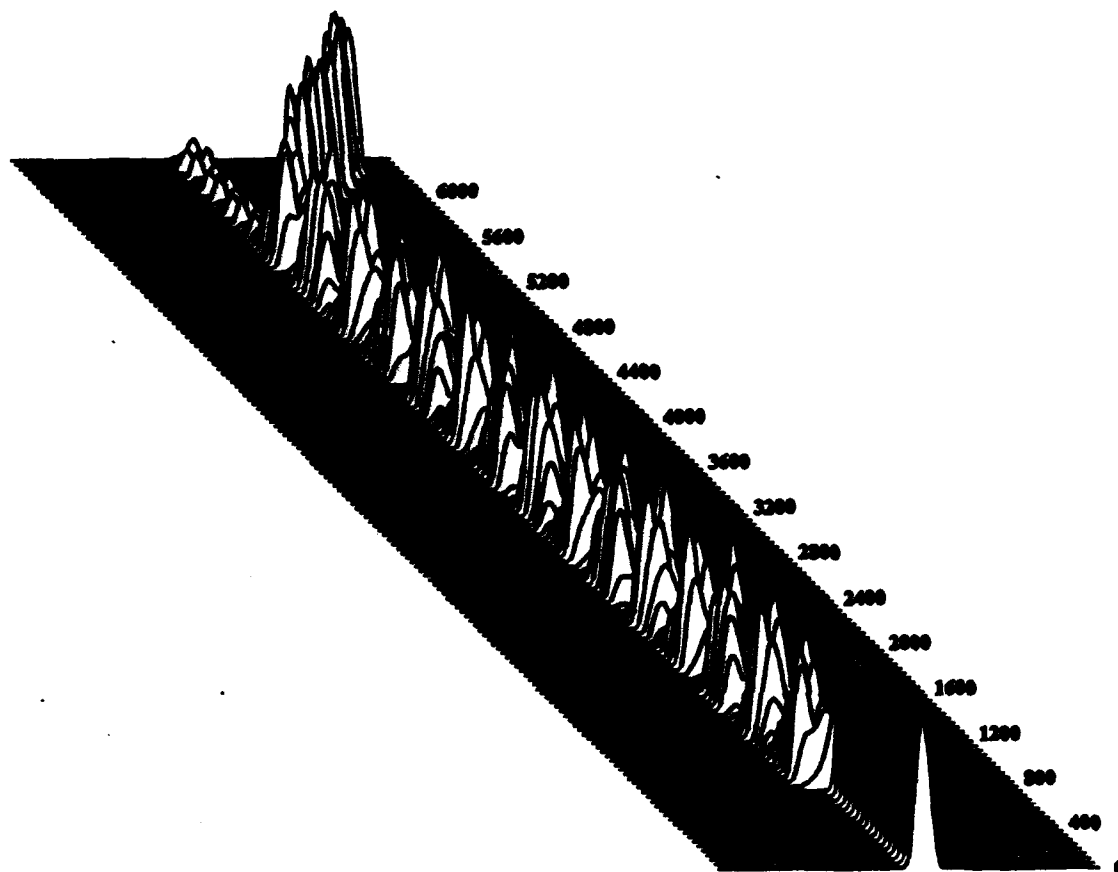


Figure 6.2.4  
Amplitudes of the Propagating Fields in an Active  $\text{Al}_{0.298}\text{Ga}_{0.351}\text{As}$  Zero-Gap  
Directional Coupler with a  $123\text{ }\mu\text{m}$  Interaction Length and  $5040\text{ }\mu\text{m}$   
Interaction Channel (Switching Voltage Applied)

a larger area of the interaction channel, the switching voltage should approach the predicted value. This was verified experimentally, where an active  $\text{Al}_x\text{Ga}_{1-x}\text{As}$  ZGDC was fabricated with a voltage electrode width of 6  $\mu\text{m}$  (see Fig. 6.2.5). Using the analysis technique described in Chapter V, a switching voltage of  $7.6 \text{ VDC} \pm 0.3 \text{ VDC}$  was measured. This is the lowest achieved switching voltage reported in the open literature for an active  $\text{Al}_x\text{Ga}_{1-x}\text{As}$  ZGDC with a 5000  $\mu\text{m}$  interaction channel length and is within 30% of the predicted voltage. With better alignment it is believed that the predicted value could be reached. Reaching the predicted voltage would also provide TTL voltage level operation without increasing the length of the device. Based on the EO properties of  $\text{Al}_x\text{Ga}_{1-x}\text{As}$ , however, 5000  $\mu\text{m}$  would be the minimum length the interaction channel could be to achieve TTL level switching for  $\text{Al}_x\text{Ga}_{1-x}\text{As}$  ZGDC's.

#### Digital Logic and Reconfigurable Interconnects

Presented in Chapter V is the first demonstrated AND logic gate reported in the open literature using an  $\text{Al}_x\text{Ga}_{1-x}\text{As}$  zero-gap directional coupler. It can easily be seen that by redefining the functions of input and output channels and cascading devices together that these simple logic gates could be expanded to more complicated digital circuits outlined in Chapter I. Reconfigurable interconnects were also demonstrated in Chapter



Figure 6.2.5  
SEM Aerial View of the Interaction Channel Section of an  
Active AlGa<sub>1-x</sub>As Zero-Gap Directional Coupler

V with the successful operation of the active  $\text{Al}_x\text{Ga}_{1-x}\text{As}$  ZGDC. The input signal could be electro-optically directed to either output. With the proof-of-concept demonstrations of these EO circuits, practical issues then become the most prominent for these devices.

From a practical viewpoint, one would have to consider the intensity limits constituting a logic 1 and a logic 0. Intensity ranges could be assigned to output logic levels in much the same way that voltage ranges are assigned to TTL voltage logic levels. Loss was high for the  $\text{Al}_x\text{Ga}_{1-x}\text{As}$  ZGDC's and would have to be addressed for more complicated logic circuits and optical interconnects. One would have to try to reduce loss through improved processing techniques or limit the number of devices cascaded together. Integration of the devices with sources and receivers would also have to be considered. In addition, integration with electronics would need to be investigated since it is anticipated that the final circuit would be an electronic/electro-optic hybrid making use of the advantages of both technologies. The voltage induced polarization rotation would have to be addressed. One would either have to employ a scheme to detect the polarization rotation at the output or compensate for it by integrating active polarizers at the outputs of each device to detect only one polarization. The sensitivity of the output versus interaction length brought up in the last section would have to be taken into account. One would either have to find

ways to more accurately control the interaction length so the coupling state could occur at no voltage or one would have to apply a voltage constantly to put the device in the coupling state. All these considerations, though primarily concerned with manufacturing, would need to be addressed before practical circuits could be realized. Possible solutions to these issues will be detailed in Chapter VII.



## CHAPTER VII

### SUMMARY AND CONCLUSIONS

In summary, the lowest switching voltage reported in the open literature for an active  $\text{Al}_x\text{Ga}_{1-x}\text{As}$  zero-gap directional coupler (ZGDC) with a  $5000\text{ }\mu\text{m}$  interaction channel length was achieved. The first AND logic gate reported in the open literature using an  $\text{Al}_x\text{Ga}_{1-x}\text{As}$  ZGDC was also demonstrated. The fact that the input signal into the  $\text{Al}_x\text{Ga}_{1-x}\text{As}$  ZGDC was switched from one channel to the other with applied voltage demonstrated a reconfigurable optical interconnect. These can be easily expanded to more complicated digital logic circuits and reconfigurable interconnects by cascading the ZGDC's and reassigning the functions of the input/output channels. The advantages of these devices, such as physical size, packing density and reconfigurability, may help enhance electronics as electronic interconnects reach their limits. Fig. 7.1.1 illustrates an envisioned circuit integrating both electronics and electro-optic Fredkin gates.

The comparisons presented in the Chapter VI show excellent agreement between the models for refractive index, interaction length, electro-optic

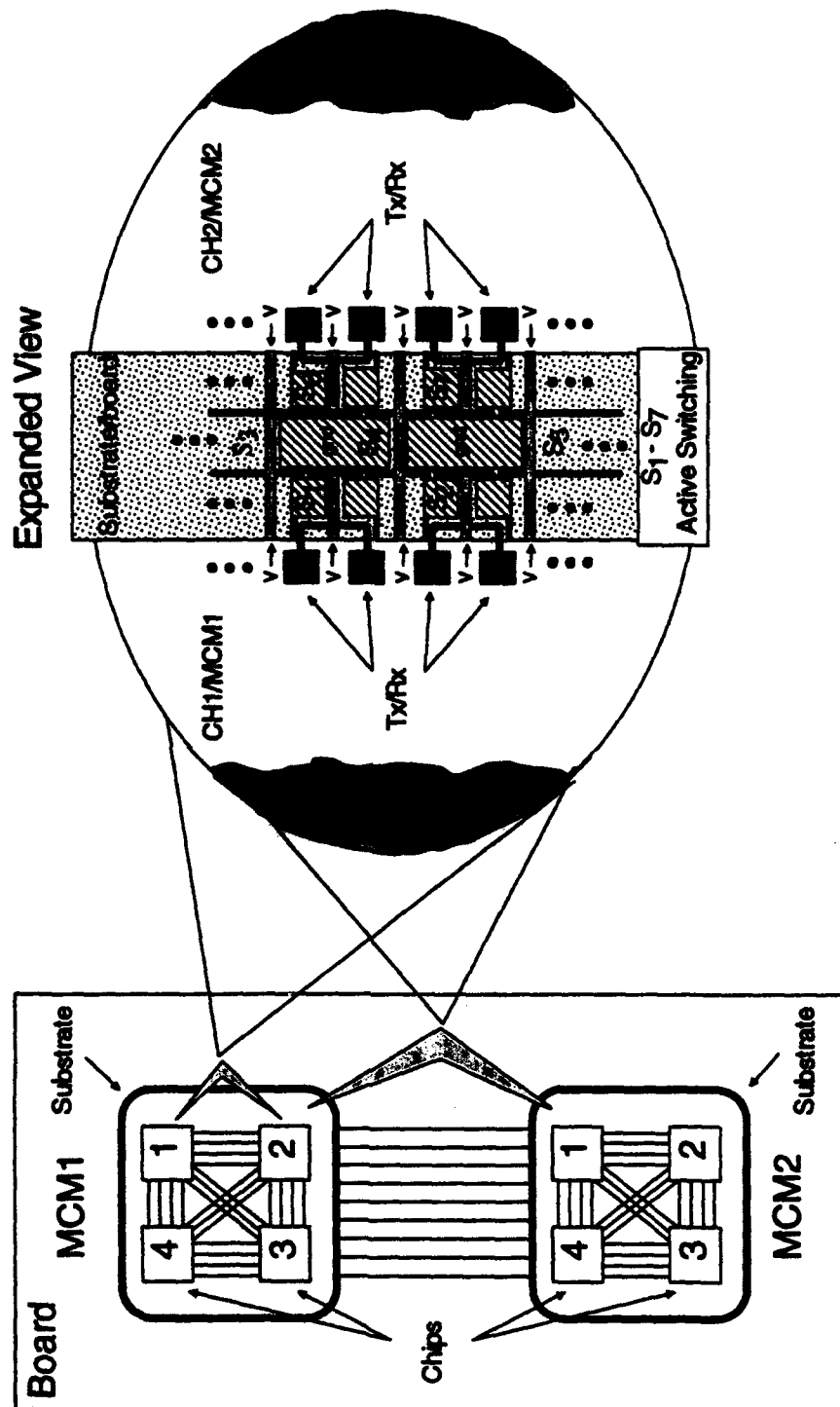


Figure 7.1.1  
Schematic of a Reconfigurable Integrated Electro-Optic Circuit

coefficient and switching voltage, and the actual performance of the devices. The data from Chapter V along with the analysis from Chapter VI provides verification of the models. These models can provide good device design as well as help predict device performance. By comparing Tables 6.1.1 and 6.2.1 with the device performance, it was determined that the best fit occurred when both the Al concentration  $x$ , measured at 300°K, and the average refractive index  $n_{avg}$  were used.

In order to approach TTL voltage levels, the interaction channel length of the active  $Al_xGa_{1-x}As$  ZGDC's needed to be 5000  $\mu m$  long. This was anywhere from 25 - 40 times longer than the optimum interaction length of the passive devices, depending on the waveguide widths. There was some concern over this until further analysis was performed. Using the models, it was found that even at these long interaction channel lengths, the active  $Al_xGa_{1-x}As$  ZGDC is 5 orders of magnitude shorter than conventional  $Al_xGa_{1-x}As$  directional couplers would be with an air interface. By substituting the measured parameters for the active device along with a waveguide separation of 0.5  $\mu m$ , the minimum resolvable spacing that could be realized with the processing equipment used for this experiment, (into the Marcatili model) yielded a predicted interaction length of 143 m. Even if one were to deposit the highest index matching fluid available ( $n = 2.31$ ) between the waveguides, the interaction length would be over 7 m or 3 orders of

magnitude longer than the ZGDC. Regrowth of  $\text{Al}_x\text{Ga}_{1-x}\text{As}$  between the waveguides was also considered. If this was done, the separation would have to reach  $1.1\text{ }\mu\text{m}$  before the interaction length would be longer than  $5000\text{ }\mu\text{m}$ . This would decrease the phase shift sensitivity and still allow us to operate at TTL voltage levels. Without extensive modifications to the growth chamber, however, one would not be able to realize adequate adhesion to the vertical sidewalls, resulting in a poor interface between the core and side cladding. This would increase the propagation loss. In addition, pattern alignment and electrode fabrication would be much more difficult, as the number of processing steps would significantly increase. More controllable processing then becomes an additional advantage of  $\text{Al}_x\text{Ga}_{1-x}\text{As}$  ZGDC's over conventional  $\text{Al}_x\text{Ga}_{1-x}\text{As}$  directional couplers. Using the above analysis, it becomes evident that an air interface is also very desirable. Waveguides can be run very close together without the risk of coupling. Packing densities for integrated circuits could be greatly increased by using integrated optics. Before the  $\text{Al}_x\text{Ga}_{1-x}\text{As}$  ZGDC can find a place in electronic circuits, questions about integration and manufacturing must be addressed.

### Suggestions for Improvement and Further Research

The major disadvantage of the 5000  $\mu\text{m}$  interaction channel length of the active  $\text{Al}_x\text{Ga}_{1-x}\text{As}$  GDC is that the phase retardation and, hence, the output intensity are very sensitive to the accuracy of the optimum interaction length. Any error in waveguide width and/or Al concentration is essentially being increased by multiples of the difference between the optimum passive interaction length and the actual active interaction channel length. For the active device, one might have to supply up to twice the voltage necessary for switching, depending on what the output phase is with no voltage. If one could operate the device at the optimum interaction length the output intensity error would be minimized. As mentioned in Chapter VI, with regard to the passive device, that even with an error in the interaction length of  $\pm 40 \mu\text{m}$ , the resulting variation in the output intensity would only be 10%. For  $\text{Al}_x\text{Ga}_{1-x}\text{As}$ , however, the voltage necessary to switch at these short distances would be well over 100 V, causing device breakdown. The only solution to achieve short devices and TTL voltage level switching would be to use a material with a higher EO coefficient. To realize, say, a 200  $\mu\text{m}$  device with 5 VDC switching, a material with an electro-optic figure of merit of  $n^3r \geq 1.5 \times 10^{-9} \text{ m/V}$  would be required. This is 25 times higher than that for  $\text{Al}_x\text{Ga}_{1-x}\text{As}$ . Potential candidates that could be used to realize shorter devices include lithium niobate ( $\text{LiNbO}_3$ ), aluminum gallium nitride ( $\text{AlGaN}$ )

and nonlinear electro-optic polymers.  $\text{LiNbO}_3$ , however, is not compatible with standard electronic fabrication processes. It is expensive to package, difficult to interface with other materials and it has a much lower data rate potential than GaAs due to its large dielectric constant.  $\text{AlGaIn}$  and nonlinear electro-optic polymers look very promising but they have only just recently begun to be investigated for electro-optic devices. There is still much development and characterization that needs to be done before these materials can start to compete with GaAs. These materials are currently being investigated through several joint Wright Laboratory (WL)/Advanced Research Projects Agency (ARPA) contracts as well as through a joint effort between the Solid State Electronics Directorate (WL/EL) and the Materials Directorate (WL/ML).

For the present, however, one needs to explore ways to improve the accuracies of material growth and fabrication processing for  $\text{Al}_x\text{Ga}_{1-x}\text{As}$  in order to fabricate practical TTL voltage level active ZGDC switches. For active  $\text{Al}_x\text{Ga}_{1-x}\text{As}$  ZGDC's, assuming a  $\pm 10\%$  variation in the output intensity or a  $\pm 0.5\%$  accuracy in the phase retardation, one would need to be able to control the interaction length to within  $\pm 0.5 \mu\text{m}$ . In order to achieve this kind of accuracy, the tolerance for the refractive index must be  $\pm 0.00006$  (which translates into a  $\pm 0.01\%$  accuracy for the Al concentration) and the tolerance for the waveguide widths must be controlled to within  $\pm 0.02 \mu\text{m}$ .

Aspnes, Quinn and Gregory have recently investigated ways to improve on the accuracy of  $\text{Al}_x\text{Ga}_{1-x}\text{As}$  growth.<sup>18c</sup> They claim that by using in-situ spectroellipsometric monitoring, the compositional precision of  $\text{Al}_x\text{Ga}_{1-x}\text{As}$  can be controlled to better than  $\pm 0.1\%$ . WL/EL is trying similar methods to improve growth accuracies of their MBE machines. On a test run using a modified GEN 2 MBE, an  $\text{Al}_x\text{Ga}_{1-x}\text{As}$  composition to within  $\pm 0.02\%$  was achieved.<sup>57</sup>

For control of the waveguide width, there is a UV based lithographic tool being developed on a WL/ARPA program that has the potential to provide submicron patterning and nanometer alignment accuracies for electronic multichip modules (MCM's) and flat panel displays. This would also serve as an excellent tool for the fabrication of integrated electro-optic circuits.

Polarization rotation is another important issue that needs be addressed before practical circuits can be realized. As mentioned in Chapter VI, using an active polarizer at the output of the ZGDC might be a possible solution. A probable scheme could be to use the EO properties of the  $\text{Al}_x\text{Ga}_{1-x}\text{As}$  material by placing electrodes over the output channels of the device. For no-switching (i.e., no voltage), the output would remain at the same polarization as the input. For switching, the voltage would be applied over the output channel as well as over the interaction channel of the ZGDC. The signal would go through two polarization rotations and the polarization

at the output of the device would be the same as that at the input. This scheme suggests that the output channels would have to be the same length as the interaction channel in order to ensure that the two sections introduced the same amount of polarization rotation. The total length of the ZGDC switch would then be over 1 mm. This is still orders of magnitude shorter than the conventional directional coupler. In addition, the electrodes for the output channels could be fabricated in the same steps as the voltage electrode for the interaction channel and ground electrode. No additional fabrication steps would be required.

Loss is another parameter that needs to be investigated. BPM models were run using S-bends as inputs into the interaction channels of ZGDC's. The BPM predicted a significantly lower loss for these devices. This is due to the fact that S-bends maximize mode confinement, minimize radiative loss and optimize wavefront tilt.<sup>95</sup> In-plane right angle corner bends have also been investigated for both  $\text{Al}_x\text{Ga}_{1-x}\text{As}$  and polymer optical devices.<sup>3,43</sup> The  $\text{Al}_x\text{Ga}_{1-x}\text{As}$  corner bends had air interfaces and used total internal reflection for operation.<sup>3</sup> These  $\text{Al}_x\text{Ga}_{1-x}\text{As}$  bends proved lossy. The polymer cornerbends on the other hand were fabricated with metal deposited at the corner. The polymer bends had negligible loss.<sup>43</sup> Out-of-plane right angle corner bends have also been fabricated in polymers.<sup>43</sup> Out-of-plane corner bends are beneficial for integrating the sources and receivers to the



waveguides within EO circuits and EO MCM's.

Electro-optic transceivers and modulators are other areas of investigation at WL/EL. In order to utilize EO circuits to their full potential, multi-GHz transceivers and/or multi-GHz modulators will be required. Without a transceiver or modulator capable of high data rates, optical interconnects may not progress much further than research devices. Many of the optical waveguide materials have been characterized out to frequencies ranging anywhere from 40 - 100 GHz. This promises good potential for achieving high data rate EO modulators. The transceiver is the remaining device that requires major development for EO circuits. Plans to develop a 100 GHz frequency modulated transceiver are currently underway at WL/EL.

The optical interconnect is beginning to find acceptance within the electronic community. Prototype 2 GHz data rate MCM's using optical interconnects are currently being fabricated on WL/ARPA programs and plans to use optical interconnects for 600 MHz clock distribution in supercomputers is planned for the near future. These programs will provide the mechanism for insertion of active ZGDC's to provide electro-optic reconfigurability when they are fully developed.

## APPENDIX A

### PHOTOLUMINESCENCE MEASUREMENTS

The following pages are the photoluminescence measurements taken of  $\text{Al}_x\text{Ga}_{1-x}\text{As}$  Samples 121 (at 3°K and 300°K), 562 (at 3°K), 1108 (at 3°K) and 179 (at 3°K). These measurements represent the uniformity of the aluminum concentration present in the  $\text{Al}_x\text{Ga}_{1-x}\text{As}$  samples grown by the MOCVD and the three MBE machines used for this experiment as well as the difference between PL measurements taken at the two temperatures. To measure the PL at 3°K, a 200 mW Spectra Physics 375B dye laser source pumped with a 15 W Spectra Physics 171 argon ion laser was used along with two 2 m Bausch and Lomb Spectrograph monochrometers placed end to end. To measure the PL at 300°K, a Spectra Physics 165 argon ion laser source operating at 100 mW was used along with a 0.5 m Jarrell Ash 82-0000 spectrometer.<sup>159</sup>

GROTE G-121

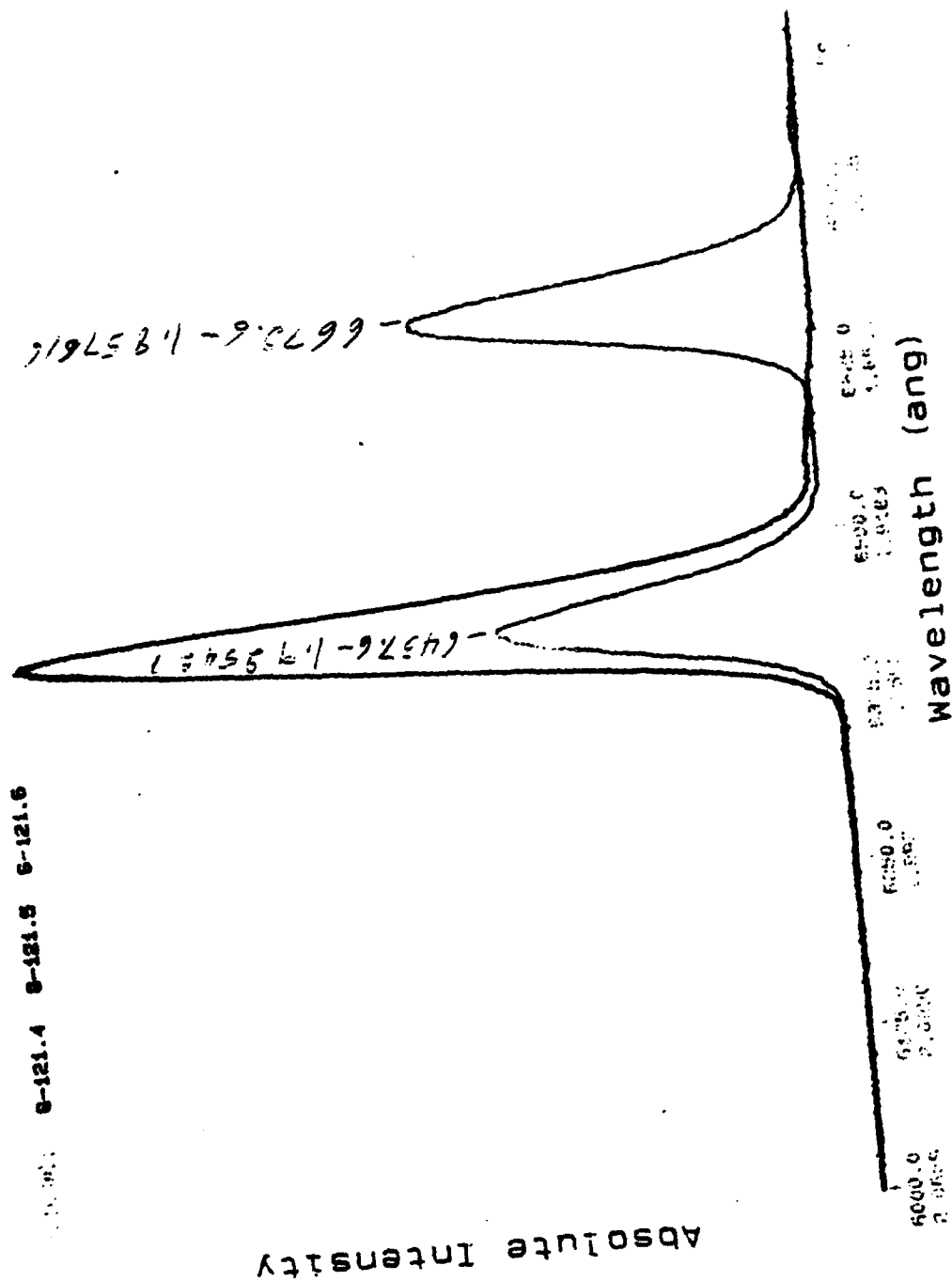


Figure A.1  
Photoluminescence Measurement of Sample 121 taken at 3°K

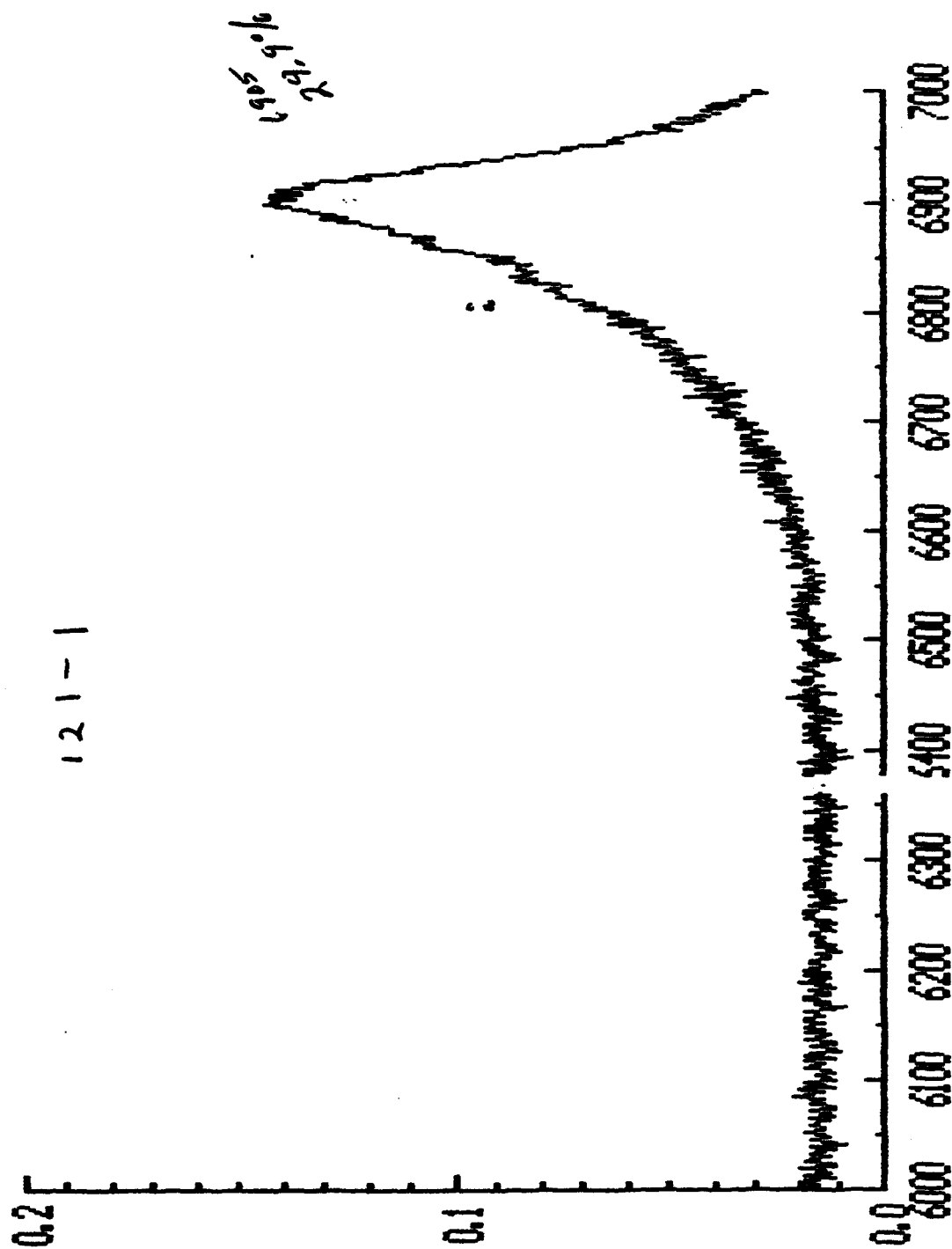


Figure A.2  
Photoluminescence Measurement of Sample 121 taken at 300°K

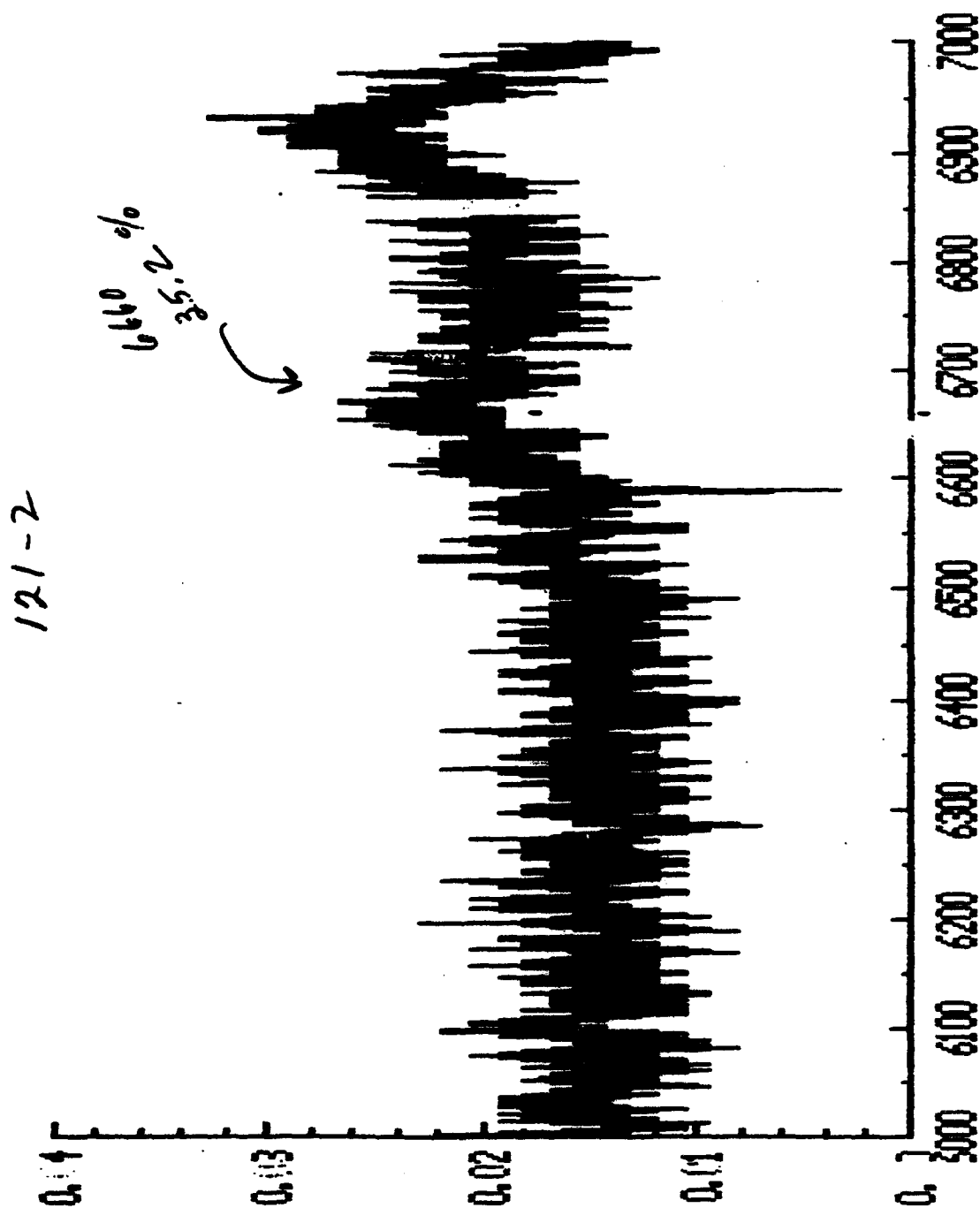


Figure A.3  
Photoluminescence Measurement of Sample 121 taken at 300°K

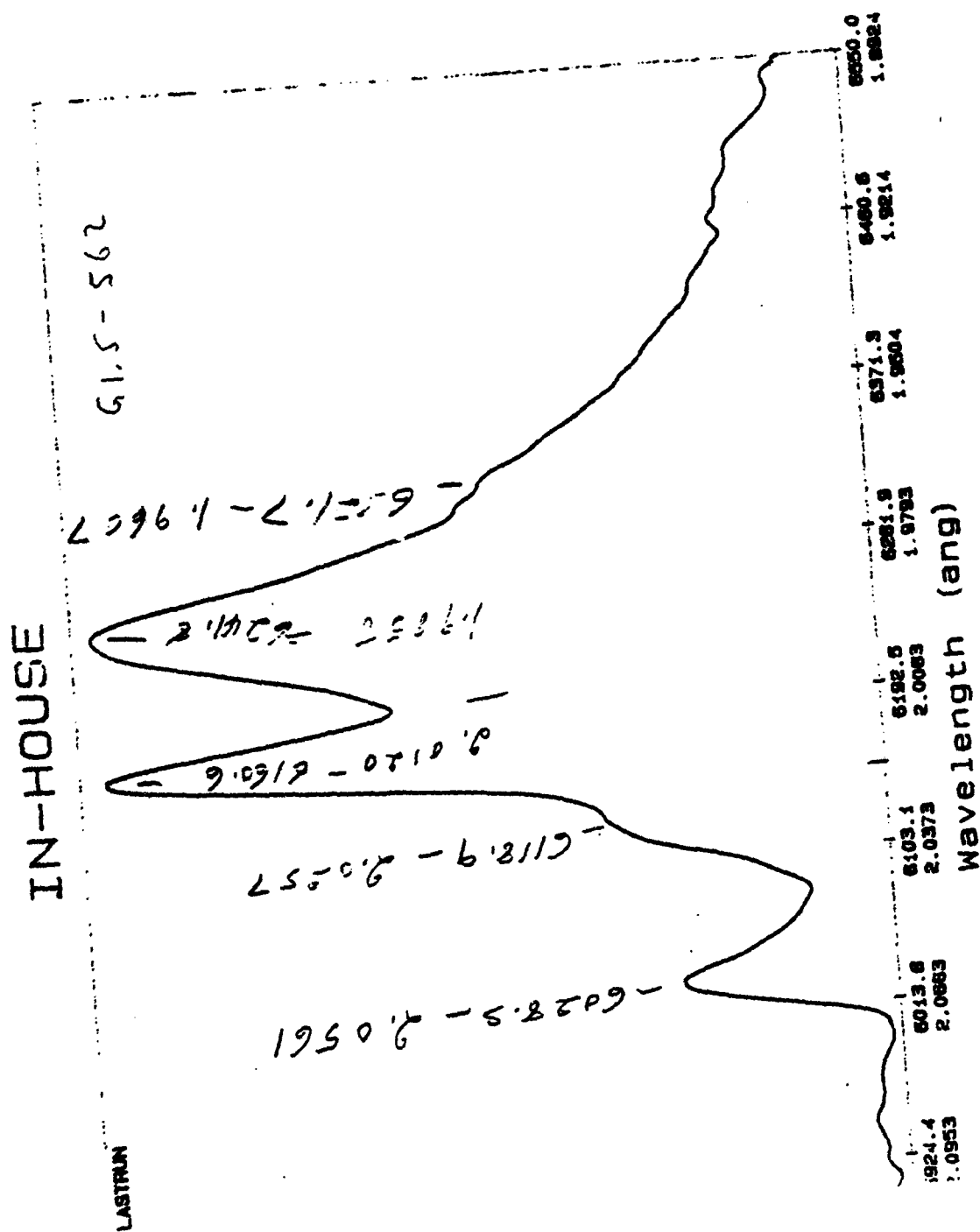


Figure A.4  
Photoluminescence Measurement of Sample 562 taken at 3°K

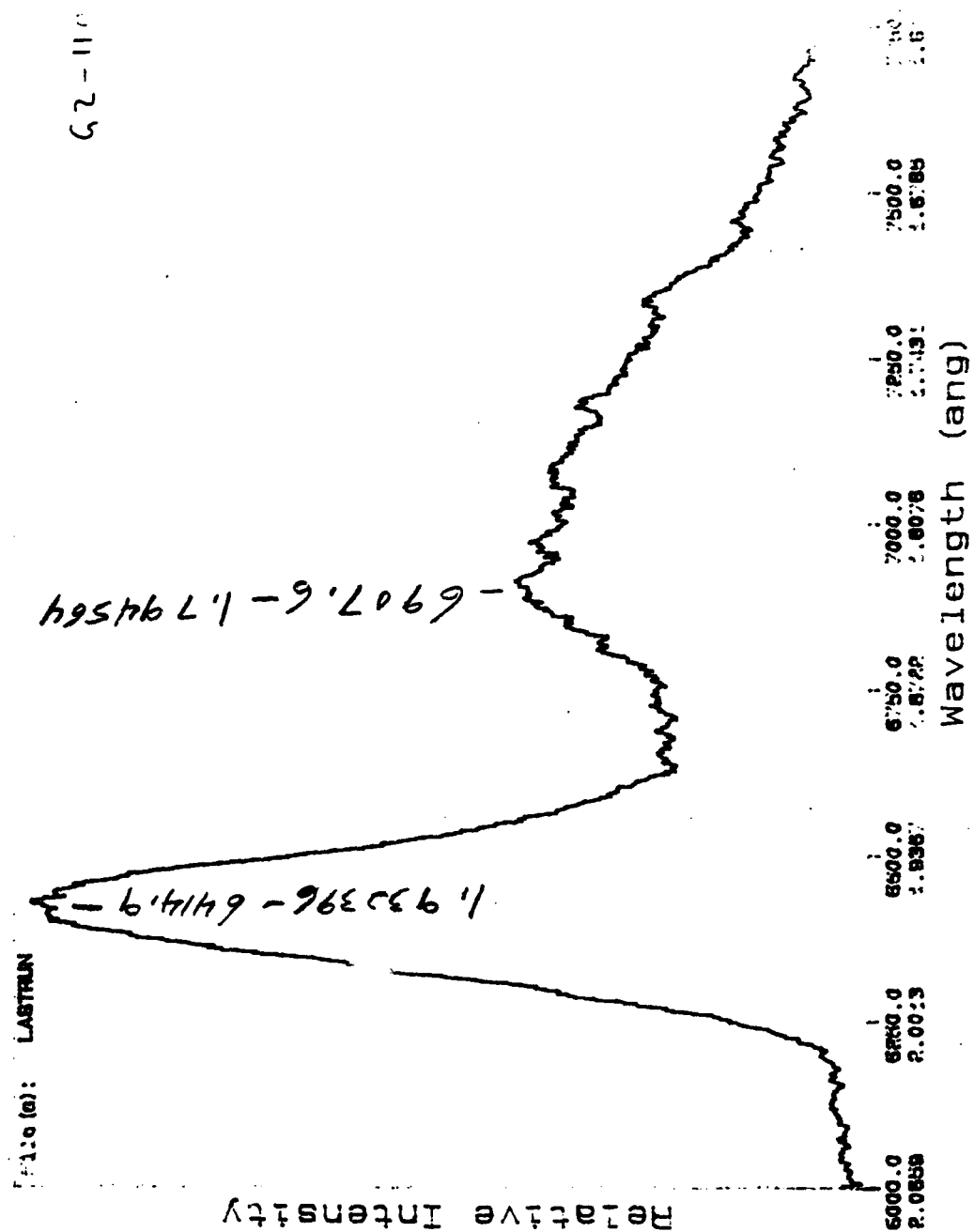


Figure A.5  
Photoluminescence Measurement of Sample 1108 taken at 3°K

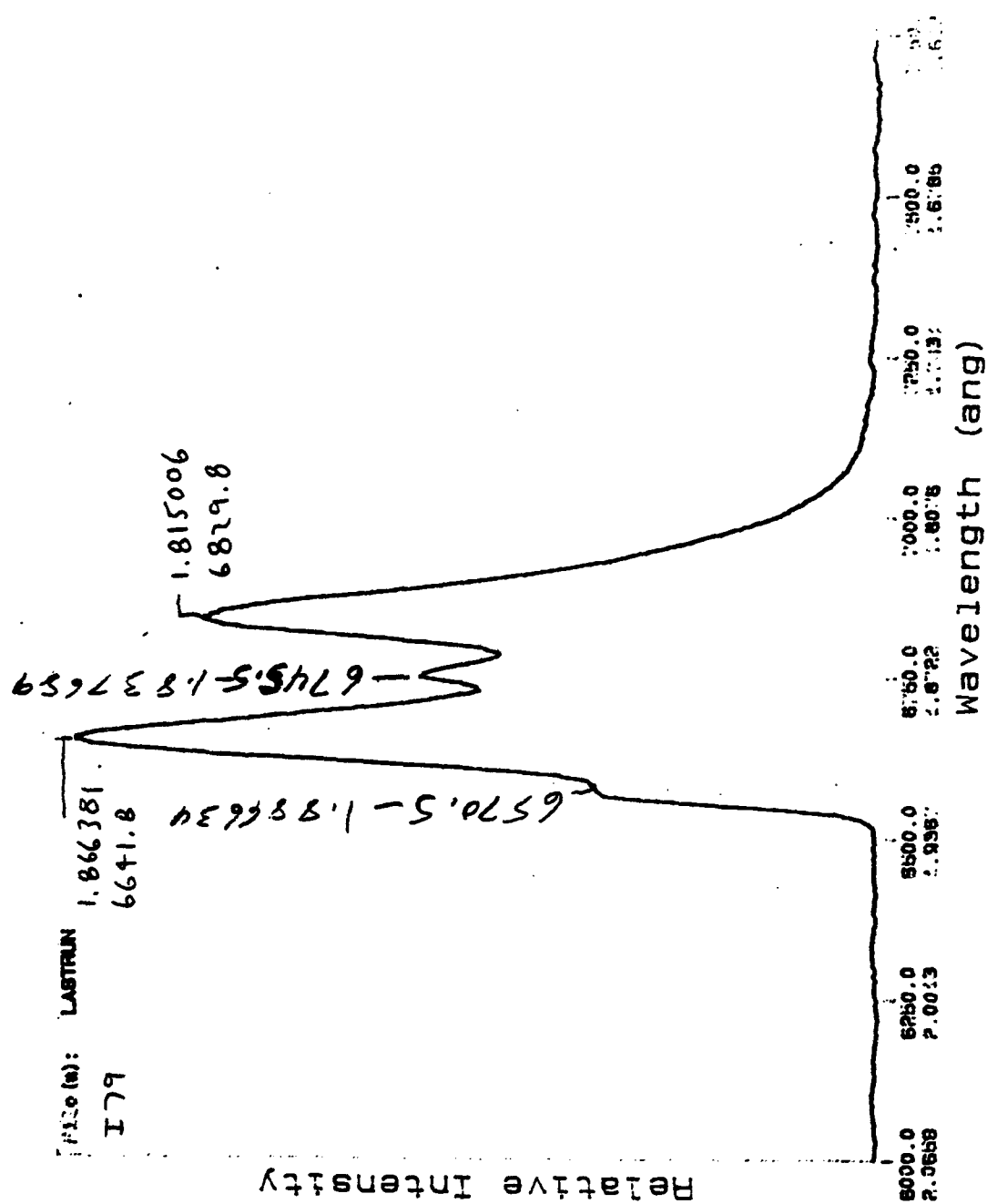


Figure A.6  
Photoluminescence Measurement of Sample I79 taken at 3°K



## **APPENDIX B**

### **PROCESSING TECHNIQUES**

Included here are the processing techniques used to fabricate the  $\text{Al}_x\text{Ga}_{1-x}\text{As}$  optical Fredkin gates. The processing steps start with grown material on top of a GaAs substrate.

#### **Passive Devices**

The passive devices were fabricated using the following procedures:

**A) Clean the surface using a wafer spinner:**

Acetone (ACE) rinse at 1000 rpm for 30 sec

Methanol (MTH) rinse at 1000 rpm for 30 sec

Isopropyl (ISO) rinse at 1000 rpm for 30 sec

Deionized distilled water (DI) rinse at 1000 rpm for 30 sec

Blow dry with dry nitrogen ( $\text{N}_2$ )

Bake at 100°C on a hot plate for 5 min

Cool to room temperature

**B) Deposit Shipley 1400-27 positive photoresist using a wafer spinner:**

Deposit several drops of 1400-27 to the center of the top surface of wafer using a syringe

Spin wafer at 3000 rpm for 30 sec (spinning at 3000 rpm the 1400-27 photoresist will be 1.7  $\mu\text{m}$  thick)

Bake at 100°C on a hot plate for 5 min

Cool to room temperature

Remove the edge bead of resist using a cotton swab and ACE

- C) Expose the surface to the waveguide pattern on the mask using a Karl Suss MJB-3 mask aligner and 505 optical energy controller with  $\lambda = 320 \text{ nm}$  source:

(Align the waveguide pattern so it is perpendicular to the major flat (OF) so that the length of the waveguides will be along the  $\langle 011 \rangle$  direction)

Expose the photoresist at 20  $\text{mW}/\text{cm}^2$  for 40 sec

- D) Develop the waveguide pattern in the resist with a 1:5 ratio of Shipley AZ351 developer to DI using a wafer spinner:

AZ351:DI (1:5) develop at 500 rpm for 35 sec

DI rinse at 500 rpm for 1 min

Blow dry with dry  $\text{N}_2$

Bake at 100°C on a hot plate for 5 min

Cool to room temperature

- E) Remove any photoresist left in the waveguide channels with oxygen ( $\text{O}_2$ ) plasma using a Plasma-Therm Series 70 reactive ion etch (RIE):

Set  $\text{O}_2$  at 90 sccm

Set pressure at 150 mT

Set RF power at 75 W

Set DC bias at 220 V

Operate for 1 min

F) Just before RIE of waveguide pattern:

Dip the wafer in a 1:10 ratio of Shipley buffered oxide etch (BOE) to DI for 15 sec

Dip in running DI for 1 min

Blow dry with dry N<sub>2</sub>

Bake at 100°C on a hot plate for 3 min

Cool to room temperature

G) Etch the waveguide pattern using a Plasma-Therm Series 700 RIE:

1) Set helium (He) flow rate at 45 sccm

2) Set boron trichloride (BCl<sub>3</sub>) flow rate at 60 sccm

3) Set pressure at 25 mT

4) Set RF power at 100 W

5) Set DC bias at 230 V

6) Etch for 30 min

Pump Down

7) Turn RF power off

8) Turn gas flow off

9) Reduce pressure to  $5 \times 10^{-6}$  mT

10) Hold pump down parameters for 10 min

Repeat steps 1 - 10 for two (2) additional times

Repeat steps 1 - 6

(This gives a total etch time of 120 min. The 10 min pump down after each 30 min of etch is to prevent the resist from over heating from the RF)

H) Remove the remaining photoresist from the surface with oxygen ( $O_2$ ) plasma using a Plasma-Therm Series 70 RIE:

Set  $O_2$  at 90 sccm

Set pressure at 100 mT

Set RF power at 75 W

Set DC bias at 240 V

Operate for 10 min

### Active Devices

The active devices were fabricated using the following procedures:

A) Clean the surface using the cleaning procedure described in the previous section

B) Deposit Shipley PMGI positive photoresist using a wafer spinner:

Deposit several drops of PMGI to the center of the top surface of the wafer using a syringe

Spin at 4000 rpm for 30 sec (spinning at 4000 rpm the PMGI photoresist will be  $0.95 \mu\text{m}$  thick)

Bake at 270°C on a hot plate for 5 min

Cool to room temperature

- C) Deposit Shipley 1400-27 positive photoresist using a wafer spinner:

Deposit several drops of 1400-27 to the center of the top of the wafer (over the PMGI) using a syringe

Spin at 4000 rpm for 30 sec (spinning at 4000 rpm the 1400-27 photoresist will be 1.35  $\mu\text{m}$  thick)

Bake at 100°C on a hot plate for 5 min

Cool to room temperature

- D) Expose the 1400-27 photoresist with the electrode pattern using a Karl Suss MJB-3 mask aligner and 505 optical energy controller with  $\lambda = 320 \text{ nm}$  source:

(Align the electrode pattern so that it is perpendicular to the major flat (OF) so that the length of the electrodes will be along the  $\langle 011 \rangle$  direction)

Expose the 1400-27 photoresist at 20  $\text{mW}/\text{cm}^2$  for 30 sec

- E) Develop the electrode pattern in the 1400-27 resist with a 1:5 ratio of Shipley AZ351 developer to DI using a wafer spinner:

AZ351:DI (1:5) develop at 500 rpm for 25 sec

DI rinse at 500 rpm for 1 min

Blow dry with dry  $\text{N}_2$

- F) Expose the developed electrode pattern in the PMGI using a deep ultra violet source with  $\lambda = 205 \text{ nm}$ :

Expose the PMGI photoresist at 900 W for 200 sec

- G) Develop the electrode pattern in the PMGI resist with Shipley SAL 101 developer using a wafer spinner:

**SAL 101 develop at 500 rpm for 50 sec**

**DI rinse at 500 rpm for 1 min**

**Blow dry with dry N<sub>2</sub>**

- H) Plasma etch the surface to remove any remaining developed resist from the electrode channels using a Plasmaline O<sub>2</sub> plasma system:**

**Plasma etch at 30 W RF, 1.0 Torr of pressure and a flow rate of 2 scfm for 6 min**

**Bake at 100°C on a hot plate for 5 min**

**Cool to room temperature**

- I) Just before metallization:**

**Dip the wafer in a 1:1 ratio of Shipley BOE to DI for 15 sec**

**Dip in running DI for 1 min**

**Blow dry with dry N<sub>2</sub>**

- J) Deposit 300 Å of titanium (Ti), 400 Å of platinum (Pt) and 3500 Å of gold (Au), in that order, to the wafer using a Temescal FC-1800 electron beam evaporator**

- K) Remove all the unpatterned metal from the surface:**

**Dip the wafer in ACE for 53 min to remove the 1400-27**

**Dip in ISO for 1 min**

**With the surface still wet place the wafer on the wafer spinner**

**ACE rinse at 700 rpm for 30 sec**

**MTH rinse at 700 rpm for 30 sec**

**ISO rinse at 700 rpm for 30 sec**

DI rinse at 700 rpm for 30 sec

Blow dry with dry nitrogen ( $N_2$ )

(This performs a metal liftoff. All metal on top of unexposed resist is removed. The electrode pattern has now been defined on the surface)

- L) Dip the wafer in 90°C Shipley 1165 remover for 2 min to remove the PMGI

Dip in running DI for 2 min

Blow dry with dry nitrogen ( $N_2$ )

- M) Plasma etch any remaining resist following step H above

- N) Perform steps A and B from the previous section

- O) Expose the surface of the wafer with the waveguide pattern using a Karl Suss MJB-3 mask aligner and 505 optical energy controller with  $\lambda = 320$  nm source:

(Align the waveguide pattern on the mask so that the interaction length sections of the zero-gap directional couplers line up with the electrode patterns on the wafer)

Expose the 1400-27 photoresist at 20 mW/cm<sup>2</sup> for 40 sec

- P) Complete the device fabrication using steps D - H from the previous section

## **APPENDIX C**

### **EQUIPMENT LIST**

Below is a list of the equipment used during the course of this experiment.

#### **Modelling**

Sun Sparc Station 2 computer

IBM personal computer with Intel 486 processor

#### **Material Growth**

Varian 360 molecular beam epitaxy (MBE)

Varian 1.5 MBE

Varian 2 MBE

Aixtron AIX 200 metal-organic chemical vapor deposition (MOCVD)

#### **Fabrication**

Omni-Dex Design Workshop 2000 graphics programming environment



Jeol JBX-5D11 electron beam fine lithography system

Solitec wafer spinner

Karl Suss MBJ-3 mask aligner

Karl Suss 505 optical energy controller

Jerry Bachur & Associates JBA 205 nm deep UV light source and constant intensity controller with JBA 55 shutter controller

Tegal Plasmaline O<sub>2</sub> plasma system

Temescal FC-1800 electron beam evaporator

Plasma-Therm Series 700 reactive ion Etch (RIE)

Plasma-Therm Series 70 RIE

### Characterization

SPEX Industries 1269 Spectrometer

3°K photoluminescence (Spectra Physics 375B dye laser, Spectra Physics 171 argon ion laser and two 2 m Bausch and Lomb Spectrograph monochrometers placed end to end)

300°K photoluminescence (Spectra Physics 165 argon ion laser and a 0.5 m Jarrell Ash 82-0000 spectrometer)

Cambridge Stereoscan 250 Mk2 scanning electron microscope (SEM)

Jeol JSM-IC 845A SEM

Tencor Alpha-Step 250 surface profiler

Carl Zeiss Axioplan MC80 microscope

Cohu 6315-2001/AL16 CCD camera

Data Translation DT 3852-2 flexible frame processor

Data Translation GLOBAL LAB image analysis software

Hewlett-Packard HP 6115A precision power supply

Miscellaneous

ILX Lightwave LDX-3207B precision current source

ILX Lightwave LDT-5910 temperature controller

ILX Lightwave LDM-4412 laser diode mount

Alessi MH4 probe micropositioners

Klinger Scientific MC4 programmable stepping motor controller

Klinger Scientific MD4 stepping motor driver

Klinger Scientific UZ80 PP stepping motor driven vertical translation stage

Klinger Scientific UR80 PP stepping motor driven rotation stage

Klinger Scientific UT100 PP stepping motor driven linear translation stage

Klinger Scientific BG50 PP stepping motor driven goniometric cradle

## BIBLIOGRAPHY

1. T. C. Edwards, Foundations for Microstrip Circuit Design, John Wiley and Sons, New York, NY, 1985.
2. J. W. Goodman, F. I. Leonberger, S-Y Kung and R. A. Athale, "Optical Interconnections for VLSI Systems," Proceedings of the IEEE, Vol. 72, 850, (1984).
3. C. T. Sullivan, "III-V Optical Waveguide Technology," United States Air Force Technical Report, WRDC-TR-90-5027, Wright-Patterson Air Force Base, OH, (1990).
4. E. Fredkin and T. Toffoli, "Conservative Logic," International Journal of Theoretical Physics, Vol. 21, 219, (1982).
5. R. Cuykendall and D. R. Anderson, "Reversible Optical Computing Circuits," Optics Letters, Vol. 12, 542, (1987).
6. R. Cuykendall, "Three-Port Reversible Logic," Applied Optics, Vol. 27, 1772, (1988).
7. R. Cuykendall and D. McMillin, "Control-Specific Optical Fredkin Circuits," Applied Optics, Vol. 26, 1959, (1987).
8. J. Shamir, H. J. Caulfield, W. Miceli and R. J. Seymour, "Optical Fredkin Gate," SPIE Journal on Optical Computing, Vol. 625, 2, (1986).
9. J. Shamir, H. J. Caulfield, W. Micelli and R. J. Seymour, "Optical Computing and the Fredkin Gates," Applied Optics, Vol. 25, 1604, (1986).

10. K. M. Johnson, M. R. Surette and J. Shamir, "Optical Interconnection Network Using Polarization-Based Ferroelectric Liquid Crystal Gates," Applied Optics, Vol. 27, 1727, (1988).
11. E. M. Dianov, A. A. Kuznetsov, S. M. Nejjodov and G. G. Voevodkin, "Optical Realization of Fredkin Gates Matrix Using Liquid Crystal Light Valve," SPIE Journal on Digital Optical Computing II, Vol. 1215, 314, (1990).
12. R. A. Fisher, ed., Optical Phase Conjugation, Academic Press, New York, NY, 1983.
13. C. S. Tsai, B. Kim and F. R. El-Akkari, "Optical Channel Waveguide Switch and Coupler Using Total Internal Reflection," IEEE Journal of Quantum Electronics, Vol. QE-14, 513, (1978).
14. R. Golshan and J. S. Bedi, "Reversible Nonlinear Interface Optical Computing," Optical Engineering, Vol. 28, 683, (1989).
15. M. Schienle, L. Stoll, G. Schulte-Roth, R. Muller-Nawrath, H. F. Mahlein, R. Marz and C. Cremer, "GaInAsP/InP Zero-Gap Directional Couplers as Compact Optical WDM Filters," Electronics Letters, Vol. 25, 1180, (1989).
16. A. Yariv and P. Yeh, Optical Waves in Crystals, John Wiley and Sons, New York, NY, 1984.
17. D. L. Lee, Electromagnetic Principles of Integrated Optics, John Wiley and Sons, New York, NY, 1986.
18. R. A. Forber and E. Marom, "Symmetric Directional Coupler Switches," IEEE Journal of Quantum Electronics, Vol. QE-22, 911, (1986).
19. M. J. Robertson, S. Ritchie and P. Dayan, "Semiconductor Waveguides: Analysis of Optical Propagation in Single Rib Structures and Directional Couplers," IEE Proceedings, Vol. 132, Pt. J, 336, (1985).

20. G. E. Betts and W. S. C. Chang, "Crossing-Channel Waveguide Electrooptic Modulators," IEEE Journal of Quantum Electronics, Vol. QE-22, 1027, (1986).
21. M. Papuchon and Am. Roy, "Electrically Active Optical Bifurcation: BOA," Applied Physics Letters, Vol. 31, 266, (1977).
22. K. Goel and W. S. C. Chang, "Extinction Ratio Degradation Due to Asymmetry in Zero-Gap Directional Coupling and Crossing Channel Switches," IEEE Journal of Quantum Electronics, Vol. QE-23, 2216, (1987).
23. K. Goel and W. S. C. Chang, "Design Considerations for Crossing Channel Switches," IEEE Journal of Quantum Electronics, Vol. QE-25, 47, (1989).
24. K. Goel, E. Wooten and W. S. C. Chang, "Design Considerations for Low Switching Voltage Crossing Channel Switches," Journal of Lightwave Technology, Vol. 6, 881, (1988).
25. R. A. Forber and E. Marom, "Optimization of Symmetric Zero-Gap Directional Couplers for Large Switch-Array Applications," Conference of Lasers and Electro-Optics Technology Digest, 288, (1985).
26. S. Gevorgyan and A. Hovsepyan, "Power Distribution in Symmetric Integrated Optic X Junction," Electronics Letters, Vol. 26, 788, (1990).
27. A. Neyer, "Electro-Optic X-Switch Using Single-Mode Ti:LiNbO<sub>3</sub> Channel Waveguides," Electronics Letters, Vol. 19, 553, (1983).
28. F. Rottmann, A. Neyer, W. Mevenkamp and E. Voges, "Integrated-Optic Wavelength Multiplexers on Lithium Niobate Based on Two-Mode Interference," Journal of Lightwave Technology, Vol. 6, 946, (1988).

29. C. De Bernardi, S. Morasca, C. Rigo, B. Sordo, A. Stano, I. R. Croston and T. P. Young, "Two Mode Interference Wavelength Demultiplexer Monolithically Integrated on InP, For 1.5 or 1.3  $\mu\text{m}$  Operation," SPIE Journal of the 5th European Conference on Integrated Optics: ECIO '89, Vol. 1141, 238, (1989).
30. J. Shamir and H. J. Caulfield, "High-Efficiency Rapidly Programmable Optical Interconnections," Applied Optics, Vol. 26, 1032, (1987).
31. J. Shamir, "Three-Dimensional Optical Interconnection Gate Array," Applied Optics, Vol. 26, 3455, (1987).
32. R. Cuykendall and D. R. Anderson, "Reversible Computing: All-Optical Implementation of interaction and Priesse Gates," Optics Communications, Vol. 62, 232, (1987).
33. G. J. Milburn, "Quantum Optical Fredkin Gate," Physical Review Letters, Vol. 62, 2124, (1989).
34. P. W. Smith, "On the Physical Limits of Digital Optical Switching and Logic Elements," Bell System Technical Journal, Vol. 61, 1975, (1982).
35. J. Shamir, "Fundamental Speed Limitations on Parallel Processing," Applied Optics, Vol. 26, 1567, (1987).
36. K. Goel and W. S. C. Chang, "Effect of Asymmetry on Extinction Coefficient of Crossing Channel LiNbO<sub>3</sub> Waveguide Switches," SPIE Journal on Integrated Optical Circuit Engineering V, Vol. 835, 118, (1987).
37. E. L. Johnson and M. A. Karim, Digital Design: A Pragmatic Approach, Prindle, Weber and Schmidt, Boston, MA, 1987.
38. R. G. Hunsperger, Integrated Optics: Theory and Technology, Second edition, Springer-Verlag, New York, NY, 1985.

39. L. D. Hutcheson, ed., Integrated Optical Circuits and Components: Design and Applications, Marcel Dekker, New York, NY, 1987.
40. T. Tamir, ed., Topics in Applied Physics Volume 7: Integrated Optics, Second edition, Springer-Verlag, New York, NY, 1985.
41. S. Martellucci and A. N. Chester, eds., Integrated Optics: Physics and Applications, Plenum Press, New York, NY, 1983.
42. G. W. Taylor, "Three Terminal Opto-Electronic Array," United States Air Force Technical Report, WL-TR-91-5008, Wright-Patterson Air Force Base, OH, (1992).
43. G. F. Lipscomb, "Integrated Optical Organic Devices," United States Air Force Technical Report, WL-TR-93-5007, Wright-Patterson Air Force Base, OH (1993).
44. T. E. Van Eck, Principal Investigator, "Optical Interconnect Technology," On Going Wright Laboratory Contract, Lockheed Missiles and Space Company, Palo Alto, CA, Private Conversations, (1992-1994).
45. J. T. Boyd, "Theory of Parametric Oscillation Phase Matched in GaAs Thin-Film Waveguides," IEEE Journal of Quantum Electronics, Vol. QE-8, 788, (1972).
46. M. Illegems and G. L. Pearson, "Infrared Reflection of  $\text{Ga}_{1-x}\text{Al}_x\text{As}$  Mixed Crystals," Physical Review B, Vol. 1, 1576, (1970).
47. H. C. Casey Jr., D. D. Sell and M. B. Panish, "Refractive Index of  $\text{Al}_x\text{Ga}_{1-x}\text{As}$  Between 1.2 and 1.8 eV," Applied Physics Letters, Vol. 24, 63, (1974).
48. S. Adachi, "GaAs, AlAs, and  $\text{Al}_x\text{Ga}_{1-x}\text{As}$ : Material Parameters for use in Research and Device Applications," Journal of Applied Physics, Vol. 58, R1, (1985).

49. S. Adachi and K. Oe, "Internal Strain and Photoelastic Effects in  $\text{Ga}_{1-x}\text{Al}_x\text{As}$  and  $\text{In}_{1-x}\text{Ga}_x\text{As}_y\text{P}_{1-y}/\text{InP}$  Crystals," Journal of Applied Physics, Vol. 54, 6620, (1983).
50. O. Berolo and J. C. Woolley, "Electroreflectance Spectra of  $\text{Al}_x\text{Ga}_{1-x}\text{As}$  Alloys," Canadian Journal of Physics, Vol. 49, 1335, (1971).
51. H. J. Lee, L. Y. Juravel, J. C. Woolley and A. J. SpringThorpe, "Electron Transport and Band Structure of  $\text{Ga}_{1-x}\text{Al}_x\text{As}$  Alloys," Physical Review B, Vol. 21, 659, (1980).
52. D. E. Aspnes, S. M. Kelso, R. A. Logan and R. Bhat, "Optical Properties of  $\text{Al}_x\text{Ga}_{1-x}\text{As}$ ," Journal of Applied Physics, Vol. 60, 754, (1986).
53. S. Adachi, "Optical Dispersion Relations for GaP, GaAs, GaSb, InP, InSb,  $\text{Al}_x\text{Ga}_{1-x}\text{As}$ , and  $\text{In}_{1-x}\text{Ga}_x\text{As}_y\text{P}_{1-y}$ ," Journal of Applied Physics, Vol. 66, 6030, (1989).
54. S. Adachi, "Optical Properties of  $\text{Al}_x\text{Ga}_{1-x}\text{As}$ ," Physical Review B, Vol. 38, 345, (1988).
55. S. Logothetidis, L. Viña and M. Cardona, "Temperature Dependence of the Dielectric Function and the Interband Critical Points of InSb," Physical Review B, Vol. 31, 947, (1985).
56. A. K. Ghatak, K. Thyagarajan and M. R. Shenoy, "Numerical Analysis of Planar Optical Waveguides Using Matrix Approach," Journal of Lightwave Technology, Vol. LT-5, 660, (1987).
57. K. Evans, Research Division, Solid State Electronics Directorate, Wright-Patterson Air Force Base, OH, Private Conversations, (1992-1994).
58. C. Sullivan, Honeywell, Inc., Bloomington, MN, Private Conversations, (1990-1993).



59. M. Rona, Arthur D. Little, Inc., Cambridge, MA, Private Conversations, (1992).
60. E. D. Palik, ed., Handbook of Optical Constants of Solids II, Academic Press, San Diego, CA, 1991.
61. E. A. J. Marcatili, "Dielectric Rectangular Waveguide and Directional Coupler for Integrated Optics," Bell System Technical Journal, Vol. 48, 2071, (1969).
62. D. Marcuse, Theory of Dielectric Optical Waveguides, Academic Press, New York, NY, 1974.
63. D. Marcuse, Light Transmission Optics, Second edition, Van Nostrand Reinhold, New York, NY, 1982.
64. J. E. Goell, "A Circular-Harmonic Computer Analysis of Rectangular Dielectric Waveguides," Bell System Technical Journal, Vol. 48, 2133, (1969).
65. D. Marcuse, ed., Integrated Optics, IEEE Press, New York, NY, 1973.
66. W. K. Burns and A. F. Milton, "Mode Conversion in Planar-Dielectric Separating Waveguides," IEEE Journal of Quantum Electronics, Vol. QE-11, 32, (1975).
67. H. Nishihara, M. Haruna and T. Suhara, Optical Integrated Circuits, McGraw-Hill, New York, NY, 1985.
68. J. A. Fleck, J. R. Morris and M. D. Feit, "Time-Dependent Propagation of High Energy Laser Beams Through the Atmosphere," Applied Physics, Vol. 10, 129, (1976).
69. M. D. Feit and J. A. Fleck, "Light Propagation in Graded-Index Optical Fibers," Applied Optics, Vol. 17, 3990, (1978).
70. M. D. Feit and J. A. Fleck, "Calculation of Dispersion in Graded-Index Multimode Fibers by a Propagating-Beam Method," Applied Optics, Vol. 18, 2843, (1979).

71. M. D. Feit and J. A. Fleck, "Computation of Mode Properties in Optical Fiber Waveguides by a Propagating Beam Method," Applied Optics, Vol. 19, 1154, (1980).
72. M. D. Feit and J. A. Fleck, "Computation of Mode Eigenfunctions in Graded-Index Optical Fibers by the Propagating Beam Method," Applied Optics, Vol. 19, 2240, (1980).
73. J. A. Fleck, Jr. and M. D. Feit, "Mode Properties and Dispersion for Two Optical Fiber Profiles by the Propagating Beam Method," Applied Optics, Vol. 19, 3140, (1980).
74. J. Van Roey, J. van der Donk and P. E. Lagasse, "Beam-Propagation Method: Analysis and Assessment," Journal of the Optical Society of America, Vol. 71, 803, (1981).
75. J. A. Fleck, Jr. and M. D. Feit, "Beam Propagation in Uniaxial Anisotropic Media," Journal of the Optical Society of America, Vol. 73, 920, (1983).
76. N. Mabaya, P. E. Lagasse and P. Vandenbulcke, "Finite Element Analysis of Optical Waveguides," IEEE Transactions, Vol. MTT-29, 600, (1981).
77. B. M. A. Rahman and J. B. Davies, "Finite-Element Solution of Integrated Optical Waveguides," Journal of Lightwave Technology, Vol. LT-2, 682, (1984).
78. B. M. A. Rahman and J. B. Davies, "Vector-H Finite Element Solution of GaAs/GaAlAs Rib Waveguides," IEEE Proceedings, Vol. 132, Pt. J, 349, (1985).
79. K. S. Chiang, "Dual Effective-Index Method for the Analysis of Rectangular Dielectric Waveguides," Applied Optics, Vol. 25, 2169, (1986).

80. P. C. Kendall, M. J. Adams, S. Ritchie and M. J. Robertson, "Theory for Calculating Approximate Values for the Propagation Constants of an Optical Rib Waveguide by Weighting the Refractive Indices," IEE Proceedings, Vol. 134, Pt. A, 699, (1987).
81. J. J. G. M. Van Der Tol and N. H. G. Baken, "Correction to Effective Index Method for Rectangular Dielectric Waveguides," Electronics Letters, Vol. 24, 207, (1988).
82. J. J. Gribble and J. M. Arnold, "Beam Propagation Method and Geometrical Optics," IEE Proceedings, Vol. 135, Pt. J, 343, (1988).
83. E. A. J. Marcatili and A. A. Hardy, "The Azimuthal Effective-Index Method," IEEE Journal of Quantum Electronics, Vol. 24, 766, (1988).
84. H. F. Taylor and A. Yariv, "Guided Wave Optics," Proceedings of the IEEE, Vol. 62, 1044, (1974).
85. A. Hardy and W. Streifer, "Coupled Mode Theory of Parallel Waveguides," Journal of Lightwave Technology, Vol. LT-3, 1135, (1985).
86. E. A. J. Marcatili, "Improved Coupled-Mode Equations for Dielectric Guides," IEEE Journal of Quantum Electronics, Vol. QE-22, 988, (1986).
87. H. A. Haus, W. P. Huang, S. Kawakami and N. A. Whitaker, "Coupled-Mode Theory of Optical Waveguides," Journal of Lightwave Technology, Vol. LT-5, 16, (1987).
88. A. Neyer, W. Mevenkamp, L. Thylen and B. Lagerström, "A Beam Propagation Method Analysis of Active and Passive Waveguide Crossings," Journal of Lightwave Technology, Vol. LT-3, 635, (1985).
89. J. T. Boyd, Integrated Optics Devices and Applications, IEEE Press, New York, NY, 1991.

90. Working Group I, COST-216, "Comparison of Different Modeling Techniques for Longitudinally Invariant Integrated Optical Waveguides," IEE Proceedings, Vol. 136, Pt. J, 273, (1989).
91. M. Born and E. Wolf, Principles of Optics, Sixth edition, Pergamon Press, New York, NY, 1986.
92. S. M. Selby, ed., Standard Mathematical Tables, Twenty-third edition, CRC Press, Cleveland, OH, 1975.
93. J. W. Goodman, Introduction to Fourier Optics, McGraw-Hill, New York, NY, 1968.
94. A. Ticknor, Lockheed Missiles & Space Company, Palo Alto, CA, Private Conversations, (1990-1994).
95. W. J. Minford, S. K. Korotky and R. C. Alferness, "Low-Loss Ti:LiNbO<sub>3</sub> Waveguide Bends at  $\lambda = 1.3 \mu\text{m}$ ," IEEE Journal of Quantum Electronics, Vol. QE-18, 1802, (1982).
96. S. Namba, "Electro-Optical Effect of Zincblende," Journal of the Optical Society of America, Vol. 51, 76, (1961).
97. M. Young, Optics and Lasers: Including Fibers and Optical Waveguides, Fourth edition, Springer-Verlag, New York, NY, 1992.
98. R. T. Weidner and R. T. Sells, Elementary Physics: Classical and Modern, Allyn and Bacon, Boston, MA, 1975.
99. J. D. Kraus and K. R. Carver, Electromagnetics, Second edition, McGraw Hill, New York, NY, 1973.
100. J. F. Nye, Physical Properties of Crystals, Second edition, Oxford University Press, New York, NY, 1985.
101. J. P. van der Ziel and A. C. Gossard, "Absorption, Refractive Index, and Birefringence of AlAs-GaAs Monolayers," Journal of Applied Physics, Vol. 48, 3018, (1977).

102. A. Yariv, Quantum Electronics, Second edition, John Wiley & Sons, New York, NY, 1975.
103. R. C. Weast, ed., CRC Handbook of Chemistry and Physics, Sixty sixth edition, CRC Press, Boca Raton, FL, 1985.
104. R. Scherer and J. Grote, "Scribe and Break Experiments to Determine Preferential Cleave Planes of GaAs Wafer," Unpublished, 1990.
105. A. Yariv, Optical Electronics, Third edition, Holt, Rinehart and Winston, New York, NY, 1985.
106. M. A. Karim, Electro-Optical Devices and Systems, PWS-Kent Publishing, Boston, MA 1990.
107. M. A. Karim and A. A. S. Awwal, Optical Computing: An Introduction, John Wiley & Sons, New York, NY, 1992.
108. A. Sommerfeld, Optics: Lectures on Theoretical Physics, Volume IV, Academic Press, New York, NY, 1959.
109. E. Hecht and A. Zajac, Optics, Addison-Wesley Publishing, Reading, MA, 1974.
110. E. B. Brown, Modern Optics, Reinhold Publishing, New York, NY, 1965.
111. A. Yariv, C. A. Mead and J. V. Parker, "5C3-GaAs as an Electrooptic Modulator at 10.6 Microns," IEEE Journal of Quantum Electronics, Vol. QE-2, 243, (1966).
112. S. Somekh, E. Garmire, A. Yariv, H. L. Garvin and R. G. Hunsperger, "Channel Optical Waveguide Directional Couplers," Applied Physics Letters, Vol 22, 46, (1973).
113. J. Faist, F. -K. Reinhart, D. Martin and E. Tuncel, "Orientation Dependence of the Phase Modulation in a p-n Junction GaAs/Al<sub>x</sub>Ga<sub>1-x</sub>As Waveguide," Applied Physics Letters, Vol. 50, 68, (1987).

114. S. Somekh, E. Garmire, A. Yariv, H. L. Garvin and R. G. Hunsperger, "Channel Optical Waveguides and Directional Couplers in GaAs-Imbedded and Ridged," Applied Optics, Vol 13, 327, (1974).
115. J. C. Campbell, F. A. Blum, D. W. Shaw and K. L. Lawley, "GaAs Electro-Optic Directional-Coupler Switch," Applied Physics Letters, Vol. 27, 202, (1975).
116. J. Faist and F. -K. Reinhart, "Phase Modulation in GaAs/AlGaAs Double Heterostructures. II. Experiment," Journal of Applied Physics, Vol. 67, 7006, (1990).
117. J. P. Donnelly, N. L. DeMeo, Jr. and G. A. Ferrante, "Three-Guide Optical Couplers in GaAs," Journal of Lightwave Technology, Vol. LT-1, 417, (1983).
118. B. H. Kolner, "Picosecond Electro-Optic Sampling in Gallium Arsenide," PhD Dissertation, Stanford University, Stanford, CA, 1985.
119. J. C. Shelton, F. K. Reinhart and R. A. Logan, "Rib Waveguide Switches With MOS Electrooptic Control for Monolithic Integrated Optics in GaAs-Al<sub>x</sub>Ga<sub>1-x</sub>As," Applied Optics, Vol. 17, 2548, (1978).
120. T. E. Walsh, "Gallium-Arsenide Electro-Optic Modulators," RCA Review, Vol. 27, 323, (1966).
121. B. A. Auld, D. M. Bloom, J. L. Freeman, R. Majidi-Ahy, M. J. W. Rodwell and K. J. Weingarten, "Picosecond Electrooptic Investigations of Integrated Circuits," United States Air Force Technical Report, AFWAL-TR-88-1071, Wright-Patterson Air Force Base, OH (1989).
122. C. Shih and A. Yariv, "A Theoretical Model of the Linear Electro-Optic Effect," Journal of Physics C: Solid State Physics, Vol. 15, 825, (1982).
123. Properties of Gallium Arsenide, Second edition, INSPEC, New York, NY, 1990.

124. S. Adachi and K. Oe, "Linear Electro-Optic Effects in Zincblende-Type Semiconductors: Key Properties of InGaAsP Relevant to Device Design," Journal of Applied Physics, Vol. 56, 74, (1984).
125. N. Suzuki and K. Tada, "Elastooptic and Electrooptic Properties of GaAs," Japanese Journal of Applied Optics, Vol. 23, 1011, (1984).
126. A. Hernández-Cabrera, C. Tejedor and F. Meseguer, "Linear Electro-Optic Effects in Zinc Blende Semiconductors," Journal of Applied Physics, Vol. 58, 4666, (1985).
127. E. H. Turner and I. P. Kaminow, "Electro-Optic Effect in GaAs," Journal of the Optical Society of America, Vol. 53, 523, (1963).
128. L. Ho and C. F. Buhrer, "Electro-Optic Effect of Gallium Arsenide," Applied Optics, Vol. 2, 647, (1963).
129. M. Sugie and K. Tada, "Measurements of the Linear Electrooptic Coefficients and Analysis of the Nonlinear Susceptibilities in Cubic GaAs and Hexagonal CdS," Japanese Journal of Applied Physics, Vol. 15, 421, (1976).
130. Yu. V. Shaldin and D. A. Belogurov, "Determination of Nonlinear (Quadratic) Optical Susceptibility of GaAs and GaP From Electro-Optic Measurements," Soviet Journal of Quantum Electronics, Vol. 6, 897, (1976).
131. V. N. Bagdavadze and Yu. N. Berozashvili, "Electrooptic Effect in Noncentrosymmetric Cubic Semiconductor Crystals With Allowance for Spatial Dispersion," Soviet Physics - Semiconductors, Vol. 12, 1115, (1978).
132. I. P. Kaminow, "Measurements of the Electrooptic Effect in CdS, ZnTe and GaAs at 10.6 Microns," IEEE Journal of Quantum Electronics, Vol. QE-4, 23, (1968).

133. M. I. Bell, "Electro-Optic Coefficients of Cubic Semiconductors," 11 International Conference on the Physics of Semiconductors - Proceedings, Vol. 2, 845, (1972).
134. R. J. Pressley, ed., Handbook of Lasers With Selected Data on Optical Technology, CRC Press, Cleveland, OH, 1971.
135. A. Kumar and T. P. Sharma, "Non-Linear Susceptibility of GaAs," Indian Journal of Pure Applied Physics, Vol. 17, 110, (1979).
136. S. C. Varshney and A. A. Gundjian, "First-Order Raman Coefficient as Related to Elasto-Optic, Linear Electro-Optic, and Second-Harmonic-Generation Coefficients in Zinc-Blende Crystals," Journal of Applied Physics, Vol. 52, 6301, (1981).
137. S. Adachi, Physical Properties of III-V Semiconductor Compounds: InP, InAs, GaAs, GaP, InGaAs, and InGaAsP, John Wiley and Sons, New York, NY, 1992.
138. J. C. Shelton, F. K. Reinhart and R. A. Logan, "Characteristics of Rib Waveguides in AlGaAs," Journal of Applied Physics, Vol. 50, 6675, (1979).
139. F. K. Reinhart, R. A. Logan and W. R. Sinclair, "Electrooptic Polarization Modulation in Multielectrode  $\text{Al}_x\text{Ga}_{1-x}\text{As}$  Rib Waveguides," IEEE Journal of Quantum Electronics, Vol. QE-18, 763, (1982).
140. G. Lengyel, "GaAlAs p-i-n Junction Waveguide Modulator," Journal of Lightwave Technology, Vol. LT-1, 251, (1983).
141. L. D. Hutcheson and D. G. Hall, eds., Integrated Optics III - Volume 408, SPIE, Bellingham, WA, 1983.
142. Topical Meeting: Integrated and Guided Wave Optics - Technical Digest, LEOS and OSA, Atlanta, GA, 1986.



143. M. Glick, F. K. Reinhart, G. Weimann and W. Schlapp, "Quadratic Electro-Optic Light Modulation in a GaAs/AlGaAs multiquantum Well Heterostructure Near the Excitonic Gap," Applied Physics Letters, Vol. 48, 989, (1986).
144. R. T. Sahara, W. H. Steier, S. G. Hummel and P. D. Dapkus, "AlGaAs/GaAs Optically Controlled Wave-Plate Modulator," Optics Letters, Vol. 16, 1958, (1991).
145. M. Glick, F. K. Reinhart and D. Martin, "Linear Electro-Optic Effect: Comparison of GaAs/AlGaAs Multi-Quantum-Well Heterostructures With an AlGaAs Solid Solution at 1.1523  $\mu\text{m}$ ," Journal of Applied Physics, Vol. 63, 5877, (1988).
146. C. W. Higginbotham, M. Cardona and F. H. Pollak, "Intrinsic Piezobirefringence of Ge, Si and GaAs," Physical Review, Vol. 184, 821, (1969).
147. S. M. Sze, Physics of Semiconductor Devices, Second edition, John Wiley and Sons, New York, NY, 1981.
148. P. Z. Peebles, Probability, Random Variables and Random Signal Principles, Second edition, McGraw-Hill, New York, NY, 1987.
149. E. H. C. Parker, ed., The Technology and Physics of Molecular Beam Epitaxy, Plenum Press, New York, NY, 1985.
150. R. Williams, Modern GaAs Processing Methods, Artech House, Norwood, MA, 1990.
151. J. Bristow, Principal Investigator, "Optical Interconnect Technology," On Going Wright Laboratory/Advanced Research Projects Agency Contract, Honeywell, Inc., Bloomington, MN, Private Conversations, (1992-1994).
152. G. F. Lipscomb, AKZO Electronic Products, Redwood City, CA, Private Conversations, (1991-1994).

153. A. Husain, Microelectronics Division, Advanced Research Projects Agency, Arlington, VA, Private Conversations, (1992-1994).
154. M. A. Karim, Center for Electro-Optics, University of Dayton, Dayton, OH, Private Conversations, (1990-1994).
155. J. Brandelik, Electro-Optics Division, Solid State Electronics Directorate, Wright-Patterson Air Force Base, OH, Private Conversations, (1990-1994).
156. M. Heiblum, E. E. Mendez and L. Osterling, "Growth by Molecular Beam Epitaxy and Characterization of High Purity GaAs and AlGaAs," Journal of Applied Physics, Vol. 54, 6982, (1983).
157. M. Heiblum, E. E. Mendez and L. Osterling, "Summary Abstract: High Purity GaAs and AlGaAs Grown by MBE," Journal of Vacuum Science and Technology, Vol. B 2, 233, (1984).
158. W. T. Tsang, "The Preparation of Materials for Optoelectronic Applications by Molecular Beam Epitaxy," Journal of Vacuum Science and Technology, Vol. A 2, 409, (1984).
159. M. Hibbs-Brenner, Honeywell, Inc., Bloomington, MN, Private Conversations, (1991-1994).
160. P. J. Pearah, W. T. Masselink, J. Klem, T. Henderson, H. Moroc, C. W. Litton and D. C. Reynolds, "Low Temperature Optical Absorption in  $\text{Al}_x\text{Ga}_{1-x}\text{As}$  Grown by Molecular-Beam Epitaxy," Physical Review B, Vol. 32, 3857, (1985).
161. J. S. Solomon, M. Y. Yen, P. T. Murray, D. A. Walsh, C. Hegde, S. R. Smith, J. T. Grant, I. Maartense, J. A. Detrio and F. Szmulowicz, "Electronic Materials Characterization," United States Air Force Technical Report, WL-TR-92-4026, Wright-Patterson Air Force Base, OH (1992).

162. H. C. Casey and M. B. Panish, Heterostructure Lasers Part A: Fundamental Principles, Academic Press, New York, NY, 1978.
163. H. C. Casey and M. B. Panish, Heterostructure Lasers Part B: Materials and Operating Characteristics, Academic Press, New York, NY, 1978.
164. W. C. Johnson, Transmission Lines and Networks, McGraw-Hill, New York, NY, 1950.
165. D. E. Aspnes, W. E. Quinn and S. Gregory, "Optical Control of Growth of  $\text{Al}_x\text{Ga}_{1-x}\text{As}$  by Organometallic Molecular Beam Epitaxy," Applied Physics Letters, Vol. 57, 2707, (1990).